



THE UNIVERSITY *of* EDINBURGH

This thesis has been submitted in fulfilment of the requirements for a postgraduate degree (e. g. PhD, MPhil, DClinPsychol) at the University of Edinburgh. Please note the following terms and conditions of use:

- This work is protected by copyright and other intellectual property rights, which are retained by the thesis author, unless otherwise stated.
- A copy can be downloaded for personal non-commercial research or study, without prior permission or charge.
- This thesis cannot be reproduced or quoted extensively from without first obtaining permission in writing from the author.
- The content must not be changed in any way or sold commercially in any format or medium without the formal permission of the author.
- When referring to this work, full bibliographic details including the author, title, awarding institution and date of the thesis must be given.

Towards Predicting and Tailoring Properties of Energetic Materials



THE UNIVERSITY
of EDINBURGH

Jack Michael Hemingway

Submitted for the Degree of Doctor of Philosophy

University of Edinburgh

January 2024

Abstract

The field of energetic materials (EMs) involves the study of materials (explosives, propellants, and pyrotechnics) that can release a significant amount of energy when initiated. This property renders EMs particularly useful to a wide array of industries including space travel (rocket propellants), mining (demolition charges), and defence applications. The propensity to release a significant amount of energy upon initiation means these materials are inherently dangerous, as such they are subjected to stringent safety requirements, and must be rigorously characterised prior to use. The safety of an EM is often quantified through the evaluation of the sensitivity (propensity to initiate) with respect to different stimuli such as impact, shock, friction, and electric spark. The focus of this work is the impact sensitivity, a solid-state property which can be influenced through changes in the orientation of molecules in 3D space (polymorphism or co-crystallisation) as well as through changing the structure or bonding environment of the molecules comprising the material. Prediction of this metric has been shown in previous work within the group to be computationally achievable for molecular EMs if the crystal structure of the material is known. This is completed through use of the vibrational up-pumping methodology.

Vibrational up-pumping refers to the process by which mechanical impact energy excites delocalised low energy motions in a material and is subsequently channelled upwards into localised molecular vibrations. The vibrational states excited through up-pumping are termed the two-phonon density of states, which represents a measure of how efficiently the initial energy can become trapped on the molecular vibrations. Projection of the two-phonon density of states onto the underlying vibrational character yields the up-pumped density which shows a correlation with experimental impact sensitivity. To this date, this method has been applied exclusively to molecular EMs, successfully reproducing experimental sensitivities. While important, focusing on solely molecular materials overlooks those of growing importance such as co-crystals, salts and coordination polymers. Application of the

vibrational up-pumping methodology to materials from these areas of growing interest forms the backbone for the work presented in this thesis.

Chapter 2 addresses a number of areas within the vibrational up-pumping methodology that could be improved upon, namely, the generation of consistent phonon density of states ($g(\omega)$) spectra as well as partial $g(\omega)$ spectra, the determination of the location of uppermost phonon frequency (Ω_{\max}) and the interrogation of vibrational modes within the solid-state vibrations to track the local modes of vibration (bond stretches and angle bends). Three Python scripts have been developed to address these problems and improve the efficiency and applicability of the process by which the impact sensitivity of an EM is predicted via the vibrational up-pumping methodology.

Chapter 3 focuses on two unexpected findings that had recently come to light in the EMs group at Edinburgh: a co-crystal of FOX-7 with the non-energetic p-phenylenediamine (PPD) that appeared to be more hazardous to mechanical impact than the pure EM, and a new high-pressure polymorph of 3,4,5-trinitro-1H-pyrazole (TNP) that was markedly more sensitive to initiation than the ambient pressure polymorph. For the former study, strong hydrogen bonding interactions significantly altered the molecular conformation of FOX-7. For the latter, the molecular conformation remained unchanged in the ambient and high-pressure polymorphs, meaning that crystal packing or pressure-induced vibrational mode hardening must account for the increase in mechanical sensitivity. Taken together both studies present challenges for the up-pumping model, which if successful would allow important structure/property connections to be made.

Chapter 4 focuses on salt coordination polymers, all of which present as exceptionally sensitive EMs. The study began with lead azide (LA), which is often used in small quantities as a detonator for a much larger mass of a less sensitive EM. It is well documented that lead has drastic adverse effects to both people and the environment and as such REACH (Registration, Evaluation, Authorisation and Restriction of Chemicals) has issued a ban on the use of LA. This has necessitated the development of a number of 'green' copper-containing replacements (DBX-1, DBX-2, DBX-3 and Cu(ADNP)) with

comparable impact sensitivity and detonation characteristics such that they could potentially be used as drop-in replacements. This type of EM has not been studied before using the vibrational up-pumping procedure; they present a number of unique challenges, exemplified primarily by the need to separate the lattice modes from the molecular modes, which is a key requirement of the vibrational up-pumping model. In this chapter a full discussion on a range of mechanochemical models are investigated, from simple phonon heating, through to up-pumping and consideration of target (i.e. trigger mode) activation. Culminating in the development of a workflow for the treatment of such materials in the future within the vibrational up-pumping methodology.

In Chapter 5 the emphasis switches towards applying the up-pumping model in a wider capacity to explore the effects of molecular structure on the impact sensitivity of molecular energetics. Here, the investigation centred on a series of chemically related EMs from three common families, namely pyrazoles, tetrazoles and nitrate esters. A number of these materials only differ by the location or substitution of a single functional group, and yet taken together cover a wide range of impact sensitivity response. Successful predictions of their respective impact sensitivities by the up-pumping model would therefore present a unique opportunity to fully explore structure/property relationships, with molecular flexibility, functional group identity and proximity being key structural features to explore. The data set also allowed further exploration of the trigger mode activation introduced in Chapter 4, where only the weakest bonds in the molecules are vibrationally excited by up-pumping. This approach improves the physical basis for impact sensitivity prediction.

Collectively, this thesis explores the application of the vibrational up-pumping methodology to various EMs that present with greater structural complexity than the single-component molecular materials that it was initially designed to model. This work has been aided by the development of supplementary Python scripts which attempt to improve both the efficiency and applicability of the vibrational up-pumping methodology. If successful this work will act to considerably validate vibrational up-pumping, as well as to provide the opportunity to explore in-depth structure/property relationships, to understand

the physical basis of impact sensitivity. Such understanding may lead to the development of tailored EMs with desired physical properties in the future.

Lay Summary

The field of energetic materials (EMs) focuses on materials that can release a large amount of energy, such as explosives. This makes them particularly dangerous as they can cause damage upon detonation. They have found common use in the military but also have several civilian applications, ranging from demolitions to mining and as rocket propellants. Due to the potentially disastrous consequences of such materials, their properties and therefore their safety, must be well understood prior to their regular use. The safety of an EM is often measured using the sensitivity which simply represents the amount of energy required to cause an explosion. The most commonly referred to and the focus of this work is the impact sensitivity, which represents the amount of energy required to hit a sample of an EM to cause it to explode. The effect of changing the molecular structure and the 3D arrangement of molecules with respect to one another on the impact sensitivity is explored. The impact sensitivity can be predicted computationally through modelling how the energy moves through the material (vibrational up-pumping).

Vibrational up-pumping aims to explain the mechanism by which impact energy leads to an explosion. This achieved by mimicking the vibrations in the material that are excited when an impact occurs, excitation of higher energy vibrations follows as the energy is up-pumped. The predicted sensitivity is determined through considering the likelihood of energy being up-pumped as well as it being able to cause a response on the molecular level. This procedure has successfully predicted the impact sensitivity of a number of well-studied EMs but has not been applied to several material types that are increasing in popularity in the field, such as, co-crystals, salts and coordination polymers. Consideration of these previously unstudied material types forms most of the work in this thesis.

Chapter 2 involves the development of a number of programs that help to make the vibrational up-pumping methodology easier to use and consistent. These scripts are an attempt to unify the process of making the input data ($g(\omega)$) such that all future results will be comparable to one another. Additionally, scripts to mathematically break down the movement of the atoms within the vibrations

to remove the need for visual examination of them, potentially reducing the extent of human error, again in an attempt to improve the consistency of the process.

Chapter 3 explores the effect of changing the way that molecules interact with one another when in the solid-state on the impact sensitivity using two different examples. Firstly, consideration of a material comprised of molecules of both an EM (FOX-7) and a non-EM (PPD) also known as a co-crystal and secondly, comparison between two different crystal packing arrangements (polymorphs) of an EM known as TNP (one being formed when exposed to high pressure). Both the co-crystal of FOX-7/PPD and the high-pressure polymorph of TNP were found to be more sensitive to impact than the parent materials. Both EMs provide a good test for the applicability of the vibrational up-pumping methodology to their respective structure types, and if successfully predicted to be more sensitive than their parent EMs, an excellent opportunity to gain understanding as to why the sensitivity increases in both cases.

Chapter 4 focuses on metal containing coordinated structures which were previously unstudied using the vibrational up-pumping methodology and are generally very sensitive to impact, a common example is lead azide (LA). Explosives are often detonated using a small mass of a very sensitive material as trigger, LA is an example of a commonly used detonator. The field is trying to move away from the use of LA due to the toxicity of lead to the environment and human life, resulting in it being regulated in the EU. As such many more environmentally friendly EMs with similar properties have been developed based on copper instead of lead (DBX-1, DBX-2, DBX-3 and Cu(ADNP)). The suitability of vibrational up-pumping for impact sensitivity prediction of such materials was tested in this work and a workflow procedure for future materials was designed. The predicted impact sensitivity of each EM was found to be in good agreement with experiment.

The relationship between the impact sensitivity of an EM and the molecular structure was explored in Chapter 5. This was achieved through comparing predicted sensitivities of a series of EMs with small structural changes to one another. Three chemical families were considered (pyrazoles, tetrazoles and

nitrate esters). In general, the predicted sensitivities of all EMs were in good agreement with experiment. Comparison between the impact sensitivity and the flexibility of the molecule (determined using the Kier molecular flexibility index, KMF), along with various structural identifiers provided the main body of this work. Additionally, the weakest chemical bonds in each molecule were found to be stretched slightly (likely the reason for explosion) when exposed to impact. When only the energy that results in this motion is considered the relationship between predicted and experimental sensitivity improves for several EMs. This suggests a possible route for future development of the predictive model.

The work in this thesis attempts to test the impact sensitivity prediction model on types of EMs that have not been studied in this way before and improve the model through development of additional programs which increase the efficiency of use. An additional goal was to develop an understanding of which structural features of an EM result in a sensitive material. Such that this work may be used as a starting point for the development of a new, safe EM entirely from computational efforts.

Declaration

I declare that this thesis was composed by myself, that the work contained herein is my own except where explicitly stated otherwise in the text, and that this work has not been submitted for any other degree or professional qualification except as specified.

Jack M. Hemingway

Acknowledgements

Firstly, I would like to thank my supervisors Prof. Carole Morrison and Prof. Colin Pulham. To Carole, who gave me my first experience of computational chemistry in my 3rd year of my Undergraduate degree which inspired me to pursue my masters and PhD in the subject. To Colin, for all the guidance on the experimental side of energetic materials and keeping my work grounded. I couldn't have asked for a better PhD experience, thank you.

I would like to thank Dr. Adam Michalchuk for not only laying the groundwork for my project but also for always being enthusiastically available to answer my many questions and making time for my long emails and video calls.

To Imogen, Lisette, Heather and Cian, thank you for all the helpful discussions during meetings. To everyone who has passed through office 82 throughout my four years at Edinburgh thank you for making it such a welcome and enjoyable place to work. A huge thank you for the many pub nights and meals out, as well as making our trips to Prague and Boston so memorable (despite the missing luggage).

A huge thank you to the US Air Force Studentship for funding my PhD studies and the Edinburgh Computing and Data Facilities and the UK Materials and Molecular Modelling Hub for providing the computational resources. Thank you to Prof. Graeme Day, Dr. Peter Portius, Dr. Ranko Vrcelj and Joe for the helpful insights during our regular discussions.

A massive thank you to Rachel (along with Brodie and Neeps) for all the support throughout my time in Edinburgh and looking after me during the long thesis writing days.

To all my friends, thank you for all the laughs and weekend getaways to London. Special thanks to Sam for dealing with all my questions about Python during this work.

Finally, a special thank you to my family, particularly Mum and Dad, for all the support. This would not have been possible without you.

- Jack

Abbreviations

1,3-DNP – 1,3-dinitro-1H-pyrazole
1,4-DADNP – 1,4-diamino-3,5-dinitro-1H-pyrazole
1-N-3-TNMP – 1-nitro-3-(trinitromethyl)-1H-pyrazole
3,4-DNP – 3,4-dinitro-1H-pyrazole
3,5-DNP – 3,5-dinitro-1H-pyrazole
3-NP – 3-nitro-1H-pyrazole
4-ADNP – 4-amino-3,5-dinitro-1H-pyrazole
5-ADNP – 5-amino-3,4-dinitro-1H-pyrazole
AIRSS – Ab Initio Random Structure Searching
BDE – Bond Dissociation Energy
BOA – Born-Oppenheimer Approximation
BP-1 – 3,3'-5,5'-tetranitro-1H,1'H-4,4'-bipyrazole
BP-2 – 3,3',5-trinitro-1H,1'H-4,4'-bipyrazole
BP-3 – 3,3'-dinitro-1H,1'H-4,4'-bipyrazole
BZ – Brillouin Zone
CASTEP – Cambridge Serial Total Energy Package
CL-20 – hexanitrohexaazaisowurtzitane
CoM – Centre of Mass
CP – Coordination Polymer
C_{tot} – Total vibrational heat capacity
C_{ph} – Vibrational heat capacity of the phonon bath
Cu(ADNP) – Cu(4-amino-3,5-dinitro-1H-pyrazolate)
DBX-1 – Cu(I)-5-nitrotetrazolate
DBX-2 – Cu(I)₃-(5-nitrotetrazolate)₂Cl
DBX-3 – Cu₄-(3,5-dinitro-1H-1,2,4-triazolate)₃Cl
DFT – Density Functional Theory
DFTB – Density Functional Tight Binding
EMs – energetic materials
ESP – Electrostatic Potential
FOX-7 – 1,1-diamino-2,2-dinitroethylene
FWHM – Full Width Half Maximum
GGA – Generalised Gradient Approximation
g(ω) – Phonon Density of States
HF – Hartree-Fock Theory
HMX – cyclotetramethylene-tetranitramine
HNB – hexanitrobenzene
HOMO – Highest Occupied Molecular Orbital
KMF – Kier Molecular Flexibility
LA – Lead Azide
LDA – Local density approximation
LModeA – Local Mode Analysis
LUMO – Lowest Unoccupied Molecular Orbital
LUVNAS – 1-(2-nitro-2-azapropyl)-5-aminotetrazole
LUVNIA – 1-methyl-5-(2-nitro-2-azazpropyl)-nitriminotetrazole
LUVPAU – 2-methyl-5-(2-nitro-2-azapropyl)-nitriminotetrazole
LUVPEY – 1-methyl-4-(2-nitro-2-azapropyl)-aminotetrazole
LUVPIC – 1-(2-nitro-2-azapropyl)-tetrazole

LUVPOI – 2,5-bis(2-nitro-2-azapropyl)-nitriminotetrazole
MF – mercury fulminate
NCI – Non-Covalent Interaction
NG – nitroglycerin
Ntet – 5-nitrotetrazole
NTO – nitrotriazolone
OB – Oxygen Balance
PA – picric acid
PBX – Polymer-bonded Explosive
PES – Potential Energy Surface
PETN – pentaerythritol tetranitrate
PPD – para-phenylenediamine
QTAIM – Quantum Theory of Atoms In Molecules
RDX – 1,3,5-trinitro-1,3,5-triazine
REACH – Registration, Evaluation, Authorisation and Restriction of Chemicals
TATB – 1,3,5-triamino-2,4,6-trinitrobenzene
TNP – 3,4,5-trinitropyrazole
TNT – 2,4,6-trinitrotoluene
TS – Tkatchenko Scheffler
T_{shock} – Shock temperature applied during vibrational up-pumping
Q_D – Doorway vibrational mode
Q_T – Target vibrational mode
Y – Number of amalgamated modes
Z – Number of molecules in the crystallographic unit cell
Z_{eff} – Number of molecules used for normalisation purposes in the vibrational up-pumping procedure
 $\Omega^{(2)}$ – Two-Phonon Density of States
 Ω_{\max} – Upper limit of the phonon bath

Table of Contents

| | |
|--|---------------|
| 1. Introduction | 1 |
| 1.1 An Overview of Energetic Materials | 1 |
| 1.1.1 The Field to Date | 1 |
| 1.1.2 Understanding the Physical Properties of EMs | 4 |
| 1.1.2.1 Initiation | 4 |
| 1.1.2.2 Deflagration and Detonation | 5 |
| 1.1.3 Characterisation of EMs | 6 |
| 1.1.3.1 Impact Sensitivity of EMs | 7 |
| 1.2 Attempts to Predict Impact Sensitivities Using Computational Modelling | 9 |
| 1.2.1 Gas Phase Approaches | 9 |
| 1.2.2 Solid-State Approaches | 17 |
| 1.2.3 Vibrational Up-pumping Based Approaches | 19 |
| 1.3 Vibrational Up-pumping Methodology | 22 |
| 1.3.1 Vibrational Up-pumping as Described by Michalchuk et al., | 22 |
| 1.3.2 Vibrational Up-pumping of Energetic Azides | 24 |
| 1.3.3 Vibrational Up-pumping of Molecular Energetics | 27 |
| 1.3.4 Zone Centre Vibrational Up-pumping | 28 |
| 1.3.5 Vibrational Up-pumping in this Work | 30 |
| 1.4 Computational Methodology | 32 |
| 1.4.1 Quantum Mechanics in Computational Chemistry | 32 |
| 1.4.2 Hartree-Fock Theory | 33 |
| 1.4.3 Density Functional Theory | 33 |
| 1.4.3.1 Introduction to DFT | 33 |
| 1.4.3.2 Exchange/Correlation Functionals | 34 |
| 1.4.3.3 Dispersion Corrections | 35 |
| 1.4.3.4 Hybrid DFT | 35 |
| 1.4.4 Basis Sets | 35 |
| 1.4.5 Solid-State Modelling and Bloch's Theorem | 36 |
| 1.4.6 Geometry Optimisation | 37 |
| 1.4.7 Vibrational Frequency Calculations | 39 |
| 1.4.7.1 Gas Phase Vibrational Frequencies | 39 |
| 1.4.7.2 Phonon (Solid-State) Frequencies | 39 |
| 1.4.8 Additional Software | 39 |
| 1.4.8.1 Accelrys Materials Studio | 39 |
| 1.4.8.2 CASTEP | 40 |
| 1.4.8.3 CRITIC2 | 40 |
| 1.4.8.4 AIRSS (Ab Initio Random Structure Searching) | 40 |
| 1.4.8.5 Gaussian | 41 |
| 1.4.8.6 LModeA | 41 |
| 1.4.8.7 Vibrational up-pumping script | 41 |
| 1.5 Project Outlines and Aims | 41 |
| 1.6 References | 43 |
| 2. Development of Python Scripts to Supplement the Vibrational Up-pumping Procedure | 49 |
| 2.1 Introduction | 49 |
| 2.2 Generation of Complete and Partial Density of States Plots | 49 |
| 2.3 Determination of Ω_{\max} through Consideration of Molecular Centre of Mass | 58 |

| | |
|---|------------|
| 2.4 Tracking of Local Modes of Vibration | 62 |
| 2.5 Conclusions | 68 |
| 2.6 References | 69 |
| 3. Tuning the Effects of Energetic Materials through Altering Crystal Packing | 71 |
| 3.1 Introduction | 71 |
| 3.2 Co-crystallising FOX-7 with PPD | 71 |
| 3.2.1 Introduction and Aims | 71 |
| 3.2.2 Computational Methodology | 75 |
| 3.2.3 Results and Discussion | 75 |
| 3.2.4 Conclusions | 87 |
| 3.3 Probing the High-Pressure Response of TNP | 88 |
| 3.3.1 Introduction and Aims | 88 |
| 3.3.2 Computational Methodology | 91 |
| 3.3.3 Results and Discussion | 92 |
| 3.3.4 Conclusions | 107 |
| 3.4 Overall Conclusions | 108 |
| 3.5 References | 108 |
| 4. Towards a Lead-free High Sensitivity Material to Replace Lead Azide | 112 |
| 4.1 Introduction | 112 |
| 4.2 Computational Methodology | 112 |
| 4.3 Lead Azide | 113 |
| 4.3.1 Introduction | 113 |
| 4.3.2 Results and Discussion | 114 |
| 4.3.3 Conclusions | 127 |
| 4.4 Copper(I)-based Coordination Polymer Energetics | 127 |
| 4.4.1 Introduction | 127 |
| 4.4.2 Results and Discussion | 130 |
| 4.4.3 Conclusions | 145 |
| 4.5 A Copper Based Coordinated Energetic | 146 |
| 4.5.1 Introduction | 146 |
| 4.5.2 Results and Discussion | 147 |
| 4.5.3 Conclusions | 159 |
| 4.6 Overall Conclusions | 160 |
| 4.7 References | 161 |
| 5. Towards Developing Structure/Property Relationships for the Prediction of Impact Sensitivities in EMs | 164 |
| 5.1 Introduction | 164 |
| 5.2 Computational Methodology | 164 |
| 5.3 Pyrazole Investigation | 165 |
| 5.3.1 Introduction | 165 |
| 5.3.2 Results and Discussion | 167 |
| 5.3.3 Conclusions | 194 |
| 5.4 Tetrazole Investigation | 196 |
| 5.4.1 Introduction | 196 |
| 5.4.2 Results and Discussion | 198 |
| 5.4.3 Conclusions | 214 |

| | |
|--|------------|
| 5.5 Nitrate Ester Investigation | 215 |
| 5.5.1 Introduction | 215 |
| 5.5.2 Results and Discussion | 217 |
| 5.5.3 Conclusions | 232 |
| 5.6 Overall Conclusions | 233 |
| 5.7 References | 235 |
| 6. Conclusions and Future Outlook | 239 |
| 6.1 Conclusions | 239 |
| 6.2 Future Outlook | 246 |
| 6.3 References | 248 |
| Appendix A | 249 |
| Appendix B | 253 |
| Appendix C | 254 |

Chapter 1: Introduction

1.1 An Overview of Energetic Materials

1.1.1 The Field to Date

Energetic materials (EMs) are named for their ability to store and subsequently release significant amounts of energy, and common applications include explosives, propellants and pyrotechnics [1]. The first reported EM dates back to roughly 220 BC, where reports of a formulation known as blackpowder (more commonly known as gunpowder, a mixture of sulphur, charcoal and potassium nitrate) was accidentally discovered in China [2, 3]. This discovery was mirrored in Europe in the 13/14th centuries, but it was not until the 15th century that this early EM was studied in sufficient detail for production to be made safe enough for regular use in military applications [1, 2, 3]. These early attempts at safe material manufacture were to produce a dehydrated product, in a process known as corning, that resulted in a material with more predictable combustion properties [4]. Gunpowder still finds some limited military applications today, primarily for blasting fuses, despite its known tendency to spontaneously initiate [5].

The next significant advance in the field of EMs was the first report on nitroglycerin (NG) – a liquid EM that is exceptionally prone to accidental initiation [6]. Its manufacture was made widely accessible by Alfred Nobel, who developed a small production plant in Stockholm in 1865 [7]. In an attempt to mitigate the dangers of NG, Nobel mixed NG with powdered minerals, such as shells and clays. This yielded a solid formulation he patented as dynamite, which is still used in the mining and demolitions industries [8]. Alfred Nobel is also credited with the invention of the successor to gunpowder, known as mercury fulminate (MF) which has also seen use as blasting fuses and was used to detonate early dynamite formulations [9]. Nobel, motivated by a number of accidental detonations which occurred at his NG plant, one of which killed his brother, dedicated himself to improving the safety of NG. This commitment is a sentiment that has remained at the heart of the energetics community to the modern day, where development of insensitive EMs

(materials which require increased energy to initiate) is still of high priority [10, 11].

A number of additional energetic formulations were produced throughout the 19th and 20th centuries [1]. The first one of note was picric acid (2,4,6-trinitrophenol - PA) which was used extensively as a blasting charge to fire shells in the late 19th century [12]. A key problem with PA, however, was its corrosive nature, and the metal salts that formed in shell casings (such as copper picrate) were found to be significantly more prone to accidental initiation. [1, 2, 13]. This led to the development of 2,4,6-trinitrotoluene (TNT), a structural analogue of PA with marked improved safety characteristics and which could be used as a straight swap alternative for military applications [1, 2, 12]. TNT was used extensively throughout both the first and second world wars (WWI and WWII) [14]. During WWII the thicker hulls employed on German U-boats lead to the need for EMs with a greater explosive power. This led to the development of 1,3,5-trinitro-1,3,5-triazine (RDX); mixing this with TNT and aluminium powder gave rise to the formulation known as Torpex [15].

RDX had an increased impact sensitivity compared to TNT, meaning that it required less mechanical stimulation to initiate. In an effort to improve its safety features it would often be mixed with a polymeric material, known as a plasticiser (e.g. polystyrene) to produce mouldable polymer-bonded explosives (PBXs) which are relatively safe to handle [16]. Some common examples here are C-4 and Semtex [17]. A structural analogue of RDX is cyclotetramethylene-tetranitramine (HMX) which was synthesised in the decades following WWII and was found to be an even more powerful EM, and more sensitive to mechanical impact, meaning that it too is regularly plasticised to render it more applicable to military applications [1, 2, 12]. Another WWII EM is hexanitrobenzene (HNB), which was found to be too sensitive to mechanical impact, and hygroscopic, for commercial application [1].

A more recent example of a novel EM was reported in 1997 by the Naval Air Warfare Centre, who synthesised hexanitrohexaazaisowurtzitane (HNIW, more commonly referred to as CL-20) which is an EM comprised of strained cage system and six weakly bound nitramine functional groups [18]. This EM

has also never seen application as a result of its high mechanical impact sensitivity and a number of other problems associated with its synthesis. However, a recent study reported that a co-crystal formed between CL-20 and HMX had an impact sensitivity somewhere between the two EMs, suggesting that co-crystallisation is a potential route to significantly alter the physical properties of known materials [19, 20]. This is particularly pertinent for the EM industry, where material safety and conservatism has resulted in the majority of all industrial formulations to the present day being primarily based on just a handful of materials. [1, 2, 12].

In recent years, development of novel EMs has shifted even more in the direction of safer (reduced sensitivity) materials, to create the class of compounds referred to as insensitive munitions [10, 11]. One example here is nitrotriazolone (NTO), first synthesised in 1905 but not investigated as an EM until the 1980s, it has seen increased attention in recent times as a component in a number of formulations to replace TNT [1, 2]. Two additional low sensitivity EMs, namely 1,1-diamino-2,2-dinitroethylene (FOX-7) and 1,3,5-triamino-2,4,6-trinitrobenzene (TATB) have been developed by the Swedish defence agency and the US military, respectively [21, 22]. In an unusual step for EMs, both of these compounds contain hydrogen bond donor (-NH_2) groups, and the resulting H-bond interactions with the -NO_2 groups are thought to result in improved safety characteristics, through a process that is not particularly well understood, whilst maintaining performance similar to that of RDX and TNT respectively. The structures of a number of the EMs introduced thus far, which will be used as a set of standard, well-understood EMs throughout this thesis are shown in Figure 1.1.

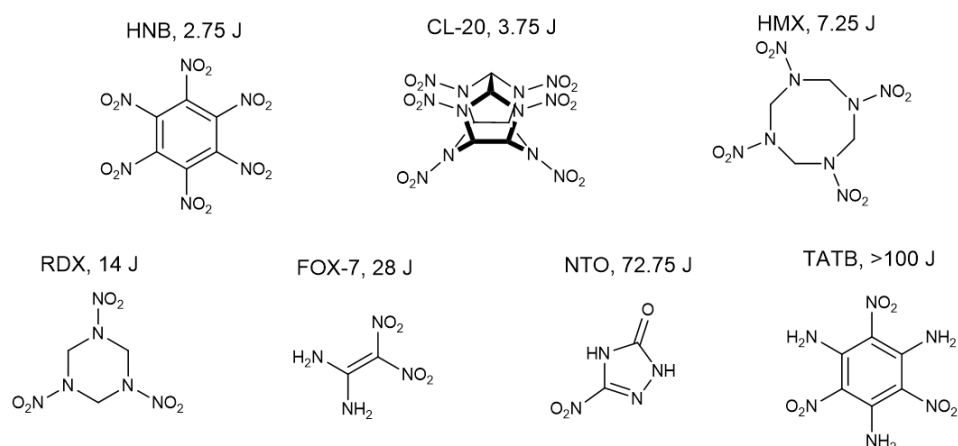


Figure 1.1: Structures of a number of EMs discussed with their respective sensitivities to impact outlined. Impact sensitivity values taken from previous work [23, 24].

While a number of the more recently developed EMs adhere to the philosophy of insensitive munitions, development remains slow, in large part due to the inherent dangers associated with such materials and the conservative nature of the energetic materials industry. Understanding the physical process behind EM initiation is an important consideration to help improve the new materials discovery pipeline, and to help rationalise their material properties.

1.1.2 Understanding the Physical Properties of EMs

It is generally understood that exposure to an external stimulus (impact, shock, friction, electric spark etc.) causes an initiation process within the EM that leads to a physicochemical chain reaction that ultimately leads to an explosion [1, 2, 12]. The physicochemical reaction is believed to be the rupture of a weak bond within a molecule, typically C/N-NO₂ bonds, to give rise to a concept referred to as trigger bond initiation [25 26]. The different stages of the explosion process are outlined below.

1.1.2.1 Initiation

Explosions arising from mechanical impact are the primary focus of the work presented in this thesis, and as such the following discussion considers the likely sequence of events that follow on from a mechanical impact event. Impact-driven explosions are believed to be thermal in origin, with one argument for a physicochemical response being that energy is localised in

small regions in the material known as hot spots, where temperatures soar to high enough values for chemical reactions to take place while the remainder of the bulk material remains too cold to react [27, 28]. Two types of hot spot have been proposed to form after an impact event, namely critical and sub-critical. In the former, the chemical reaction is self-sustaining and thus propagates into the bulk regions, while for the latter the reactions are not self-sustaining and so are subsequently quenched.

Physical parameters of critical hot spots were described by Bowden and Yoffe as being roughly 10^{-6} m in diameter, supporting temperatures of greater than 700 K, and occurring over lifetimes of $10^{-5} - 10^{-3}$ s, and generally form around crystal defects and voids [29, 30]. Hot spots generated by impact were shown to be achievable through both shock and impact, with impact producing larger and therefore more self-sustaining regions of reactivity. While it is generally agreed that the formation of hot spots is a key step in the explosion of an EM, a number of different hypotheses for their generation exist. These include compression of trapped gas within the material, frictional heating as a result of grains moving against one another, and through material being forced into voids within the crystal.

While the formation of critical hot spots provides the mechanism for high temperatures to build up in an EM to initiate runaway chemical reactions to arise, it is a physical, rather than chemical, model.

1.1.2.2 Deflagration and Detonation

Initiation of an EM results in a chemical reaction taking place which releases a large amount of energy through the formation of stable, gaseous, reaction products, namely N_2 , CO_2 and H_2O [1, 2]. Forming large amounts of gas in a short period of time results in intense pressurisation of the material, which presents as a shock wave that travels through the EM at the speed of sound. If the chemical transformations occur at a rate slower than the pressure-induced shock wave, the material is said to deflagrate. If, however, the pressure continues to rise such that the transformation rate exceeds the speed of sound the material is said to undergo a detonation. This phenomenon is

known as the deflagration-to-detonation transition, which often results in a much louder and more dangerous explosion.

During the detonation of an ideal explosive the reaction proceeds through propagation of a shock front through the material perpendicular to the reaction [31]. Here a thin layer of material is compressed, increasing the pressure and temperature, which initiates further chemical reactions in the reaction zone that sits behind the shock front (see Figure 1.2). Here the temperature and pressure falls, and the point at which a chemical equilibrium is reached is denoted as the Chapman-Jouguet point. From this point the reaction proceeds at a constant speed, which is referred to as the detonation velocity. This value is unique for each explosive and a typical value is within the range 4000 – 10000 ms⁻¹.

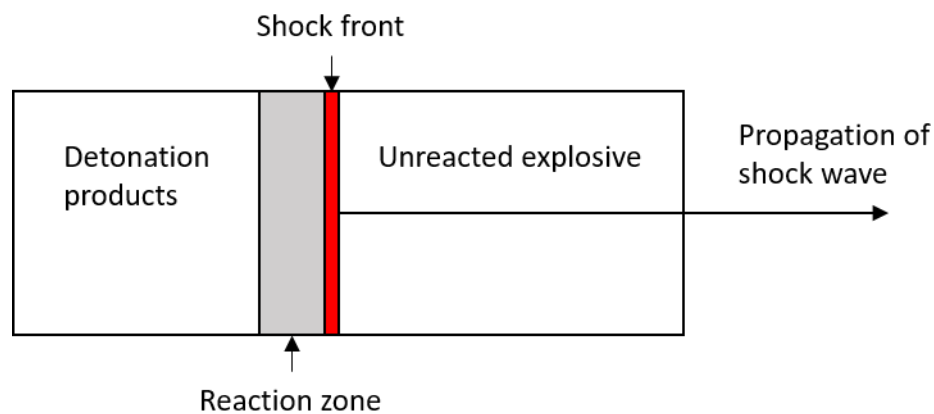


Figure 1.2: A schematic of a shock front and corresponding reaction zone propagating through a material resulting in explosion.

In a non-ideal system, the transformation from reactants to products is not instantaneous and the shock front propagates as a curve rather than a straight line, which further complicates the process. The specifics of this process are not explored in this work, but Reference 32 provides further discussion [32].

1.1.3 Characterisation of EMs

For obvious reasons, EMs must be subjected to extensive physical property characterisation. The first classification that an EM is assigned to is whether it is a high or low explosive, the difference being whether they explode (through deflagration or detonation) or simply burn [1, 2]. High explosives are what are

typically referred to as explosives, while low explosives are materials such as propellants and pyrotechnics. High explosives are then further classified as either primary or secondary explosives, where the former are easily detonated and the latter are not.

Sensitivity is the metric that is generally used to quantify the safety of an EM, as it represents the propensity of the material to initiate when exposed to one of a number of stimuli such as impact, heat, friction, electric spark and exposure to laser light. Highly sensitive materials require less energy to initiate than insensitive materials. This body of work focusses exclusively on the sensitivity to mechanical impact, as it is the most quoted and generally used to represent the overall safety characteristics of an EM.

1.1.3.1 Impact Sensitivity of EMs

Impact sensitivity is a numerical measure of how much energy is required (in the form of a mechanical impact) to begin the initiation process. Experimentally, impact sensitivity is typically measured using a drop weight apparatus, where a known mass is dropped from a variable height until the minimum energy required to routinely initiate the material is established. A common experimental set up is the BAM fall hammer, shown in Figure 1.3 [33]. The impact sensitivity is occasionally referred to by the height the weight is dropped from which results in initiation of 50 % of the EM (H_{50}) alongside the mass of the insult projectile, the two numbers are then combined to give the energy, presented as Joules (J). Sensitive EMs typically have impact energies below 5 J, whereas measurements for insensitive EMs span the range 5-100+ J.



Figure 1.3: A BAM Fall hammer impact sensitivity testing apparatus.

Whether initiation has occurred in the drop weight test is based on a 'go/no-go' decision from the user based on an audio or visual response. This results in a great deal of uncertainty as a result of human error, highlighted in a study by Doherty in which seven commercial standards of RDX containing differing amounts of HMX were sent to a number of laboratories to be ranked in order of descending impact sensitivity [34]. Each laboratory returned a different ranking for the samples. This study highlighted that a number of different material variables, such as particle size, crystallinity, sample purity, temperature and humidity all affect the impact sensitivity readings. Moreover, papers in the EM literature will often report impact sensitivity values without clearly stating how the measurements were made, which leads to further difficulties when attempting to use sensitivity values for a range of compounds in a comparative sense.

Despite extensive experimental impact sensitivity testing being a requirement for EMs, very little regarding the physicochemical basis of initiation can be understood from this experimental procedure alone. As such, computational modelling investigations in this area have been widespread for a number of decades.

1.2 Attempts to Predict Impact Sensitivities Using Computational Modelling

A number of predictive computational models have been developed in an attempt to determine the physical basis of impact sensitivity, with varying degrees of success. These models are discussed here, split into gas-phase (molecular) descriptors and solid phase (material) descriptors, and their relative strengths and weaknesses are evaluated.

1.2.1 Gas Phase Approaches

Gas phase models are inherently quicker and simpler than their solid-state counterparts, allowing for high throughput computational screening methods to be developed. Initial gas phase methods were explored as a consequence of limited computational resources and access to crystal structure information of EMs, both of which have improved in recent years, thereby fuelling a more recent shift towards solid-state modelling approaches.

The simplest models used for sensitivity prediction are so-called linear regression models that are based on finding correlations between a number of different chemical descriptors or molecular features with impact sensitivity. Early efforts by Vaullerin et al., correlated the impact sensitivity with the C4 criterion (defined by Equation 1.1) provided by the CHEETAH code (a software programme that uses a mass of chemical data to predict a vast array of thermodynamic properties) which is heavily dependent on the maximum reaction heat [35].

$$C4 = \frac{10\Delta H_{max}^2 M}{n} \quad \text{Equation 1.1}$$

Where ΔH_{max}^2 represents maximum heat of reaction, M is the EMs molecular weight and n is the number of atoms. This was found to successfully group a wide array of materials into clusters as sensitive, moderately sensitive and insensitive, but had limited success within each respective grouping.

A number of alternative approaches have been presented by Keshavarz, in which the impact sensitivity can be predicted based on a linear regression model that takes into account the chemical composition of the energetic

molecule [36, 37, 38]. The general approach here takes the number of each of the component atoms of a CHNO EM, where C, H, N and O are represented by a-d respectively, alongside the scaling parameters shown in Equation 1.2 [37].

$$\log(H_{50}) = c_1a + c_2b + c_3c + c_4d \quad \text{Equation 1.2}$$

The exact values of the scaling parameters vary depending on the chemical family the EM in question belongs to (e.g. $c_1=11.8$, $c_2=61.72$, $c_3=26.9$ and $c_4=11.5$ for polynitroarenes). This highlights one of the major drawbacks of this approach, namely the inability to compare across structurally diverse energetics. Moreover, such regression-based methods can simply return a predicted value and provide no insight into the physical basis for sensitivity. They cannot, therefore, help rationalise helpful design criteria for future materials. While these drawbacks are undoubtedly limiting, the simplicity and speed by which predictions can be made by such methods should not be understated.

A common metric often determined for EMs is the oxygen balance (OB) as it provides an intuitive indication as to how well the EM oxidises its own decomposition, according to the equation below [1, 2, 12, 39].

$$OB = \frac{100(2n_o - n_H - 2n_C - 2n_{COO})}{Mol.Wt} \quad \text{Equation 1.3}$$

Where n_x denotes the number of the atom or functional group in question contained within the material. Kamlet compared the OB for a series of 38 nitroaromatic EMs to their respective $\log(H_{50})$ values [39]. It was noted that when plotted the data appeared to form two distinct linear correlations, one comprised of materials which had a hydrogen atom in the alpha position relative to a ring bound nitro group (solid points), and the other comprised of materials that do not (empty points). These trends are shown in Figure 1.4.

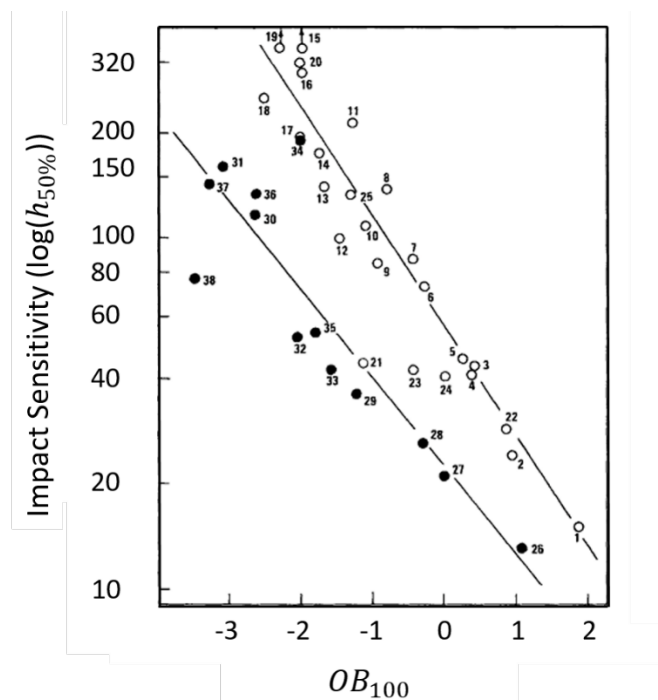


Figure 1.4: Relationship between the oxygen balance (OB) and a measure of the impact sensitivity ($\log(H_{50})$). Solid circles representing EMs with a hydrogen atom in the alpha position to the aromatic ring, and open circles representing those that do not. Taken from Kamlet [39].

This observation is an improvement over linear regression models, as OB is a factor that is considered in the development process of an EM and is used as a design criterion. However, the approach is still limited to correlations between a set of structurally similar EMs and cannot be expanded to include more structurally diverse energetic molecules.

Another promising approach to predicting the impact sensitivity is through consideration of the weakest bond in the molecule; these generally arise between the organic skeleton and the nitro groups, $-R-NO_2$, where $R = C$ or N . Rupture of this weak covalent bond has been proposed as the first step in a cascade chemical reaction [1, 2, 40]. A number of characteristics of the weakest bond have been compared against impact sensitivity, with great success. This includes studies that have investigated the electron density in the centre of the bond and the bond dissociation energy. Owens first explored the amount of energy required to rupture a bond for a series of nitro group containing CHNO EMs [41]. This was achieved through incrementally increasing the $R-NO_2$ bond length from the equilibrium geometry and noting

the change in energy of the system. This is repeated until the bond is broken. The energy barrier to bond rupture was found to correlate well with impact sensitivity (Figure 1.5), with an increase in energy found for the less sensitive EMs.

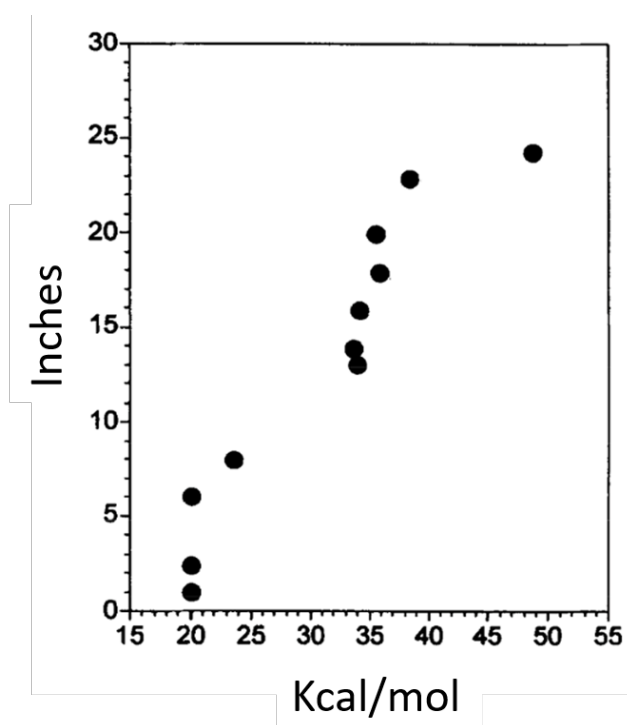


Figure 1.5: Relationship between the impact sensitivity (measured as height of drop weight in inches) and the energy required to rupture the weakest C-NO₂ bond given in Kcal/mol of a series of CNHO containing EMs. Taken from Owens [41].

Stemming from this work, Rice et al., investigated the formal bond dissociation energy (BDE) of a series of R-NO₂ groups in a number of nitroaromatics [42]. The BDE of the nitro group bond was determined from comparison of *ab initio* energy calculations of the nitroaromatics and the products of the bond dissociation. When compared to measured impact sensitivity a similar relationship to that shown by Owens was achieved (Figure 1.6), but it is not clear whether this approach extends beyond the set of nitroaromatic EMs that were reported.

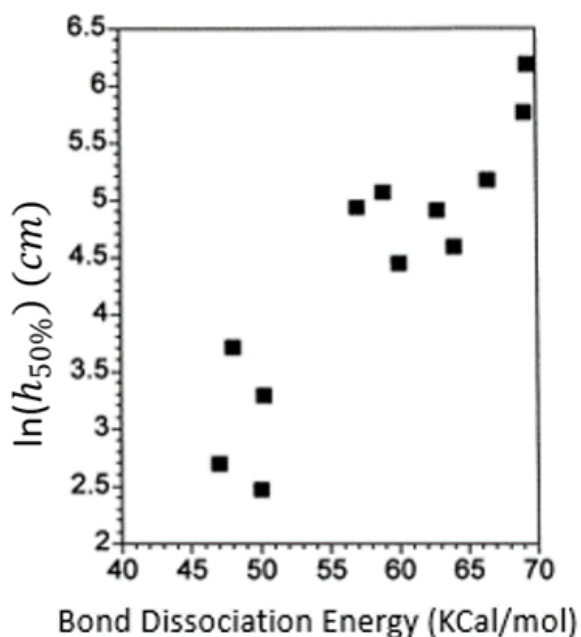


Figure 1.6: Relationship between the impact sensitivity ($\ln(h_{50\%})$) and the BDE of the nitro bond (C-NO₂) of a series of nitroaromatics, showing weaker bonds are found on more sensitive EMs. Taken from Rice et al [42].

The chemical specificity of the BDE approach was outlined starkly in a study by Mathieu, where a defined sensitivity index (the ratio between the BDE and the decomposition enthalpy per mole of compound) was compared to the impact sensitivity for four different EM types, specifically nitroaromatics (blue), nitramines (black), compounds which have a terminal C-(NO₂)₃ group (green) and compounds which do not have a terminal C-(NO₂)₃ group (red), as shown in Figure 1.7 [43]. The fact that each structural class sits on its own line of best fit suggests that the universality of a predictive method through this route will not be forthcoming.

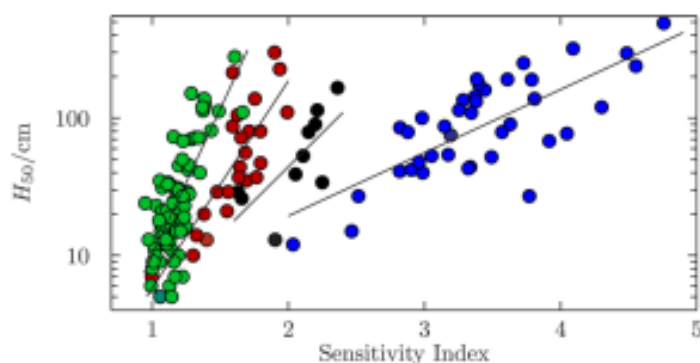


Figure 1.7: Relationship between the defined sensitivity index (ratio of BDE and enthalpy of decomposition per mole of EM) and the impact sensitivity of a number of EMs from four chemical families, taken from Mathieu et al [43].

Work focussing on correlating electrostatic potential (ESP) with the impact sensitivity was pursued by Politzer and Murray, who followed on from initial work by Owens and produced analogous arguments to those raised for BDE. Their initial work showed that a reasonable correlation is obtained when the deviation in ESP across a weak C-NO₂ bond is compared with impact sensitivity, such that an increase in positive ESP relates to an increase in sensitivity [40, 44]. The rationale here was that a decrease in bond electron density indicates bond instability and thus increased sensitivity. Further work suggested that increased impact sensitivity in nitroaromatic EMs is associated with a separation of charge over the molecule, with the effect being particularly pronounced if a positive charge builds up over the central aromatic ring [45]. The following analytical expression was derived:

$$\text{predicted } h_{50} = \alpha(\Pi^2 V_{s,\max}(\text{ring}))^{-1} + \beta \Pi^2 + \gamma \quad \text{Equation 1.4}$$

Where Π is the average deviation of the ESP, $V_{s,\max}(\text{ring})$ is the maximum ESP value in the ring, and α , β and γ are fitting constants [45]. When plotted against the experimental sensitivity an excellent agreement is obtained (Figure 1.8).

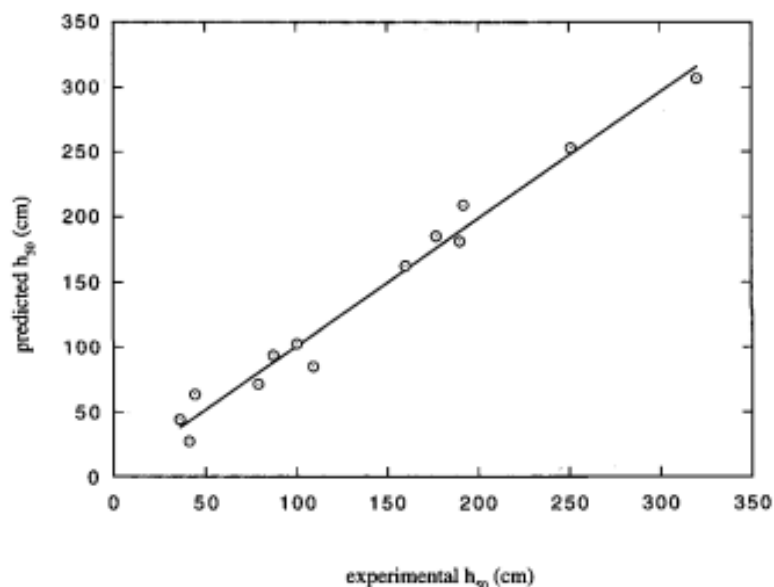


Figure 1.8: Outlines the relationship between experimental and predicted impact sensitivity based on Equation 1.4 relating to ESPs, taken from Murray et al., [45].

This correlation can be readily explained as the aromatic stabilisation effect being counteracted by the presence of a number of strong electron withdrawing groups ($-\text{NO}_2$). A comprehensive study of ESPs of a number of nitroaromatic molecules (split into a number of groups comprised of similar structure) was conducted by Rice et al., which very clearly highlights the build-up of positive charge over the central aromatic region of the EMs with increasing numbers of explosophoric groups (Figure 1.9) [46].

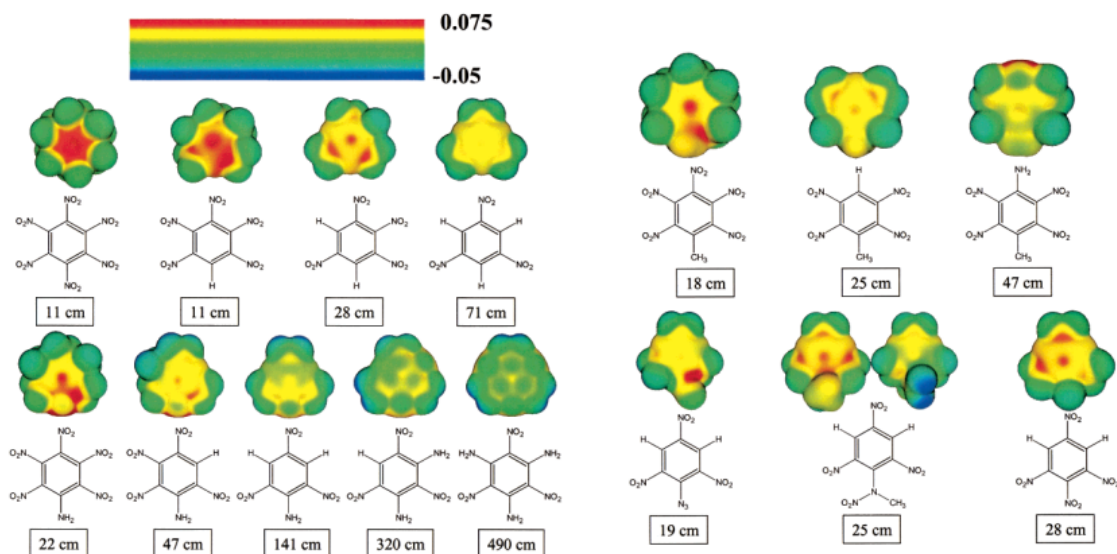


Figure 1.9: Shows the ESP diagrams of a number of nitroaromatic EMs, with red denoting positive charge build up and green negative, alongside their respective H_{50} values showing that EMs with positive charge build up are found to be more sensitive. Taken from Rice et al [46].

The red regions of positive ESP are clearly more pronounced for the more sensitive EMs (smaller H_{50} values). However, this problem again suffers from limitation of application: in that it only holds for nitroaromatic EMs.

It has been suggested by Gilman that narrowing of the electronic band gap (often to the extent that the material becomes a conductor) when exposed to impact may facilitate the onset of explosive breakdown [47]. However, the electronic band gap is a solid-state property, which will be discussed in more detail in the following Section and is computationally expensive to calculate. In an attempt to reduce calculation costs the molecular HOMO-LUMO gap (highest occupied molecular orbital and lowest unoccupied molecular orbital respectively) has instead been investigated by a number of groups. While rough trends outlining smaller HOMO-LUMO gaps for more sensitive EMs have been postulated, [48, 49] recent work by Politzer and Murray suggest that this is not a good metric to correlate against impact sensitivity, primarily as the derivation of the molecular orbitals in an ab initio calculation is not precise enough [50].

1.2.2 Solid-State Approaches

While reasonable success in predicting impact sensitivity has undoubtedly been shown, results have often been restricted to particular structural classes of EM, and the semi-empirical equations that have been put forward have little physical meaning beyond a fitting function. Moreover, the molecular approach neglects the importance of solid-state interactions, which must play a part, as impact sensitivity is, after all, a material property effect.

An attempt to include the effects of the solid-state lattice was put forward by Jones et al, who outlined a so-called bond bundle description within the QTAIM (quantum theory of atoms in molecules) framework, which provided a descriptor of the spatial bond volume [51]. The relative number of electrons in the bond bundles was used to describe the trigger linkage, with a low electron count suggesting trigger linkage behaviour. This approach was used for both gas phase and solid-state RDX and showed that the trigger linkage was likely the C-N ring bonds in the gas phase, but N-NO₂ in solid state. This change in trigger bond identity was rationalised through an increase in intermolecular interactions in the solid-state that modified the N-NO₂ bonds more than the invariant C-N ring bonds, highlighting the need to include the effects of the crystallographic lattice.

Politzer et al. have also pursued a solid-state approach and offered a comparison between the amount of free space in the lattice per molecule and increasing impact sensitivity [52]. This was based on the idea that an increased amount of space within the lattice results in increased compressibility and therefore an increase in adiabatic heating. This increase in temperature may correlate with higher instances of critical hot spot formation, and therefore lead to increased sensitivity. However, as with the BDE approach discussed in the previous section, while encouraging correlations were found for different structural chemical groups, the correlation breaks down when all data were compared on the same plot. Additionally, this approach provides a physical model and as such gives no insight to the underlying chemical reaction pathways.

Taylor centred efforts on consideration of the intermolecular interactions, more precisely the interaction energy between pairs of molecules within the crystallographic unit cell [53]. A good trend of increased interaction energy for less sensitive EMs was found for a series of nitroaromatic compounds. FOX-7 was also considered as part of this data set, but bucked the observed trend as it was found to have a significantly larger interaction energy than any of the nitroaromatics due to the presence of intermolecular hydrogen bonding. This once again suggests that any positive correlations observed by the approach will once again only be applicable to certain structural chemistry groupings. In a similar vein, Ma et al., considered a number of novel EM/EM co-crystals taken from the work conducted by Landenberger et al [54, 55]. These compounds showed improved (reduced) sensitivities when compared to the parent EMs, suggesting that an increase in intermolecular interactions between the co-crystallites when compared to the parent EMs results in sufficient stabilisation to improve the sensitivity. This led to the overall conclusion that an increase in hydrogen-bonding strength provides a route towards the stabilisation of EMs, while an increased anisotropy between the intra and interlayer interactions was also suggested as an indicator for low sensitivity [54]. An example that directly contradicts this conclusion is explored in Chapter 3 of this thesis, where a co-crystal involving FOX-7 and a non-EM was found to be more sensitive to mechanical impact than FOX-7 itself, despite an increase in hydrogen bonding strength between the two moieties.

Several authors have pursued a correlation between electronic band gap and impact sensitivity, as a material's reactivity is often heavily influenced by the accessibility of a low-lying conduction band. Despite the well-known propensity for density functional theory to underestimate the size of electronic band gaps, a number of studies have attempted to relate calculated band gaps to the impact sensitivity [56]. For instance, Zhu et al. showed that the calculated electronic band gaps of the four polymorphs of HMX correlate with their respective impact sensitivities, with the least sensitive (β) polymorph having the largest band gap [57]. Work from the same group showed a similar relationship for the polymorphs of CL-20 but with a less convincing trend, suggesting that the sensitivity of the γ -polymorph is lower than found to be

experimentally. Work by Michalchuk et al. showed that the computed band gaps for a series of chemically unrelated EMs did not correlate very well experimental sensitivity values, suggesting that the band gap alone is not a sufficient descriptor for impact sensitivity [58].

1.2.3 Vibrational Up-pumping Based Approaches

The approaches to computationally predict impact sensitivity values outlined above have had differing degrees of success, and it is clear they have lacked a universal applicability across the whole spectrum of molecular EMs. One method which has attempted to unify molecular EMs on a common footing is the vibrational up-pumping model.

Initially proposed by Coffey and Toton, vibrational up-pumping explains the process by which mechanical impact energy is channelled upwards from low energy vibrations to higher energy vibrations [59]. More precisely, the mechanical impact results in development of a shock front in the material which directly excites the phonon vibrations of a crystal. Such modes rapidly undergo phonon-phonon collisions which result in the creation of a third, higher energy, phonon state. The strength of coupling between the three phonon states (two initial and one final) is termed the anharmonic coupling coefficient and is known to be significantly larger for delocalised phonon vibrations, q , than for localised molecular vibrations, Q [60]. As such the energy rapidly equilibrates over the q modes. This creates what is referred to as the phonon bath, which is marked by the upper frequency limit Ω_{\max} . The disparity in anharmonic coupling coefficients therefore results in a vibrationally hot phonon bath, with colder high energy modes that are later excited by further phonon-phonon scattering events. The excitation of the phonon bath process is effectively instantaneous, occurring on the time scale of molecular vibrations ($10^{-15} - 10^{-12}$ s). This time scale is well below the speed of sound threshold that resembles the rate of propagation of the shock wave through an EM, meaning that vibrational up-pumping could be used to explain the link between mechanical impact and molecular excitation. This idea was shown in the initial work of Coffey and Toton, who demonstrated that energy imparted onto a sample of RDX is sufficient to result in the cleavage of a weak bond when channelled into a

specific molecular vibration. This suggests that localisation of energy into molecular vibrations following an impact event can manifest in chemical bond breakage [59].

Dlott and Fayer built on this idea by exploring the possible vibrational pathways for energy up-pumping, in which the excitation of doorway modes (Q_D which lie between $1-2 \Omega_{\max}$), molecular vibrations named for their ability to become involved in further scattering events, is mediated by up-pumping from the lower energy phonon bath (q) modes [61]. Similar work suggested that scattering events involving Q_D states represents the rate limiting factor in the up-pumping process [62].

The first attempts to rationalise impact sensitivity through the vibrational up-pumping model was undertaken by Fried and Ruggiero, and McNesby and Coffey. Collectively their papers showed that the rate of vibrational up-pumping based on vibrational spectra (phonon density of states from inelastic neutron scattering and Raman spectroscopy, respectively) showed a promising relationship with experimental sensitivities of a number of EMs [63, 64]. Due to limitations in the experimental data and the existing model at the time, the value of Ω_{\max} was arbitrarily placed at 200 and 250 cm^{-1} respectively for each investigation and vibrations up to the frequencies of 600 and 700 cm^{-1} were considered to capture the up-pumped energy. Despite these limitations and approximations, the experimental sensitivities of a number of EMs showed excellent correlations with predicted values. This approach was utilised by Ye et al., who calculated *ab initio* gas phase vibrational frequencies for a number of energetic molecules and suggested that impact sensitivity was solely based on the number of Q_D modes a molecule possesses [65]. The relationship between the two is shown in Figure 1.10.

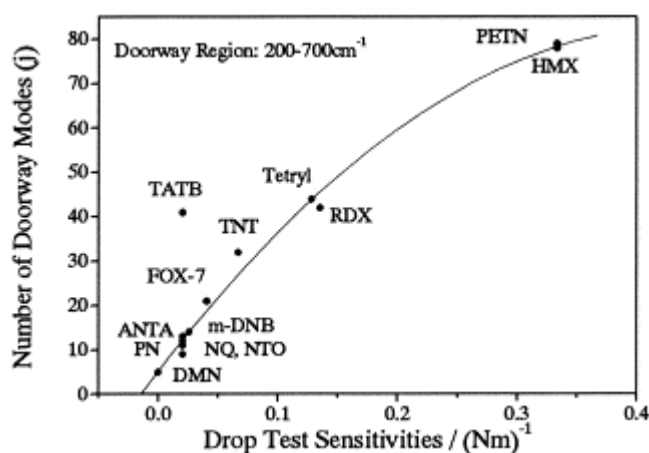


Figure 1.10: Shows the relationship between the number of doorway modes (vibrations of energy 200 – 700 cm^{-1}) and the reciprocal of experimental impact sensitivity for a number of EMs. Taken from Ye et al [65].

An excellent correlation between the number of Q_D modes in the region 200 – 700 cm^{-1} and the experimental impact sensitivity was observed, suggesting that an increase in vibrational character could potentially result in more efficient transfer of impact energy to the vibration responsible for energetic response. Further work from the same group also correlated the rate of vibrational up-pumping with the impact sensitivity to some success [66].

The vibrational up-pumping method was expanded on by Bernstein, through calculation of the vibrational frequencies of crystalline energetic materials and the contribution of overtone excitations of all low energy phonon modes [67]. Overtone (in this sense being used to draw a similarity to spectroscopy) refers to a phonon bath mode of frequency, ω , combining with itself to excite a vibration of frequency 2ω ($\pm 10 \text{ cm}^{-1}$). Once again, an arbitrary window of 200 – 700 cm^{-1} was considered representative of molecular EMs and a new parameter, named the phonon-vibron coupling, ζ , which represents the number of excited modes normalised to the number of atoms and molecules in the structure, was defined. Plotting this parameter with experimental sensitivities led to excellent ranking of EMs (Figure 1.11).

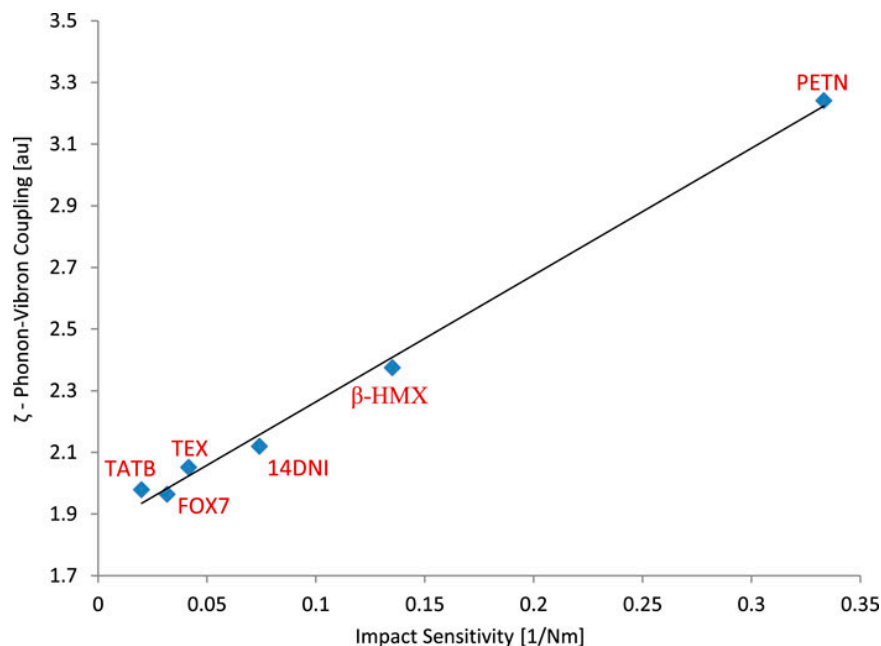


Figure 1.11: Shows the relationship between phonon-vibron coupling (ζ) and reciprocal of the experimental sensitivity. Taken from Bernstein et al [67].

It should be noted that this work projected all the overtones of phonon bath modes up to 700 cm^{-1} suggesting the physically unlikely scenario where a mode self-scatters a number of times.

Michalchuk et al. noted this work and developed a more physically robust up-pumping pathway in which both contributions from two-phonon combination and overtone scattering (generally up to second order) were considered as routes for the up-pumping of energy [23, 24, 58, 68, 69, 70,]. Additionally, the adiabatic heating of the phonon bath as a result of the initial impact was considered and implemented through shock heating of the phonon bath vibrations. This approach is outlined in more detail in the following section.

1.3 Vibrational Up-pumping Methodology

1.3.1 Vibrational Up-pumping as Described by Michalchuk et al.,

The vibrational up-pumping model presented by Michalchuk et al., in simple terms represents a simulation of the impact event, which leads to excitation of vibrations in the material and subsequent initiation. The initial mechanical impact can cause two primary changes to the material, namely compression and potential fracture.

Compression of the material can be understood as propagation of an acoustic wave through the material, exciting the low energy phonons dramatically. More particularly, this energy is channelled into the three acoustic vibrations, those which represent the displacement of every atom in the crystal along one of the three coordinate axes. Additionally, the experienced increase in pressure causes vibrational mode hardening to occur, the extent of which is defined by the materials Grüneisen parameter (Γ). This increase in energy within the lattice results in adiabatic heating of the material, as described by Equation 1.5.

$$\left(\frac{T}{T_0}\right) = \left(\frac{V}{V_0}\right)^{-\Gamma} \quad \text{Equation 1.5}$$

In simple terms, the more compressible the material the larger the change in temperature (T). This adiabatic heating is largely centred on the delocalised phonon modes which comprise the phonon bath which reaches temperatures typically in the thousands of Kelvin compared to the room temperature value for the bulk material. This high temperature is referred to as T_{shock} , and the net effect is a hot vibrationally active set of phonon vibrations which are able to scatter and up-pump the energy onto the higher energy molecular vibrations in the region $1-3 \Omega_{\text{max}}$, which is termed the up-pumping window. In practice, T_{shock} can be estimated from the specific heat capacity (C_V) of the material, which in turn can be calculated directly from the phonon spectrum.

The vibrational up-pumping of energy is mediated through one of two possible phonon-phonon collision pathways: between two phonon bath (q) modes (either self-scattering via the overtone route, or two separate phonons scattering via the combination route), or through collisions of one q mode with one Q_D mode. The outcome of these permitted pathways is that the maximum frequency capable of being excited to is $3\Omega_{\text{max}}$. It is assumed that this up-pumped energy is channelled into particular vibration(s) associated with initiation of the material, termed the target modes, Q_T that fall in this up-pumped window region. A schematic diagram for vibrational up-pumping is outlined in Figure 1.12.

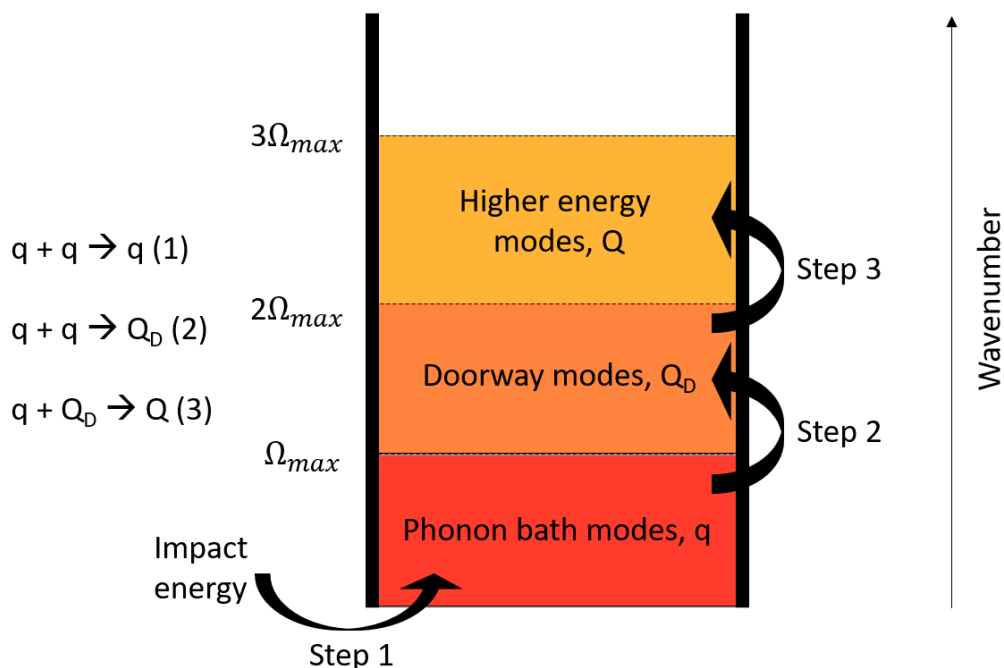


Figure 1.12: Shows a schematic of the vibrational up-pumping procedure with three primary phonon-phonon scattering steps outlined. The nature of the phonon modes (q – phonon bath mode, Q_D – doorway mode and Q – higher energy mode) involved in the steps are denoted on the left-hand side (1-3). It is assumed that one of the Q_D or Q modes acts as a target mode (Q_T) leading to energetic response.

The complete set of higher energy vibrational states that are excited as a result of the vibrational up-pumping of the impact energy are termed the two-phonon density of states ($\Omega^{(2)}$), which provides a metric for quantifying the amount of energy channelled upwards by the material following impact. The predicted impact sensitivity is obtained through evaluation of the $\Omega^{(2)}$ trace when projected onto the underlying vibrational character within the up-pumping window. This represents the localisation of energy onto the molecular vibrations. A number of applications of this model have been explored by Michalchuk et al. and are outlined below.

1.3.2 Vibrational Up-pumping of Energetic Azides

The first computational investigation to predict the impact sensitivity through the vibrational up-pumping model outlined in the previous Section, focussed on a series of energetic azides, which were chosen for their structural simplicity and also for the broad range of impact sensitivity values that this structural class provided. It should be noted that the T_{shock} contributions to the phonon

bath were not considered in this early work as they had yet to be implemented in the procedure. The test set was selected to contain a large array of sensitivities and structural types (semi-coordinated, molecular, ionic).

The initiation of azides progresses through cleavage of a covalent N-N bond, the structural simplicity of the ion allowed for in depth exploration of vibrations which would trigger such an event. It was noted that the excited state of the ion was of antibonding character, prompting an investigation in the change in energy of the potential energy surface for a number of common distortions present in vibrations. It was noted that excitation of the N-N-N angle bend beyond 120° resulted in accessing a conical intersection, which provided a direct route to electronic excitation to overcome the large energy barrier to achieve covalent bond rupture. This vibration was therefore considered the target vibrational mode and was found to be present within the up-pumping region ($1-3 \Omega_{\max}$) for each of the azide EMs. As such the magnitude of $\Omega^{(2)}$ was rationalised when projected onto the target frequency for each material. Excellent agreement between the experimental and predicted sensitivities were achieved for each of the azide materials (See Figure 1.13, (A) - with the exception of BaN_3 which was rectified (B) by the inclusion of the 2nd and 3rd overtone coupling pathways). Thus, the set of azide EMs were successfully grouped into one of three classifications (sensitive, low sensitivity and insensitive).

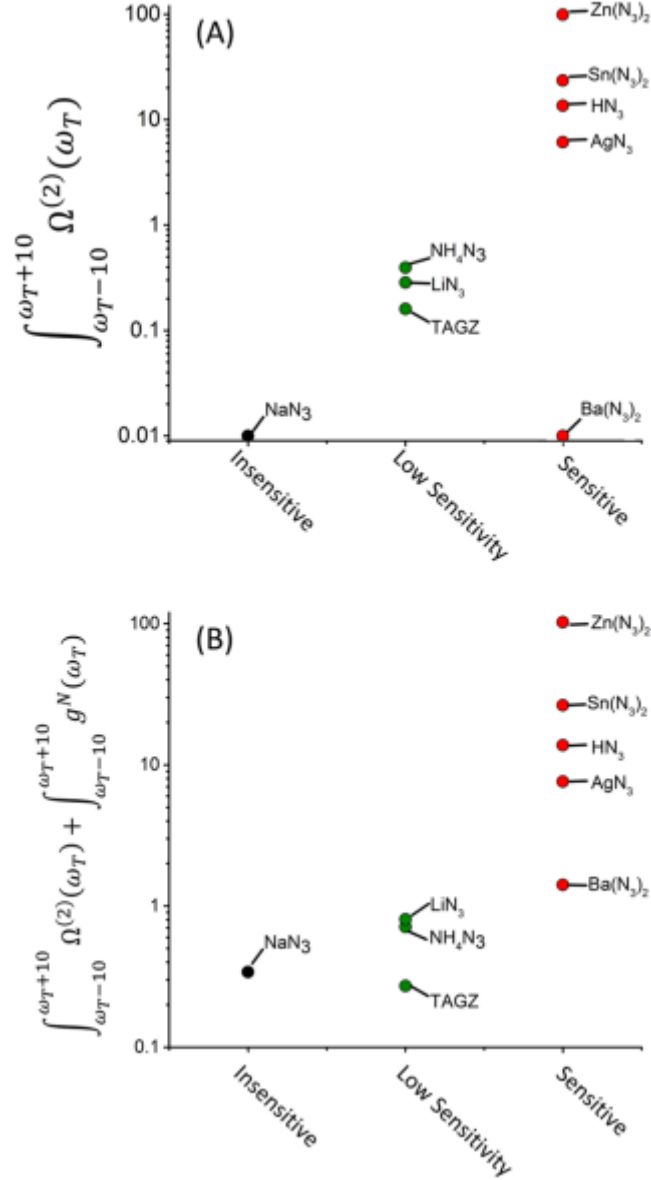


Figure 1.13: Shows the up-pumped density projected onto the target mode for each azide EM grouped into their respective sensitivity classifications. (A) is based on scattering and first overtone contributions to $\Omega^{(2)}$ and (B) includes the second and third overtones. Taken from Michalchuk et al. [67].

This work provided confidence in the ability of the vibrational up-pumping procedure to reproduce a complex material property to a good enough agreement with experimental findings when the exact nature of the target vibrational mode is known.

1.3.3 Vibrational Up-pumping of Molecular Energetics

Following the work on azide-based EMs, a number of widely used molecular EMs (from differing structural chemistry classes) were selected for impact sensitivity prediction. It was noted that with increasing molecular complexity the difficulty in determining the exact nature of the target vibrational frequencies increased, meaning that $\Omega^{(2)}$ could not be rationalised by projecting onto target vibrations of molecular EMs. Instead, the up-pumped density was rationalised through projection of the $\Omega^{(2)}$ across the entire up-pumping window. This action was justified as visualisation of the modes that fell within each up-pumping window appeared to include C/N-NO₂ bond stretching character.

The outcome was a good correlation (Figure 1.14) between the up-pumped density and the experimental sensitivity for the molecular EMs with a notable outlier, namely NTO when Ω_{\max} is located at 170 cm⁻¹ (two points are present for NTO due to uncertainty in the location of Ω_{\max} – this is addressed in more detail in Chapter 2).

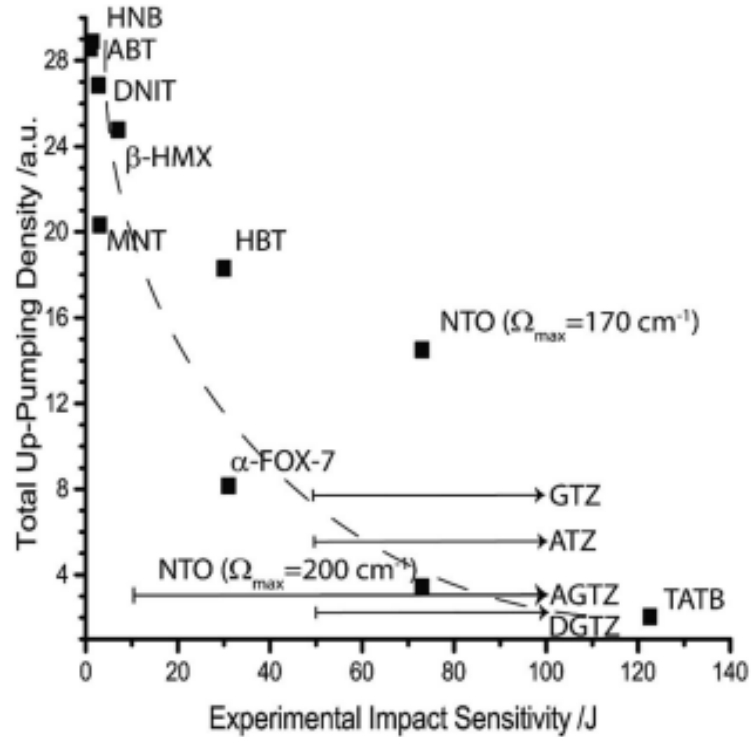


Figure 1.14: Shows the total up-pumping density projected onto all vibrational modes between $1-3\Omega_{\max}$ for a number of molecular EMs vs. the experimental sensitivity taken from Michalchuk et al. [57].

While this trend is very promising it suffered from a significant drawback in that each phonon calculation was derived from multiple sample points across the Brillouin Zone (BZ), meaning that predictions were both very computationally intensive and severely limited in terms of the size of crystallographic unit cells that could be studied in this way. In an attempt to reduce the computational cost, the next step therefore explored the predictive power of the up-pumping method based solely on zone-centre vibrational frequencies.

1.3.4 Zone Centre Vibrational Up-pumping

In this context, zone centre refers to the calculation of the vibrational frequencies solely at the gamma (Γ) point in the BZ (i.e., the centre of the BZ), which serves to dramatically reduce the amount of computational resources required for a sensitivity prediction. Whether or not zone centre frequencies alone would be sufficient for the reliable prediction of the impact sensitivity was unknown, as such many of the EMs considered in the full BZ sampling investigation were once again investigated, with some additional

materials added into the test set. A primary concern with the zone-centre approach was the systematic under sampling of the phonon bath, resulting in increased uncertainty in the location of Ω_{\max} . This resulted in additional steps being implemented to the process to locate Ω_{\max} (see Chapter 2) and potential for it be placed in the incorrect location, resulting in a badly defined up-pumping window. The under sampled phonon bath also resulted in a reduced intensity $\Omega^{(2)}$ trace and subsequently reduced magnitude of up-pumped density. Despite this, a good trend between experimental and predicted impact sensitivities was found (Figure 1.15).

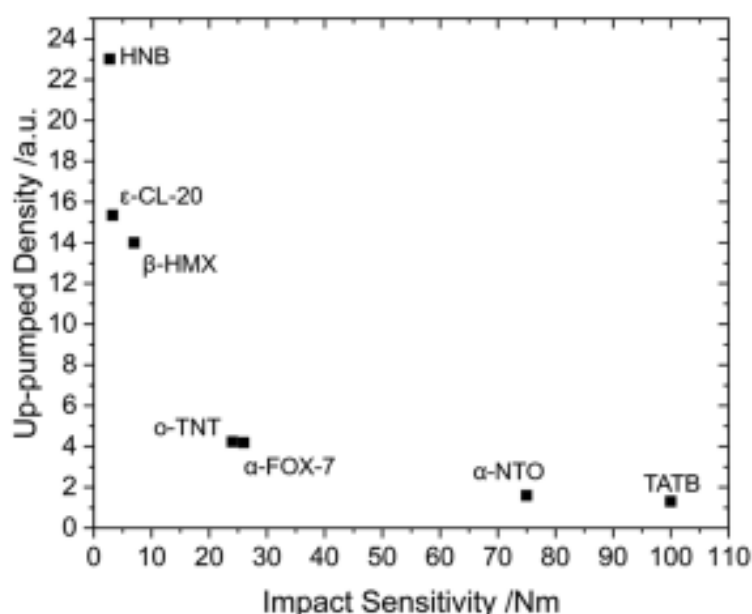


Figure 1.15: Shows the up-pumped density projected onto all modes between 1- $3\Omega_{\max}$ for a number of molecular EMs based on zone-centre frequencies vs. the experimental sensitivity taken from Michalchuk et al. [23].

The nature of the relationship between the up-pumped density and the experimental impact sensitivity appears more as a decay curve when zone centre only frequencies are used. Despite this, the ability to readily discern between primary and secondary EMs is apparent. This approach clearly suggests that a sufficient understanding of the vibrational energy transfer can be obtained through consideration of the BZ centre in isolation, drastically reducing both the amount of computational resources and time required to obtain a sensitivity prediction. For this reason, consideration of the zone centre

frequencies was deemed sufficient for reliable impact sensitivity prediction and was chosen as the method by which predictions in this work would be made.

1.3.5 Vibrational Up-pumping in this Work

In practice the vibrational up-pumping procedure used in this thesis follows a number of well-defined steps, as outlined below.

- A Γ -point vibrational frequency calculation is completed based on a relaxed primitive unit cell of an EM.
- The phonon density of states ($g(\omega)$) is generated (by subjecting a 5 cm^{-1} Gaussian smearing to each mode to approximate dispersion – more detail in Chapter 2). This acts as the input for the vibrational up-pumping procedure.
- The maximum frequency of the phonon bath (Ω_{max}) is determined through the use of centre of mass analysis (see Chapter 2).
- The specific heat capacity (C_V) is calculated from the Gaussian broadened phonon density of states through the use of Equation 1.6.

$$C_V = \int \frac{\partial n}{\partial T} \hbar \omega g(\omega) d\omega \quad \text{Equation 1.6}$$

- The T_{shock} is determined through consideration of the contributions to the total heat capacity of the phonon bath (C_{ph}) and the complete set of vibrations (C_{tot}). Previous work has assigned the value of $C_{\text{tot}}/C_{\text{ph}} = 5.22$ to 3423 K for HNB which is used as a reference allowing for T_{shock} values of novel EMs to be determined through a simple proportionality relationship, shown by Equation 1.7.

$$\frac{\left(\frac{C_{\text{tot}}}{C_{\text{ph}}}\right)_{\text{HNB}}}{\left(\frac{C_{\text{tot}}}{C_{\text{ph}}}\right)_{\text{EM}}} = \frac{T_{\text{shock HNB}}}{T_{\text{shock EM}}} \quad \text{Equation 1.7}$$

- The input $g(\omega)$ is normalised to the number of vibrations that comprise the phonon bath (denoted by $Z(6+Y)$) where Z is the number of molecules in the unit cell and Y is the number of amalgamated

vibrations (delocalised vibrations with a small degree of localised character – discussed in more detail in Section 2.3 in Chapter 2).

- The $g(\omega)$ is thermally populated according to Bose-Einstein statistics and then subsequently exposed to the shock temperature resulting in increased excitation of the low energy phonon vibrations with respect to high energy vibrations.
- Through consideration of three phonon scatterings the $\Omega^{(2)}$ trace is generated, representing the total area over which energy can be up-pumped onto. Explicit calculation of cubic anharmonic coupling constants is neglected as they are deemed too computationally expensive, instead the coupling constants are assumed to follow the following relationship, $qqq > qqQ > qQQ$, with four phonon couplings and those including solely localised vibrations (Q) being deemed too statistically unlikely to occur. This results in an up-pumping window of $1-3\Omega_{\max}$ being considered.
- The $\Omega^{(2)}$ trace is then projected onto the underlying $g(\omega)$ trace between the values of $1-3\Omega_{\max}$. This is achieved through use of Equation 1.8.

$$\text{projected } \Omega^{(2)} = \Omega^{(2)} \phi(g(\omega)) \quad \text{Equation 1.8}$$

Where $\phi(g(\omega))$ is a binary function which is equal to 1 at values of ω where $g(\omega) > 0$ and equal to 0 at values of ω where $g(\omega) = 0$. This represents the amount of the $\Omega^{(2)}$ trace that can be captured by underlying vibrational character.

- The up-pumped density is evaluated by taking the integral of the projected $\Omega^{(2)}$ trace between $1-3\Omega_{\max}$ as per Equation 1.9.

$$\text{Up - pumped density} = \int_{\Omega_{\max}}^{3\Omega_{\max}} \text{projected } \Omega^{(2)} . d\omega \quad \text{Equation 1.9}$$

The up-pumped density gives a measure of the energy that is channelled upwards as a result of the phonon-phonon scatterings.

- The up-pumped density is then scaled per Z (i.e. per molecule) to account for the vibrational energy becoming trapped on a single

molecule within the crystallographic unit cell. The values of Z used for each EM studied in this work are based on the space group and are provided in Tables A1-3 in Appendix A.

- The normalised up-pumped density is compared to the experimental sensitivity, providing a value that can be readily compared between different EMs.

1.4 Computational Methodology

First principles simulation was performed for all EMs studied in this thesis, in order to (i) produce a fully optimised crystallographic unit cell, and (ii) to provide the density of states, $g(\omega)$ as input data for the vibrational up-pumping model. Background information on the simulation methods used are discussed here.

1.4.1 Quantum Mechanics in Computational Chemistry

The time independent Schrödinger equation (Equation 1.10) relates the Hamiltonian (\hat{H}) to the energy of a system of electrons and nuclei, through consideration of the wavefunction (Ψ) [71, 72].

$$\hat{H}\Psi = E\Psi \quad \text{Equation 1.10}$$

The total energy expressed by the Hamiltonian is easily split into five component parts (Equation 1.11), namely the kinetic energies of the electrons and nuclei (K) as well as the repulsive self-interaction energies and the attractive interaction energy between the electrons and nuclei (P).

$$\hat{H} = K_{elec} + K_{nuc} + P_{elec-elec} + P_{nuc-nuc} + P_{elec-nuc} \quad \text{Equation 1.11}$$

This expression can be simplified using the Born-Oppenheimer Approximation (BOA) which assumes that the nuclei are static with respect to the electrons as they have significantly larger mass [73]. This removes two terms from Equation 1.11 as the kinetic energy of the nuclei is now zero, and the nuclei-nuclei interaction energy is now readily solvable via Coulomb's law. Despite this simplification the time independent Schrödinger equation remains unsolvable for materials with more than one electron as a result of the many-body problem [74]. As such approximations must be used in order for a solution to be obtained.

1.4.2 Hartree-Fock Theory

One such approximation, developed by Hartree and Fock in the late 1920s (Hartree-Fock Theory – HF), assumes that the electrons within the system move independently with respect to one another [74, 75]. Simply put, the wavefunction is replaced by N single electron wavefunctions (spin orbitals) for a system comprised of N electrons. The approximate wavefunction of the N electron system is obtained by taking the antisymmetric product of each individual electron wavefunction (this is referred to as the Slater determinant). This ensures that no electrons can occupy the same set of quantum numbers as defined by the Pauli Exclusion Principle and gives an exact measure of the electron exchange energy. This process does not yield an approximation for the electron correlation energy, resulting in the determined energy being systematically larger than the true ground state energy of the system. Despite this, HF is able to reproduce energies to within 10 % of a number of more modern approaches, which were subsequently developed in an attempt to quantify the absent electron correlation energy; examples here include coupled cluster methods, Møller-Plesset methods, and configuration interaction methods). However, all of these higher levels of theory suffer from the major drawback of being more computationally expensive [76, 77]. To this end, density functional theory, an alternative approach to HF theory which retains relative computational cheapness, is of considerable attraction.

1.4.3 Density Functional Theory

1.4.3.1 Introduction to DFT

Rather than focussing on approximating the wavefunction, DFT focuses on the relationship between the total electron density of a system, $\rho(r)$, and the energy of the system [72, 76, 77]. This is an attractive alternative for two reasons, firstly the $\rho(r)$ function is often significantly simpler than that of the many electron wavefunction and secondly $\rho(r)$ is an experimentally observable characteristic. This approach was developed by Hohenberg and Kohn in 1964, however the exact mathematical expression of the energy functional relating to $\rho(r)$ remains unknown [78]. As such, approximate functionals are used in

which the ground state energy of the system is split into component parts that can be considered separately, shown by Equation 1.12.

$$E_0 = E(\rho(r)) = P_{elec-elec} + P_{elec-nuc} + K(\rho) \quad \text{Equation 1.12}$$

Where P represents the potential energy terms between pairs of electrons or the interaction between electrons and nuclei and K represents the kinetic energy of the system, which is once again plagued with difficulties arising from the many-body problem.

Kohn and Sham developed an approach in which a series of one-electron Kohn-Sham equations are defined, in an analogous approach to that taken in HF theory, to represent a series of molecular orbitals which when summed represent the total $\rho(r)$ of a non-interacting system [79]. When this is applied to an interacting system of the same $\rho(r)$ the calculated energy will once again not represent the ground state (as in HF theory) as a result of the electron correlation and exchange terms which have thus far been ignored. The contributions to the systems energy from the electron correlation and exchange are given the term E_{xc} (exchange correlation functional) which must be added to Equation 1.12. This energy must be approximated, which can be approached in a number of ways, depending on the system in question.

1.4.3.2 Exchange/Correlation Functionals

One approach to approximating E_{xc} is through the Local Density Approximation (LDA) which approximates $\rho(r)$ to that of a uniform electron gas of the same $\rho(r)$ [72, 76, 77]. This approach provides a good approximation for materials that exhibit predominantly uniform electron density, such as densely packed metals, however it fails when the electron density varies dramatically as is the case in molecular structures. In an attempt to correct for this, the Generalised Gradient Approximation (GGA) was developed in which the rate of change of the $\rho(r)$ is considered as well as the $\rho(r)$ itself [72, 76, 77]. This means that changes in $\rho(r)$ are accounted for more accurately. There are a number of well-known GGA functionals namely, BLYP (named for the Becke's exchange functional and Lee, Yang and Parr's correlation functional), PW91 (named after Perdew and Wang) and PBE (named after Perdew, Burke and Ernzerhof). The latter was chosen for this work as it had already been shown

to accurately reproduce the geometry and vibrational frequencies of a number of EMs [80, 81, 82, 83].

1.4.3.3 Dispersion Corrections

While the methods outlined for approximating E_{XC} each have their merits, they are primarily defined to explain electronic interactions within molecular arrangements. This means that long range electronic correlations (i.e. intermolecular interactions, such as dispersion interactions) are systematically under-represented. A large proportion of the EMs considered in this body of work are molecular crystals, meaning intermolecular interactions are vitally important to the structure. As such a dispersion correction term must be included. There are two different correction schemes used throughout this body of work namely, Tkatchenko-Scheffler (TS) and Grimme-D2 (G-06) [84, 85].

1.4.3.4 Hybrid DFT

As has been outlined, the use of DFT requires approximation of both the electron exchange and correlation energy in the form of E_{XC} . Utilisation of the exact determination of electron exchange from HF theory results in only correlation being approximated. A significant number of different ‘fit for purpose’ functionals have been developed in which differing amounts of incorporated HF exact exchange are included. An example of a commonly used hybrid DFT functional that is comprised of differing amounts of LDA and GGA functionals as well as 20 % HF exact exchange is B3LYP [72, 76, 77]. This level of theory was used throughout this thesis for the isolated-molecule simulations.

1.4.4 Basis Sets

The wavefunction can be obtained through a linear combination of a number of more simple functions, and the resulting collection of basis functions is known as a basis set. While increasing the number of basis functions generally leads to an improved description of the wavefunction, a balance must be drawn between accuracy and computational cost. There are two commonly used types of basis sets: (i) localised (typically Gaussian) functions commonly used

to describe atomic/molecular orbitals (typically in gas phase calculations) and (ii) delocalised (typically plane wave) functions commonly used to describe periodic solids [72, 76, 77]. Both approaches were used in this thesis. For the latter, an added complication is the need to treat the core electrons in a different manner to the valence electrons. This arises as the core electrons complicate the electronic wavefunction dramatically, meaning that a significant number of plane waves are required for accurate modelling work. As such, the core electrons are replaced by ‘frozen’ cores described by atom specific pseudopotentials, making the number of plane waves needed to describe the wavefunction more tractable. Two common types used in solid-state modelling are norm-conserving and ultra-soft pseudopotentials [72, 76, 77]. The main body of this work uses norm-conserving pseudopotentials as they allow for the use of DFPT (density functional perturbation theory) to calculate the vibrational frequencies (Section 1.4.7.2) [86]. The term norm-conserving is used as the total electron density below the cut off energy is made to match the total electron density. This generally requires an increased plane wave cut-off energy when compared to ultra-soft pseudopotentials.

1.4.5 Solid-State Modelling and Bloch’s Theorem

A solid lattice can be considered as an infinite system of repeating structural units, and the simplest way of describing this is through consideration of the repeating (primitive) unit cell. A primitive cell which has a lattice point at its centre is known as the Wigner-Seitz cell, and its corresponding reciprocal space representation is known as the Brillouin Zone (BZ). This provides a useful construct to consider how waves (electrons and vibrations) interact with matter, in the reciprocal units of wavevector, rather than the real space wavelength notation.

The electrons in the primitive cell are sufficient to determine the wavefunction of the system as a result of the periodicity of solid, as stated by Bloch’s theorem. This states that the electronic wavefunction of a periodic system can be represented as Bloch wave which takes the form shown in Equation 1.13 [87, 88].

$$\psi(r) = \mu(r).e^{ikr} \quad \text{Equation 1.13}$$

Where $\mu(r)$ represents a periodic function where $\mu(r + R)$ is equivalent when R represents the lattice vector and i and k represent the imaginary unit, the wave vector respectively. The wave vector, k , represents the vector of the plane wave electronic wavefunction within the first BZ. Typically, k is sampled evenly throughout the BZ using a 'Monkhurst-Pack grid' of points spread throughout the space [89]. The number of points which comprise the grid depend on the size of the primitive cell dimensions, with larger cells requiring fewer sample points as a result of a smaller BZ. Throughout this thesis, calculations were performed using a minimal Monkhurst-Pack sampling grid of 0.05 \AA^{-1} .

1.4.6 Geometry Optimisation

For a given set of atomic positions within a unit cell there exists a single ground state energy in which the energy of the system is at minimum. The energy of the system is dependent on the atom positions, represented by the potential energy surface (PES), which is comprised of $3N$ variables (for N atoms). The initial geometry adopted for a calculation from e.g. single crystal diffraction measurements will likely not be representative of the global minimum of the PES, meaning that the energy of the system needs to be reduced by iteratively changing the geometry of the system (optimisation) until a number of convergence criteria are met. This is achieved first through approximation of the wavefunction through a self-consistent field method (SCF) and calculation of the associated single point energy. From here, geometry optimisation can begin [72, 76, 77].

A common optimisation procedure is rooted in calculation of the rate of change of the PES (which represents the forces on the atoms) and defining a new point on the gradient line at which the energy of the system is lower. This is known as steepest descent method. This method is often computationally expensive as many iterations are required to get close enough to the global minimum [76]. In order to improve on this the curvature of the PES with respect to $3N$ is often rationalised through the estimation of the force constants (second derivatives) which are stored within a Hessian matrix. This information allows for much quicker location of a minimum, as the positions of the atoms

can be moved by varying displacements towards the minimum energy surface. A number of algorithms have been determined for locating minima and are readily implemented to improve calculation speeds. One such example that is used in this thesis is the Broyden-Fletcher-Goldfarb-Shanno (BFGS) method [90, 91, 92, 93].

In this way the electronic structure and atomic positions are updated according to the series of steps outlined in Figure 1.16 until a set of convergence criteria are met. These typically include: the forces experience by the atoms, the stress experienced by the unit cell vectors, the change in energy of the system per iteration and the change in position of each atom in the system.

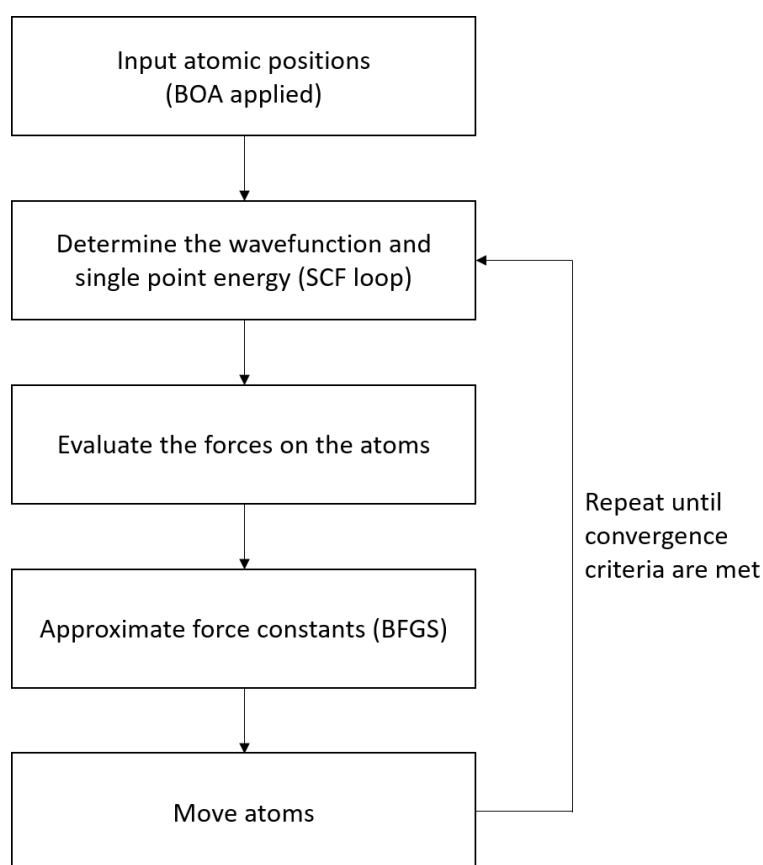


Figure 1.16: Shows a flowchart for the geometry optimisation process utilised for each EM considered in this body of work.

1.4.7 Vibrational Frequency Calculations

1.4.7.1 Gas Phase Vibrational Frequencies

Calculating the force constants directly permits evaluation of the molecular vibrational frequencies [72, 76, 77]. The nature of the frequencies also yields information about the associated stationary point that the optimisation procedure located. An energy minimum will result in $3N-6$ real vibrations (for a non-linear molecule), representing positive curvature in all directions on the PES, whereas a saddle point or a maximum will have one, or more, imaginary vibrational frequencies suggesting negative curvature. Therefore, the ground state structure will always yield $3N-6$ real frequencies.

Gas phase frequencies are calculated in this work such that force constants of a variety of molecular bond strengths could be compared through use of LModeA (discussed in more detail in Section 1.4.8.6) [94].

1.4.7.2 Phonon (Solid-State) Frequencies

There are two common methods for conducting phonon calculations, namely finite displacements and density functional perturbation theory, DFPT. The latter was used extensively in this thesis and so is briefly discussed here. In essence, DFPT is represented by a Taylor expansion (truncated at the second term due to the harmonic approximation) of a number of very small atomic position perturbations, which allow the surrounding curvature of the potential energy surface to be explored. In this way the $3N$ directional curvatures, associated with $3N$ force constants and therefore vibrational frequencies, can be obtained. This can be projected along a k -point path within the BZ to calculate frequencies without explicit optimisation of a supercell [72, 76, 77, 86].

1.4.8 Additional Software

1.4.8.1 Accelrys Materials Studio

Materials Studio is a computational modelling package with a vast number of functionalities. In this work it was primarily used to generate the input files (.cell and .param) for CASTEP calculations from an experimental crystal structure.

Additionally, it was used to generate partial phonon density of states traces to compare to the in-house script developed (outlined in Chapter 2) [95].

1.4.8.2 CASTEP

In this body of work, CASTEP V16 was used as the principle computational modelling suite for solid-state calculations. Both geometry optimisation and vibrational frequency (phonon) calculations using the BFGS and DFPT algorithms as implemented respectively. Additionally, the included dos.pl script was used to develop comparison traces for the in-house density of states script developed in this work (more details in Chapter 2) [96].

1.4.8.3 CRITIC2

CRITIC2 has been used as a post-processing script in this work to evaluate and visualise a number of non-covalent interactions. This is achieved through defining the location of the stationary points in the electron density. The reduced density gradient (deviation in $\rho(r)$ from a homogeneous distribution of electron density) is compared to the $\text{sign}(\lambda_2)$ value (where λ_2 represents the second density Hessian value) which quantifies whether an interaction is attractive or repulsive [97, 98, 99, 100]. In this thesis, this method has been applied to a co-crystal as well as two polymorphs of an EM to quantify the relative strengths of the hydrogen bonding interactions present in the structures.

1.4.8.4 AIRSS (Ab Initio Random Structure Searching)

AIRSS can be used to generate a number of 'random' structures by defining an area surrounding an atom in which a number of additional atoms can be placed randomly, with the subsequent structure being optimised to loose convergence criteria (using CASTEP). This process is repeated a number of times with the optimised geometries ranked according to their energies. The process is ended when the lowest energy structure is produced a number of times (giving confidence it is the ground state energy) [101]. In this work, AIRSS is used to locate the hydrogen atoms in a crystal structure of a metal-containing coordination polymer that presented with poor crystallinity, and thus

an incomplete model was obtained by X-ray diffraction analysis. The computational details undertaken are outlined in greater depth in Chapter 4.

1.4.8.5 Gaussian

Gaussian V16 is an *ab initio* computational modelling package that was used in this thesis to complete geometry optimisation and vibrational frequency calculations for a series of gas-phase energetic molecules. Hybrid DFT (B3LYP) with a Pople basis set (6-31G*) was used for each calculation [102].

1.4.8.6 LModeA

In order to elucidate the weakest bonds in the molecular EMs pursued in this work, local mode analysis was undertaken using LModeA [94]. This approach takes an optimised gas phase structure and its vibrational frequencies as an input and de-convolutes the $3N-6$ normal modes of vibration onto their local mode contributions (the corresponding bond stretches, angle bends and dihedral torsions). This also allows for direct computation of mass decoupled force constants, meaning that bond strengths of bonds containing different atoms can be readily compared. These force constants are used as a guide to identify the weak bonds in the EM molecules, the stretching of which could act as target modes.

1.4.8.7 Vibrational up-pumping script

The determination of the up-pumped density for each EM in this work was completed through use of the in-house Python script developed by Dr. Adam Michalchuk [23, 57, 67, 68, 69, 103]. This script takes the $g(\omega)$ spectrum as an input alongside a number of additional parameters (Ω_{\max} , $Z(6+Y)$ and T_{shock}) and returns both the complete and projected $\Omega^{(2)}$ alongside the up-pumped density value which is subsequently compared to the experimental sensitivity.

1.5 Project Outlines and Aims:

To date, the development of a reliable computational workflow to predict the impact sensitivity of single component molecular EMs, for a broad structural class of materials by Michalchuk et al., has shown good success. This

approach, however, requires explicit definition of Ω_{max} for each material which at current cannot be achieved quickly and quantitatively leading to a degree of human error.

Moreover, a number of increasingly common EM structure types have yet to be tested by the up-pumping model, such as co-crystals and coordinated metal salts. Such materials can have strikingly different impact sensitivities to those that they are based on, and thus provide a number of interesting case studies to test whether the methodology can accurately describe these systems too. If the model proves successful for such EMs, the insight that can be gained may be used to rationalise the changes in sensitivity from their molecular counterparts, and thus potentially allowing for design criteria and structure/property relationships to be defined.

Additionally, the ability to predict the impact sensitivity of single component molecular energetics provides an excellent opportunity to explore the effects of varying the molecular structure on the impact sensitivity. In short, an opportunity has presented itself to develop structure/property relationships which can be used in the design process to guide synthesis towards the development of novel, insensitive, EMs.

This thesis therefore attempts to address the following aims over a series of Chapters:

- Chapter 2 outlines the development of a Python script to address the difficulty in locating the upper limit of the phonon bath (Ω_{max}). Additionally, scripts to improve the efficiency and applicability of the procedure through unification of input file generation and interrogate solid-state vibrations in an attempt to identify target modes are outlined.
- Chapter 3 explores the effect of co-crystallisation and pressure-induced polymorphism on the impact sensitivity of EMs as well as attempting to outline a workflow for the treatment of co-crystals in the vibrational up-pumping procedure.
- Chapter 4 aims to test the applicability of the vibrational up-pumping methodology when applied to coordinated metal salts and if

successful, develop a workflow for the sensitivity prediction of such EMs. Moreover, comparison between coordinated salts and their molecular counterparts in an attempt to rationalise the high sensitivity exhibited by such EMs.

- Chapter 5 outlines efforts to develop in-depth structure/property relationships for three series of structurally related molecular EMs, to develop a set of criteria required to produce primary or secondary EMs.

1.6 References

1. T. M. Klapötke, *Chemistry of High-Energy Materials*, De Gruyter, Berlin, 5th edn., 2019.
2. J. Akhavan, *The Chemistry of Explosives*, The Royal Society of Chemistry, Cambridge, UK, 2nd edn., 2004.
3. W. D. Cocroft, *Dangerous Energy: The archaeology of gunpowder and military explosives manufacture*, Liverpool University Press, Cambridge, UK, 1st edn., 2000.
4. J. Kelly, *Gunpowder, Alchemy, Bombards, and Pyrotechnics: The History of the Explosive that Changed the World*, Basic Books, New York City, USA, 2004.
5. T. S. Ritchie, K. E. Riegner, R. J. Seals, C. J. Rogers and D. E. Riegner, *Evolution of Medieval Gunpowder: Thermodynamic and Combustion Analysis*, ACD Omega, 2021, **6**, 22848-22856.
6. T. L. Davis, *The Chemistry of Powder and Explosives*, reprint, Angriff Press, 1972.
7. A. Nobel, *Alfred Nobel, Inventor of Dynamite*, J. Chem. Educ., 1928, **5**, 1480.
8. C. E. Munroe and C. Hall, *Explosives in Metal Mining and Quarry Operations*, Wexford College Press, London UK, 2003.
9. W. Beck, J. Evers, M. Göbel, G. Oehlinger and T. M. Klapötke, *The Crystal and Molecular Structure of Mercury Fulminate (Knallquecksilber)*, Z. Anorg. Allg. Chem., 2007, **633**, 1417-1422.
10. I. J. Powell, *Insensitive Munitions – Design Principles and Technology Developments*, Propellants Explos. Pyrotech., 2016, **41**, 409-413.
11. E. Baker, M. van der Voort and M. Pope, *NATO Standards and Practice for Munitions Safety and Insensitive Munitions*, NATO HQ, Brussels, 2018.
12. J. P. Agrawal, *High Energy Materials: Propellants, Explosives and Pyrotechnics*, Wiley, New Jersey, USA, 2010.
13. Working safely with picric acid, *Handling of Picric Acid by Laboratory Personnel (HSE Tool #22)*. Department of Health, Safety and Environment, University of British Columbia.
14. M. K. Shukla, V. M. Boddu, J. A. Steevens, R. Damavarapu, and J. Leszczynski, *Energetic Materials From Cradle to Grave*, Springer, New York, USA, 2017.
15. C. F. Baxter, *The Secret History of RDX: The Super-Explosive that Helped Win World War II*, University Press of Kentucky, Lexington, Kentucky, USA, 2018.
16. L. L. Altgilbers, J. Baird and B. L. Freeman, *Explosive Pulsed Power*, Imperial College Press, Covent Garden, London, UK, 2011.

17. A. Elbeih, M. Jungová, S. Zeman, P. Vávra and Z. Akštein, *Explosive Strength and Impact Sensitivity of Several PBXs Based on Attractive Cyclic Nitramines, Propellants, Explos. Pyrotech.*, 2012, **37**, 329–334.
18. A. T. Nielsen, *Caged polynitramine compound*, U.S Patent #5693794, 1997.
19. O. Bolton, L. Simke, P. F. Pagoria, A. J. Matzger, *High Power Explosive with Good Sensitivity: A 2:1 Cocrystal of CL-20/HMX*, *Cryst. Growth Des.*, 2012, **12**, 4311–4314.
20. M. Ghosh, A. K. Sikder, S. Banerjee and R. G. Gonnade, *Studies on CL-20/HMX (2:1) Cocrystal: A New Preparation Method and Structural and Thermokinetic Analysis*, *Cryst. Growth Des.*, 2018, **18**, 3781–3793.
21. W. A. Trzcinski and A. Belaada, *1,1-Diamino-2,2-dinitroethene (DADNE, FOX-7) – Properties and Formulations (a Review)*, *Cent. Eur. J. Energ. Mater.*, 2016, **13**, 527–544.
22. V. M. Boddu, D. S. Viswanath, T. K. Ghosh, R. Damavarapu, *2,4,6-triamino-1,3,5-trinitrobenzene (TATB) and TATB-based formulations – A review*, *J. Hazard. Mater.*, 2010, **181**, 1–8.
23. A. A. L. Michalchuk, J. Hemingway and C. A. Morrison, *Predicting the impact sensitivities of energetic materials through zone-center phonon up-pumping*, *J. Chem. Phys.*, 2021, **154**, 064105.
24. I. L. Christopher, C. R. Pulham, A. A. L. Michalchuk and C. A. Morrison, *Is the impact sensitivity of RDX polymorph dependant?*, *J. Chem. Phys.*, 2023, **158**, 124115.
25. R. Cheret, *Detonation of Condensed Explosives*, Springer New York, New York, USA, 2012.
26. T. L. Jensen, J. F. Moxnes, E. Unneberg and D. Christensen, *Models for predicting impact sensitivity of energetic materials based on the trigger linkage hypothesis and Arrhenius kinetics*, *J. Mol. Model.*, 2020, **26**, 65.
27. S. A. Shackelford, *A General Concept Concerning Energetic Material Sensitivity and Initiation*, *J. Phys. IV*, 1995, **5**, 485–499.
28. R. Meyer, J. Köhler and A. Homberg, *Explosives*, Wiley, Weinheim, 6th edn., 2007.
29. F. P. Bowden, A. Yoffe, *Hot Spots and the Initiation of Explosion*, *Symp. Combust. Flame Explos. Phenom.*, 1949, **3**, 551–560.
30. F. P. Bowden, A. D. Yoffe, *Initiation and Growth of Explosion in Liquids and Solids*, Cambridge University Press, Cambridge, UK, 1952.
31. J. H. S. Lee, *The Detonation Phenomenon*, Cambridge University Press, Cambridge, UK, 2014.
32. W. Davis and C. Fauquignon, *Classical Theory of Detonation*, *Journal de Physique IV Proceedings*, 1995.
33. *Test Method Standard Safety and Performance Tests for the Qualification of Explosives (High Explosives, Propellants and Pyrotechnics)*; Indian Head, MD., 1999.
34. R. Doherty, *Relationship Between RDX Properties and Sensitivity*, *Propellants Explos. Pyrotech.*, 2008, **33**, 4–13.
35. M. Vaullerin, A. Espagnacq and L. Morin-Allory, *Prediction of Explosives Impact Sensitivity*, *Propellants, Explos. Pyrotech.*, 1998, **23**, 237–239.
36. M. H. Keshavarz, *Prediction of impact sensitivity of nitroaliphatic, nitroaliphatic containing other functional groups and nitrate explosives*, *J. Hazard. Mater.*, 2007, **148**, 648–652.
37. M. H. Keshavarz, *A New General Correlation for Predicting Impact Sensitivity of Energetic Compounds*, *Propellants Explos. Pyrotech.*, 2013, **38**, 754–760.

38. M. H. Keshavarz, K. Esmaeilpour, H. Khoshandam, Z. Keshavarz, H. R. H. Atabak, S. Damiri, A. Afzali, *A Novel Method for the Prediction of the Impact Sensitivity of Quaternary Ammonium-based Energetic Ionic Liquids*, *Cent. Eur. J. Energ. Mater.*, 2017, **14**, 520-533.
39. M. J. Kamlet and H. G. Adolph, *The relationship of Impact Sensitivity with Structure of Organic High Explosives. II. Polynitroaromatic explosives*, *Propellants Explos. Pyrotech.*, 1979, **4**, 30-34.
40. F. J. Owens, *Relationship between impact induced reactivity of trinitroaromatic molecules and their molecular structure*, *J. Mol. Struc. THEOCHEM*, 1985, **22**, 213-220.
41. F. J. Owens, *Calculation of energy barriers for bond rupture in some energetic molecules*, *J. Mol. Struc. THEOCHEM*, 1996, **370**, 11-16.
42. B. M. Rice, S. Sabu and F. J. Owens, *Density functional calculations of bond dissociation energies for NO₂ scission in some nitroaromatic molecules*, *J. Mol. Struc. THEOCHEM*, 2002, **583**, 69-72.
43. D. Mathieu, *Towards a Physically Based Quantitative Modelling of Impact Sensitivities*, *J. Phys. Chem. A.*, 2013, **117**, 2253-2259.
44. J. S. Murray, P. Lane, P. Politzer and P. R. Bolduc, *A relationship between impact sensitivity and the electrostatic potentials at the midpoints of C-NO₂ bonds in nitroaromatics*, *Chem. Phys. Lett.*, 1990, **168**, 135-139.
45. J. S. Murray, P. Lane, P. Politzer, *Relationships between impact sensitivities and molecular surface electrostatic potentials of nitroaromatic and nitroheterocyclic molecules*, *Mol. Phys.*, 1995, **85**, 1-8.
46. B. M. Rice and J. J. Hare, *A Quantum Mechanical Investigation of the Relation between Impact Sensitivity and the Charge Distribution in Energetic Molecules*, *J. Phys. Chem. A*, 2002, **106**, 1770-1783.
47. J. J. Gilman, *Chemical-Reactions at Detonation Fronts in Solids*, *Philos. Mag. B.*, 1995, **71**, 1057.
48. G. N. Pallewela, R. P. A. Bettens, *Theoretical investigation of impact sensitivity of nitrogen rich energetic salts*, *Comput. Theor. Chem.*, 2021, **1201**, 113267.
49. L. Türker, *Tunneling effect and impact sensitivity of certain explosives*, *J. Hazard. Mater.*, 2009, **169**, 819-823.
50. P. Politzer, J. S. Murray, *Are HOMO-LUMO gaps reliable indicators of explosive impact sensitivity?*, *J. Mol. Model.*, 2021, **27**, 327.
51. T. E. Jones, *Role of Inter- and Intramolecular Bonding on Impact Sensitivity*, *J. Phys. Chem. A.*, 2012, **116**, 11008-11014.
52. P. Politzer and J. S. Murray, *Impact sensitivity and crystal lattice compressibility/free space*, *J. Mol. Model.*, 2014, **20**, 2223.
53. D. E. Taylor, *Prediction of the Impact Sensitivity of Energetic Molecules Using Symmetry Adapted Perturbation Theory*, *Army Research Laboratory*, 2011.
54. Y. Ma, L. Meng, H. Li and C. Zhang, *Enhancing intermolecular interactions and their anisotropy to build low-impact-sensitivity energetic crystals*, *Cryst. Eng. Comm.*, 2017, **19**, 3145-3155.
55. K. B. Landenberger, O. Bolton and A. J. Matzger, *Energetic-Energetic Cocrystals of Diacetone Diperoxide (DADP): Dramatic and Divergent Sensitivity Modifications via Cocrystallization*, *J. Am. Chem. Soc.*, 2015, **137**, 5074-5079.

56. J. P. Perdew et al., *Understanding band gaps of solids in generalized Kohn-Sham theory*, *Proc. Natl. Acad. Sci. USA*, 2017, **114**, 2801-2806.
57. W. Zhu and H. Xiao, *First-principles band gap criterion for impact sensitivity of energetic crystals: a review*, *Struct. Chem.*, 2010, **21**, 657-665.
58. A. A. Michalchuk, M. Trestman, S. Rudic, P. Portius, P. T. Fincham, C. R. Pulham and C. Morrison, *Predicting the reactivity of energetic materials: an ab initio multi-phonon approach*, *J. Mat. Chem. A*, 2019, **7**, 19539-19553.
59. C. S. Coffey and E. T. Toton, *A Microscopic Theory of Compressive Wave-Induced Reactions in Solid Explosives*, *J. Chem. Phys.*, 1982, **76**, 949-954.
60. J. R. Hill, E. L. Chronister, T. C. Chang, H. Kim, J. C. Postlewaite and D. D. Dlott, *Vibrational Relaxation of Guest and Host in Mixed Molecular Crystals*, *J. Chem. Phys.*, 1988, **88**, 2361-2371.
61. D. D. Dlott and M. D. Fayer, *Shocked Molecular Solids: Vibrational up Pumping, Defect Hot Spot Formation, and the Onset of Chemistry*, *J. Chem. Phys.*, 1990, **92**, 3798-3812.
62. H. Kim and D. D. Dlott, *Theory of Ultrahot Molecular Solids: Vibrational Cooling and Shock-Induced Multiphonon up Pumping in Crystalline Naphthalene*, *J. Chem. Phys.*, 1990, **93**, 1695-1709.
63. L. E. Fried and A. J. Ruggiero, *Energy-Transfer Rates in Primary, Secondary, and Insensitive Explosives*, *J. Phys. Chem.*, 1994, **98**, 9786-9791.
64. K. L. McNesby and C. S. Coffey, *Spectroscopic Determination of Impact Sensitivities of Explosives*, *J. Phys. Chem. B*, 1997, **101**, 3097-3104.
65. S. Ye, K. Tonokura and M. Koshi, *Energy Transfer Rates and Impact Sensitivities of Crystalline Explosives*, *Combust. Flame*, 2003, **132**, 240-246.
66. S. Ye and M. Koshi, *Theoretical Studies of Energy Transfer Rates of Secondary Explosives*, *J. Phys. Chem. B*, 2006, **110**, 18515-18520.
67. J. Bernstein, *Ab Initio Study of Energy Transfer Rates and Impact Sensitivities of Crystalline Explosives*, *J. Chem. Phys.*, 2018, **148**, 084502.
68. A. A. Michalchuk, P. T. Fincham, P. Portius, C. R. Pulham and C. A. Morrison, *A Pathway to the Athermal Impact Initiation of Energetic Azides*, *J. Phys. Chem. C.*, 2018, **122**, 19395 - 19408.
69. A. A. L. Michalchuk, S. Rudic, C. R. Pulham and C. A. Morrison, *Vibrationally Induced Metallisation of the Energetic Azide α -NaN₃*, *Phys. Chem. Chem. Phys.*, 2018, **20**, 29061-29069.
70. A. A. L. Michalchuk, S. Rudic, C. R. Pulham and C. A. Morrison, *Predicting the impact sensitivity of a polymorphic high explosive: the curious case of FOX-7*, *Chem. Commun.*, 2021, **57**, 11213.
71. E. Schrödinger, *An Undulatory Theory of the Mechanics of Atoms and Molecules*, *Phys. Rev.*, 1926, **28**, 1049-1070.
72. P. Atkins and R. Friedman, *Molecular Quantum Mechanics*, Oxford University Press, Oxford, UK, 5th edn., 2011.
73. M. Born and J. R. Oppenheimer, *On the Quantum Theory of Molecules*, *Ann. Phys.*, 1927, **389**, 457-484.
74. D. R. Hartree, *The Wave Mechanics of an Atom with a Non-Coulomb Central Field. Part I. Theory and Methods*, *Math. Proc. Cambridge Philos. Soc.*, 1928, **24**, 89-100.
75. V. Fock, *Approximation method for solving the quantum mechanical multibody problem*, *Zeitschrift für Phys.*, 1930, **61**, 126-148.

76. J. Harvey, *Computational Chemistry*, Oxford University Press, Oxford, UK, 2017.
77. C. J. Cramer, *Essentials of Computational Chemistry Theories and Models*, WILEY, New Jersey, USA, 2nd edn., 2013.
78. P Hohenberg and W. Kohn, *Inhomogeneous electron gas*, *Phys. Rev.*, 1964, **136**, B864 – B871.
79. W. Kohn and L. J. Sham, *Self-Consistent Equations Including Exchange and Correlation Effects*, *Phys. Rev.*, 1965, **140**, A1133.
80. A. D. Becke, Density-functional exchange-energy approximation with correct asymptotic behaviour *Phys. Rev. A*, 1988, **38**, 3098–3100
81. C. Lee, W. Yang and R. G. Parr, *Development of the Colle-Salvetti correlation-energy formula into a functional of the electron density*, *Phys. Rev. B Condens. Matter.*, 1988, **37**, 785–789.
82. K. Burke, J. P. Perdew and Y. Wang, *Electronic Density Functional Theory*, eds., Springer, Boston, MA, 1998, pp. 81–111J.
83. P. Perdew, K. Burke and M. Ernzerhof, *Generalized Gradient Approximation Made Simple*, *Phys. Rev. Lett.*, 1996, **77**, 3865–3868.
84. Tkatchenko and M. Scheffler, *Accurate molecular van der Waals interactions from ground-state electron density and free-atom reference data*, *Phys. Rev. Lett.*, 2009, **102**, 073005 1–4
85. S. Grimme, *Semiempirical GGA-type density functional constructed with a long-range dispersion correction*, *J. Comput. Chem.*, 2006, **27**, 1787–1799.
86. S. Baroni, S. D. Gironcoli, A. D. Corso and P. Giannozzi, *Phonons and related crystal properties from density-functional perturbation theory*, 2001 73, 516-557.
87. F. Bloch, *On the quantum mechanics of electrons in crystal lattices*, *Zeitschrift für Phys.*, 1929, **52**, 555–600.
88. J. Gazalet, S. Dupont, J. C. Kastelik, Q. Rolland and B. Djafari-Rouhani, *A tutorial survey on waves propagating in periodic media: electronic, photonic and phononic crystals. Perception of Bloch theorem in both real and Fourier domains*, *Wave Motion*, 2013, **50**, 619–654
89. H. J. Monkhorst and J. D. Pack, *Special points for Brillouin-zone integrations*, *Phys. Rev. B*, 1976, **13**, 5188.
90. C. G. Broyden, *The convergence of a class of double-rank minimization algorithms: 2. The new algorithm*, *IMA J. Appl. Math.*, 1970, **6**, 222–231.
91. R. Fletcher, *Practical Methods of Optimisation*, WILEY, New Jersey, USA, 2nd edn., 2000.
92. D. Goldfarb, *A family of variable-metric methods derived by variational means*, *Math. Comput.*, 1970, **24**, 23.
93. D. F. Shanno, *Conditioning of quasi-Newton methods for function minimisation*, *Math. Comput.*, 1970, **24**, 647.
94. Y. Tao, W. Zou, M. Friendorf, M. Makos, N. Verma and E. Kraka, *Local vibrational mode analysis, Program LMODEA(F90), Ver. 2.0.0, Computational and Theoretical Chemistry Group (CATCO)*, SMU, Dallas, Texas 75275 USA, 2020.
95. Accelrys, Materials Studio, 2016, <http://accelrys.com/products/collaborative-science/biovia-materials-studio/>
96. S. J. Clark, M. D. Segall, C. J. Pickard, P. J. Hasnip, M. J. Probert, K. Refson and M. Payne, *First principles methods using CASTEP*, *Z. Kristall.*, 2005, **220**, 567–570.

97. A. Otero-de-la-Roza, M. A. Blanco, A. M. Pendás and V. Luaña, *Critic: a new program for the topological analysis of solid-state electron densities*, *Comput. Phys. Commun.*, 2009, **180**, 157–166.
98. J. Contreras-García, E. R. Johnson, S. Keinan, R. Chaudret and J. Piquemal, *NCIPLOT: a program for plotting non-covalent interaction regions*, *J. Chem. Theory, Comput.*, 2011, **7**, 625-632
99. A. Otero-de-la-Roza , E. R. Johnson and J. Contreras-García, *Revealing non-covalent interactions in solids: NCI plots revisited*, *Phys. Chem. Chem. Phys.*, 2012, **14** , 12165.
100. A. Otero-De-La-Roza, E. R. Johnson and V. Luaña, *Critic2: A program for real-space analysis of quantum chemical interactions in solids*, *Comput. Phys. Commun.*, 2014, **185**, 1007–1018.
101. C. J. Pickard and R. J. Needs, *Ab initio random structure searching*, *J. Phys. Condens. Matter*, 2011, **23**, 053201.
102. M. J. Frisch et al., *Gaussian 16, Revision A.03*, Gaussian, Inc., Wallingford CT, 2016.
103. Dr A. A. L. Michalchuk, Personal Communication, University of Birmingham, 2020 – 2023.

Chapter 2: Development of Python Scripts to Supplement the Vibrational Up-pumping Procedure

2.1 Introduction

Throughout the course of this work, three areas around data processing for the vibrational up-pumping methodology were identified where improvements could be made. These are documented in this Chapter, where an overview of each of the Python 3 scripts developed is outlined.

2.2 Generation of Complete and Partial Density of States

Plots

As outlined in Chapter 1, the vibrational up-pumping procedure is used to predict the impact sensitivity through consideration of the phonon up-pumping pathways within the $g(\omega)$ [1, 2, 3, 4, 5, 6]. Simply put, the $g(\omega)$ represents the density (amount) of vibrational character at a given frequency with increased vibrational character resulting a larger peak height [7, 8]. The spectrum can be developed from a list of vibrational frequencies through the application of a variety of methods (Gaussian smearing, Lorentzian smearing or histogram-based approaches) [8]. The most commonly used approach, and that used in previous work conducted by Michalchuk et al., is through the application of a Gaussian smearing regime. The size of the smearing (peak width) has a direct impact on the up-pumped density attained as a broader $g(\omega)$ will both enhance and capture more of the $\Omega^{(2)}$ trace. This can be mitigated against provided a consistent peak width (in this work 5 cm^{-1}) is adopted throughout.

Historically the group has used two different approaches to develop the $g(\omega)$ for the vibrational up-pumping procedure. Initially, a Perl script, `dos.pl`, that is included within the CASTEP code was used, however, this code lacked the functionality to generate partial $g(\omega)$ traces which are of interest when multicomponent systems, such as co-crystals and salts, are investigated [9]. The $g(\omega)$ can also be generated by the Accelrys Materials Studio software package (V 5.5.3 used in this work, hereafter referred to as Materials Studio), and here the capacity to separate the $g(\omega)$ onto different molecular

components exists. Assignment of an eigenvector to one molecular component (e.g. an anion or a cation in the unit cell) is based on a contribution cut off, such that any eigenvector motion that contains less than a 20% contribution from one molecular species is ignored [10].

There are two problems with the continued use of both methods in the vibrational up-pumping procedure. The first is minor inconsistencies in how dos.pl and Materials Studio plot the acoustic modes, which are omitted with dos.pl and presented just above 0 cm^{-1} as a Gaussian tail when Materials Studio is used (see Figure 2.1, where data is shown for α -FOX-7, formally 1,1-diamino-2,2-dinitroethylene). The second issue is that it is clear from Figure 2.1 that Materials Studio employs a different peak smearing method to dos.pl, as the peaks appear much broader, and shorter, despite a common smearing of 5 cm^{-1} being applied. Finally, the inability to adjust the 20% eigenvector cut off contribution in Materials Studio is an issue, as it is likely set too high for vibrational up-pumping (i.e. a 20% eigenvector contribution would not be considered negligible). It was therefore decided that a bespoke Python script was required.

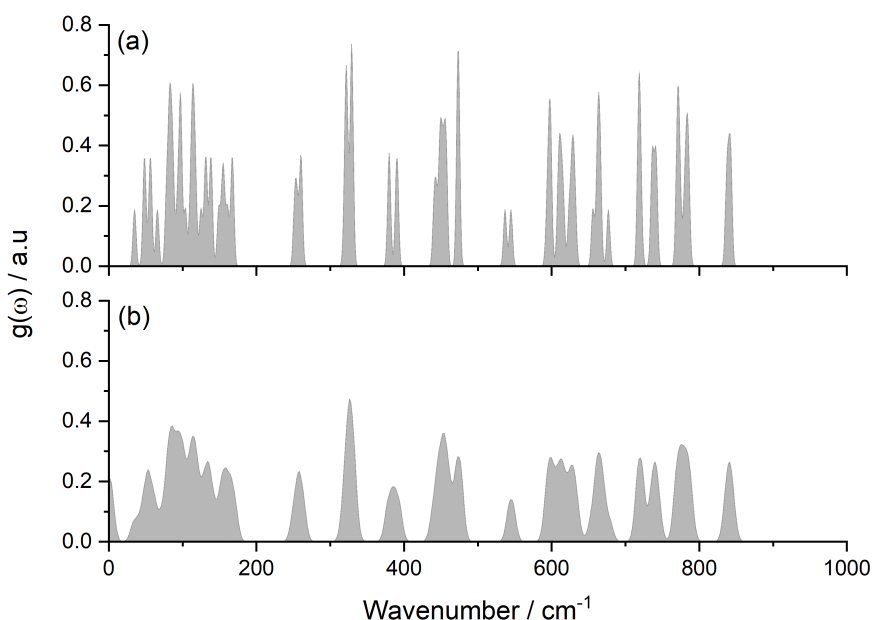


Figure 2.1: Shows the $g(\omega)$ spectrum of α -FOX-7 determined by dos.pl (a) and Materials Studio (b) with a Gaussian smearing of 5 cm^{-1} applied.

To determine the source of the difference between dos.pl and Materials Studio, a closer look at how a Gaussian peak is generated from the vibrational frequency is first required. The Gaussian function is given in Equation 2.1 [11].

$$f(x) = ae^{(-\frac{(x-b)^2}{2c^2})} \quad \text{Equation 2.1}$$

Where a represents the height of the peak applied (set to 1 in the first instance), b denotes the centre of the peak (i.e. the vibrational frequency itself) and c is the standard deviation of the peak. The standard deviation of the peak is related to the full width half maximum (FWHM, that is the width of the peak at half its maximum height) by the relationship given in Equation 2.2.

$$FWHM = 2\sqrt{2\ln(2)}c \quad \text{Equation 2.2}$$

The value of FWHM is the Gaussian smearing referred to throughout this work (5 cm^{-1}). From this it can be determined that when a smearing regime of 5 cm^{-1} is applied, the standard deviation of the peak is 2.12. This distinction between standard deviation and Gaussian smearing width was found to be the source of error when Materials Studio was used to generate the $g(\omega)$. For dos.pl the smearing was directly taken to be the FWHM (5 cm^{-1}) whereas in Materials Studio the provided number was taken to be the standard deviation, meaning that when '5' was selected the actual FWHM being applied to the peaks was $2\sqrt{2\ln(2)}$ times larger, such that the user entered 5 cm^{-1} subsequently became 11.77 cm^{-1} . This explains why the Materials Studio spectrum was comprised of peaks roughly twice as wide as those from the dos.pl spectrum. To check this the Materials Studio $g(\omega)$ was reproduced using a standard deviation of 2.12 (to equate to a FWHM of 5 cm^{-1}). The output is shown in Figure 2.2.

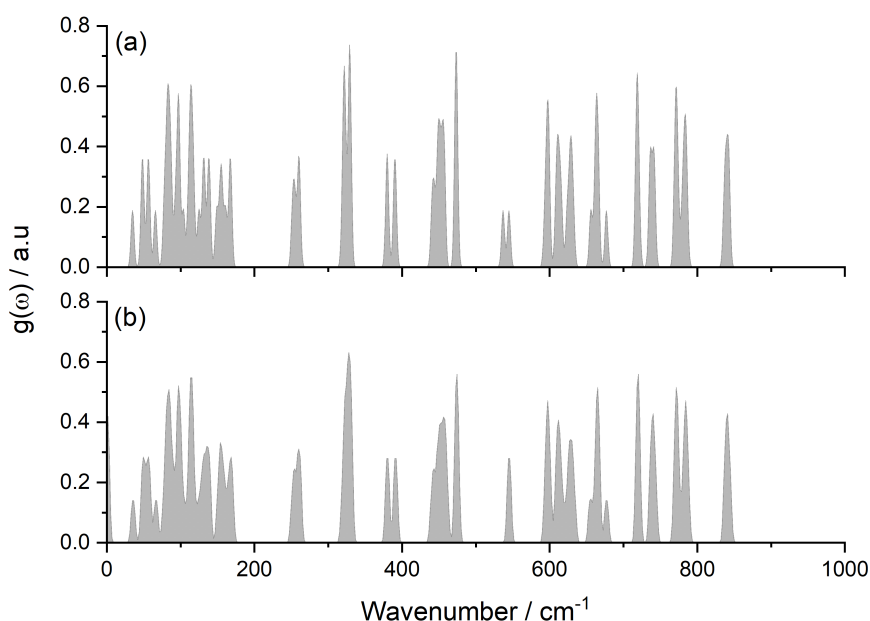


Figure 2.2: Shows the $g(\omega)$ spectrum of α -FOX-7 determined by dos.pl (a) and Materials Studio (b) with a FWHM of 5 cm^{-1} applied for both.

It is clear that the two spectra shown in Figure 2.2 are significantly more compatible than those in Figure 2.1, however there are still a number of irregularities, namely the height of the peaks, some peak splitting effects and of course the presence of acoustic mode bleeding in the Materials Studio trace. Some of the effects are likely as a result of the normalisation and the Gaussian summation process, i.e., how often a data point is selected – this is every 1 cm^{-1} for dos.pl, and every 1.83 cm^{-1} for Materials Studio, meaning that the finer details are sometimes missed. For these reasons, the Materials Studio programme was abandoned at this stage and a Python script was developed to closely reproduce the outputs obtained from dos.pl, while incorporating the partial $g(\omega)$ generation option offered by the Materials Studio approach.

The generation of a $g(\omega)$ trace is achieved through the parsing of the calculated vibrational frequencies from the output file which are then stored. Initially, each of the $3N$ vibrational frequencies are taken in isolation and subject to Gaussian (function outlined in Equation (2.1)) smearing regime of to match that of dos.pl (FWHM = 5 cm^{-1}).

An example of one such Gaussian peak with 5 cm^{-1} smearing applied to a single hypothetical vibrational frequency at the value of 500 cm^{-1} is shown in Figure 2.3.

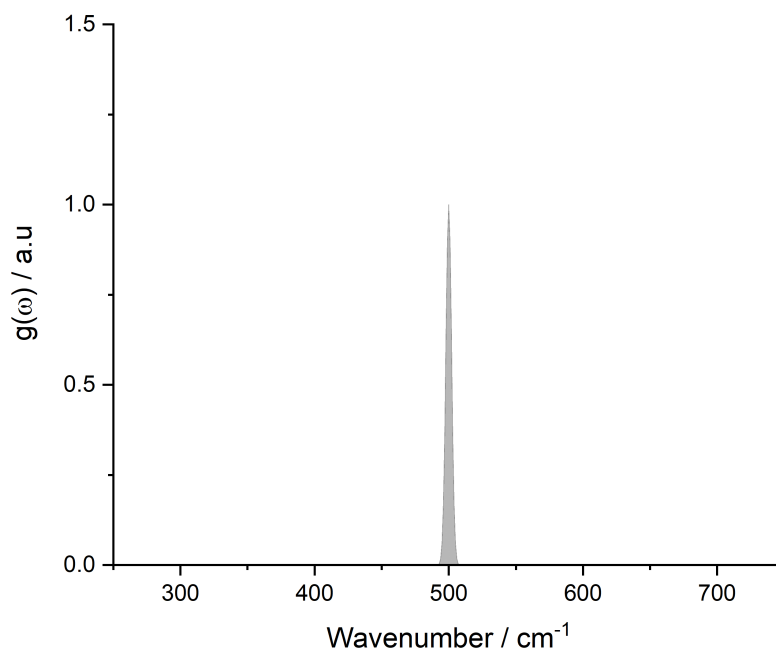


Figure 2.3: Shows the Gaussian smearing regime applied to a single vibrational mode present at 500 cm^{-1} with a Gaussian smearing of 5 cm^{-1} .

With $3N$ individual spectra resembling that shown in Figure 2.3, a cumulative spectrum is obtained by summing each of the individual plots point by point to give a plot with a number of peaks present. An example of a number of separate peaks (150 cm^{-1} , 200 cm^{-1} , $3 \times 300\text{ cm}^{-1}$ and 500 cm^{-1}) that were combined to produce a single spectrum is shown in Figure 2.4.

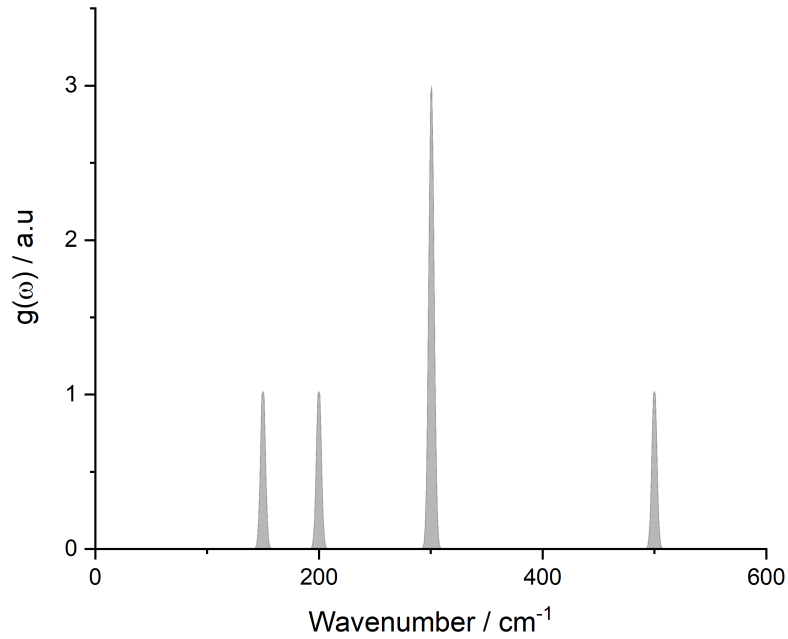


Figure 2.4: Illustrates the process by which the separate Gaussian peaks (150 cm^{-1} , 200 cm^{-1} , $3 \times 300 \text{ cm}^{-1}$ and 500 cm^{-1}) combine to give a continuous spectrum.

As can be seen from Figure 2.4, if N modes are present at the same (or very similar) frequency, when summed they result in a peak that is N times as tall as the peaks comprising it, with the y-axis height representing the $g(\omega)$. Finally, the $g(\omega)$ trace is normalised, such that the total integral is equal to $3N - 3$ as the acoustic modes do not fall within the positive range of frequencies (they are equal to 0 cm^{-1} but often present as small negative numbers in calculations due to numerical noise arising from assumptions used in the computational model), keeping with the dos.pl approach. The resulting output of the Python code is now indistinguishable from that of dos.pl (see Figure 2.5), and reassuringly both $g(\omega)$ gave identical outputs when subjected to the up-pumping process.

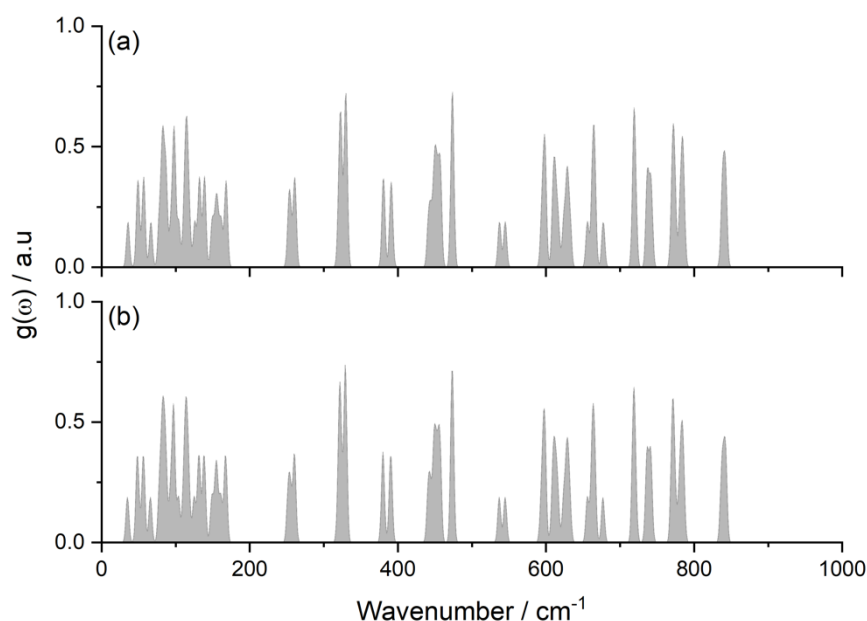


Figure 2.5: Shows the complete $g(\omega)$ for α -FOX-7 determined through the script outlined in this work (a) as well as the $g(\omega)$ previously generated from dos.pl (b).

With the $g(\omega)$ plot now successfully generated by the Python script, attention turned to incorporating the partial $g(\omega)$ functionality. This was achieved as follows:

1. The user selects the individual atoms for which the partial $g(\omega)$ is sought. This could be a complete molecule in the unit cell, or just part of a molecule. The identified atom locations in the input file are then passed to the script as a numerical list.
2. The script then searches through the CASTEP vibrational frequency calculation output file (.phonon), to scan the eigenvector descriptions for each of the vibrational mode frequencies to calculate the fraction of the total eigenvector motion attributed to the selected atom(s) for each mode.
3. From this a modified $g(\omega)$ trace, referred to as a scaling spectrum, is generated and passed through the same Gaussian smearing process as outlined previously, with the only difference being that the height of the Gaussian peak is now set to the fraction of motion attributed to the

assigned atoms, rather than to 1. This is then multiplied point by point with the original $g(\omega)$ spectrum to produce a partial $g(\omega)$. This process is outlined graphically in Figure 2.6, where the contributions from just the $-\text{NO}_2$ group motions to each eigenvector is highlighted by the $g(\omega)$.

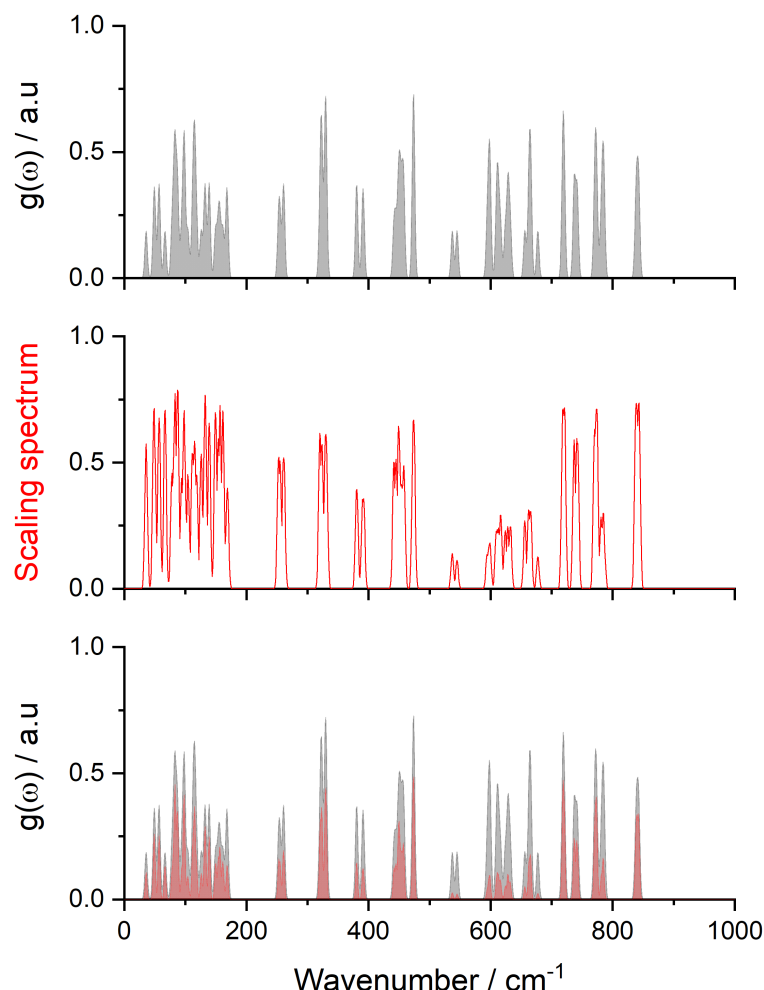


Figure 2.6: Shows the complete $g(\omega)$ (grey) alongside the ‘scaling spectrum’ (red line) and the resulting partial $g(\omega)$ trace for $-\text{NO}_2$ vibrational contributions only, overlaid on the underlying $g(\omega)$ for α -FOX-7.

The peak height of the scaling spectrum for a number of the low energy vibrations is roughly 75 %, meaning 75 % of the atomic motions in these eigenvectors is attributed to the $-\text{NO}_2$ groups. The partial $g(\omega)$ therefore mirrors the complete $g(\omega)$ at 75 % height. It should be noted that the partial spectrum outlined in Figure 2.6 has included all contributions to all modes from the $-\text{NO}_2$ groups, with e.g. the small peak at 540 cm⁻¹ comprising 14 % $-\text{NO}_2$ motion.

With the Materials Studio partial $g(\omega)$ process containing a fixed motion cut off of 20 %, this peak assignment motion would have been lost. This is important as this region lies within the vibrational up-pumping window, and any vibrational excitation of so-called weak trigger linkages such as C-NO₂ should be considered [12, 13, 14]. As a last check, a final comparison between the –NO₂ partial $g(\omega)$ of α -FOX-7, determined by the script outlined in this work and by Materials studio, with the same 20 % cut off and Gaussian peak smearing is shown in Figure 2.7. The resulting traces are in excellent agreement with one another, showing that the script developed here is capable of reproducing such spectra.

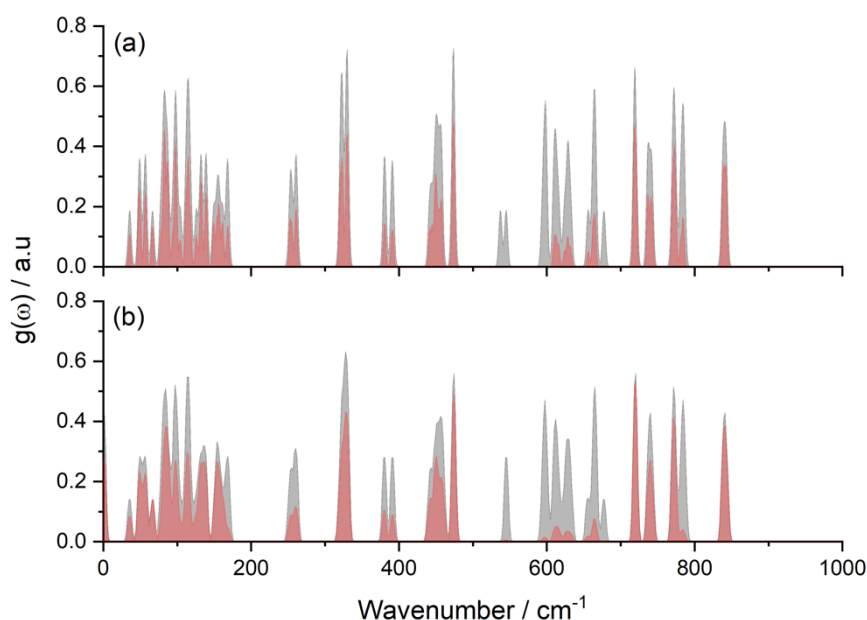


Figure 2.7: Shows the complete $g(\omega)$ trace (grey) and nitro group partial $g(\omega)$ (red) for α -FOX-7 when a % cut off of motion is applied for both the script outlined (a) as well as Materials Studio (b).

The development of the script was necessitated as the rather arbitrary 20 % cut off in motion adopted by Materials Studio results in a number of non-zero contributions to the partial $g(\omega)$ being omitted. For EMs the excitation of any molecular mode associate with activation of the weakest bonds are likely to be important, particularly given the high temperatures (and thus pronounced vibrational motions) associated with the energetic initiation process. Having

the ability to rigorously identify these vibrational modes is a significant step forward in both data handling and interrogation.

2.3 Determination of Ω_{\max} through Consideration of Molecular Centre of Mass

The vibrational up-pumping procedure as outlined in the previous Chapter has a number of key parameters that must be defined for each $g(\omega)$ data set [1, 2, 3, 4, 5, 6]. One particularly important one is defining the uppermost value of the phonon bath (Ω_{\max}), which denotes the frequency at which the vibrational mode character transitions from delocalised (external) lattice modes to localised (internal) molecular vibrations. This is a key feature of the up-pumping model, as it not only defines the size of the phonon bath, and therefore the number of modes excited by the initial impact event, but it also holds influence over the size of the up-pumping window ($1-3 \Omega_{\max}$), which is the area over which the up-pumped energy is projected.

A variety of approaches have been utilised previously to determine the location of Ω_{\max} , with the first exploration in vibrational up-pumping conducted by Bernstein et al., simply suggesting that a value of 200 cm^{-1} was appropriate for every material, as this represents a rough average for a variety of molecular crystals [15]. In an attempt to apply an increased degree of mathematical rigor to the determination, Michalchuk et al., considered the number of lattice modes that a crystal would exhibit based on the number of molecules (Z) that comprised it. This gives $6Z$ (i.e., three translations and three rotational modes, per molecule), however simply assuming that the location of Ω_{\max} falls at the peak number $6Z$ resulted in a major problem: this peak would often clearly fall within the continuous region of the phonon bath [3]. Thus $6Z$ undercounts the number of lattice modes for a molecular crystal. The additional modes are termed amalgamated modes (Y), and they are typically small librational motions of functional groups, such as C-NO_2 , that include significant lattice mode character, and their number is not straightforward to predict for any given molecular crystal.

The natural progression from the simple 6Z count was to consider the first frequency at which the $g(\omega)$ trace falls to zero, after the minimum 6Z vibrations have been counted. However, this also presented problems as if Γ -point vibrational frequency calculations are used, instead of full Brillouin zone sampling (as is the case in this thesis), the phonon bath regions are naturally under-sampled, which can result in discontinuities appearing in the phonon bath regions that could be misinterpreted as denoting the external to internal mode transition [4].

The final attempt to determine the location of Ω_{\max} was an extension of the lattice mode (6Z) counting approach, which tried to quantify the number of amalgamated modes (Y), such that the phonon bath could be described by $Z(6+Y)$. The rationale was that the 6Z lattice modes can easily be located in a solid-state vibrational frequency calculation, which corresponds to a rough location for the lower limit of Ω_{\max} , while a quick gas phase molecular vibrational frequency calculation would identify the number of molecular vibrations present that fall below this frequency [4]. In theory, this should yield the value of Y, however this does not take into account crystal field effects that will be highly likely to directly affect the positions of the molecular modes when they are recast into a crystalline environment, meaning that uncertainty in the mode counting remained.

While the above methods did give reasonable estimations for Ω_{\max} for a number of molecular crystals, their adoption often fell back on the need to verify through qualitative eigenvector visualisation, which is a complex process when a large number of similar vibrational motions are presented in the low energy range. It was clear that a more quantitative procedure was required, and thus it was decided to track the changes in molecular centre of mass (CoM) for each molecule contained within the unit cell. It was expected that the deviation in CoM would sharply fall away as the mode behaviour switched from delocalised to localised.

As with the $g(\omega)$ script outlined in the previous Section, it is desirable that the output file from the vibrational frequency calculation is used directly as the input data, in order to reduce the amount of data post processing required.

Using 'phonon2xyz', a Perl script included in the CASTEP software suite, the output phonon file was parsed and rewritten to include only the atom types and positions (x y and z) alongside the changes in each of the positions (Δx , Δy and Δz) for each atom in each unique vibrational frequency [9]. This '.xyz' file contains all the information required for the CoM analysis to be completed with the exception of assigning individual atoms into complete molecules (of which there are Z in the unit cell). This grouping was achieved by generating Z atomic coordinate files through reformatting the optimised '.cif' file produced from the geometry optimisation calculation. This step was performed using Mercury V.2021.3, by selecting the packing/slicing drop down menu and then the 'that fit' option, meaning all atoms are located within the unit cell [16]. The resulting '.xyz' file contains all N atoms arranged in order of the molecules in the cell, meaning that this file simply needs to be split into Z different fractions to represent each individual molecule.

Next, the atomic positions of each atom in the reformatted cif '.xyz' and 'phonon2xyz' output files are matched to one another, such that the 'phonon2xyz' output file is reordered. Resulting in Z lists comprised of atom types, atom positions and atom position deviations. From this, the positions of the atoms at the termini of each eigenvector motion (formed by adding/subtracting Δx , Δy and Δz to the x, y and z atomic positions defined in the 'phonon2xyz' output file) are calculated, and used to calculate the CoM in the x, y and z directions according to Equations 2.3a-c:

$$CoM_x = \frac{\sum_{i=1}^N m_i x_i}{M} \quad \text{Equation 2.3a}$$

$$CoM_y = \frac{\sum_{i=1}^N m_i y_i}{M} \quad \text{Equation 2.3b}$$

$$CoM_z = \frac{\sum_{i=1}^N m_i z_i}{M} \quad \text{Equation 2.3c}$$

$$CoM = (CoM_x, CoM_y, CoM_z)$$

Where N is the number of atoms in the molecule, M is the total molecular weight, m_i and x_i , y_i and z_i are the atomic weight and the x, y and z positions for the atom, i. The resulting deviation in CoM can therefore be obtained through calculating the distance between both calculated CoM values through

evaluating the length of the vector between them. This is then repeated for each of the $3N$ vibrational modes and averaged across the Z molecules in the unit cell. The resulting deviation in CoM values averaged per molecule, per mode, are then normalised to unity with respect to the vibrational mode that results in the biggest deviation. This is typically one of the acoustic vibrations, as by definition acoustic modes result in rigid molecular motion along the coordinate axes. The resulting deviation in CoM per vibrational mode plot for α -FOX-7 is given in Figure 2.8.

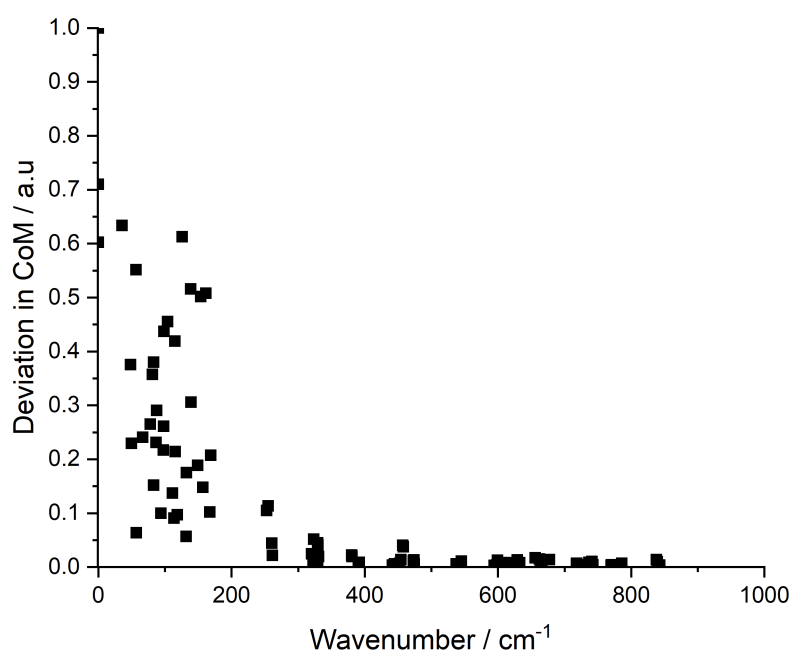


Figure 2.8: Shows how the deviation in molecular CoM varies for each vibrational mode for α -FOX-7.

Figure 2.8 confirms there is a notable and significant drop off in the deviation in the CoM of the α -FOX-7 molecules with increasing wavenumber, however, this value does not drop to zero, meaning that a degree of uncertainty in defining Ω_{\max} exists with this method too. In an effort to combat this a cut off was defined for the residual CoM motion, which was derived by considering a number of EMs that have been very well-studied within the group, and for which the positions of Ω_{\max} were considered to be reasonably well defined [3, 4]. This is presented in Figure 2.9, from which it was apparent that selecting a CoM deviation of near or below 0.1 (i.e. 10% of the maximum mode distortion) was a reasonable cut-off value. This CoM code has been used extensively

throughout this thesis to help guide the location of Ω_{\max} , with visual inspection of the surrounding eigenvectors often then employed to confirm this assignment.

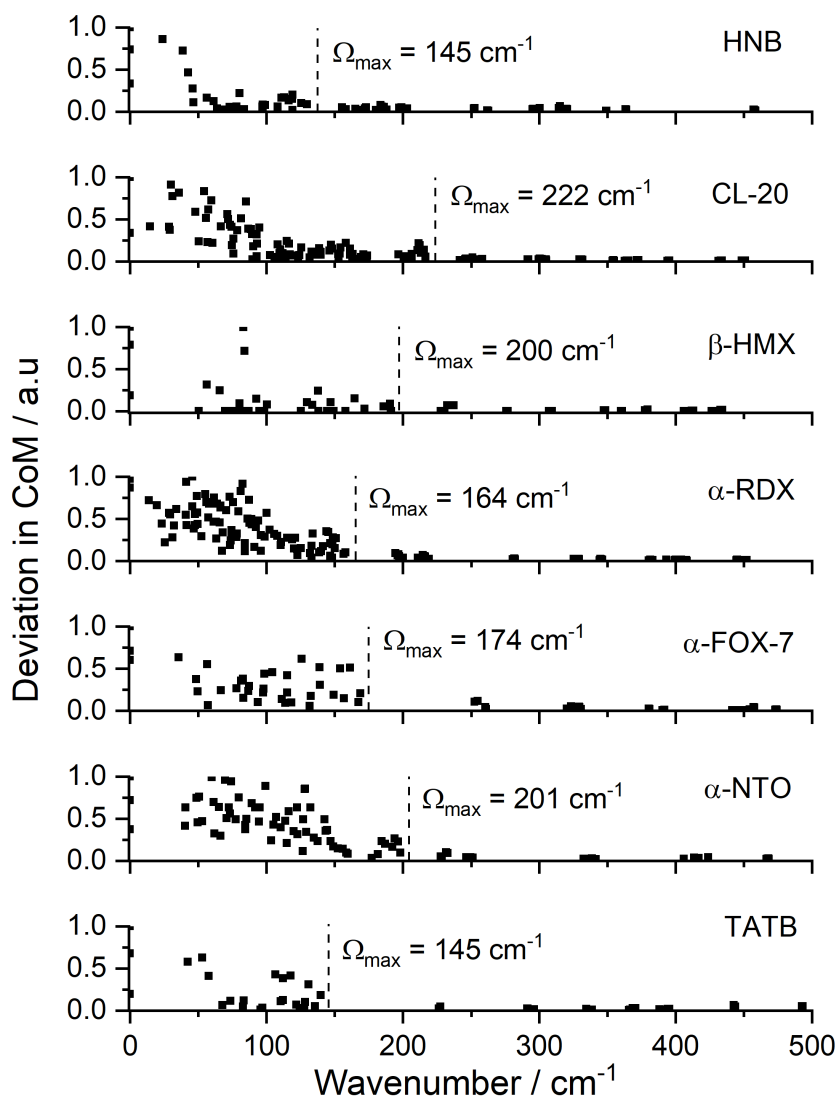


Figure 2.9: Shows how the deviation in molecular CoM varies for each vibrational mode for a group of well-studied EMs.

2.4 Tracking of Local Modes of Vibration

As was outlined in the previous Chapter, the vibrational up-pumping procedure operates under the assumption that the energy that is channelled into the up-pumping window induces an excitation in a mode associated with an energetic response (the target, or trigger mode, Q_T) [2, 3]. A normal, or fundamental, vibrational mode can be described as bond stretching, angle bending or dihedral torsional motions, and the modes of vibration that typically fall in the

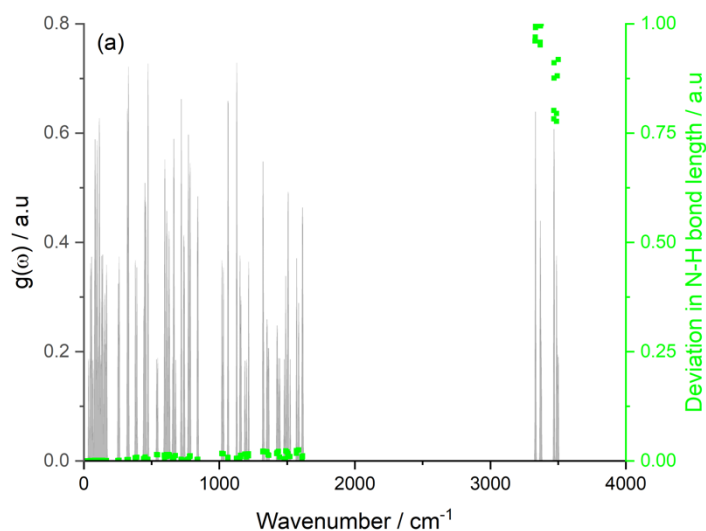
vibrational up-pumping window (ca. $200 - 600 \pm 100 \text{ cm}^{-1}$) are likely to be a combination of all three. Previous work by Michalchuk et al., showed that Q_T for energetic azide metal salts (MN_3) was the N-N-N angle bend at 600 cm^{-1} , activation of which leads to a conical intersection on the potential energy surface that reduces the barrier to N-N bond dissociation [2]. While this provides a nice example, the molecular structure of the azide anion is much simpler to study than e.g., a pyrazole or tetrazole ring, where complex correlations between molecular vibrations make the identification of a single trigger motion much harder to define [1, 2, 3]. However, the concept of trigger bond initiation, i.e., severing of the weakest bond in the molecular structure being the first chemical step in initiation, is a widely accepted and understood phenomenon in the field of EM research. The weakest bonds are likely to be C-NO₂ or N-NO₂ bonds, and thus looking for vibrational modes in the up-pumping windows that include these bond stretching motions is a reasonable attempt to identify the Q_T modes [12, 13, 14]. To this end, a variant of the CoM code outlined in Section 2.3 was developed in which a bond length or angle bend can be tracked through the calculated eigenvector motions that result from a vibrational frequency calculation. Details of the Python script, as well as some examples of outputs, are outlined below.

In addition to interrogating calculated solid-state vibrational frequencies through eigenvector analysis, local model analysis (through the code LModeA) provides a straightforward route to deconvolute the normal vibrational motion into its constituent local modes (the individual bond stretches, angles bends, etc) for gas phase structures [17, 18]. Moreover, this deconvolution provides access to the mass-independent local mode force constants. These are direct and comparable measures of bond strength, and in this way the weakest bonds in a molecular structure can be readily identified. Several outputs from LModeA are documented below, to demonstrate that success was achieved with the eigenvector analysis code.

As noted in the previous Section, eigenvector analysis was pursued via an edited version of the CoM script. As such the procedure is identical up to the point where the molecule '.xyz' file has been used to generate Z lists of

molecules comprised of atom types, atoms positions (x, y and z) and atom deviations (Δx , Δy and Δz). After this point the workflow diverges.

Once the above molecule lists have been generated, it is possible to calculate the change in distance between any two selected atoms or the angle change between any three selected atoms as a result of the vibrational modes. These calculations then run across all eigenvectors and deviations in their values are logged and normalised with respect to the biggest molecular distortion. Note, for this, the range of eigenvector motion explored by adding the Δx , Δy and Δz increments to the equilibrium (x,y and z) geometry is small (i.e. one tenth of an increment). The reason for this is to ensure that the range of molecular vibrational motion explored is small, such that deviations between the rectilinear description of molecular motion does not deviate substantially from the more geometrically correct curvilinear motion. This is particularly important for angle bends. The results obtained for tracking the eigenvector displacements of the N-H distance for each vibrational mode of α -FOX-7 is shown in Figure 2.10(a).



(b)

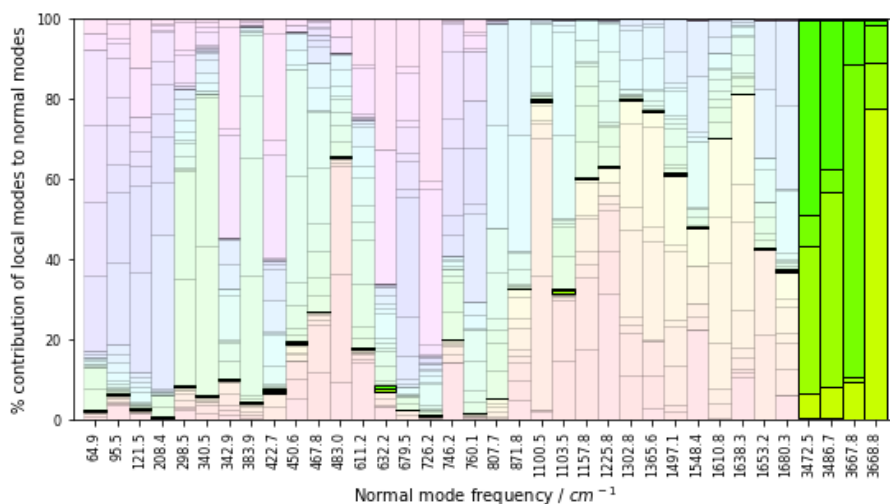


Figure 2.10: Shows the deviation in N-H bond length (green) per vibrational frequency in the $g(\omega)$ (grey) of α -FOX-7, based on a solid-state calculation (a). As well as the local mode contributions to the normal modes of a molecule of FOX-7 of the N-H stretch local modes highlighted in green, based on a gas phase calculation (b) [17, 18].

The plot shown in Figure 2.10(a) shows clearly defined motions at 3350 cm⁻¹ and at 3500 cm⁻¹, and minimal motions elsewhere, thus showing that the script has correctly identified the N-H symmetric and asymmetric vibrations. To confirm that no N-H bond stretching character was expected across any of the other vibrations, a local mode analysis was performed for the 3N-6 gas phase vibrational motions of FOX-7. The results are given in Figure 2.10(b), which shows each vibrational motion as a bar chart, showing the constituent contributions from the local modes (all possible bond stretches, angle bends, and torsional motions). Those highlighted in green are the four N-H bond stretching motions, which make up the entirety of the eigenvector characters for the modes above 3000 cm⁻¹. No contributions are apparent in the lower wavenumber motions, in agreement with the eigenvector analysis given in Figure 2.10.

One more rigorous test is shown in Figure 2.11. Here the eigenvectors that include C-NO₂ bond stretching (i.e., the weakest bond in α -FOX-7, and therefore a likely indicator of Q_T modes) is shown. Here local mode activation

across many eigenvectors is clearly apparent, and expected, and crucially also manifests in the up-pumping window region ($200\text{--}600 \pm 100 \text{ cm}^{-1}$).

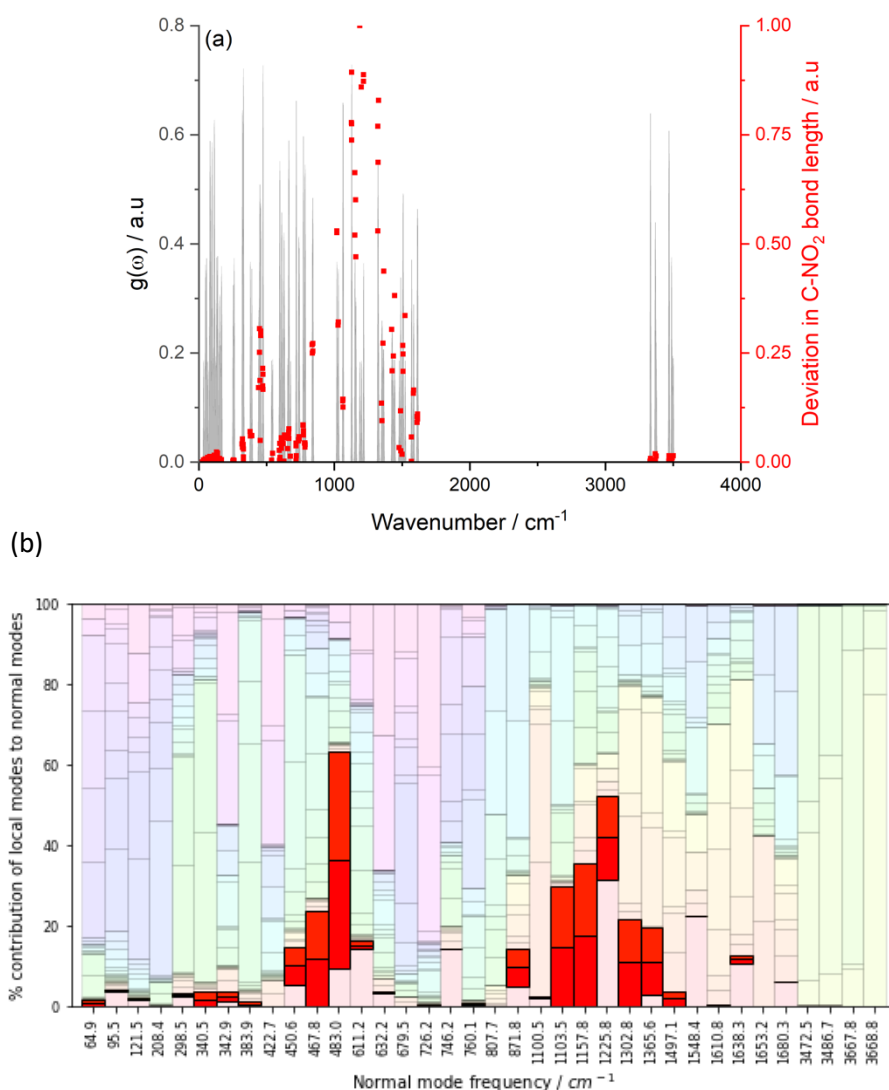
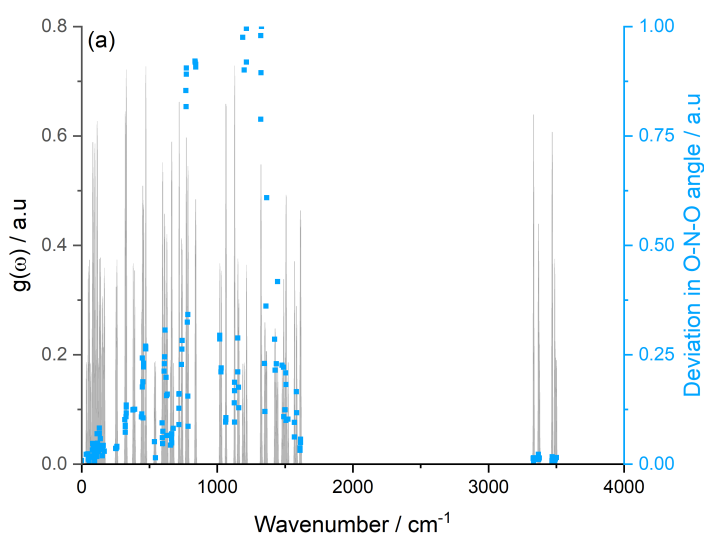


Figure 2.11: Shows the deviation in C-NO₂ bond length (red) per vibrational frequency in the $g(\omega)$ (grey) of α -FOX-7 based on a solid-state calculation (a). As well as the local mode contributions to the normal modes of a molecule of FOX-7 of the C-NO₂ bond stretch highlighted in red based on a gas phase calculation (b). [17, 18].

The matching local mode analysis output is shown in Figure 2.11(b), which confirms C-NO₂ local bond character in peaks at ca. 300-350, 450-600 and 800-1500 cm⁻¹, in agreement with the Python eigenvector script.

A final check was also carried out to assess the effectiveness of the script to track angle bends, as it was expected that such vibrations will be more widespread throughout the lower end of the vibrational landscape. The angle bend is more complex than a bond stretch, meaning that in order to be calculated the vectors describing both bonds first had to be determined, before the angle between them could be rationalised. The plots outlining the deviation in the O-N-O angle in the solid-state vibrations, alongside the respective local mode contribution (highlighted in blue) bar plots to the molecular vibrations also shown in Figure 2.12.



(b)

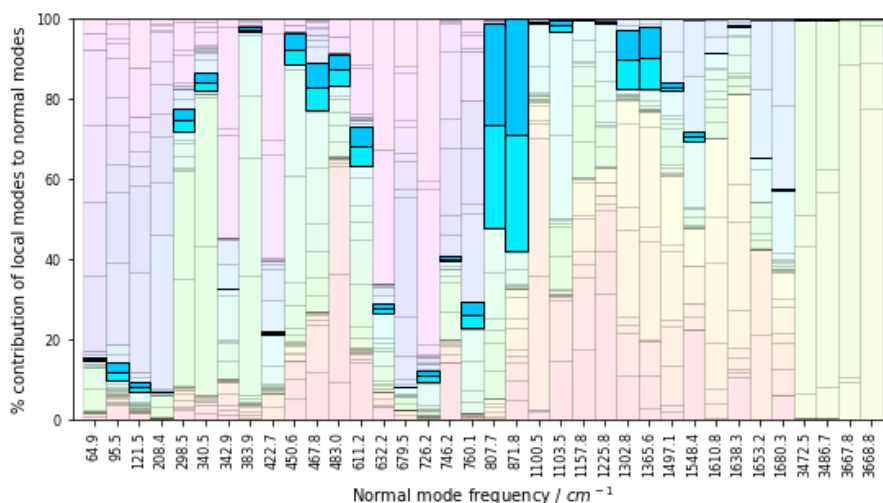


Figure 2.12: Shows the average deviation per molecule of the O-N-O angles (blue) for each vibrational mode in the $g(\omega)$ plot (grey) of α -FOX-7 based on a solid-state calculation (a). As well as the local mode contributions to the normal modes of a molecule of FOX-7 from the O-N-O angle bends based on a gas phase calculation (b) [17, 18].

It is clear that there are significantly more vibrational modes that contain the O-N-O angle bend local mode than was the case for the bond stretching local modes. Despite this, the script outlined in this work appears to be in good agreement with the molecular local mode analysis, with two prominent regions in which the O-N-O angle bend is excited, at ca. 800 cm^{-1} and $1300\text{--}1500\text{ cm}^{-1}$. This gives good confidence that the script is suitable for use of tracking angle bends within vibrations, as well as bond stretches.

2.5 Conclusions

This work has outlined the development of three scripts which can be used in the vibrational up-pumping procedure to either improve efficiency and confidence in results or to interrogate the up-pumping window with a view to determining the nature of vibrations that are associated with the initiation process (target modes).

Firstly, a script to develop $g(\omega)$ plots to a standard which matches that of the historic data, but also has the capability to generate partial $g(\omega)$ plots such that the nature of vibrations may be explored and split if appropriate, has been

developed and tested. This script is used to generate all $g(\omega)$ plots studied in this thesis.

Secondly, a novel quantitative method to assist in the determination of the location of Ω_{\max} has been outlined, in which the average deviation in CoM of the molecules within the unit cell is tracked for each vibrational mode. This resulted in a large drop-off in the deviation of the CoM as the vibrations became more localised onto the respective molecules, indicating that Ω_{\max} has been passed. This method was able to reproduce Ω_{\max} values of a number of well-studied molecular EMs which were previously determined through time consuming visualisation of the calculated eigenvectors. This script has also been applied to determine the location of Ω_{\max} for each EM considered in this body of work.

Finally, it has been shown that a simple script, based on the output of a phonon calculation is able to extract local mode distortions in the eigenvectors in good agreement with local mode analysis. This could potentially open the door to improved understanding of the mechanism of detonation of molecular EMs through systematic characterisation of vibrations within the up-pumping window, such that the identity of so-called target or trigger modes can be more easily identified. This also provides insight to help rationalise the outputs from the vibrational model, which in turn help to define structure/property relationships that will go some way towards rationalising impact sensitivity at a molecular level.

2.6 References

1. A. A. Michalchuk, P. T. Fincham, P. Portius, C. R. Pulham and C. A. Morrison, A *Pathway to the Athermal Impact Initiation of Energetic Azides*, *J. Phys. Chem. C.*, 2018, **122**, 19395 – 19408.
2. A. A. L. Michalchuk, S. Rudic, C. R. Pulham and C. A. Morrison, *Vibrationally Induced Metallisation of the Energetic Azide α -NaN₃*, *Phys. Chem. Chem. Phys.*, 2018, **20**, 29061-29069.
3. A. A. Michalchuk, M. Trestman, S. Rudic, P. Portius, P. T. Fincham, C. R. Pulham and C. Morrison, *Predicting the reactivity of energetic materials: an ab initio multi-phonon approach*, *J. Mat. Chem. A*, 2019, **7**, 19539–19553.

4. A. A. L. Michalchuk, J. Hemingway and C. A. Morrison, *Predicting the impact sensitivities of energetic materials through zone-center phonon up-pumping*, *J. Chem. Phys.*, 2021, **154**, 064105.
5. A. A. L. Michalchuk, S. Rudic, C. R. Pulham and C. A. Morrison, *Predicting the impact sensitivity of a polymorphic high explosive: the curious case of FOX-7*, *Chem. Commun.*, 2021, **57**, 11213.
6. I. L. Christopher, C. R. Pulham, A. A. L. Michalchuk and C. A. Morrison, *Is the impact sensitivity of RDX polymorph dependant?*, *J. Chem. Phys.*, 2023, **158**, 124115.
7. K. Parlinski, *Lattice Dynamics: Vibrational Modes*, *Encyclopedia of Condensed Matter Physics*, Academic Press, Cambridge MA, 1st Edn., 2005.
8. M. T. Dove, *Structure and Dynamics An atomic view of materials*, *Thermodynamics and lattice dynamics*, Oxford University Press, Oxford, UK, 1st Edn, 2003.
9. S. J. Clark, M. D. Segall, C. J. Pickard, P. J. Hasnip, M. J. Probert, K. Refson and M. Payne, *First principles methods using CASTEP*, *Z. Kristall.*, 2005, **220**, 567–570.
10. Accelrys, Materials Studio, 2016, <http://accelrys.com/products/collaborative-science/biovia-materials-studio/>
11. Ed. A. Felinger, *Data Handling in Science and Technology*, 1998, **21**, 97-124.
12. T. B. Brill and K. J. James, *Kinetics and Mechanisms of Thermal Decomposition of Nitroaromatic explosives*, *Chem. Rev.* 1993, **93**, 2667-2692.
13. P. Politzer and J. S. Murray, *Energetic Materials Part 2. Detonation, Combustion*, Elsevier, Amsterdam, 2003.
14. T. L. Jensen, J. F. Moxnes, E. Unneberg and D. Christensen, *Models for predicting impact sensitivity of energetic materials based on the trigger linkage hypothesis and Arrhenius kinetics*, *J. Mol. Model*, 2020, **26**, 65.
15. J. Bernstein, *Ab initio study of energy transfer rates and impact sensitivities of crystalline explosives*, *J. Chem. Phys.*, 2018, **148**, 084502.
16. C. F. Macrae, I. J. Bruno, J. A. Chisholm, P. R. Edgington, P. McCabe, E. Pidcock, L. Rodriguez-Monge, R. Taylor, J. van de Streek and P. A. Wood, *Mercury CSD 2.0 – new features for the visualisation and investigation of crystal structures*, *J. Appl. Cryst.*, 2008, **41**, 466-470.
17. Y. Tao, W. Zou, M. Friendorf, M. Makos, N. Verma and E. Kraka, *Local vibrational mode analysis, Program LMODEA(F90), Ver. 2.0.0, Computational and Theoretical Chemistry Group (CATCO), SMU, Dallas, Texas 75275 USA*, 2020.
18. Y. Tao, W. Zou, S. Nanayakkara and E. Kraka, *LModeA-nano: A PyMOL Plugin for Calculating Bond Strength in Solids, Surfaces, and Molecules via Local Vibrational Mode Analysis*, *J. Chem. Theory, Comput.*, 2022, **18**, 3, 1821-1837.

Chapter 3: Tuning the Effects of Energetic Materials through Altering Crystal Packing

3.1 Introduction

The vibrational up-pumping procedure can be used in a predictive sense to rationalise dramatic and unexpected changes in behaviour for novel EMs. In this Chapter, two different approaches to tailoring intermolecular interactions, namely through co-crystallisation and application of pressure leading to polymorphism, are studied. The first study concerns a novel co-crystal of the energetic compound FOX-7 (formally 1,1-diamino-2,2-dinitroethylene) and PPD (para-phenylenediamine, formally 1,4-diaminobenzene, i.e., a non-energetic compound), which when first prepared was found to be unexpectedly more mechanically sensitive to impact than FOX-7 itself [1]. The second study concerns TNP (formally 3,4,5-trinitro-1H-pyrazole) that unexpectedly initiated when held in a diamond anvil cell during a high-pressure single crystal X-ray diffraction study, suggesting that a high-pressure polymorph was more sensitive to mechanical initiation than ambient pressure TNP [2]. These two unexpected results presented an ideal opportunity to test the predictive power of the vibrational up-pumping procedure, which in turn provides a route to explore structure/property relationships in much greater depths. Which may provide a mechanism towards tailoring the properties of EMs through structure design.

3.2 Co-crystallising FOX-7 with PPD

3.2.1 Introduction and Aims

The field of EMs is renowned for having incredibly stringent safety and characterisation requirements for materials to be commercially viable, due to the inherent dangers associated with these materials [3, 4]. For this reason, development of novel EMs is a very slow process, as the performance and sensitivity criteria of a novel material will initially be completely unknown. As a direct result, a small number of well-studied and heavily characterised materials dominate the field [5]. One route to therefore expand the accepted

workspace is through the co-crystallisation of a well-studied EM with another EM, or even a non-EM, resulting in a crystal structure built from both species. This provides a route to alter important performance parameters, including oxygen balance, detonation velocities and pressures, solubilities, as well as mechanical impact sensitivities [6, 7]. This also offers the advantage of continuing to use the existing synthetic infrastructure in place to prepare the standard EMs, while looking for routes to improve material performance and safety for handling and transport [8].

There have only been a handful of energetic co-crystals synthesised to this date, most notably those of CL-20/TNT (ratio 1:1) and CL-20/HMX (ratio 2:1) [5, 9]. CL-20 is an extremely powerful energetic which is far too sensitive for safe application (having a mechanical initiation value of just 3.75 J). For this reason, it was co-crystallised with TNT (a much less sensitive and yet still powerful energetic), with a view to maintaining the energetic power but reducing the sensitivity to impact [10]. The resulting co-crystal successfully reduced the sensitivity from that of CL-20 but also reduced the energetic performance to such an extent that the resulting material is not of commercial interest. In the case of CL-20/HMX, the two co-crystallites are much more similar in terms of sensitivity and performance, and the resulting co-crystal, despite being primarily comprised of CL-20 by weight, exhibits an impact sensitivity similar to that of HMX. The remaining calculated performance parameters were reported to lie between that of pure CL-20 and pure HMX. These two examples provide an insight into the potential for the development of novel energetic co-crystals with tuned properties.

In general, the field of EMs lags behind other fields with respect to the introduction of co-crystals [7]. This approach has been successfully applied to a number of pharmaceuticals to alter physicochemical properties of active drugs such as: dissolution rates, thermal stability and bioavailability [11, 12]. There are a number of reasons why the pharmaceutical industry is so far ahead of the field of EMs in this regard, with the primary reason being the stringent safety criteria outlined above that has hindered the pace of EM development. But, in addition, chemistry itself limits the co-crystallisation landscape for EMs. In general, drug molecules tend to comprise a broad range

of functional groups, and as such can participate in hydrogen bonding as both proton donors and acceptors [13]. This allows for a great number of possible co-crystal pairs to be explored. In contrast, EMs tend to have reduced functional group variety, with the most common being the hydrogen-bond accepting nitro group ($-\text{NO}_2$). In the absence of any hydrogen bond donating groups (e.g., the amine $-\text{NH}_2$ group) the prospects for the formation of strong intermolecular interactions, which provide the thermodynamic driving force for the co-crystal to be more stable than its parent single-component structures, are diminished [14].

In this regard, FOX-7 provides an unusual case for an EM co-crystal exploration as it has both hydrogen-bond donor groups ($-\text{NH}_2$) and hydrogen-bond acceptor groups ($-\text{NO}_2$). Additionally, FOX-7 is a secondary energetic with a performance that rivals other secondary EMs but with a reduced sensitivity to impact and friction, making it an attractive material for academic research [15]. The crystal structure of FOX-7 is comprised of wave-like sheets of near-planar FOX-7 molecules with inter- and intramolecular hydrogen bonds in between the respective H-bond donor and acceptor groups, and weak intermolecular forces of attraction (Van der Waals dispersion) between the layers, as shown in Figure 3.1 [16].

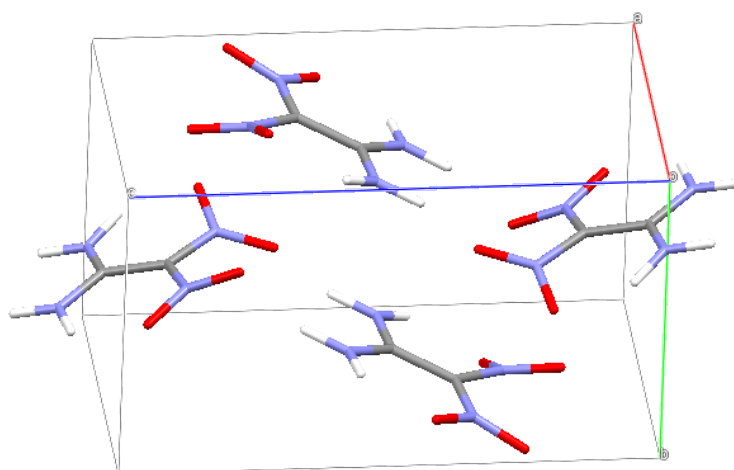


Figure 3.1: The crystal structure of the alpha-polymorph of FOX-7 (CCDC code: SEDTUQ03) showing wave-like crystal packing sheets [16].

In order to interrupt the hydrogen-bonding network in FOX-7, the co-crystallite selected will need functional groups that mimic at least one of the hydrogen-

bonding groups present in FOX-7. For this reason, the non-energetic aniline derivative, PPD was selected. A co-crystal of FOX-7/PPD was synthesised in a 1:1 ratio, and the crystal structure obtained, from which it was noted that the FOX-7 molecules were no longer planar, but in fact twisted by almost 90 ° about the central bond [1]. This suggests that significantly stronger intermolecular hydrogen-bonds had now formed, which were strong enough to support steric strain in the FOX-7 molecules. The crystal structure of FOX-7/PPD, characterised through single crystal X-ray diffraction, is shown in Figure 3.2.

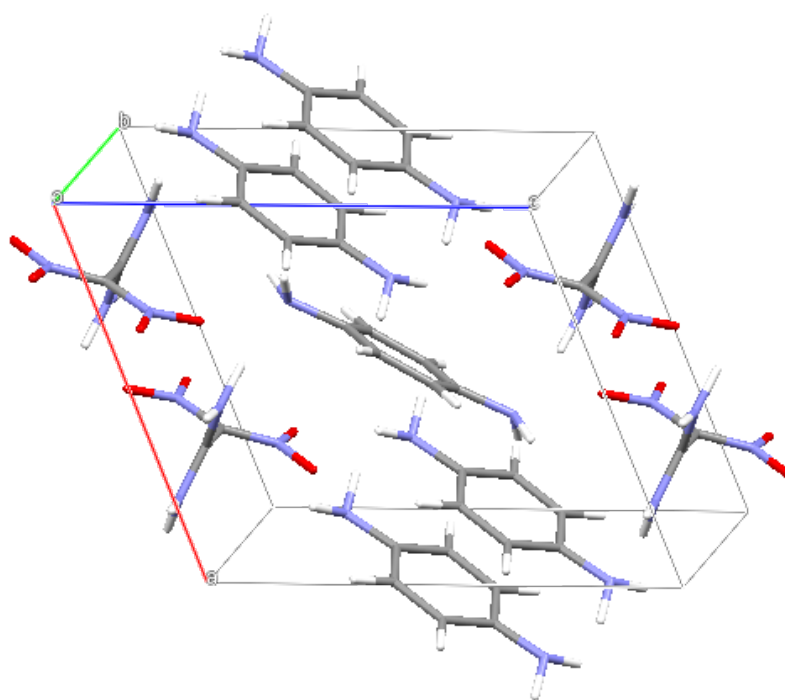


Figure 3.2: The crystal structure of FOX-7/PPD, detailing the twist observed in the FOX-7 molecules [1].

Since FOX-7/PPD is a co-crystal of an EM and a non-EM, the energetic properties of FOX-7 will be suppressed compared to the parent compound. However, while it was also expected that the sensitivity to mechanical impact would be reduced, the opposite was in fact observed, with the measured impact sensitivity of the co-crystal falling to just 10 J, compared to 28 J for pure FOX-7 [1]. This was unexpected, leading to a computational investigation into the co-crystal of FOX-7/PPD to predict its impact sensitivity compared to that of FOX-7, using the vibrational up-pumping methodology (outlined in Chapter 1), in an attempt to rationalise the experimental result.

3.2.2 Computational Methodology

A geometry optimisation calculation was completed for the co-crystal of FOX-7/PPD using CASTEP V16.11 [17, 18]. The generalised gradient approximation (GGA) functional PBE was used with the G06 dispersion correction alongside a plane wave basis set expressed at 950 eV, with norm-conserving pseudopotentials for each atom type [19, 20]. The convergence criteria for the geometry optimisation were as follows: residual atomic forces ≤ 0.001 eVÅ, atomic displacements ≤ 0.001 Å, wavefunction self-consistency $\leq 2 \times 10^{-9}$ eV and lattice vector stresses ≤ 0.01 GPa. These stringent convergence criteria, particularly with regard to the atomic forces, are required for a successful Γ -point phonon calculation, which was completed using the DFPT method as implemented in CASTEP V16.11 [21]. The vibrational frequencies obtained from this calculation were used to generate the vibrational density of states ($g(\omega)$), as detailed in Chapter 2, which is used as the input to the vibrational up-pumping procedure, expressed with a Gaussian half-height smearing function of 5 cm^{-1} . The optimised geometry, calculated vibrational frequencies and subsequent input values for the vibrational up-pumping procedure of FOX-7 were taken from previous work [22, 23]. In addition, the strength of the hydrogen bonding networks of both FOX-7 and FOX-7/PPD were investigated and visualised using non-covalent interaction (NCI) plots, which were generated from the optimised geometries via the generation of charge density cube files and processed by the CRITIC2 code [24, 25, 26, 27].

3.2.3 Results and Discussion

The geometry optimisation of FOX-7/PPD was completed to the above criteria. The experimental and optimised unit cell parameters are shown in Table A1 in Appendix A, along with the percentage change in unit cell volume, which falls well within accepted limits of variation ($\sim \pm 5 \%$) [28]. Using the optimised geometry, the 3N vibrational frequencies were calculated at the Brillouin zone-centre (Γ -point), all of which were found to be real numbers. This is another

strong indication that the geometry outlined above represents the global minimum of the potential energy surface.

The value of Ω_{\max} represents the highest energy point of the phonon bath region in the $g(\omega)$, which is signified by a change in vibrational mode character from delocalised motions of molecules with respect to one another to localised molecular vibrations (combinations of bond stretches and angle bends). This parameter is of vital importance to the up-pumping procedure as it not only defines the phonon bath states, but also the up-pumping window, which is the region over which the $\Omega^{(2)}$ is captured. For this reason, the value of Ω_{\max} must be rigorously defined. This was achieved primarily through tracking the change in centre of mass (CoM) of each molecule in the unit cell for each of the calculated eigenvectors (see Figure 3.3). The location of Ω_{\max} was considered to be in the region beyond which all higher energy modes expressed a displacement of less than 10% of the maximum displacement (based on the acoustic modes), as molecular vibrations result in very little CoM movement. This decision was validated visually through examination of the animated eigenvectors, to qualitatively confirm that vibrational motion is localised to molecules beyond the defined region.

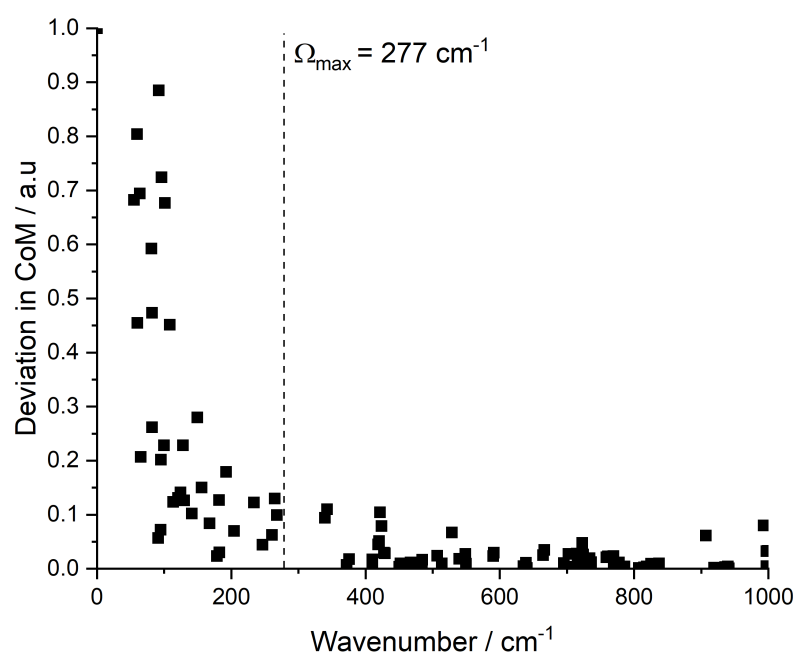


Figure 3.3: The average CoM displacement (normalised to unity) for all of the unique molecules (both FOX-7 and PPD) in the unit cell of FOX-7/PPD with the location of Ω_{\max} marked using a dashed vertical line.

There is a clear decrease in the average motion of the CoM as the vibrational mode frequency increases beyond 200 cm^{-1} , indicating a transition towards modes dominated by molecular vibrations. Moreover, it is not uncommon for a gap to be present in the vibrational mode distribution as the mode character switches behaviour [23]. This is observed here too and suggests that the transition occurs over the region $275 - 340\text{ cm}^{-1}$. The final assignment of Ω_{\max} was then determined by referring back to the $g(\omega)$ and taking the highest wavenumber value (while capturing the 5 cm^{-1} peak width) prior to the fall in CoM displacement, commensurate with the phonon gap. For FOX-7/PPD this was found to be 277 cm^{-1} . The calculated vibrational $g(\omega)$ with the location of Ω_{\max} , $2\Omega_{\max}$ and $3\Omega_{\max}$ (representing the up-pumping window) is shown in Figure 3.4.

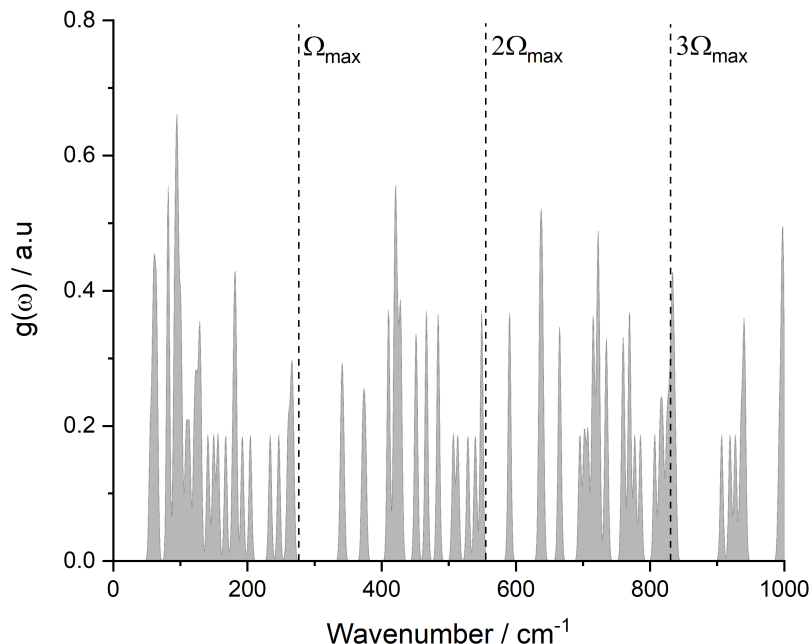


Figure 3.4: The vibrational $g(\omega)$ for the co-crystal of FOX-7/PPD with multiples of Ω_{\max} denoted by black dashed lines.

The vibrational $g(\omega)$ is used as the input for the vibrational up-pumping procedure. However, all previous work in the group has been completed on single component crystals, making FOX-7/PPD the first energetic co-crystal to be investigated using the methodology. As FOX-7/PPD contains both an EM and a non-EM, the $g(\omega)$ contains vibrational character from both components, but the energetic behaviour can only be attributed to FOX-7 molecules. It was unknown whether or not the complete $g(\omega)$ or a partial $g(\omega)$ which captures the vibrational modes of FOX-7 only, should be used to predict the sensitivity. To that end, the $g(\omega)$ was split into two partial $g(\omega)$ plots, as shown in Figure 3.5, from which it is apparent that the motions of the PPD and FOX-7 molecules are heavily coupled, that is motion from both molecules occurs in all eigenvectors.

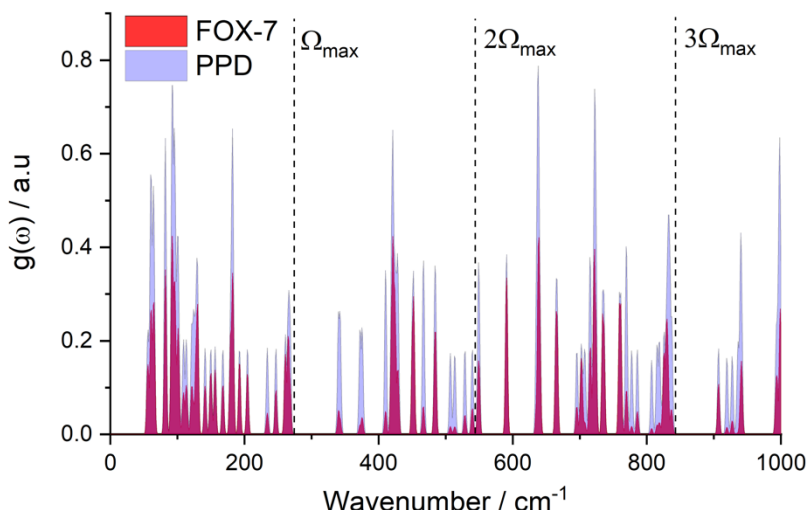


Figure 3.5: The $g(\omega)$ split into two partial $g(\omega)$ traces for the co-crystal of FOX-7/PPD with motion attributed to FOX-7 (in red) and PPD (in blue).

As can be seen from Figure 3.5, the partial $g(\omega)$ plots with respect to FOX-7 and PPD show that the phonon bath is a rough 50/50 mixture of FOX-7 and PPD, which is as would be expected since these modes present themselves as primarily translational motion of all the molecules in the unit cell. However, the vibrations beyond Ω_{\max} retain non-zero contributions from both species despite the increasing dominance of molecular motion. This raises the question of whether each mode should be considered when determining the

up-pumped density (i.e., if there is sufficient EM activation in the mode to generate energetic response, if not it should not be included in the capture process). It was decided through consideration of other ongoing work in the group that a modest contribution of EM ($>10\%$ of the total mode motion) to a vibration should be deemed significant as the motion will be exacerbated through vibrational heating [29]. This result suggests that while the entire $g(\omega)$ should be used for scattering of vibrational energy, the peaks at 507 and 514 cm^{-1} are predominantly vibrations based on PPD and as such should not be considered in vibrational energy capture.

An additional prerequisite parameter to be determined prior to the determination of a predicted sensitivity is the vibrational shock temperature, T_{shock} , which simulates the phonon bath heating as a result of the initial impact. T_{shock} is estimated via the ratio between the total cumulative heat capacity and that of the phonon bath ($C_{\text{tot}}/C_{\text{ph}}$) as shown in Figure 3.6. Previous work set the benchmark T_{shock} value of 3423 K based on a $C_{\text{tot}}/C_{\text{ph}}$ ratio of 5.22. As FOX-7/PPD presents with $C_{\text{tot}}/C_{\text{ph}} = 5.05$, through a simple proportionality sum this assigns the value for T_{shock} of 3315 K. The value used for FOX-7 was taken as 3278 K based on previous work [23].

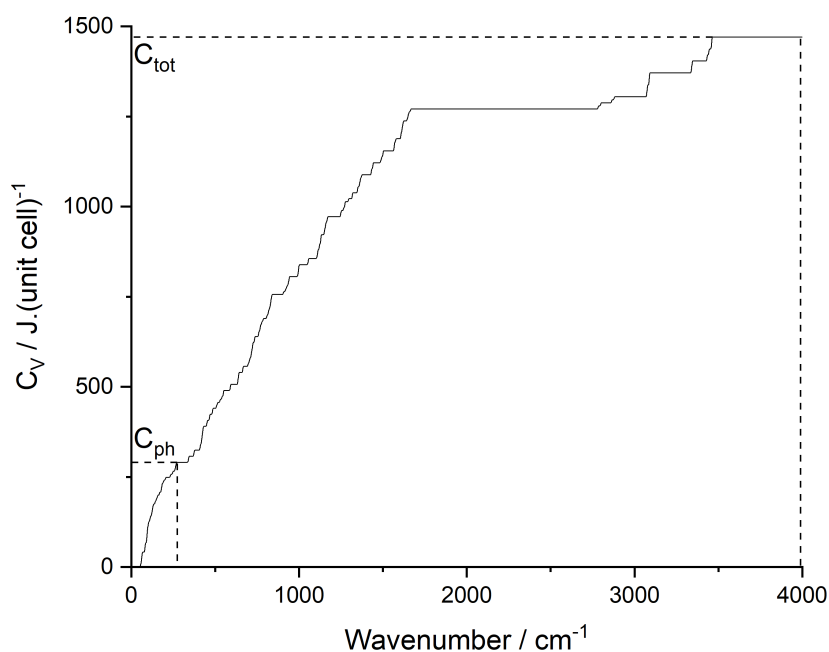


Figure 3.6: The cumulative vibrational heat capacity of FOX-7/PPD with C_{ph} and C_{tot} marked by dashed lines.

The contribution to the total heat capacity climbs as the number of vibrational states increases, with plateaus present at areas where the $g(\omega)$ is equal to zero. With the information gained from Figures 3.3-6 the parameters for the vibrational up-pumping process were finalised and are shown in Table 3.1. Here Z denotes the number of molecules present in the unit cell and Y the number of amalgamated modes (i.e., mixed molecular and lattice modes) per molecule that reside in the phonon bath, which thereby move the expected phonon bath count beyond the baseline $6Z$ value (denoting three translations and three rotational modes, per molecule).

Table 3.1: Shows input parameters for the vibrational up-pumping procedure for both FOX-7 (taken from previous work) and FOX-7/PPD along with the experimental impact sensitivity of the two materials [23].

| EM | Ω_{max} | Z | $Z(6+Y)$ | Y | T_{shock} / K | Experimental sensitivity / J |
|-----------|----------------|-----|----------|-----|-----------------|------------------------------|
| FOX-7 | 174 | 4 | 36 | 3 | 3278 | 28 |
| FOX-7/PPD | 277 | 2/2 | 38 | 3.5 | 3315 | 10 |

As can be seen from Table 3.1, the total number of vibrational modes in the phonon bath ($Z(6+Y)$) and the estimated value for T_{shock} are very similar. The number of amalgamated modes increase from 3 for FOX-7 to 3.5 per molecule for FOX-7/PPD, which is non-integer as the FOX-7 and PPD molecules have different numbers of amalgamated modes. The exact number of modes attributed to the FOX-7 and PPD molecules was unable to be determined as the vibrational motions of each species are so heavily coupled.

The much higher numerical value of Ω_{max} for the co-crystal deserves special mention, as a typical value of Ω_{max} for a molecular crystal is generally $200 \pm 50 \text{ cm}^{-1}$. Thus, the co-crystal of FOX-7/PPD has a much larger than expected phonon bath, meaning that more phonon states are present to scatter (up-pump) the mechanical impact energy. This is the first indicator to rationalise the increased sensitivity of FOX-7/PPD compared to FOX-7.

Using the vibrational up-pumping procedure with the previously calculated vibrational $g(\omega)$ as the input, the corresponding two-phonon density of states, $\Omega^{(2)}$ (i.e. scattered or up-pumped vibrational intensity), was generated and projected onto the underlying $g(\omega)$. The $g(\omega)$ with the $\Omega^{(2)}$ overlaid for both FOX-7 and FOX-7/PPD are shown in Figure 3.7, with Ω_{\max} , $2\Omega_{\max}$, and $3\Omega_{\max}$ shown using dashed lines.

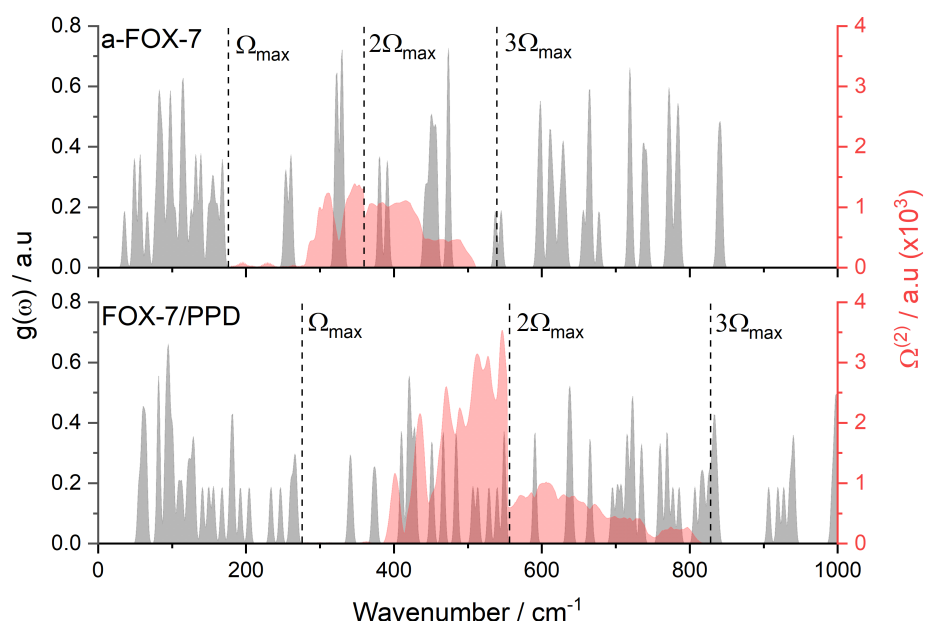


Figure 3.7: The vibrational $g(\omega)$ (grey) and the $\Omega^{(2)}$ (red) for both FOX-7 (taken from previous work) and FOX-7/PPD, with the up-pumping window marked with dashed lines [23].

It is clear from Figure 3.7 that the underlying vibrational $g(\omega)$ traces for FOX-7 and FOX-7/PPD are strikingly different, which is to be expected as the co-crystal contains an additional species which will contribute a new set of vibrational frequencies. Differences in crystal packing and the presence of hydrogen-bonding interactions will also alter the vibrational spectrum of FOX-7. As previously mentioned Ω_{\max} for FOX-7/PPD is significantly larger than that for FOX-7, resulting in a much wider up-pumping window. The up-pumped density (a measure of predicted impact sensitivity) for the two materials was determined through quantification of the integral of the $\Omega^{(2)}$ projected onto the underlying $g(\omega)$ (with the omission of the peaks at 507 and 514 cm^{-1}). This metric when plotted against the experimental sensitivity gives a curved line

(taken from previous work) on which FOX-7/PPD sits significantly above FOX-7, validating the experimental finding that FOX-7 has been sensitised through co-crystallisation with a non-EM material. A plot of the up-pumped densities of both EMs studied in this compared to a number of previously studied EMs against the experimental impact sensitivities is shown in Figure 3.8.

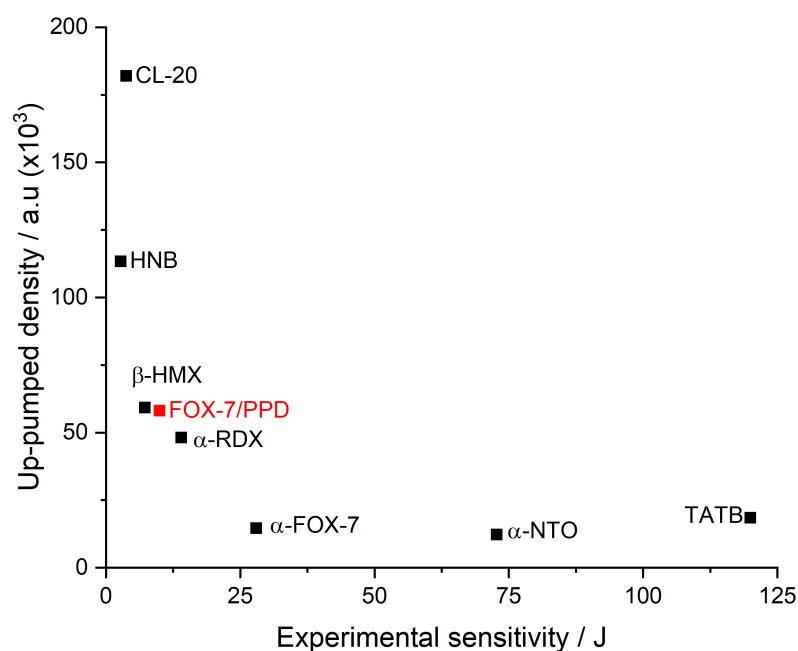


Figure 3.8: Shows the up-pumped density per molecule of a number of well-known EMs ($g(\omega)$ files taken from previous work) and FOX-7/PPD (shown in red) vs. experimental impact sensitivities [23, 29].

As is shown in Figure 3.8, the up-pumped density of FOX-7/PPD is in excellent agreement with previously studied materials, and falls above that of FOX-7, reinforcing the experimental finding of enhanced mechanical sensitisation. The up-pumped density of FOX-7/PPD and FOX-7 were found to be 58057 and 14658 a.u. respectively. Thus, with this re-enforcement of the experimental observation, the up-pumping model can provide an answer as to why enhanced sensitisation occurs, based on analysis of changes in the vibrational spectra upon co-crystallisation. To this end, further exploration into the vibrational $g(\omega)$ plots for both materials, along with an examination of changes in the hydrogen bonding networks, were pursued.

A clear difference between the $g(\omega)$ spectra of FOX-7 and FOX-7/PPD is the value of Ω_{\max} , and thus the size of the phonon bath. The number of modes in the phonon baths of FOX-7 and FOX-7/PPD are 36 and 38 respectively (Table 3.1) which indicates that the larger phonon bath of FOX-7/PPD does in fact contain more modes, but only just. This follows suit with the number of amalgamated modes per molecule increasing from 3 to 3.5 (representing 3 for one species and 4 for the other as $Z=2$ for both FOX-7 and PPD) with the co-crystallisation. This is further proven when the eigenvectors of the vibrations between 200 cm^{-1} and Ω_{\max} are interrogated for the co-crystal as they are primarily dominated by small movements of the external groups of each molecular species (NH_2 and NO_2). Such motion is reduced in FOX-7 as a result of the more rigid hydrogen bonding network.

As the phonon bath is key in the generation of the $\Omega^{(2)}$ through phonon-phonon scatterings, having a larger number of phonon bath modes, spread over a wider range, results in a broader $\Omega^{(2)}$ envelope, suggesting that more capture modes from the underlying $g(\omega)$ will be present beneath the $\Omega^{(2)}$. This idea can be captured through consideration of the number of doorway region modes ($1-2\ \Omega_{\max}$) per molecule in the unit cell. This gives a measure of both the scattering potential of the doorway region but also the capture potential of the early up-pumping window. The number of doorway modes per molecule for FOX-7/PPD and the EMs featured in Figure 3.8 are outlined in Table 3.2.

Table 3.2: Shows the value of Ω_{\max} , experimental impact sensitivity and the number of doorway modes per molecular unit for FOX-7/PPD as well as a number of well-studied molecular EMs [23, 29].

| EM | Ω_{\max} | Experimental sensitivity / J | # doorway modes per molecular unit |
|-----------------|-----------------|------------------------------|------------------------------------|
| FOX-7/PPD | 277 | 10 | 6 |
| HNB | 155 | 2.75 | 12 |
| CL-20 | 222 | 3.75 | 12 |
| β -HMX | 200 | 7.25 | 7 |
| α -RDX | 169 | 14 | 6 |
| α -FOX-7 | 180 | 28 | 3 |
| α -NTO | 216 | 72.75 | 3 |
| TATB | 151 | 122 | 3 |

The number of doorway modes per molecular of FOX-7/PPD (6) is less than that of the three materials that are experimentally more sensitive and double

that of FOX-7 itself (3). A number of the doorway region vibrational modes in FOX-7/PPD have a large contribution from motion of PPD molecules, particularly the NH_2 groups involved in the hydrogen bond network to the FOX-7 molecules. This can be seen in Figure 3.5 as a large amount of the peaks are attributed to PPD (larger partial $g(\omega)$), suggesting that the non-EM acts as a vibrational channel for the energy to pass through to excite the vibrations of FOX-7 molecules. This is exemplified perfectly by the two peaks that were removed in the capture process as they were able to scatter vibrational energy into other FOX-7 containing modes. Additionally, an increased area of the doorway region is populated by vibrational character and as such more $\Omega^{(2)}$ is captured. Both effects result in an increased up-pumped density. This is exemplified in Figure 3.7, as the $\Omega^{(2)}$ traces of FOX-7 and FOX-7/PPD are very different, with the co-crystal having a significantly more pronounced maximum to the $\Omega^{(2)}$, with an increased density of $g(\omega)$ peaks beneath. The resulting increase in up-pumped density suggests a more favourable arrangement of underlying vibrational modes for the generation of an intense $\Omega^{(2)}$, which also has a larger number of underlying capture states.

While these changes in the respective $g(\omega)$ spectra can be used to explain the difference in up-pumped densities, in order to develop structure/property relationships the differences in the $g(\omega)$ spectra must also be explained through changes in structure between the two EMs.

Analysis of the $g(\omega)$ spectra of FOX-7 and FOX-7/PPD shows a significant difference in the phonon bath region, which is made up of low energy phonons that comprise largely translational motion of molecules. Both EMs considered in this work exhibit hydrogen-bonding networks, which will affect the low energy translational modes to different degrees. From a comparison of the structures of FOX-7 and FOX-7/PPD it could be suggested that the hydrogen-bonding network is stronger in the co-crystal since there is an energetic driving force for co-crystal formation. The suggestion of a stronger hydrogen-bonding network for the co-crystal is reinforced through comparison of the experimental infra-red (IR) spectra of FOX-7, PPD and FOX-7/PPD (Figure 3.9) where a

more pronounced absorption region at 2500-3000 cm^{-1} suggests there is an increased presence of N-H...N hydrogen bonding [1].

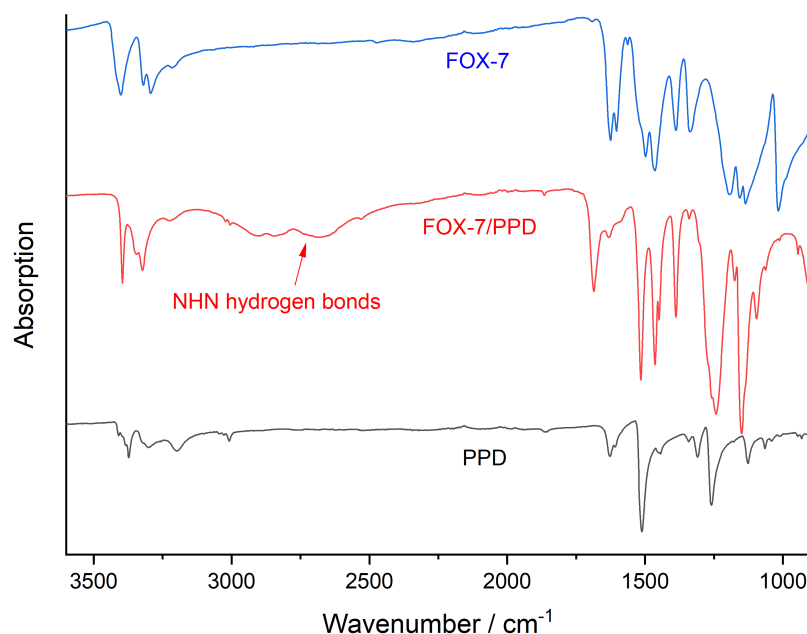


Figure 3.9: Shows the experimental IR plots for FOX-7 (blue), FOX-7/PPD (red) and PPD (black) with the pronounced region attributed to N-H...N H-bonding in FOX-7/PPD marked [1].

To further quantify the nature of the differences in intermolecular interactions between FOX-7 and FOX-7/PPD, non-covalent interaction (NCI) plots were calculated based on the optimised geometries. These are used to define stationary points in the electron density that defines an intermolecular interaction by plotting the reduced density gradient (s) vs. the sign of the λ_2 parameter of the electron density (ρ). A value approaching zero for the reduced density gradient indicates a stationary point, while the value of the sign $\lambda_2 \rho$ parameter suggests the nature of the interaction associated with the stationary point (a negative value indicates an attractive interaction, while a positive value represents a repulsive interaction) [24, 25, 26, 27].

The results from the NCI study are presented in Figure 3.10. This analysis indicates that the strongest hydrogen-bonding interaction in FOX-7 is the intermolecular N-H...O interaction with a sign $\lambda_2 \rho = -0.03$ a.u., with additional

interlayer attractive dispersion interactions between $\text{sign}\lambda_2\rho = -0.02 - 0.00$ a.u. The co-crystal of FOX-7/PPD shows a similar N-H...O interaction at $\text{sign}\lambda_2\rho = -0.03$, which occurs between the terminal $-\text{NO}_2$ groups on the FOX-7 molecules and an $-\text{NH}_2$ group on PPD, along with a similar array of weaker dispersion interactions at $\text{sign}(\lambda_2)\rho -0.02 - 0.00$. Unlike the structure of FOX-7, however, the co-crystal exhibits an additional hydrogen-bonding interaction between the $-\text{NH}_2$ groups of both molecules, resulting in an N-H...N interaction (as suggested by Figure 3.9), with a $\text{sign}(\lambda_2)\rho$ of roughly -0.05 , indicating that this is a stronger interaction than those present in FOX-7 (as it is more negative). It is perhaps surprising, on the grounds of electronegativity arguments, that N-H...N hydrogen bonds could be stronger than N-H...O hydrogen bonds. However, analysis of the respective geometries substantiates this argument with shorter bonds ($r_{\text{N-H}\cdots\text{N}} = 2.826 \text{ \AA}$ and $r_{\text{N-H}\cdots\text{O}} = 2.929 \text{ \AA}$) in FOX-7/PPD compared to $r_{\text{N-H}\cdots\text{O}} = 2.925 \text{ \AA}$ in FOX-7. The strongest H-bonding interaction for each structure (represented through a coloured isosurfaces) is shown alongside the reduced gradient plot for both FOX-7 and FOX-7/PPD in Figure 3.10.

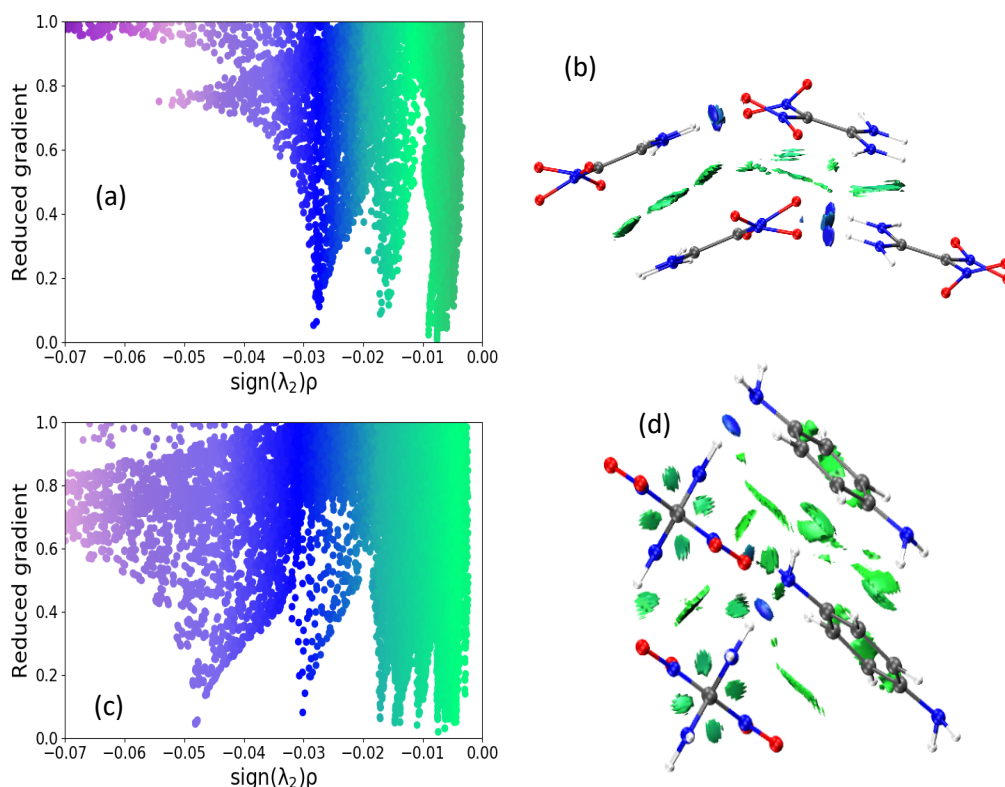


Figure 3.10: Shows the reduced gradient of the hydrogen-bonding interactions of FOX-7 (a) and FOX-7/PPD (c) with the interactions represented by coloured isosurfaces (representing a reduced gradient value of 0.4 a.u.) images (b) and (d) respectively.

As can be seen from Figure 3.10(a and c) the strength of the hydrogen bonding in FOX-7/PPD is enhanced through the presence of a strong N-H...N interaction between a FOX-7 and PPD molecule, as there is a prominent interaction with a more negative sign(λ_2) ρ . While the strength of the above interactions cannot be translated into an interaction energy, the value of sign $\lambda_2\rho$ can be used in a comparative sense to gain insight into relative strength. A key interaction to consider is the interaction between two water molecules in a dimer, which has been shown to have a strength of -0.03 which indicates that the interaction between FOX-7 and PPD molecules are particularly strong [25]. Previous work on FOX-7 has suggested that the bond order of the C=C in FOX-7 was calculated to be closer to 1.5 than 2. This suggests that it will be more easily broken than a formal C=C double bond [30]. The observed increase in hydrogen bond strength as a result of co-crystallisation with PPD is sufficiently strong to 'break' the C=C bond present in FOX-7, allowing the molecule to twist about the central bond.

The strong interaction between the two unique molecules has a two-fold effect on the phonon bath region of the co-crystal; firstly, the motions of the two unique molecular units are strongly coupled, as shown in Figure 3.5, and secondly, the lattice energy of the co-crystal is lower than that of FOX-7. As a direct result of these factors the amalgamated modes of FOX-7/PPD are difficult to separate. Additionally, such modes are present at higher frequencies because of the steeper potential well as a result of the crystal being more stable. This results in a larger, more spread-out phonon bath and thus a larger value of Ω_{\max} . As outlined previously the larger phonon bath has a direct result on both the number of modes considered to scatter energy, but area over which the energy is captured. A dramatic change in the size and nature of the phonon bath, as a result of co-crystallisation, has huge implications on the impact sensitivity of a material as has been outlined in this work.

3.2.4 Conclusions

Computational modelling of the co-crystal of FOX-7/PPD validates the experimental finding that FOX-7 is sensitised through the co-crystallisation with the non-energetic PPD. The up-pumped densities of FOX-7 and FOX-7/PPD (14658 and 58057 a.u respectively) follow the experimental trend of more sensitive EMs presenting with larger up-pumped densities (28 J and 10 J respectively). The up-pumped density of FOX-7/PPD was rationalised through projection onto vibrational modes containing sufficient FOX-7 activation, facilitated by the development of the partial $g(\omega)$ script outlined in Chapter 2. This example can be used as guideline for future energetic co-crystals studied using the vibrational up-pumping procedure. The physical basis for the sensitisation has been rationalised through examination of NCI plots which show that there is a new N-H...N hydrogen bond which is shorter and stronger than the N-H...O present in the original FOX-7 structure. In order to accommodate this new hydrogen bond the C-C bond (which formally has partial double bond character) has to twist. The co-crystal has a dramatically different $g(\omega)$ spectrum as well as an increased number of amalgamated phonon bath modes, consequently leading to an increased value of Ω_{\max} . This also results in a much wider up-pumping window, which contains an increased number of doorway states to generate the $\Omega^{(2)}$, which is then projected onto the underlying $g(\omega)$ (with the exception of the peaks at 507 and 514 cm^{-1} as there is insufficient FOX-7 activation and thus an energetic response is unlikely). As such the co-crystal has a much more efficient up-pumping pathway thus resulting in a larger up-pumped density. Co-crystallisation has been shown to have a large effect on the impact sensitivity of FOX-7. This work therefore pays testament to the unexpected consequences, and material property alteration that can arise in co-crystallisation studies.

3.3 Probing the High-Pressure Response of TNP

3.3.1 Introduction and Aims

As was briefly explored in Section 3.2.1, EMs must be rigorously characterised prior to widespread use due to safety concerns [3, 4]. The effect of co-

crystallisation on the impact sensitivity has been outlined in the previous Section, suggesting that a change in hydrogen-bonding network can result in a significant change in impact sensitivity. An additional material property that can result in a change in hydrogen-bonding network is polymorphism, where a particular molecular structure can exist in a number of different crystal packing arrangements [31]. Polymorphism is widespread throughout the field of EMs, with a number of well characterised materials having a number of known crystal structures (e.g. RDX, HMX and TNT) [32, 33, 34]. For example, RDX has five different known polymorphs, three of which are accessible through high pressure [32]. Despite their prevalence and known abundance within the energetics field, the resulting effect that the change in crystal packing has on the materials sensitivity to impact is not very well understood [35]. This poses an obvious cause for misinterpretation, as experimental determination of impact sensitivity may be performed on either the wrong polymorph (in error) or on a mixture of polymorphs, thereby clouding the true sensitivity value. This uncertainty is amplified when it is considered that RDX is often used as the standard reference material when experimentally determining impact sensitivity values [36].

Previous work in the group has attempted to quantify the impact sensitivities for three different polymorphs of FOX-7 (α, β, γ) and rationalised the findings with respect to changes in crystal packing [37]. The vibrational up-pumping procedure was used to predict the sensitivities from the vibrational $g(\omega)$ that had been validated using inelastic neutron scattering. This suggested that γ -FOX-7 was less sensitive than α -FOX-7, however experimental measurement indicated that both α -FOX-7 and γ -FOX-7 had the same impact sensitivity value. However, un-initiated samples of γ -FOX-7 recovered from the fallhammer apparatus showed that γ -FOX-7 had converted to the more stable α –form, suggesting an impact-induced phase transition had occurred. This work highlights the problems associated with polymorphic EMs; namely that while they may have different impact sensitivities, the act of measuring the values could cause a phase transition to occur, meaning that the measured value is not representative of the original material. Moreover, any polymorphs not stable at ambient conditions, but could form on the initiation pathway,

cannot be measured. This indicates that a clearer picture of how polymorphism can alter the impact sensitivity of EMs in terms of structure/property relationships is needed, in order to explain potentially erroneous experimental results, and to get a clearer idea of the energetic behaviour of the material over a range of temperatures and pressures relevant to initiation.

This section focuses on 3,4,5-trinitro-1H-pyrazole (TNP), a nitrated pyrazole which has energetic performance similar to that of RDX and HMX but with a reduced impact sensitivity, making it an attractive alternative [38]. A number of nitropyrazole EMs are used as explosives and oxidisers in rocket propellants, which can be attributed to their favourable oxygen balance, density and detonation parameters [39, 40]. A high-pressure polymorph of TNP (Form II, characterised at 5.3 GPa after a sluggish phase transition beginning at 4.3 – 4.6 GPa) has recently been synthesised, with findings suggesting it is considerably more sensitive to mechanical initiation than the ambient pressure polymorph (Form I) [2]. The crystal structures for both Form I and II of TNP are shown in Figure 3.11.

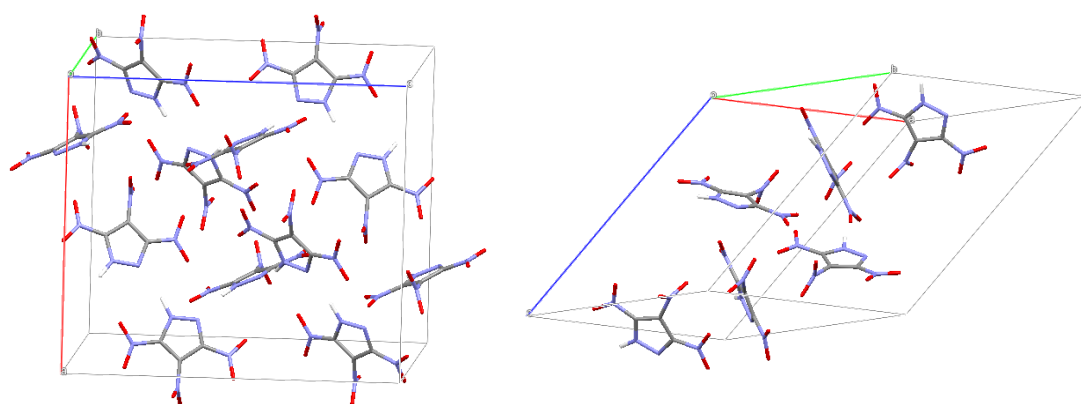


Figure 3.11: The crystal structure of TNP Form I (left – KAHHIM02) alongside the crystal structure of TNP Form II (right) [41].

A comparison of the two crystal structures of TNP Form I and Form II shows that the molecular conformation of the TNP molecules has not changed significantly between the two structures, with the nitro groups at the 3- and 5-positions lying in the plane of the pyrazole ring while that at the 4- position is twisted. While an experimental sensitivity value could not be determined for Form II, as the polymorph could not be recovered at ambient conditions, the

single crystal unexpectedly detonated when held under pressure (see Figure 3.12), suggesting this form is more susceptible to initiation.



Figure 3.12 Ruptured Ti-Zr gasket and cracked anvil after violent decomposition at 4.46 GPa [2].

In light of this observation, a computational investigation was undertaken to determine predicted impact sensitivities for Forms I and II of TNP, in an attempt to validate and rationalise the observed experimental result.

3.3.2 Computational Methodology

Full geometry optimisation calculations were completed for both TNP Form I (at ambient pressure) and Form II (at 5.3 GPa) using CASTEP V16.11 [17, 18]. The GGA functional PBE alongside the TS dispersion correction were used for both structures, with norm conserving pseudopotentials and a plane wave basis set cut-off of at least 950 eV [19, 42]. A Monkhorst Pack grid mesh of 0.05 \AA^{-1} was used to sample the electronic structure within the Brillouin zone. The following convergence criteria were used to determine when the geometries were fully converged: residual atomic forces $< 0.005 \text{ eV \AA}^{-1}$, atomic displacements $< 0.003 \text{ \AA}$, wavefunction self-consistency $< 2 \times 10^{-6} \text{ eV}$, and lattice vector stresses $< 0.005 \text{ GPa}$. Using the optimised geometries, Γ -point phonon calculations were performed using the DFPT method as implemented in CASTEP [21]. The vibrational $g(\omega)$ was calculated for each phase using the script outlined in Chapter 2 (with a Gaussian smearing regime of 5 cm^{-1}) and was used as the input for the vibrational up-pumping procedure. In addition, the hydrogen-bonding interactions for the two phases were characterised through the use of non-covalent interaction (NCI) plots by processing the

electron densities from the optimised geometries through the CRITIC2 code [24, 25, 26, 27].

3.3.3 Results and Discussion

The geometry optimisation calculations for both TNP Form I and Form II were completed in accordance with the above convergence criteria. The experimental and optimised unit cell parameters are shown in Table A1 in Appendix A, alongside the change in unit cell volume for the two materials. The unit cell parameters for the optimised geometries of Form I and II are in excellent agreement with their respective experimental structures (unit cell volume changes < 5 %) [28]. Using these optimised geometries Γ -point phonons were calculated for both phases, resulting in 3N real vibrational modes (no imaginary frequencies). This shows that the convergence criteria used in the geometry optimisation were sufficiently tight.

In order to locate the value of Ω_{\max} for both structures, the CoM code outlined in Chapter 2 was once again used. The average CoM relating to the molecules presented in the two-unit cells with respect to vibrational frequency are shown in Figure 3.13.

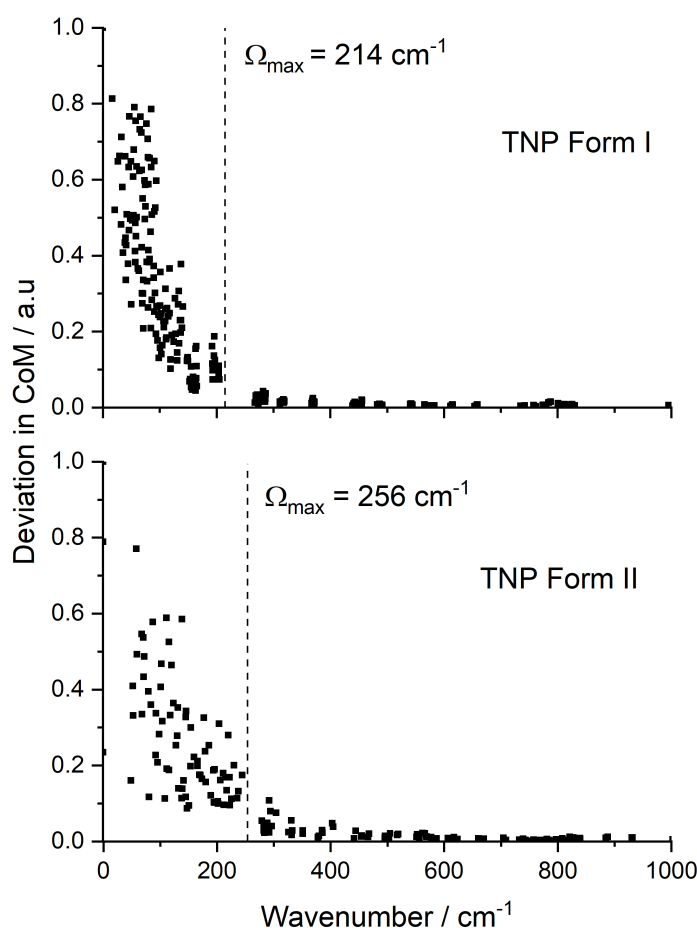


Figure 3.13: Shows the CoM displacement plots for both TNP Form I and II (normalised to unity), with values of Ω_{\max} being denoted by dashed vertical lines.

As can be seen from plots shown in Figure 3.13, Ω_{\max} for both TNP Form I and II lies above 200 cm^{-1} , after which there is a significant drop off in the deviation of the CoM, indicating a change in mode nature from delocalised to localised with increasing wavenumber. As can be seen for TNP Form II there is a single mode which contains a change in CoM above the imposed cut off (of 10 % of maximum deviation), despite this, the location of Ω_{\max} was taken to be prior to this point after careful visual examination of vibrational mode eigenvectors to ensure the mode was molecular in nature. Additionally, the presence of a defined ‘break’ in the modes along with a noticeable drop off in CoM deviation indicates that Ω_{\max} has likely been passed. The reason for the uncertainty could be due to the external pressure applied to the crystal.

The window of Ω_{\max} for Form II is at a higher wavenumber than that of Form I, however, the actual values of Ω_{\max} cannot not be determined without referring

to the $g(\omega)$ (in order to account for the applied Gaussian smearing); both plots are shown in Figure 3.14.

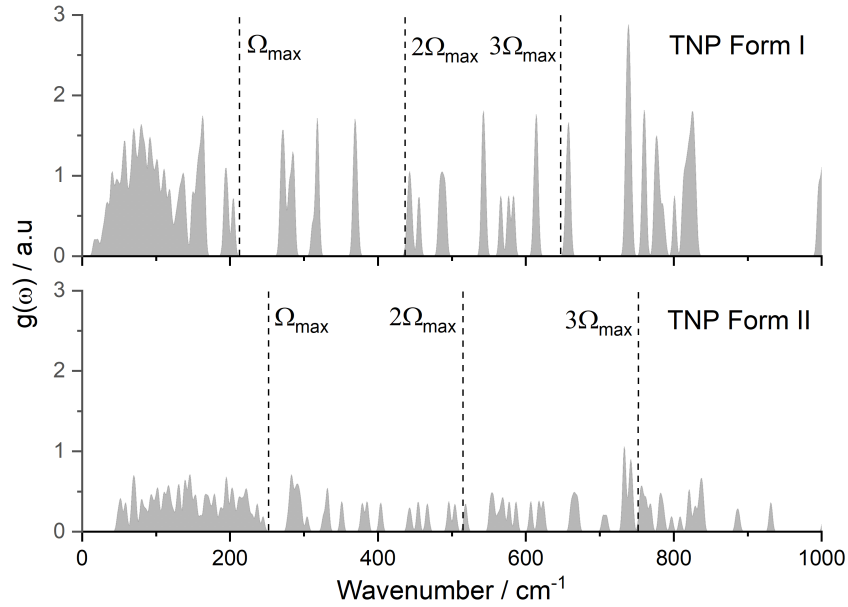


Figure 3.14: The vibrational $g(\omega)$ plots of Forms I and II of TNP, with multiples of Ω_{max} shown using dashed lines.

From both Figures 3.13 and 3.14, the Ω_{max} values for Forms I and II have been determined as 214 cm^{-1} and 256 cm^{-1} , respectively. A direct result of TNP Form II having a larger value of Ω_{max} is that it also has a larger up-pumping window, as shown in Figure 3.14. The value of T_{shock} for both materials was also determined prior to impact sensitivity prediction, through the use of cumulative heat capacity plots, shown in Figure 3.15.

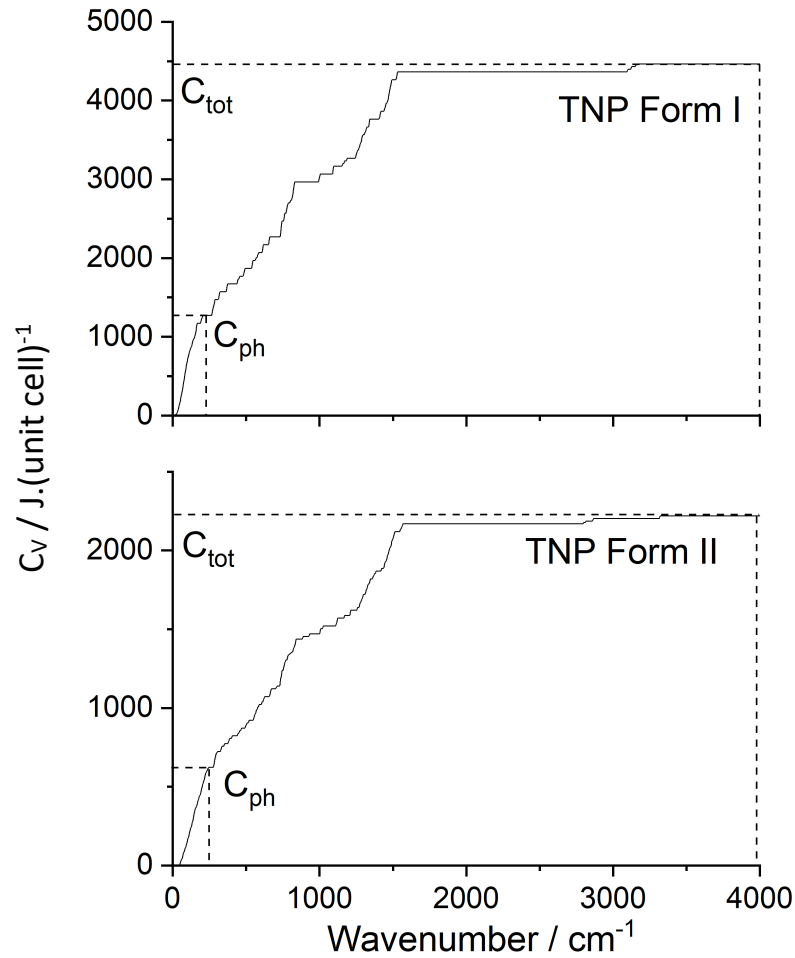


Figure 3.15: Shows the cumulative heat capacity for both TNP Form I and Form II, with C_{ph} and C_{tot} marked by dashed lines.

The marked values of C_{ph} and C_{tot} result in C_{tot}/C_{ph} values of 3.49 and 3.56 for TNP Form I and II respectively, resulting in values of 2288 K and 2334 K for T_{shock} , based on the earlier assignment of $T_{shock} = 3423$ K based on a C_{tot}/C_{ph} ratio of 5.22 [23]. The complete list of input parameters for the vibrational up-pumping procedure for both Forms I and II are listed in Table 3.3.

Table 3.3: The parameters required for the vibrational up-pumping procedure for Forms I and II of TNP, alongside experimental sensitivity values.

| EM | Ω_{max} | Z | Z(6+Y) | Y | T_{shock} / K | Experimental sensitivity / J |
|-------------|----------------|----|--------|---|-----------------|------------------------------|
| TNP Form I | 214 | 12 | 156 | 7 | 2288 | 17 |
| TNP Form II | 256 | 6 | 78 | 7 | 2334 | < 17 |

As has been stated previously, the values of Ω_{max} differ between the two Forms of TNP by roughly 40 cm^{-1} . Additionally, Table 3.3 shows that Form II contains

half the number of molecules in the unit cell (Z), as well as half the number of phonon bath modes ($Z(6+Y)$), compared to Form I. This is due to the unit cell of Form II being expressed as a smaller primitive cell of the experimentally assigned space group Cc ; this form presents a more desirable model for phonon mode computation as it is smaller (i.e., quicker to run) and maintains the single k -point sampling of the Brillouin zone, which is an important consideration in the vibrational up-pumping normalisation scheme. Form I presents as point group $P_{21/c}$, i.e. also in the primitive form; thus the $g(\omega)$ of both phases will relate to single k -point sampling of their respective Brillouin zones. Interestingly, the number of amalgamated modes (seven per molecule) is maintained across both phases, which likely reflects the conservation of molecular conformation across the phase transition. The increase Ω_{\max} is therefore likely to be attributed to mode-hardening caused by the presence of the external pressure (5.3 GPa). This point shall be returned to shortly.

Using the vibrational up-pumping procedure, and the previously determined vibrational $g(\omega)$ plots for both polymorphs of TNP, the $\Omega^{(2)}$ traces were determined and projected onto the underlying $g(\omega)$, as shown in Figure 3.16.

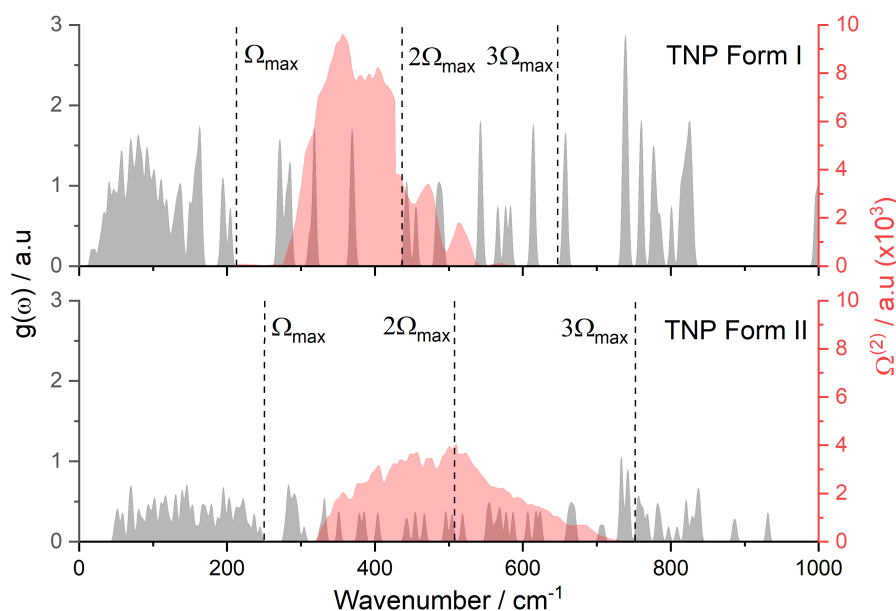


Figure 3.16: The vibrational $g(\omega)$ (grey) and the $\Omega^{(2)}$ (red) for Forms I and Form II of TNP, with multiples of Ω_{\max} shown by the dashed lines.

It is clear from Figure 3.16 that whilst both structures contain only molecules of TNP in the same molecular configuration, nevertheless their respective $g(\omega)$ plots, and therefore their $\Omega^{(2)}$, are very different. This is a key primary indicator of the extent to which polymorphism as a result of exposure to external pressure can alter the pattern of vibrational modes in a material and is the first observation to substantiate that the observed change in experimental impact sensitivity is inevitable. The up-pumped density was rationalised through evaluation of the overlap integral between the $\Omega^{(2)}$ and the underlying $g(\omega)$ states. The values of the up-pumped density plotted against the experimental impact sensitivity for Forms I and II, alongside a number of previously studied materials, are shown in Figure 3.17. Here both polymorphs of TNP are plotted at the same value of experimental sensitivity (i.e., that of Form I), as Form II cannot be measured as it cannot be recovered under ambient conditions.

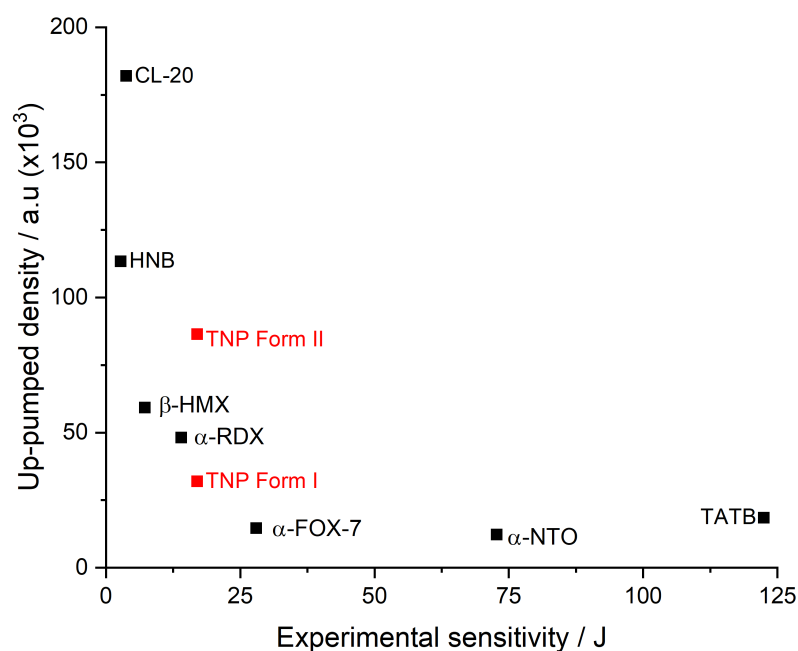


Figure 3.17: The up-pumped density of a number of well-known EMs (shown in black – taken from previous work) alongside Forms I and II of TNP (shown in red) vs. experimental impact sensitivities [23, 29]. TNP Form II (5.3 GPa) is shown at the same experimental sensitivity of Form I for comparative purposes as its impact sensitivity could not be determined.

As can be seen in Figure 3.17, the up-pumped density of TNP Form II (86448) was found to be significantly larger than that of Form I (31931), which strongly supports the high-pressure form as being more sensitive to initiation, in excellent agreement with experimental observation that the single crystal unexpectedly initiated. Note, while it is unlikely that mechanical initiation was the cause of the explosion (that said, it is not known if the crystal was being manipulated when it ruptured the gasket), it is known that mechanical impact often correlates with e.g., friction and shear initiation [3]. Thus, the up-pumping model can still give an indication of likely heightened responses to other external forces.

Figure 3.17 also shows that the predicted impact sensitivity for TNP Form I is in excellent agreement with predictions for other EMs, falling between HMX and α -FOX-7. With this validation in place, an attempt to rationalise the impact sensitivity differences according to the underlying vibrational $g(\omega)$ plots was then pursued.

There are two key differences between the Form I and II $g(\omega)$ plots. First, there appears to be a shifting of the vibrational modes upwards in frequency (by roughly $10\text{-}40\text{ cm}^{-1}$). This is particularly apparent in the up-pumping window and was quantified through (visual) cross-examination of the mode eigenvectors, this is outlined in Figure 3.18, where analogous vibrational motions have been mapped onto one another using blue dashed lines.

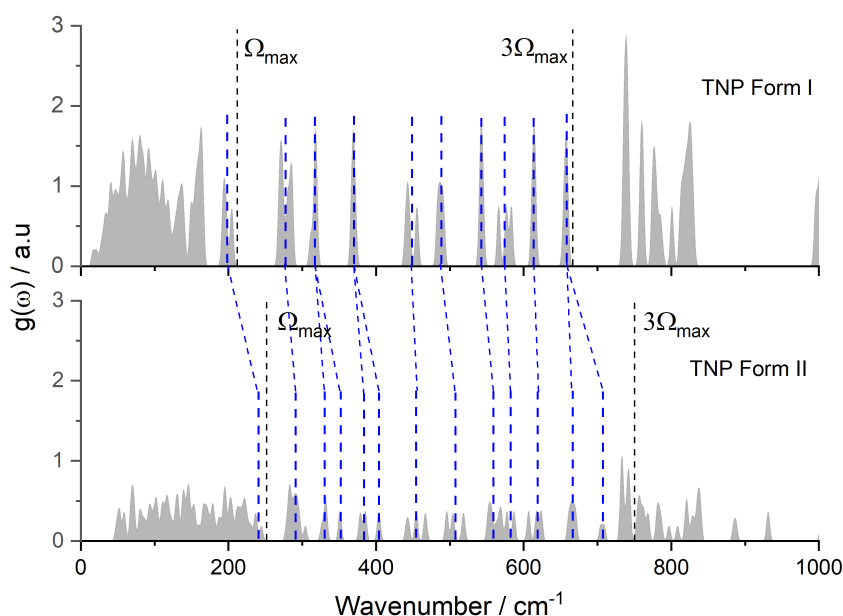


Figure 3.18: Shows the $g(\omega)$ plots of both TNP Form I and II and outlines the extent of pressure induced mode hardening with analogous modes linked with blue dashed lines.

There is a clear increase in the frequencies of the analogous vibrational modes, additionally, as previously noted, there is a roughly 40 cm^{-1} increase in the value of Ω_{max} . Two reasons could be attributed to these observations: (i) mode hardening, due to the presence of an external pressure during the optimisation of Form II, or (ii) changes in the hydrogen bonding network, as in the case of FOX-7/PPD discussed earlier in this chapter.

It has been noted previously that exposure to external pressure results in vibrational mode hardening [43]. In an attempt to rationalise whether this is the cause of the mode shift observed between Forms I and II of TNP, the optimisation of Form II was repeated in the absence of external pressure. Unfortunately, this calculation was found to be unstable, presenting as an ever-expanding unit cell on each subsequent cycle of optimisation. This suggests that TNP Form II is not stable in the absence of the external pressure, which matches the experimental observation that Form II could not be recovered at ambient pressure [2]. An alternative approach was therefore pursued where TNP Form I was re-optimised whilst being compressed to the same external pressure experienced by Form II (5.3 GPa). The resulting optimised geometry

was used as the input for a Γ -point phonon calculation (using the same methodology as outline in Section 3.3.2) and yielded 3N vibrations with one imaginary frequency (with a value of -13.19 cm^{-1}); this shows that the structure is not a minimum on the potential energy surface, indicating that TNP may undergo a phase transition with pressure, however this would need to be explored more closely to confirm. The $g(\omega)$ for compressed TNP Form I was then subjected to the same procedure for vibrational up-pumping, as outlined previously, with the corresponding data shown in Figures 3.19-21 and presented in Table 3.4.

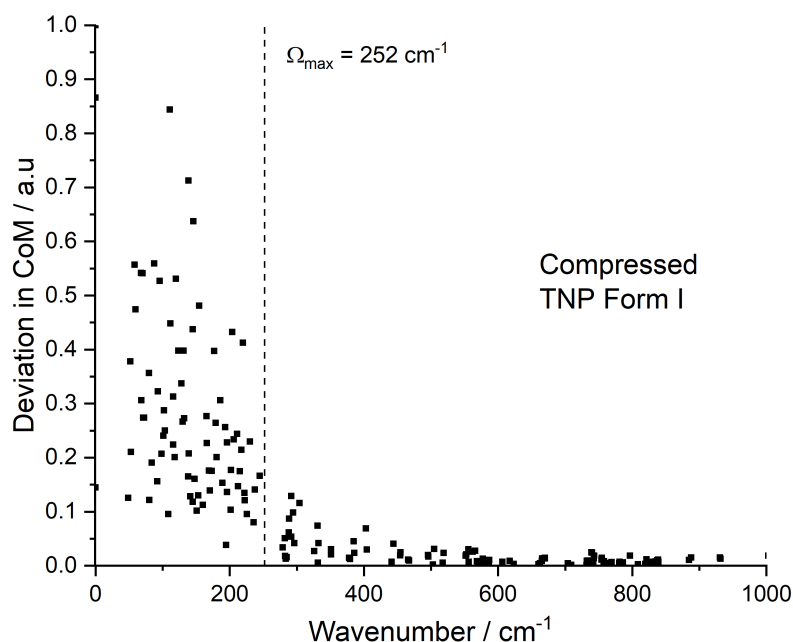


Figure 3.19: The CoM displacement for each mode of compressed TNP Form I (normalised to unity), with the location of Ω_{max} denoted using a dashed vertical line.

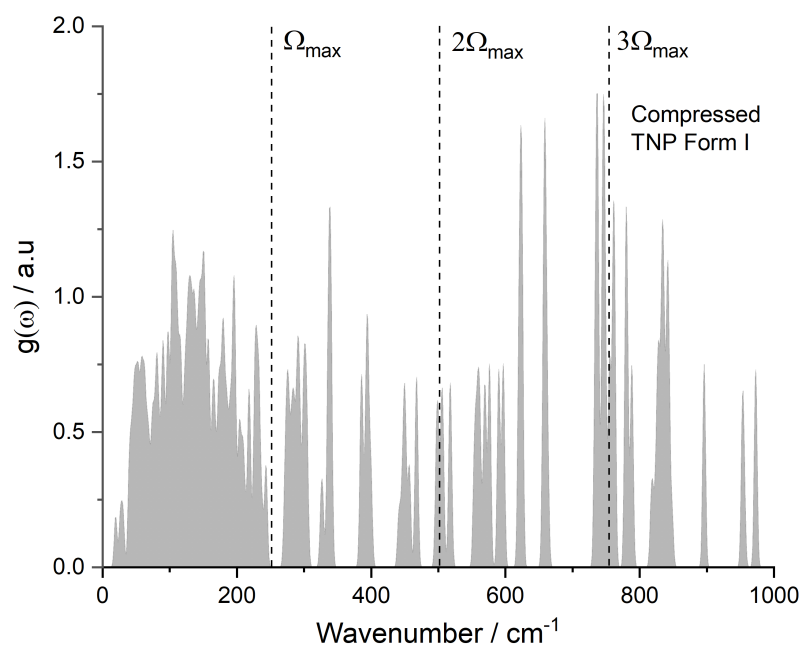


Figure 3.20: The vibrational $g(\omega)$ plot for compressed TNP Form I, with multiples of Ω_{\max} shown using dashed lines.

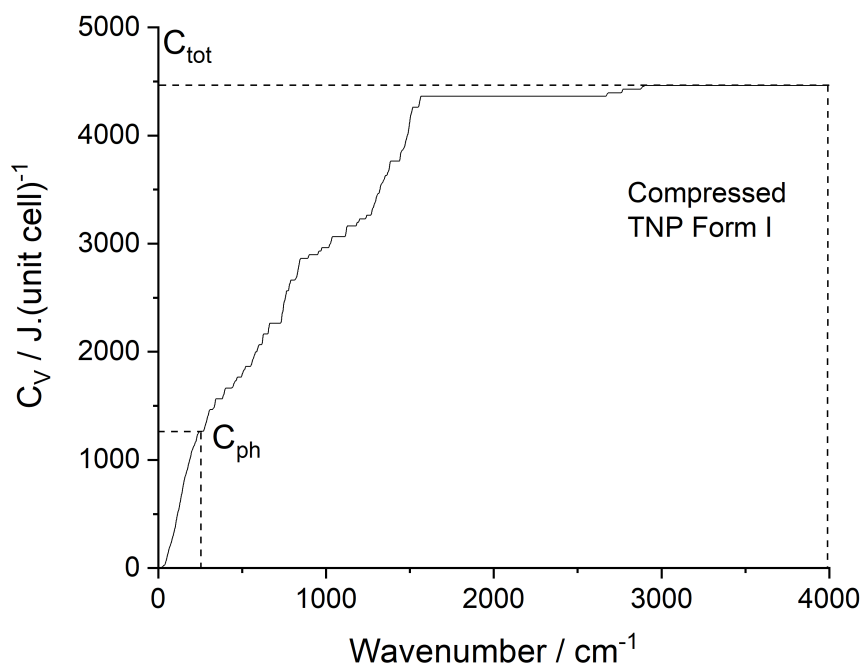


Figure 3.21: The cumulative vibrational heat capacity for compressed TNP Form I, with C_{ph} and C_{tot} marked by dashed lines.

Table 3.4: Parameters required for the vibrational up-pumping procedure for compressed TNP Form I.

| EM | Ω_{\max} | Z | Z(6+Y) | Y | T_{shock} / K |
|-----------------------|-----------------------------------|----------|---------------|----------|------------------------------|
| Compressed TNP Form I | 252 | 12 | 156 | 7 | 2314 |

As can be seen from Tables 3.3 and 3.4, the number of amalgamated modes (Y) for TNP Form I, Form II and compressed Form I are the same. This suggests that the nature of the phonon bath modes are very similar for each of the materials, and that the observed increase in sensitivity is solely based on the change in the vibrational $g(\omega)$ such that up-pumped energy is more efficiently captured and transferred into an energetic response. As can be seen from comparison of the $g(\omega)$ spectra, compressed Form I has a phonon bath and Ω_{\max} value that resembles that of Form II, suggesting that the protracted phonon bath is caused by the external pressure.

The predicted sensitivity from the vibrational up-pumping procedure obtained for compressed TNP Form I is given in Figure 3.22, from which it can be seen that its up-pumped density is very similar to that of Form II. This suggests that the effect caused by vibrational mode hardening on the $g(\omega)$ spectra is very significant to the energy transfer process and is likely to be the dominant reason for the heightened sensitivity of TNP under pressure. Polymorphism, for TNP at any rate, does not appear to be a contributing factor.

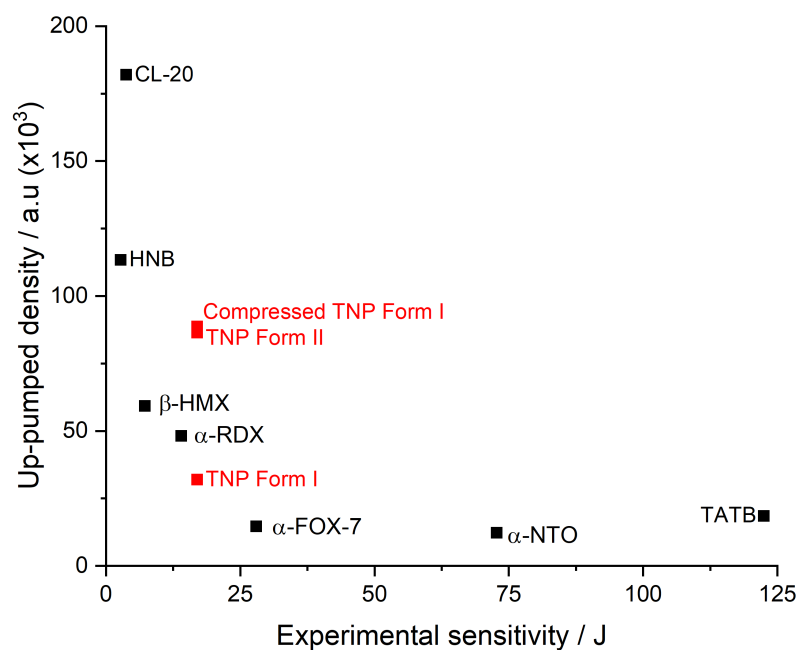


Figure 3.22: Shows the up-pumped density of a number of well-known EMs (shown in black – taken from previous work) and both Forms of TNP and pressurised Form I (shown in red) vs. experimental impact sensitivities [23, 29]. Both compressed Form I and Form II are plotted at the experimental sensitivity value of Form I as their experimental sensitivities were unable to be measured.

To further show the effects of pressure on the vibrational $g(\omega)$ of TNP, the computed plots for all three calculations are presented together, along with their $\Omega^{(2)}$ traces, in Figure 3.23.

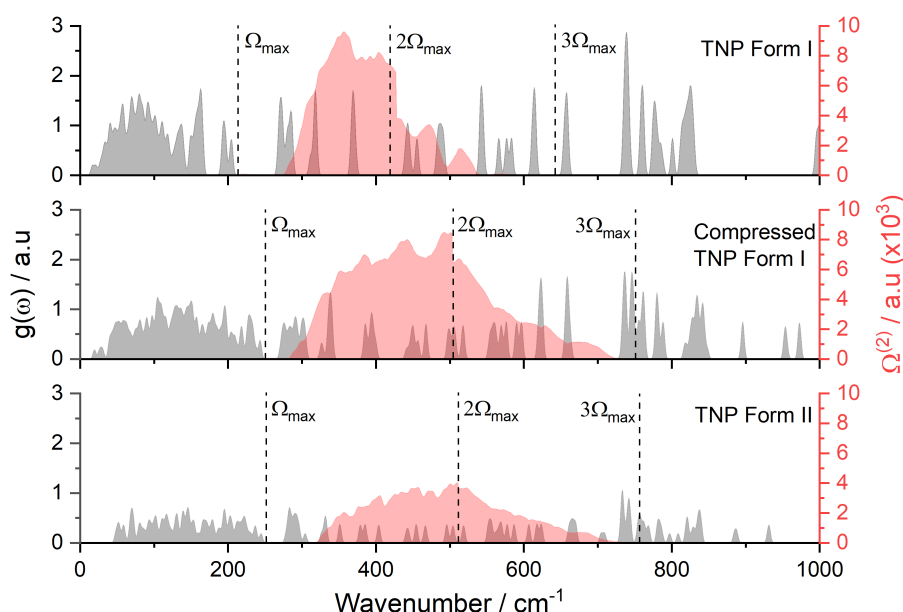


Figure 3.23: Shows the vibrational $g(\omega)$ (grey) and the $\Omega^{(2)}$ (red) for TNP Form I, compressed TNP Form I, and Form II with multiples of Ω_{\max} shown using dashed lines.

Comparison of the three $g(\omega)$ plots shown in Figure 3.23 shows the extent of vibrational mode hardening experienced by Form I when compressed, Ω_{\max} rises (by 38 cm^{-1}) and appears to have an increased number of peaks in the doorway region, which would result in increased scattering and capture potential of the $g(\omega)$ (as was shown previously for FOX-7/PPD). Consideration of the number of doorway modes per molecule for each of three structures considered in Figure 3.23 shows that TNP Form I has 4 doorway modes per molecule whereas compressed Form I and Form II have 5 doorway modes per molecule. This shows that there is an analogous increase in doorway region character as a result of pressure, likely as a result of an extension of the location of $2\Omega_{\max}$ resulting in additional modes being considered, resulting in increased scattering potential for the $g(\omega)$ spectra of the pressurised structures (increased $q + Q_D$ potential). Rather than resulting in a larger $\Omega^{(2)}$ maximum peak (as with FOX-7/PPD) this allows for a more widespread distribution extending almost to the terminus of $3\Omega_{\max}$, which was not the case in Form I as the comparatively sparse doorway region did not allow for such frequencies to be accessed. As such the up-pumped density is evaluated over an

increased number of modes resulting in a higher predicted sensitivity. Additionally, Figure 3.23 exhibited that upon the application of pressure peaks on the vibrational $g(\omega)$ of TNP Form I split into a number of peaks. The splitting of peaks in the up-pumping also creates an increased number of capture states, resulting in an increased up-pumped density.

While this analysis points strongly towards mode hardening as being a highly likely explanation for the heightened sensitivity of TNP under pressure, this still leaves the changes in hydrogen bond network, induced by the change in polymorph and exposure to pressure, unexplored. To complete the discussion, NCI plots based on the electron densities of the optimised geometries, were therefore also pursued.

The resulting NCI plots, shown in Figure 3.24, signify that there is a strong N-H...N hydrogen bond in both TNP Form I and compressed Form I with respective $\text{sign}\lambda_{2p}$ values of -0.030, -0.044 a.u which mirrors the lengths of the $r_{\text{N-H...N}}$ interactions (3.131 Å, 2.867 Å respectively) [24, 25, 26, 27]. Whereas TNP Form II has a N-H...O hydrogen bond with a $\text{sign}\lambda_{2p}$ value of -0.061 a.u. and an $r_{\text{N-H...O}}$ distance of 2.671 Å. Additionally, there are weak Van der Waals interactions between the molecules ($\text{sign}\lambda_{2p} < -0.03$ a.u.) which also increase in strength with pressure.

Form II has a unique hydrogen-bonding interaction compared to the two calculations of Form I, which is also stronger than the N-H...N interactions. Thus, overall, it can be concluded that while compression does strengthen the intermolecular interactions in Form I, those present in Form II are unique and stronger. However, this does not appear to translate into any further increase in predicted impact sensitivity given that the data point for compressed Form I already coincides with that for Form II on Figure 3.22.

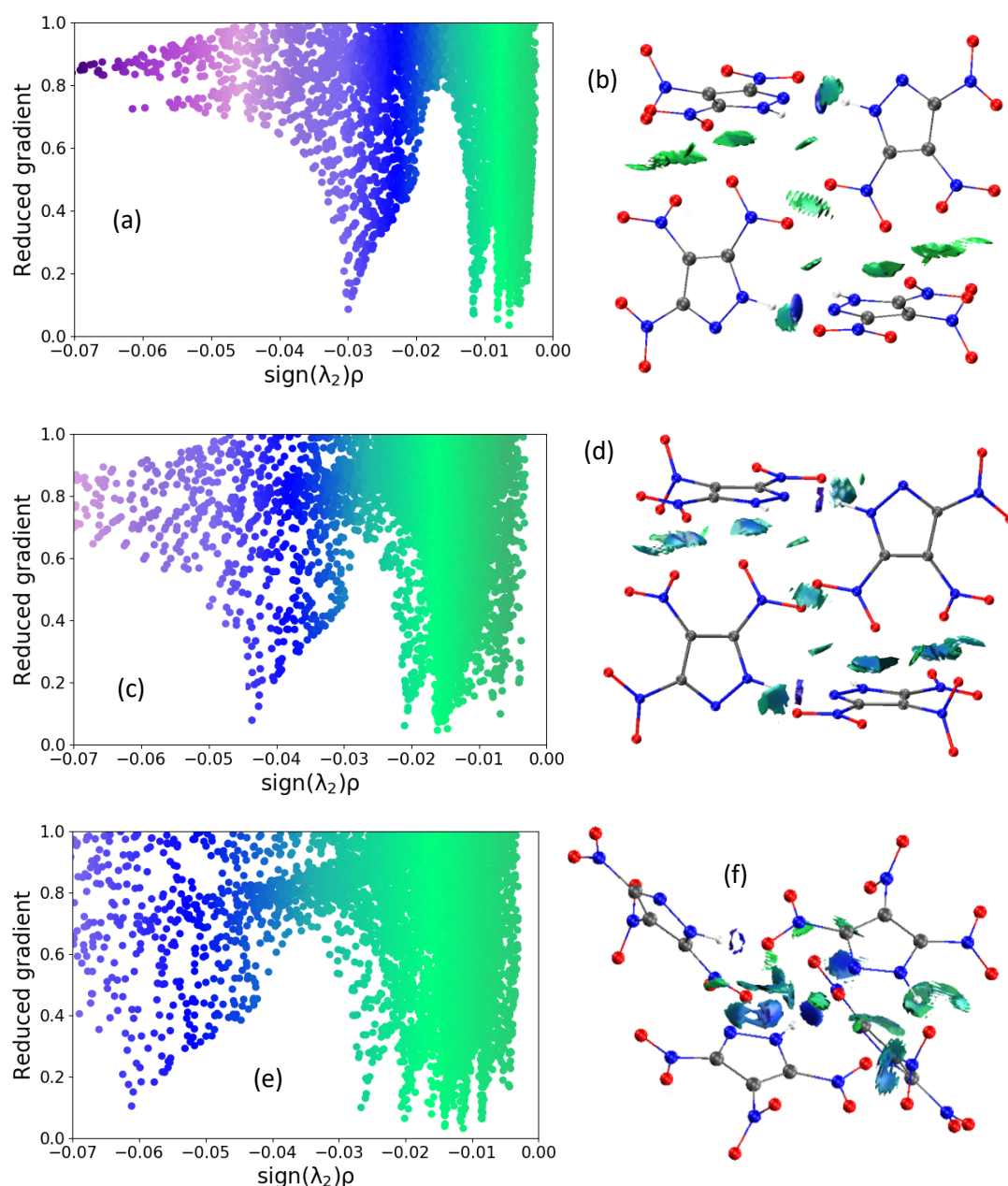


Figure 3.24: Shows the reduced gradient of the hydrogen-bonding interactions of TNP Form I (a), compressed Form I (c) and Form II (e), represented by coloured isosurfaces ($s = 0.4$ a.u.) and their respective reduced density plots (b, d and f respectively).

Overall, the NCI plots performed for TNP points towards stronger intermolecular interactions in the systems which exist under pressure, which in the case of compressed Form I is likely due to compression of the cell. Whereas for Form II, a unique H-bond is present as a result of polymorphism, which is stronger than both ambient and compressed TNP (Form I). While it appears in this instance that pressure induced vibrational mode hardening is

responsible for the heightened energetic response experienced by TNP Form II, consideration of the NCI plots for the three forms of TNP outlined in this work highlights changes in hydrogen bonding network are still accessible through polymorphism. Despite such changes not appearing to influence the impact sensitivity in the case of the TNP structures, the study into FOX-7/PPD outlines that such a finding is not universally applicable and that changes in hydrogen bonding strengths (potentially as a result of polymorphism) is an important consideration that should be given due attention when novel EMs are being considered.

3.3.4 Conclusions

Impact sensitivity predictions of TNP Form I and Form II were found to be in agreement with experimental findings, suggesting that the high-pressure polymorph (Form II) is significantly more sensitive than the ambient pressure polymorph (Form I). The dramatic increase in sensitivity was rationalised through examination of the differences in the vibrational $g(\omega)$ spectra. The primary reason for the increased sensitivity was found to be pressure induced vibrational mode hardening, which resulting in a general upwards shift of vibrational frequencies by $10\text{--}40\text{ cm}^{-1}$, exemplified through examination of the compressed structure of TNP Form I which was also predicted to be sensitised to a similar extent as Form II. Vibrational mode hardening resulted in a broadening of the phonon bath region, and subsequently the doorway region of Form II which alongside the observed pressure-induced peak splitting resulted in improved scattering efficiency and increased capture of vibrational energy. Consideration of NCI plots suggested that while compressing Form I increased the strength of the intermolecular interactions, the interactions presented by Form II were unique and stronger, but overall, this appeared to have little further influence on the predicted sensitivities as mode hardening accounted for the increase in sensitivity. As can be seen from the work outlined in this section exposure to external pressure has the ability to alter the vibrational $g(\omega)$ which has a direct consequence on certain material properties, resulting in a potentially more dangerous material. While polymorphism was found to not influence the sensitivity in this case, its consideration should not

be neglected in future as there remain a number of examples of EMs which exhibit a range of sensitivities based on polymorphic form. For these reasons novel materials found to have polymorphs will need each to be considered separately as well explicit consideration of the functioning pressure range the material is expected to be exposed to throughout its lifetime.

3.4 Overall Conclusions

This work exemplifies the utility of the vibrational up-pumping procedure for predicting impact sensitivities of EMs and the ability for this work to shed light on unexpected experimental results. The significant change in impact sensitivity observed for FOX-7/PPD when compared to FOX-7 displays that co-crystallisation has promise as an attractive route to alter the sensitivity and performance of EMs to a sufficient degree to synthesise novel materials with potentially tuneable properties. The investigation into the unexpected initiation of a sample of TNP Form II has outlined the requirement for rigorous studies into polymorphs of EMs. Additionally, the importance of a lifetime study to determine the pressures that the material will be exposed to during use, as an unexpected change in polymorph as a result of pressure, or simple pressure-induced vibrational mode hardening, could have disastrous consequences. Both methods of altering material properties considered in this Chapter (co-crystallisation introducing more amalgamated modes and exposure to external pressure leading to an increase in vibrational mode frequency) have been shown to increase the predicted sensitivity and the size of the materials phonon baths. Despite this finding, there is no reason to assume that an increase in sensitivity will always be the case; the two cases outlined in this Chapter were investigated was due to unexpected increases. But there is a chance that the changes to the vibrational $g(\omega)$ spectrum caused by co-crystallisation or pressure effects result in a much less efficient vibrational up-pumping process and may be harnessed to produce a less sensitive material.

3.5 References

1. Dr A. Khumsri, Personal Communication, University of Edinburgh, 2021.
2. Dr N. Atceken, Personal Communication, University of Edinburgh, 2020.

3. T. M. Klapötke, *Chemistry of High-Energy Materials*, De Gruyter, Berlin, 5th edn., 2019.
4. G. A. Olah and D. R. Squire, *Chemistry of Energetic Materials*, Academic Press, Cambridge, MA, 1991.
5. J. Sabatini and K. D. Oyler, *Recent advances in the synthesis of high explosive materials*, *Crystals*, 2016, **6**, 5, 1–22.
6. O. Bolton and A. J. Matzger, *Improved Stability and Smart-Material Functionality Realized in an Energetic Cocrystal*. *Angew. Chem., Int. Ed.* 2011, **50**, 8960–8963.
7. J. C. Bennion and A. J. Matzger, *Development and Evolution of Energetic Cocrystals*, *Acc. Chem. Res.*, 2021, **54**, 1699–1710.
8. K. B. Landenberger and A. J. Matzger, *Cocrystals of 1,3,5,7-Tetranitro-1,3,5,7-tetrazacyclooctane*, *Cryst. Growth Des.*, 2012, **12**, 7, 3603–3609.
9. O. Bolton, L. R. Simke, P. F. Pangoria and A. J. Matzger, *High Power Explosive with Good Sensitivity: A 2:1 Cocrystal of CL-20:HMx*, *Cryst. Growth Des.*, 2012, **12**, 9, 4311–4314.
10. U. R. Nair, R. Sivabalan, G. M. Gore, M. Geetha, S. N. Asthana and H. Singh, *Hexanitrohexaazaisowurtzitane (CL-20) and CL-20-based formulations (review)*, *Combust. Explos. Shock Waves*, 2005, **41**, 121–132.
11. O. Almarsson and M. J. Zaworotko, *Crystal engineering of the composition of pharmaceutical phases. Do pharmaceutical co-crystals represent a new path to improved medicines?*, *Chem. Commun.*, 2004, **17**, 1889–1896.
12. N. Schultheiss and A. Newman, *Pharmaceutical Cocrystals and Their Physicochemical Properties*, *Cryst. Growth Des.*, 2009, **9**, 6, 2950–2967.
13. D. D. Gadade and S. S. Pekamwar, *Pharmaceutical Cocrystals: Regulatory and Strategic Aspects, Design and Development*, 2016, **6**, 479–494.
14. C. R. Taylor and G. M. Day, *Evaluating the Energetic Driving Force for Cocrystal Formation.*, *Cryst. Growth Des.*, 2018, **18**, 892–904.
15. W. A. Trzcinski and A. Belaada, *1,1-Diamino-2,2-dinitroethene (DADNE, FOX-7) – Properties and Formulations (a Review)*, *Cent. Eur. J. Energ. Mater.*, 2016, **13**, 527–544.
16. J. Evers, T. M. Klapötke, P. Mayer, G. Oehlinger and J. Welch, *α - and β -FOX-7, Polymorphs of a High Energy Density Material, Studied by X-ray Single Crystal and Powder Investigations in the Temperature Range from 200 to 423 K*, *Inorg. Chem.* 2006, **45**, 13, 4996–5007.
17. S. J. Clark, M. D. Segall, C. J. Pickard, P. J. Hasnip, M. J. Probert, K. Refson and M. Payne, *First principles methods using CASTEP*, *Z. Kristall.*, 2005, **220**, 567–570.
18. B. G. Pfrommer, M. Cote, S. G. Louie and M. L. Cohen, *Relaxation of Crystals with the Quasi-Newton Method*, *J. Comput. Phys.*, 1997, **131**, 233–240.

19. F. Herman, J. P. Van Dyke and I. B. Ortenburger, *Improved statistical exchange approximation for inhomogeneous many-electron systems*, *Phys. Rev. Lett.*, 1969, **22**, 807–811.
20. S. Grimme, *Semiempirical GGA-type density functional constructed with a long-range dispersion correction*, *J. Comput. Chem.*, 2006, **27**, 1787–1799.
21. S. Baroni, S. D. Gironcoli, A. D. Corso and P. Giannozzi, *Phonons and related crystal properties from density-functional perturbation theory*, 2001 73, 516-557.
22. A. A. Michalchuk, M. Trestman, S. Rudic, P. Portius, P. T. Fincham, C. R. Pulham and C. Morrison, *Predicting the reactivity of energetic materials: an ab initio multi-phonon approach*, *J. Mat. Chem. A*, 2019, **7**, 19539–19553.
23. A. A. L. Michalchuk, J. Hemingway and C. A. Morrison, *Predicting the impact sensitivities of energetic materials through zone-center phonon up-pumping*, *J. Chem. Phys.*, 2021, **154**, 064105.
24. A. Otero-de-la-Roza, M. A. Blanco, A. M. Pendás and V. Luaña, *Critic: a new program for the topological analysis of solid-state electron densities*, *Comput. Phys. Commun.*, 2009, **180**, 157–166.
25. J. Contreras-Garcia, E. R. Johnson, S. Keinan, R. Chaudret and J. Piquemal, *NCIPLOT: a program for plotting non-covalent interaction regions*, *J. Chem. Theory, Comput.*, 2011, **7**, 625-632
26. A. Otero-de-la-Roza, E. R. Johnson and J. Contreras-García, *Revealing non-covalent interactions in solids: NCI plots revisited*, *Phys. Chem. Chem. Phys.*, 2012, **14**, 12165.
27. A. Otero-De-La-Roza, E. R. Johnson and V. Luaña, *Critic2: A program for real-space analysis of quantum chemical interactions in solids*, *Comput. Phys. Commun.*, 2014, **185**, 1007–1018.
28. J. Binns, M. R. Healy, S. Parsons and C. A. Morrison, *Assessing the performance of density functional theory in optimizing molecular crystal structure parameters*, *Acta Cryst.*, 2014, **B70**, 259–267.
29. I. L. Christopher, PhD Thesis, University of Edinburgh, 2023.
30. J. Najafpour, *The Structure and Chemical Bond of FOX-7: The AIM Analysis and Vibrational Normal Modes*, *Iran. J. Chem. Chem. Eng.*, 2011, **30**, 113-120.
31. J. Bernstein, *Polymorphism in Molecular Crystals*, Ox. Univ. Pres., 2nd edn., 2020
32. D. I. A. Millar, W. G. Marshall, I. D. H. Oswald and C. R. Pulham, *High-Pressure Structural Studies of Energetics Materials*, *Crystallogr. Rev.*, 2010, **16(2)**, 115-132.
33. C. S. Yoo and H. Cynn, *Equation of state, Phase Transition, Decomposition of β -HMX (Octahydro-1,3,5,7-Tetranitro-1,3,5,7-Tetrazocine) at High Pressure*, *J. Chem. Phys.*, 1999, **111(22)**, 10229-10235.
34. R. M. Vrcelj, J. N. Sherwood, A. R. Kennedy, H. G. Gallagher and T. Gelbrich, *Polymorphism in 2,4,6-Trinitrotoluene*, *Cryst. Growth Des.*, 2003, **3**, 6, 1027-1032.

35. B. W. Asay, B. F. Henson, L. B. Smilowitz and P. M. Dickson, *On the Difference in Impact Sensitivity of Beta and Delta HMX*, 2003, **21**, 223-235.
36. R. Doherty, *Relationship Between RDX Properties and Sensitivity*, Propellants Explos. Pyrotech., 2008, **33**, 4-13.
37. A. A. L. Michalchuk, S. Rudic, C. R. Pulham and C. A. Morrison, *Predicting the impact sensitivity of a polymorphic high explosive: the curious case of FOX-7*, Chem. Commun., 2021, **57**, 11213.
38. I. L. Dalinger, I. A. Vatsadze, T. K. Shkineva, G. P. Popova, S. A. Shevelev and Y. V. Nelyubina, *Synthesis and Comparison of the reactivity of 3,4,5-1H-Trinitropyrazole and Its N-Methyl Derivative*, J. Heterocycl. Chem., 2013, **50**, 911-924.
39. G. Herve, C. Roussel, H. Graindorge, *Selective Preparation of 3,4,5-Trinitro-1H-Pyrazole: A Stable All-Carbon-Nitrated Arene*, Angew. Chem. Int. Ed., 2010, **49**, 3177-3181.
40. S. Zhang, Z. Gao, D. Lan, Q. Jia, N. Liu, J. Zhang, and K. Kou, *Recent Advances in Synthesis and Properties of Nitrated-Pyrazoles Based Energetic Compounds*, Mol., 2020, **25(15)**, 3475.
41. Y. V. Nelyubina, I. L. Dalinger, K. A. Lyssenko, *Pseudosymmetry in Trinitropyrazole: The Cost of Error in Space-Group Determination*, Angew Chem., 2011, 50, 2892-2894.
42. A. Tkatchenko and M. Scheffler, *Accurate molecular van der Waals interactions from ground-state electron density and free-atom reference data*, Phys. Rev. Lett. 2009, **102**, 073005.
43. S. Hunter, *High-Pressure Computational and Experimental Studies of Energetic Materials*, University of Edinburgh, 2013, Edinburgh.
44. F. Han, *A Modern Course in the Quantum Theory of Solids*, World Scientific, Singapore, 2012.

Chapter 4 – Towards a Lead-free High Sensitivity Material to Replace Lead Azide

4.1 Introduction

The vibrational up-pumping methodology has been shown in the previous Chapter, and in previous work within the group, to accurately predict the trends in experimental impact sensitivities for a number of molecular EMs [1, 2, 3, 4, 5]. In this Chapter the focus is on non-molecular, coordination polymer (CP) EMs, which have generated excitement in the field due their altered properties from their molecular counterparts, where they often present as highly sensitive primary EMs [6]. Given that the up-pumping methodology was developed for molecular EMs, it is not clear how applicable it will be to this other important class of EM. To this end, a number of CP EMs are considered in this Chapter, namely lead azide (LA), a series of copper(I) nitrotetrazolates/nitrotriazolates known as DBX-1-3, formally, Cu(I)-5-nitrotetrazolate (DBX-1), Cu(I)₃-(5-nitrotetrazolate)₂Cl (DBX-2), Cu₄-(3,5-dinitro-1H-1,2,4-triazolate)₃Cl (DBX-3), and a copper(I) pyrazole, Cu(4-amino-3,5-dinitro-1H-pyrazolate) known as Cu(ADNP) [7, 8, 9]. All five of the structures covered in this work are extremely sensitive to mechanical impact and are therefore considered as primary EMs [10]. It is unclear if the vibrational up-pumping procedure will accurately represent the sensitivity of CPs as there are no discrete molecular units into which the up-pumped energy can become trapped. As such a computational investigation was needed to develop a workflow regime for the prediction of CP EM sensitivities, and to assess the applicability of the up-pumping method for this class of material, such that future studies can develop in-depth structure/property relationships that may guide material design.

4.2 Computational Methodology

Geometry optimisation calculations for LA, DBX-1, DBX-2, DBX-3 and Cu(ADNP) were completed using the BFGS optimisation method as implemented in CASTEP V.16.11 [11, 12]. A generalised gradient approximation (GGA) functional, namely PBE, was used with the TS dispersion correction scheme alongside a plane wave basis set of at least 1000

eV cut off [13, 14]. The core electrons in the structures were represented using norm-conserving pseudopotentials. The geometry optimisation calculations were completed to the following convergence criteria: residual atomic forces ≤ 0.025 eVÅ, atomic displacements $\leq 5 \times 10^{-4}$ Å, wavefunction self-consistency $\leq 5 \times 10^{-6}$ eV and lattice vector stresses ≤ 0.01 GPa. A grid scale of 2.0 was used for each material with a fine grid scale of at least 2.0 (2.0 for LA, DBX-1 and DBX-3 and 4.0 for DBX-3 and Cu(ADNP)). Particularly stringent convergence criteria were used such that the following Γ -point phonon calculations could be completed. The DFPT method was used as implemented within CASTEP to calculate the vibrational frequencies which are used to generate a vibrational $g(\omega)$ as per the script outlined in Chapter 2 [15]. The resulting data files were then subsequently used as the input for the vibrational up-pumping procedure.

4.3 Lead Azide

4.3.1 Introduction

LA is a primary energetic that was first synthesised in the late 1800s as a replacement for mercury fulminate and has been bulk produced since the 1930s [16]. The impact sensitivity of LA is dependent on the crystal morphology, with needle-like crystals reported to be more sensitive than round crystals, which could potentially raise problems if the incorrect morphology is used in a commercial setting. It is for this reason that LA is often ground into a fine powder and mixed with stabilising additives such as dextrin, to produce a primary explosive that is markedly safer and more reliable than its native crystalline state [17, 18, 19].

LA is comprised of two unique atom types (Pb and N) which results in a 3-dimensional structure of azide units connected by Pb atoms to create a coordination polymer. The unit cell for LA, which exemplifies the coordinated nature of the material, is shown in Figure 4.1 [7].

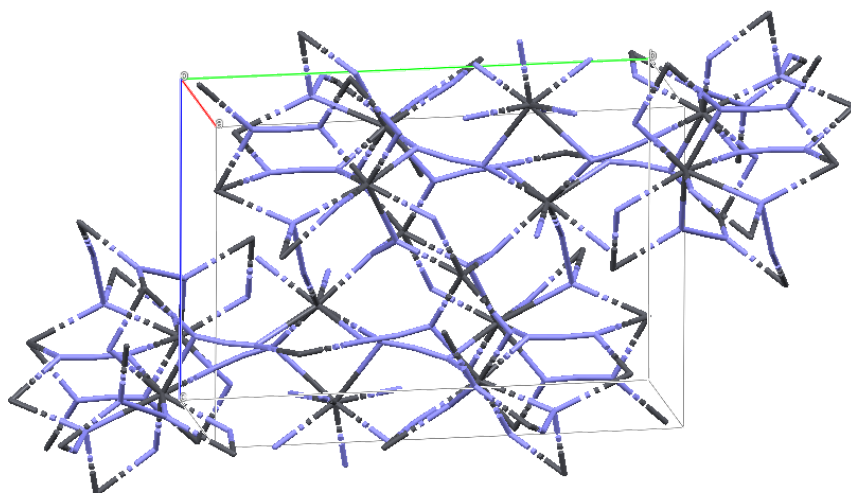


Figure 4.1: Shows the unit cell of LA with Pb atoms shown in grey and N atoms shown in blue, crystal structure taken from Reference [7].

Figure 4.1 shows that the structure of the LA repeat unit is relatively simple, but the unit cell is quite complex and occupies a large volume. Prior work in the group has shown that the vibrational up-pumping methodology was able to correctly rank a number of molecular and ionic azides with respect to experimental impact sensitivity when full Brillouin Zone sampling is used for the density of states calculation [1]. At the time LA was omitted from this study due to the computational expense associated with the large unit cell. It is studied here, in part to observe if Γ -point phonon calculations provide sufficient sampling of the Brillouin zone to correctly predict its impact sensitivity, and in part to highlight the challenges associated with applying vibrational up-pumping to CP EMs.

4.3.2 Results and Discussion

The geometry optimisation calculation of LA was completed to the convergence criteria outlined in Section 4.2. Comparison between the experimental and optimised unit cell parameters alongside percentage change in unit cell volume are shown in Table A2 in Appendix A. The unit cell parameters of LA changed slightly through the optimisation process, but the unit cell volume change is within acceptable limits (ca. 5 %) [20].

The optimised geometry was used as the input for a zone centre (Γ -point) vibrational frequency calculation, which resulted in 3N real vibrations, indicating that the convergence criteria were sufficiently tight.

As was outlined in Chapters 1 and 2, Ω_{\max} represents the uppermost frequency of the phonon bath and is a key piece of information required in the vibrational up-pumping model. It should once again be noted that the EMs studied in this Chapter are primarily CPs which pose a unique challenge in locating Ω_{\max} through the standard route of monitoring CoM changes. This is because the atoms in the unit cell act as a single ‘molecular unit’ and as such the distinction between delocalised phonon modes and localised molecular modes becomes even more blurred. A plot of the deviation in CoM for each vibrational mode of LA (in which the entire cell is taken to be an extended ‘molecular unit’) is shown in Figure 4.2. The deviation in CoM is usually normalised with respect to the mode which exhibits the maximum deviation in CoM, which is often one of the acoustic modes (as shown in 4.2 (a)). However, as the entire unit cell was considered a single unit in this case the extent of the acoustic mode motion was significantly larger than the smaller magnitude vibrations at higher wavenumbers. As such the plot was renormalized to the maximum deviation in CoM of the first non-acoustic mode (Figure 4.2 (b)).

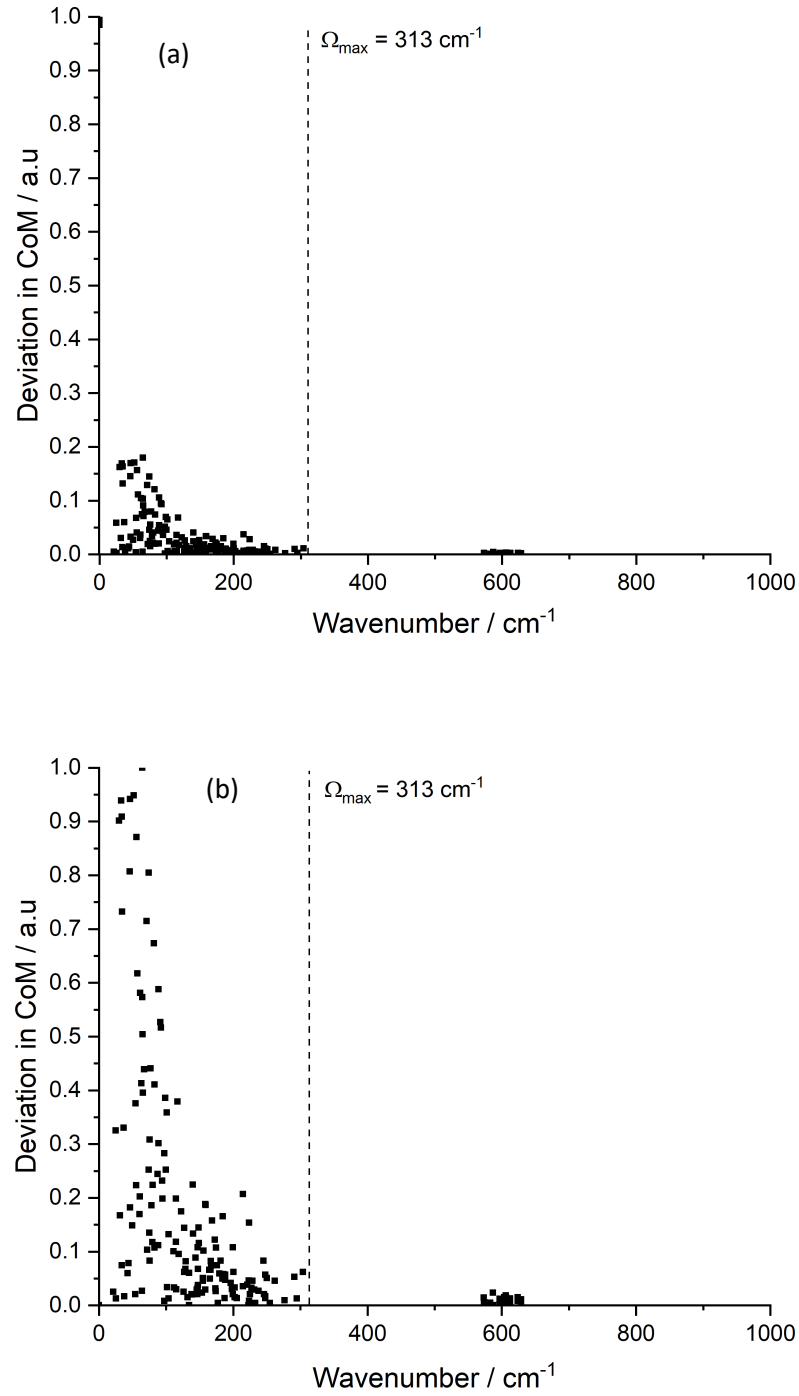


Figure 4.2: Shows the deviation in CoM for each vibrational mode of LA normalised to the deviation in the acoustic modes (a) and the first non-acoustic mode (b) (both plots normalised to unity).

As can be seen from Figures 4.2 (a) and (b) there is significant deviation in the change of CoM as a result of the acoustic modes, which is to be expected as the acoustic modes represent translations of the unit cell along the three

Cartesian axes. The renormalized plot (b) shows a more typical trace with the deviation in CoM decreasing as mode frequency is increased, towards the marked value of Ω_{\max} which was also located by the presence of an abrupt break in vibrational modes following the large continuous region typically expected for a phonon bath. Through these means, the value of Ω_{\max} was set to 313 cm^{-1} , after taking into accounting the 5 cm^{-1} Gaussian peak smearing used to plot the density of states ($g(\omega)$); this is shown in Figure 4.3, where the values of Ω_{\max} , $2\Omega_{\max}$, and $3\Omega_{\max}$ are also shown.

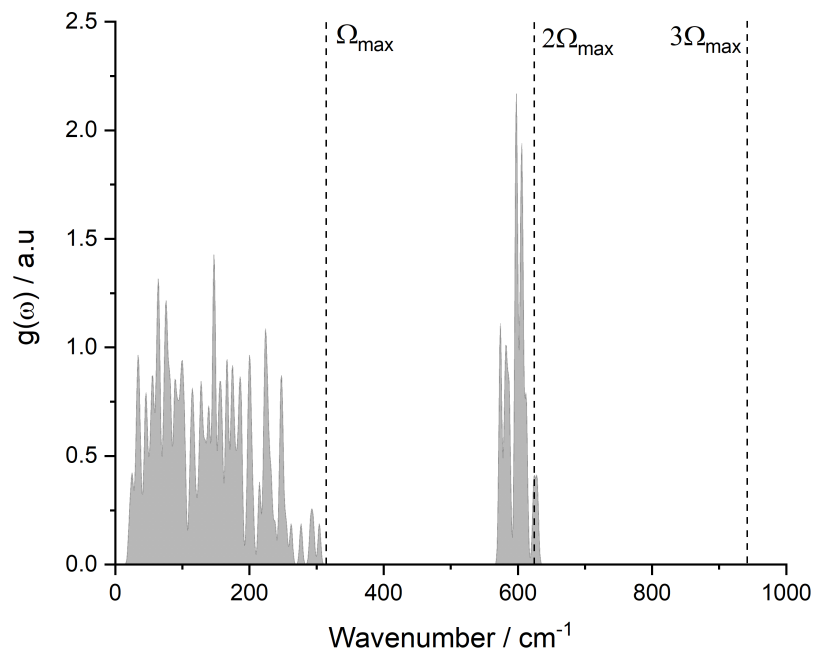


Figure 4.3: Shows the $g(\omega)$ of lead azide with the value of Ω_{\max} , $2\Omega_{\max}$, and $3\Omega_{\max}$ marked using dashed lines.

Figure 4.3 shows that the phonon bath of LA is large and almost continuous, as a result of a large number of similar low energy phonons modes. Additionally, it is readily apparent that the up-pumping window ($1-3 \Omega_{\max}$) is sparsely populated, which is usually synonymous with insensitive materials. There is only one pronounced region of peaks at $\approx 2\Omega_{\max}$ that will be able to capture and contribute to the up-pumped energy.

After assigning Ω_{\max} , the next piece of input data required for the vibrational up-pumping model is the vibrational shock temperature (T_{shock}). This is a

measure of how much vibrational heating occurs in the low energy phonon vibrations, compared to the molecular based vibrations. This is calculated through consideration of the cumulative contributions of the vibrational modes to the heat capacity. From this the contributions from the phonon bath modes (C_{ph}) and the total set of phonons (C_{tot}) can be obtained. This is then compared to the benchmark T_{shock} value of 3423 K, derived from C_{tot}/C_{ph} ratio of 5.22 [4]. The values of C_{tot} and C_{ph} calculated for LA are shown in Figure 4.4.

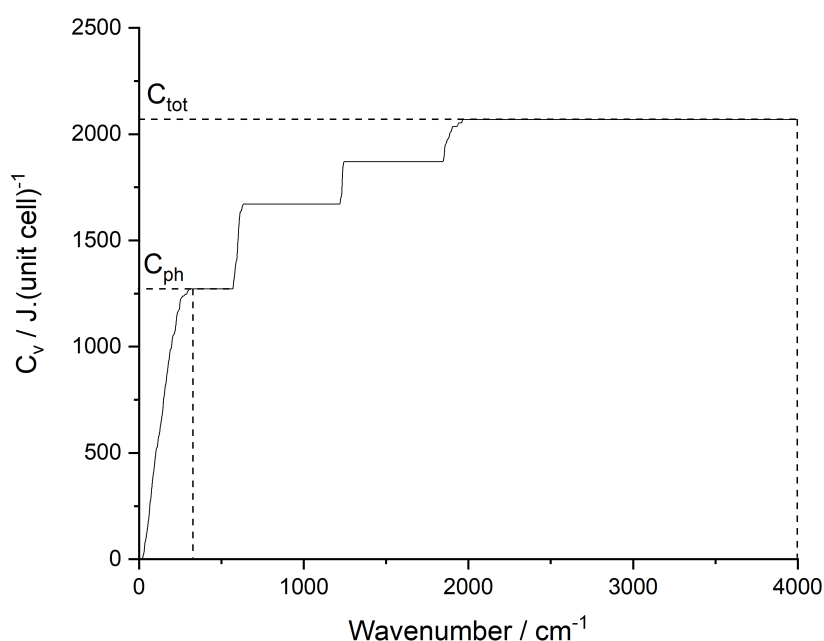


Figure 4.4: Shows the cumulative contribution to the heat capacity, C_v , for lead azide. The values of C_{ph} and C_{tot} are denoted by dashed lines.

As can clearly be seen from Figure 4.4, C_{ph} makes up a significant fraction of C_{tot} indicating that a significant percentage of the vibrational character is present in the phonon bath. C_{tot}/C_{ph} equals 1.63 for LA, resulting in a T_{shock} value of 1067 K which is noticeably lower than values typically derived for molecular crystals (shown in Table 4.1). This is a reflection of the high contribution from the phonon bath modes to the cumulative heat capacity in LA, which in turn can be attributed to the large phonon bath expressed by the CP nature of the crystal lattice.

The final pieces of information needed for the vibrational up-pumping model are the number of vibrations in the phonon bath and the number of molecules

in the unit cell. The number of phonon bath modes is formally denoted by $Z(6+Y)$, where Z is the number of molecules in the unit cell. In this case, Z is redefined as Z_{eff} (effective Z) which is set to 1 due to the CP nature of the crystal packing (preventing localisation onto single molecular units) and will be used in place of Z for the entirety of the work considering LA. Both the value of Z derived by the space group and the value of Z_{eff} are given in Table A2 in Appendix A. A summary of the parameters used as input to the vibrational up-pumping procedure are shown in Table 4.1. Also shown are reported experimental values for the impact sensitivity of LA as well as the associated values for a number of well-studied molecular EMs.

Table 4.1: Shows the input parameters for the vibrational up-pumping procedure for LA (with its Z value denoted with an asterisk to indicate Z_{eff}) and a number of well-studied EMs, alongside the experimental impact sensitivity values taken from previous work [4, 5]. Additionally, both the shocked phonon bath and up-pumped densities of each EM is provided.

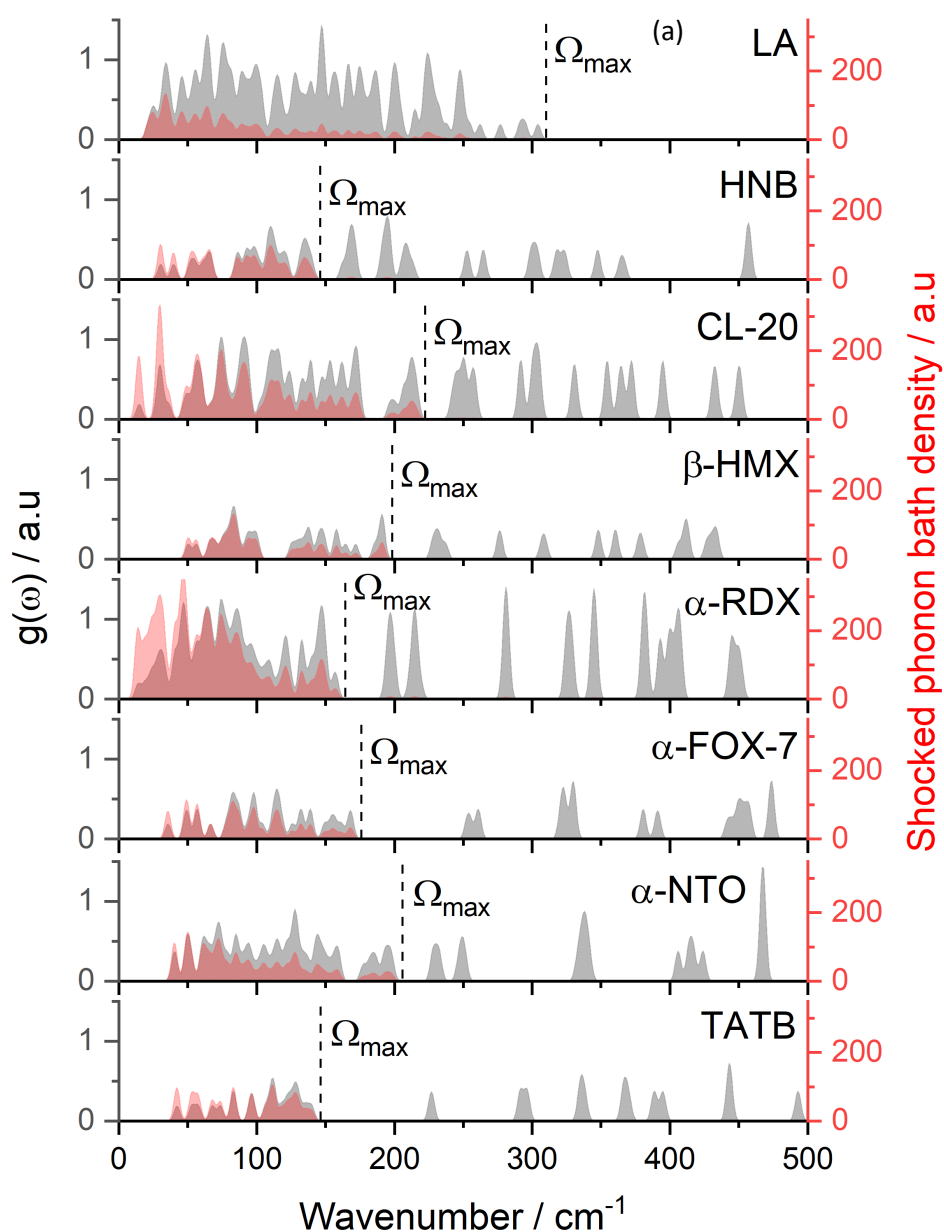
| EM | Ω_{max} | Z | $Z(6+Y)$ | Y | $T_{\text{shock}} / \text{K}$ | Experimental sensitivity / J | Shocked phonon bath density / a.u | Up-pumped density / a.u |
|-----------------|-----------------------|-----|----------|-----|-------------------------------|------------------------------|-----------------------------------|-------------------------|
| LA | 313 | 1* | 156 | 150 | 1067 | 2.5 – 4 | 7963 | 64992 |
| HNB | 155 | 2 | 30 | 9 | 3423 | 2.75 | 2691 | 113400 |
| CL-20 | 222 | 4 | 88 | 16 | 3278 | 3.75 | 3580 | 181937 |
| β -HMX | 200 | 2 | 34 | 11 | 3488 | 7.25 | 2486 | 59254 |
| α -RDX | 164 | 8 | 96 | 6 | 3265 | 13 | 2635 | 48100 |
| α -FOX-7 | 180 | 4 | 36 | 3 | 3278 | 28 | 1405 | 14658 |
| α -NTO | 216 | 8 | 64 | 2 | 2642 | 72.75 | 971 | 12280 |
| TATB | 151 | 2 | 24 | 6 | 4399 | 120 | 2541 | 18537 |

As a result of the large phonon bath, which follows on from the coordinated nature of the crystal structure, the question of whether two phonon up-pumping is required at all must first be addressed. This question arises as it could be that T_{shock} heating of the phonon bath modes alone is sufficient to result in initiation of the material, i.e., excitation via two phonon scattering to reach the higher energy modes is redundant for these materials. For this reason, the integral of the phonon bath region of the initially shocked phonon density of states ($g(\omega)^*$) was calculated (as shown by Equation 4.1) and compared to the molecular materials studied in previous work, to determine whether the phonon

bath of LA experiences a particularly pronounced effect (numerical values shown in Table 4.1).

$$\text{shocked phonon bath density} = \int_0^{\Omega_{\max}} g(\omega)^* \cdot d\omega \quad \text{Equation 4.1}$$

The output is shown in Figure 4.5, with plot (a) showing the shocked phonon bath overlaid on the underlying $g(\omega)$ and plot (b) showing how the shocked phonon bath density varies with experimental sensitivity. For plot (a) the datasets have been normalised with respect to the number of phonons in the phonon bath (i.e., per phonon bath mode) and the resulting shocked intensity normalised with respect to the number of molecules in the unit cell (i.e. per Z).



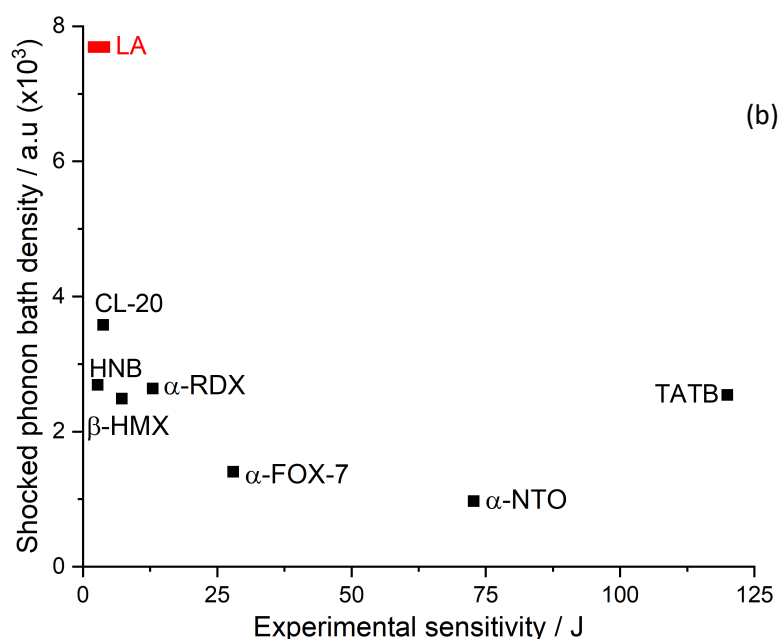


Figure 4.5: Shows the shocked phonon bath density of states (red) overlaid on the underlying $g(\omega)$ (grey) (a), and the integral (shocked phonon bath density – defined by Equation 4.1) vs. experimental impact sensitivity (b), with LA shown in red alongside a number of previously studied molecular EMs shown in black [4, 5].

As can be seen from Figure 4.5, consideration of the shocked phonon bath density (a measure of the amount of energy available in the phonon bath after impact) suggests that LA does experience notably increased energy uptake in these modes compared to the molecular crystals. Interestingly, the data points follow a reasonable trend, with the insensitive TATB the only significant outlier.

Next, the regular two-phonon scattering vibrational up-pumping procedure was pursued, resulting in the generation of two-phonon density of states ($\Omega^{(2)}$) trace with the output shown in Figure 4.6.

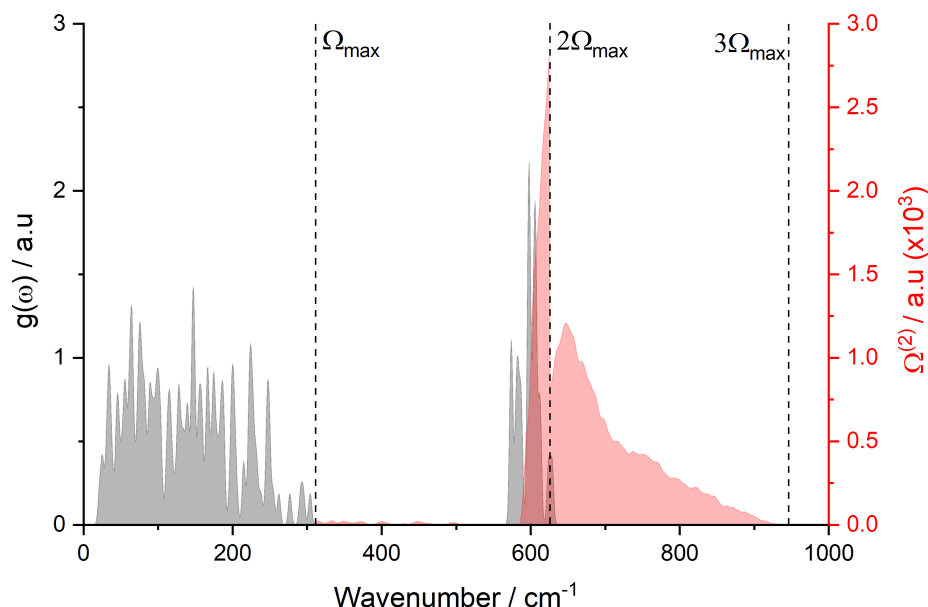


Figure 4.6: Shows the overlay of the $g(\omega)$ (grey) and the $\Omega^{(2)}$ (red) with Ω_{\max} , $2\Omega_{\max}$, and $3\Omega_{\max}$ marked using dashed lines for LA.

The increased number of vibrational modes within the phonon bath allow for pronounced multiple two phonon scattering pathways in LA, resulting in a sharp peak in the $\Omega^{(2)}$ at $2\Omega_{\max}$. Additionally, despite there being very few modes in the up-pumping window, those that are present all fall below (or on) $2\Omega_{\max}$, meaning that they are classed as doorway modes and are able to scatter the energy further resulting in a trailing off of the $\Omega^{(2)}$ trace.

Despite the sparsely populated up-pumping window, the peak of the $\Omega^{(2)}$ is captured by the underlying vibrations present in the $g(\omega)$, signifying that phonon up-pumping will result in excitation of higher energy modes. The up-pumped density was evaluated through the integral of the $\Omega^{(2)}$ between Ω_{\max} and $3\Omega_{\max}$ when projected onto underlying vibrational character and is plotted alongside the previously studied molecular crystals in Figure 4.7. The data is normalised in the usual way (i.e., prior to up-pumping, the $g(\omega)$ is presented on a per-phonon bath mode basis, and the resulting up-pumping intensity is divided by Z , i.e., per molecule).

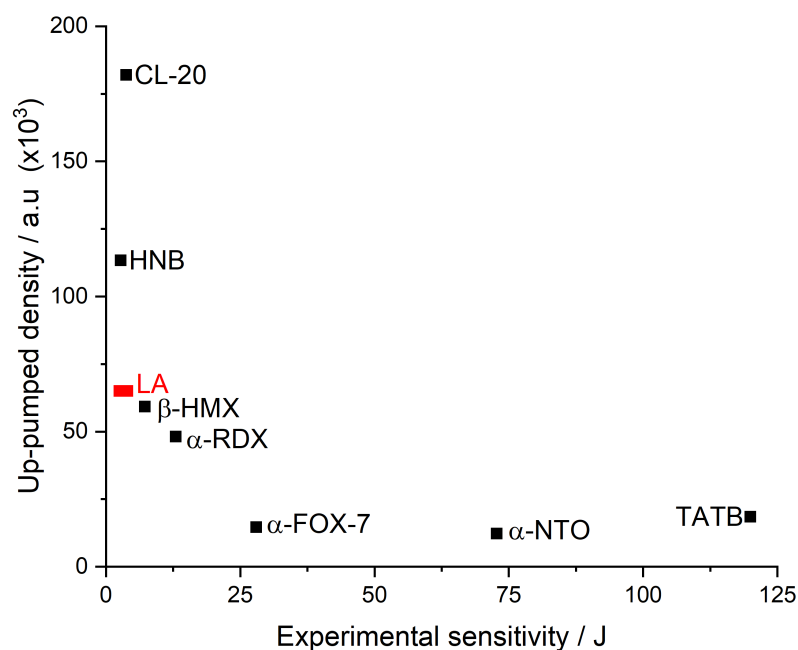


Figure 4.7: Shows the up-pumped density of LA (red) and a number of previously studied materials (black) plotted against the experimental sensitivity [4, 5, 9].

As can be seen from Figure 4.7, the up-pumped density of LA was found to be in reasonable agreement with the previously studied materials, albeit slightly under predicted. Despite this, the up-pumping model would still suggest that LA is a primary EM (taking the data point β -HMX as being on the boundary of primary/secondary EM behaviour) [21].

As consideration of both the shocked phonon bath density and vibrational up-pumping appear to give reasonable predictions for the sensitivity of LA, exploration of the vibrational mode eigenvectors was completed next in order to assess which approach was the most physically realistic. This point arises, since, in order for one model to be preferred over the other, it is important to establish that the phonon excitation results in energy transfer into vibrations that act as trigger modes to induce initiation. The simplicity of the azide system has allowed the trigger, or target modes, (Q_T) to be established for this class of EMs, with prior work highlighting the importance of activating eigenvectors associated with the N-N-N angle [1, 2]. In short, acute excitation of this angle allows access to a conical intersection on the potential energy surface, which

lowers the barrier to N–N bond dissociation. This process has been termed dynamic metallisation [2].

Interrogating the calculated eigenvectors for LA, to show which modes exhibit the strongest N-N-N angle bend behaviour (calculated using the script outlined in Chapter 2, and normalised with respect to the mode that gives the biggest angle distortion) results in the plot shown in Figure 4.8.

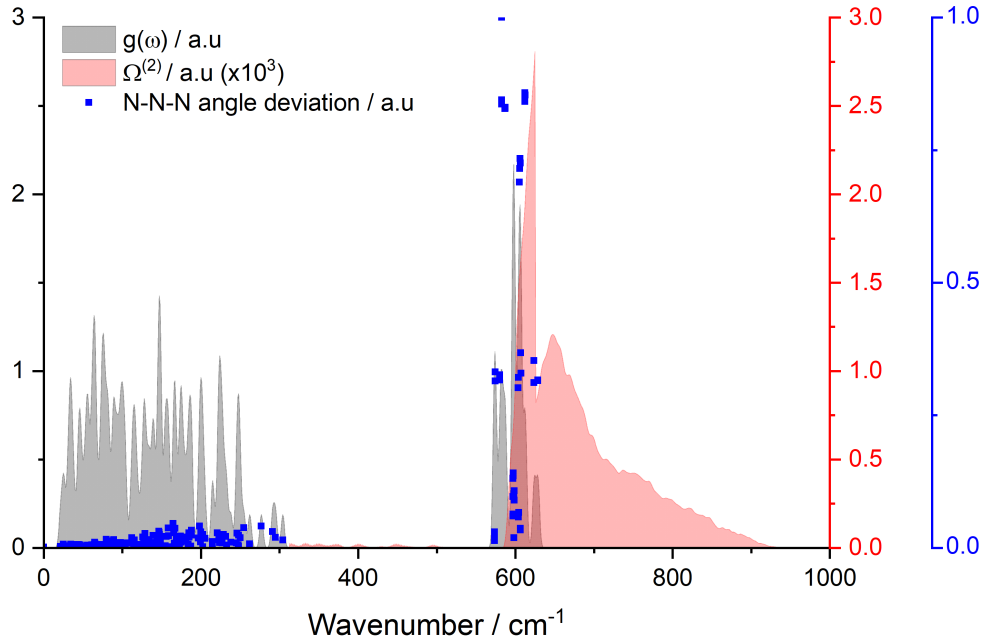


Figure 4.8: Shows the $g(\omega)$ (grey), $\Omega^{(2)}$ (red) with the average change in N-N-N angle per vibrational mode normalised to 1 overlaid (blue).

Figure 4.8 shows unequivocally that the modes of vibration clustered around 600 cm^{-1} are the N-N-N angle bends, while limited activation occurs within the prolonged phonon bath of LA. Therefore, consideration of the shocked phonon bath density alone will unlikely result in large eigenvector distortions of the N-N-N angles needed to promote mechanical initiation. In contrast, the two-phonon scattering model presented by the vibrational up-pumping method does appear to better explain the transfer of energy into the modes that are known to be responsible for initiation. Thus, the latter model is the more appropriate model to use for LA.

While the underlying physical processes favour the up-pumping approach, the outcome for LA is a little disappointing, with the predicted value sitting slightly

lower than expected on the experimental/theory plot shown in Figure 4.7. Two reasons may account for this. First, it could arise due to the current vibrational up pumping procedure not accurately representing the underlying physics of a CP; the model was, after all, developed for molecular EMs. Second, it could be that insufficient sampling of the Brillouin zone, by calculating the Γ -point only vibrations, has generated a $g(\omega)$ that is too sparsely populated, which consequently creates an underpopulated $\Omega^{(2)}$. The previous study on azide-based EMs was undertaken using full Brillouin zone sampling, which lends support to this point.

In order to explore if Γ -point only vibrational sampling is the reason for the apparent underprediction, a comparison of LA with two additional azide-based EMs, namely LiN_3 (classed as a moderately sensitive EM) and NaN_3 (an insensitive EM) was performed next, using previously reported data where full Brillouin zone sampling was undertaken; the previous reports had successfully ranked the impact sensitivity of LiN_3 above NaN_3 , which suggests that the up-pumping model is likely working for such materials [1, 2]. For this analysis, the Γ -point only $g(\omega)$ was extracted from the full Brillouin zone calculations, and then subjected to the same up-pumping procedure as was performed for LA in this work. The outcome is shown in Figure 4.9.

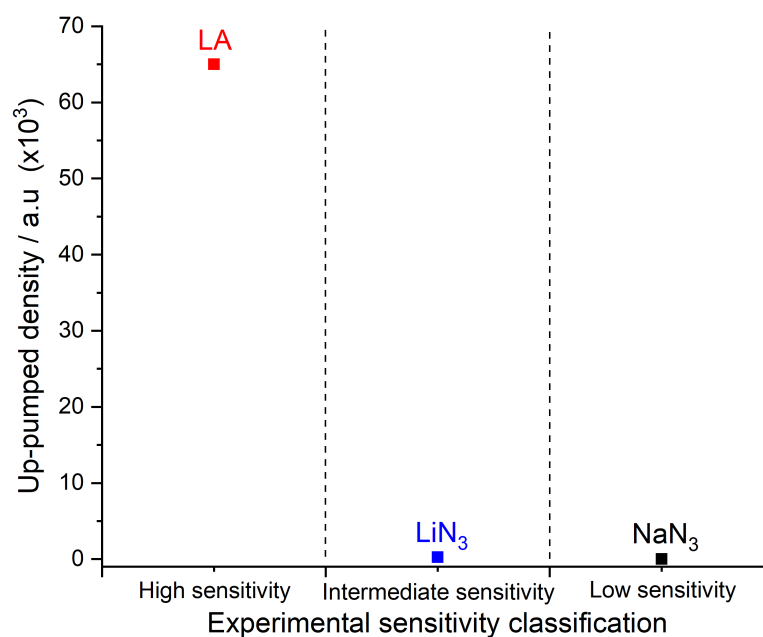


Figure 4.9: Shows up-pumped density of LA, LiN₃ and NaN₃ with each being split into their respective sensitivity classification [4].

As can be seen in Figure 4.9, LA is (correctly) predicted to be significantly more sensitive than both LiN₃ and NaN₃, while LiN₃ is (now incorrectly) predicted to be comparable to NaN₃, and effectively classed as an insensitive EM. This therefore strongly suggests that Γ -point only sampling of the $g(\omega)$ is an under-representation for azides. Increased sampling would bolster the phonon bath region, particularly in the lower energy region with the addition of the acoustic to optical transition branch in the $g(\omega)$. This feature in the $g(\omega)$ is of particular note as very low energy vibrations are able to scatter with a vast number of other modes and have the greatest impact on the $\Omega^{(2)}$. This explains why Γ -point only up-pumped densities are often much smaller than those observed from full Brillouin zone sampling. Activation of the azide bending modes was already achieved through vibrational up-pumping of the Γ -point $g(\omega)$, meaning that an increased $\Omega^{(2)}$ will likely result in an increase in the up-pumped density. Whilst it is true that the up-pumped densities of the molecular EMs would also increase with the same treatment, it stands to reason that the vastly increased magnitude of the $\Omega^{(2)}$ of LA would amplify this effect, result in a vastly increased prediction.

While the Γ -point only sampling of the $g(\omega)$ has likely affected the outcome of the vibrational up-pumping process for LA, it is worth remembering that even with this simplification LA is still predicted to be a very sensitive EM, and is only slightly under predicted with respect to the molecular EMs.

4.3.3 Conclusions

In conclusion, geometry optimisation and Γ -point frequency calculations were undertaken for LA, in order to explore the robustness of the vibrational up-pumping model to predict its impact sensitivity. As a CP structure, this presents a particular challenge for a methodology that was originally developed for molecular EMs.

Prior to vibrational up-pumping excitation, a simpler model, where the phonon bath modes were populated according to the calculated shock temperature, was explored. While this did show a good correlation across a range of EMs, it was ultimately discounted as eigenvector analysis (made possible by development of the local mode tracking code in Chapter 2) showed that the modes attributed to initiation of azide-based EMs (the azide bend) were not activated in this process. In contrast, the up-pumping method did result in energy transfer to the target vibrational modes, and thus is likely a more physically correct model to account for initiation.

The sensitivity of LA by vibrational up-pumping was slightly under predicted when compared to a number of molecular EMs studied by the same method. Through comparison with two additional azide EMs, the likely reason for this was under sampling of the vibrational frequencies by restricting calculation of the $g(\omega)$ to Γ -point only. Despite this under prediction, LA was still correctly predicted to be a primary EM, suggesting that the vibrational up-pumping procedure is appropriate for coordinated EM systems.

4.4 Copper(I)-based Coordination Polymer Energetics

4.4.1 Introduction

Recent years have seen an increased drive towards the development of novel primary EMs to replace LA due to the numerous public health and

environmental concerns surrounding the use of lead [8, 16]. In addition to these concerns, LA has a tendency to slowly decompose in ambient conditions to HN_3 which can readily react with copper (often present in the form of a container or wiring) to produce small quantities of copper azide which is exceptionally sensitive to mechanical initiation, thereby increasing the risk of accidental initiation [17]. As a result of the problems outlined, REACH (Registration, Evaluation, Authorisation and Restriction of Chemicals) have put specific restrictions on the production and use of lead azide within the EU [22].

The market for a novel 'green' replacement is clear and has resulted in a number of coordinated copper(I) based EMs being explored, namely DBX-1, DBX-2 and DBX-3 (see Figure 4.10) [8, 9]. Each of the lead-free structures have desirable properties over LA, such as comparable (if not reduced) sensitivity to impact and preferential energy densities. Despite this, these structures are far from a perfect solution as the production of DBX-1 is complex and its synthesis can result in small amounts of DBX-2 also being produced. This is problematic as DBX-2 is slightly more sensitive to mechanical initiation than DBX-1 (1.9 J vs 4.4 J), meaning that large scale synthesis could inadvertently result in a mixture being more sensitive to impact than expected.

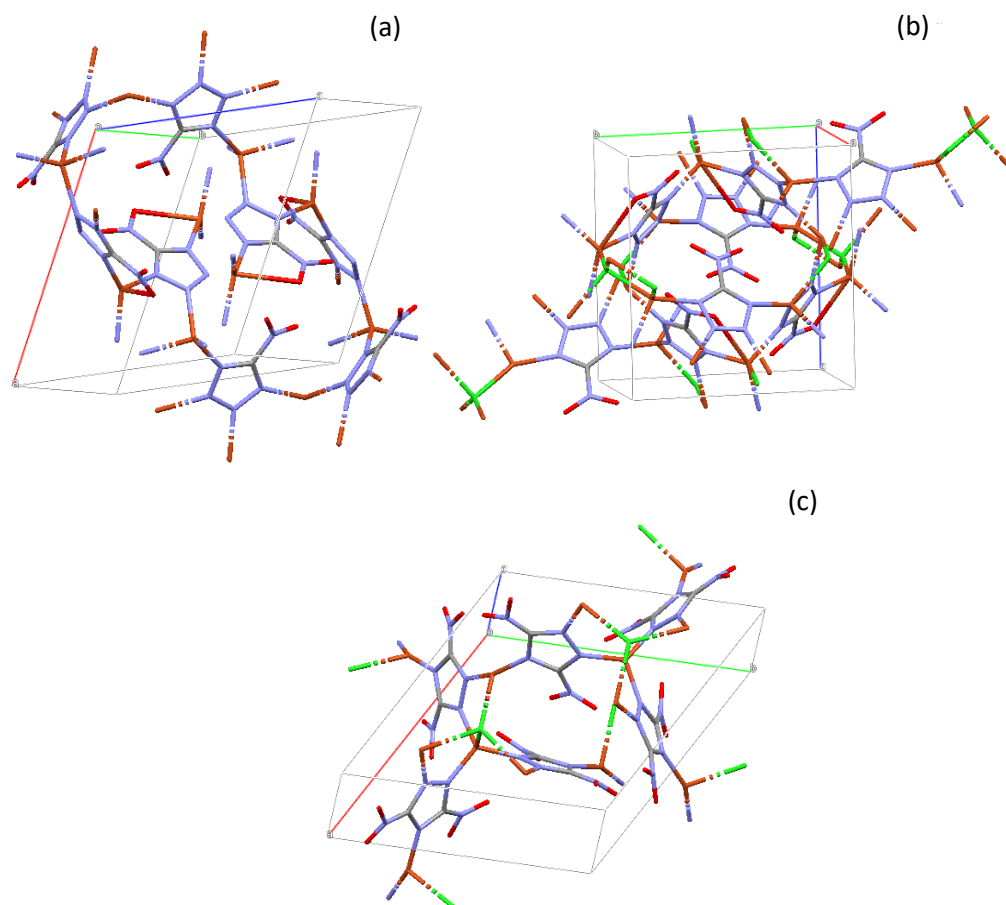


Figure 4.10: Shows the unit cells of DBX-1 (a), DBX-2 (b) and DBX-3 (c) with Cu atoms coloured orange and Cl atoms coloured green. The crystal structure for DBX-3 (unpublished work) was provided by Dr. P. Portius, University of Sheffield [8, 9].

Figure 4.10 shows that each of the structures are CPs, with bridging copper ions present in all structures, and bridging chloride ions in DBX-2 and DBX-3. The organic component of DBX-1 and DBX-2 is 5-nitrotetrazole (Ntet), whereas DBX-3 contains 3,5-dinitro-1,2,4-triazole. Despite the similarities between the structures, and the fact that they are all very sensitive primary EMs, there are subtle differences between the experimental sensitivity values, with DBX-3 (1.6 J) > DBX-2 (1.9 J) > DBX-1 (4.4 J). A computational investigation was undertaken to, firstly, establish whether the vibrational up-pumping model correctly classifies these materials as primary energetics and if so, develop a workflow for the treatment of future EMs. Secondly, to attempt to relate the impact sensitivity values back to structural properties, such that the insight gained may be used to guide further developments of lead-free primary EMs.

4.4.2 Results and Discussion

Geometry optimisation calculations were performed on DBX-1, DBX-2, and DBX-3 to the convergence criteria outlined in Section 4.2. The experimental and calculated unit cell parameters, along with the percentage change in unit cell volume, are shown in Table A2 in Appendix A. The unit cell volume of each of the three materials increase by $\sim 5\%$, which is an acceptable tolerance limit on the optimisation process [20]. Using the optimised geometries, Γ -point phonon calculations were completed for each, resulting in $3N$ real vibrational frequencies in each case, which suggests that the convergence criteria used in the optimisation were sufficiently tight.

In order to determine the location of Ω_{\max} , the CoM deviation in each of the calculated eigenvectors was considered. As was the case for LA, the coordinated nature of the crystal lattices results in plots that are dominated by the CoM change in the acoustic modes, which then skews the remaining points as a result of normalisation process. In order to account for this, the data was renormalised with respect to the largest molecular distortion observed by the eigenvectors in the phonon bath (i.e., the acoustic modes were ignored for this process); this resulted in a clearer distinction between the external phonon and internal ‘molecular’ modes, as shown in Figure 4.11.

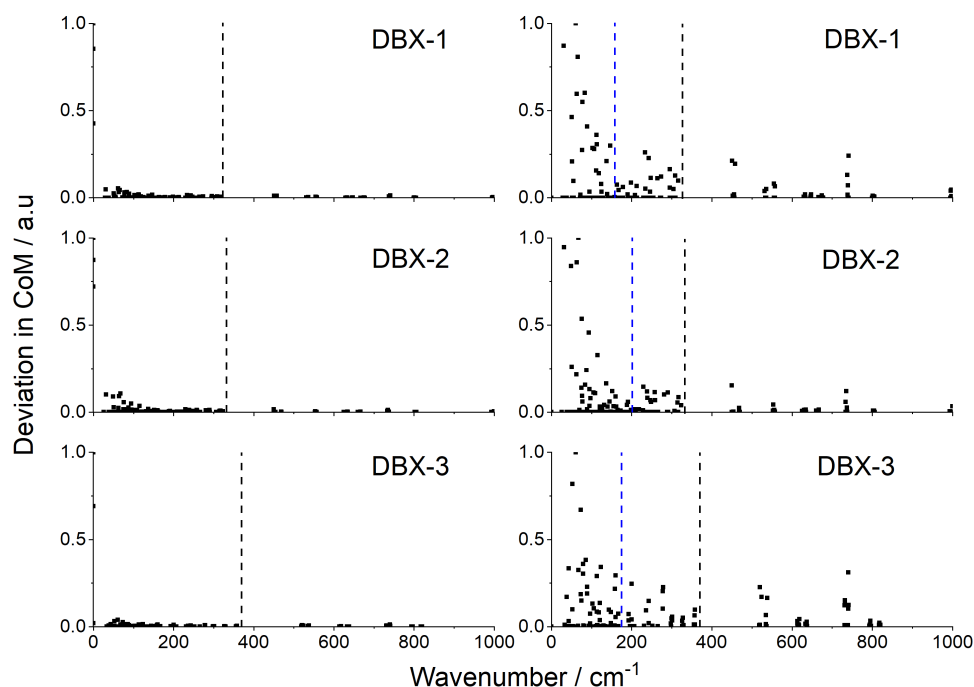


Figure 4.11: Shows the change in CoM per vibrational mode for each of the three structures, normalised to the maximum deviation in CoM (including acoustic modes – left, excluding acoustic modes – right). Blue and black dashed lines denote possible locations of Ω_{\max} .

The left-hand side plots in Figure 4.11 show how the CoM deviations are swamped by the acoustic vibrations, to give virtually no distinction between any of the remaining modes. Re-normalising to the optical modes in the phonon bath (and not plotting the three acoustic modes, which are now off the y-axis scale) gives the plots on the right-hand side. Black dashed lines denote most-probable maximum locations of Ω_{\max} , selected to lie just before large gaps in the vibrational mode distribution, denoting a separation between the external and internal vibrations commonly observed on condensed phase vibrational spectra. However, it should be noted that the drop off in CoM is not particularly uniform; thus the usual rule of looking for a sustained drop off in CoM displacement becomes problematic for these structures. In fact, in all three cases a rough plateau is reached with a drop off in CoM deviation to almost zero for a number of modes much earlier, at roughly 200 cm^{-1} . This is the region typically observed for Ω_{\max} in molecular crystals, which therefore raises legitimate uncertainty over the placement of this important parameter.

In an attempt to shine more light on the location of Ω_{\max} the vibrational density of states for each structure is shown in Figure 4.12. From this it is notable that the $g(\omega)$ plots for the three DBX materials share common features in the phonon bath regions. The black and blue dashed lines give the maximum and minimum locations of Ω_{\max} according to the CoM analysis, which also coincide with gaps (albeit very short in DBX-2) in the vibrational mode distribution; the numerical values are logged in Table 4.2.

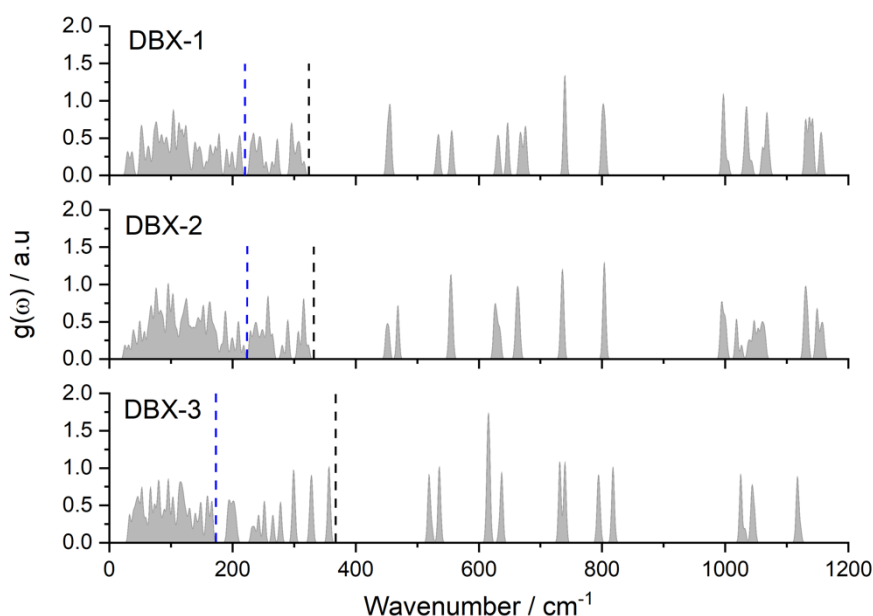


Figure 4.12: Shows the vibrational density of states ($g(\omega)$) of the three EMs discussed in this Chapter with dashed lines corresponding to two possible locations of Ω_{\max} .

Table 4.2: Shows the two possible Ω_{\max} locations for the DBX structures.

| EM | Lower bound of Ω_{\max} / cm^{-1} | Upper bound of Ω_{\max} / cm^{-1} |
|-------|---|---|
| DBX-1 | 221 | 325 |
| DBX-2 | 223 | 333 |
| DBX-3 | 176 | 364 |

The $g(\omega)$ plots and Ω_{\max} locations for DBX-1 and DBX-2 are strikingly similar, which reflects their structural similarities as they share a common organic ligand component (Ntet), while DBX-3 is built from a different (but related)

structure. In an attempt to rationalise the effect that coordination from Cu/Cl atoms has on the $g(\omega)$ of Ntet, a geometry optimisation and Γ -point vibrational frequency was completed on the reported crystal structure of Ntet (also completed to the convergence criteria outlined in Section 4.2) [23]. Note, unfortunately a similar process could not be undertaken for the organic component of DBX-3, as its crystal structure has not yet been reported. The experimental and optimised unit cell parameters are outlined in Table A2 in Appendix A. The percentage increase in unit cell volume is larger (6.98 %) than is normally expected (5 %), but this just is a reflection of the small nature of the unit cell. All vibrational frequencies were calculated to be real numbers, suggesting that the geometry optimisation criteria were sufficiently stringent. The resulting deviation in CoM and $g(\omega)$ spectrum for Ntet are shown in Figure 4.13.

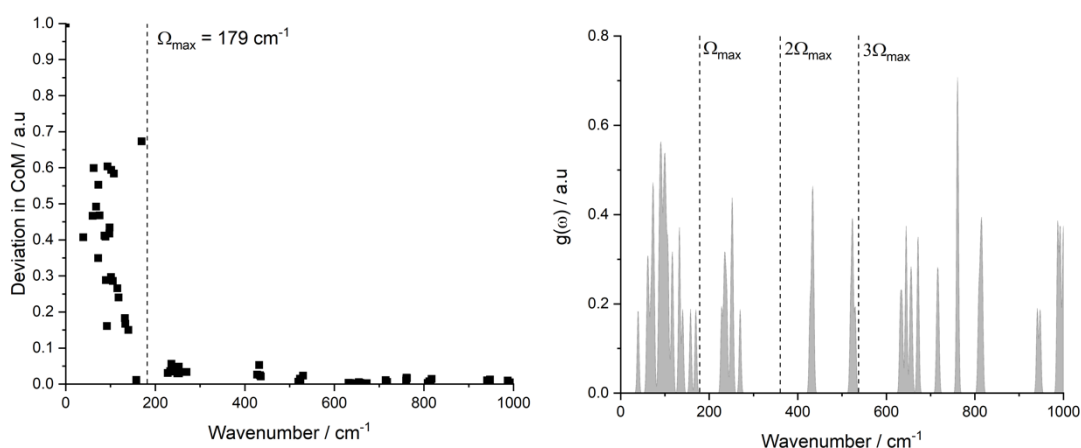


Figure 4.13: Shows the deviation in CoM per mode of Ntet (normalised to unity) with Ω_{\max} marked using a dashed line alongside the $g(\omega)$ with multiples of Ω_{\max} displayed using dashed lines.

As can be seen from Figure 4.13, there is a marked drop of in deviation in CoM for the eigenvectors present in Ntet just below 200 cm^{-1} , which correlates with a large gap in the $g(\omega)$. The resulting value of Ω_{\max} for Ntet is significantly smaller than the values shown in Table 4.2 for DBX-1 and DBX-2. This means that localised molecular motion of Ntet molecules occurs above 179 cm^{-1} ; if this is maintained in DBX-1 and DBX-2 it suggests there will be molecular motion within the phonon bath (i.e., amalgamated modes, denoted as Y), even by the lower estimated values of Ω_{\max} . From a visual analysis of the calculated

eigenvectors for Ntet it is clear that some amalgamated mode character associated with the ring nitro group occurs below Ω_{\max} , an observation typically found for molecular EMs. Visualising the eigenvectors for DBX-1 and DBX-2 shows similar amalgamated mode behaviour occurs towards the top of the lower-limit Ω_{\max} values, suggesting that the lower-limit values are feasible, as they retain the vibrational character typically expected in molecular EMs.

From this analysis the number of amalgamated modes (per molecule, Z , which is replaced by $Z_{\text{eff}} = 1$ for both DBX-1 and DBX-2 reflected by the bracketed value of Z in Table A2 in Appendix A) for the lower-limit Ω_{\max} values is 1 for Ntet, 65 for DBX-1 and 85 for DBX-2, suggesting that the introduction of Cu and Cu/Cl respectively into the systems has greatly increased the number of low energy vibrations. It should be noted that Y is particularly large for DBX-1 and DBX-2 as Z has been replaced with Z_{eff} (1) as a result of the coordination. If Z is taken as the number of molecular (i.e., Ntet) units present in each material (the unbracketed number in Table A2 in Appendix A) the value of Y per Ntet unit is still larger than that of pure Ntet at 2.9 and 5.4 for DBX-1 and DBX-2 respectively. While non integer numbers are not truly possible, it is clear that there is an increase in general amalgamated character with the non-integer numbers being indicative of the material likely acting as a single molecular unit.

In the previous Section (4.3.1) the need for vibrational up-pumping for CPs was called into question, as there is the potential for phonon bath activation alone (via T_{shock}) to excite molecular vibrations (i.e., amalgamated modes) to elicit an energetic response. For LA, it was shown that the target modes (azide bending modes) were inaccessible without vibrational up-pumping, and so in this case this simple model was discounted. However, for DBX-1, DBX-2 and DBX-3 the organic components are significantly more complex, with more correlated ring-based vibrations than the simple azide anion. As a result, the target modes are much more difficult to identify with any degree of certainty. However, it is highly likely that they will involve movement associated with the C–NO₂ bond, as this group has often been highlighted as a trigger bond in the decomposition pathways of EMs. The fact that amalgamated modes are present in the DBX structures suggests that molecular activation of the organic

component of the materials may occur just through phonon bath excitation. Thus, as with LA, both models will be considered, with the additional complication of two possible locations for Ω_{\max} for the three DBX compounds [24, 25, 26].

The next step of the process requires calculation of T_{shock} , which was determined through cumulative heat capacity graphs in the usual way. Plots are shown in Figure 4.14, for both possible Ω_{\max} locations, and the resulting shock temperatures are quoted in Table 4.3 [4].

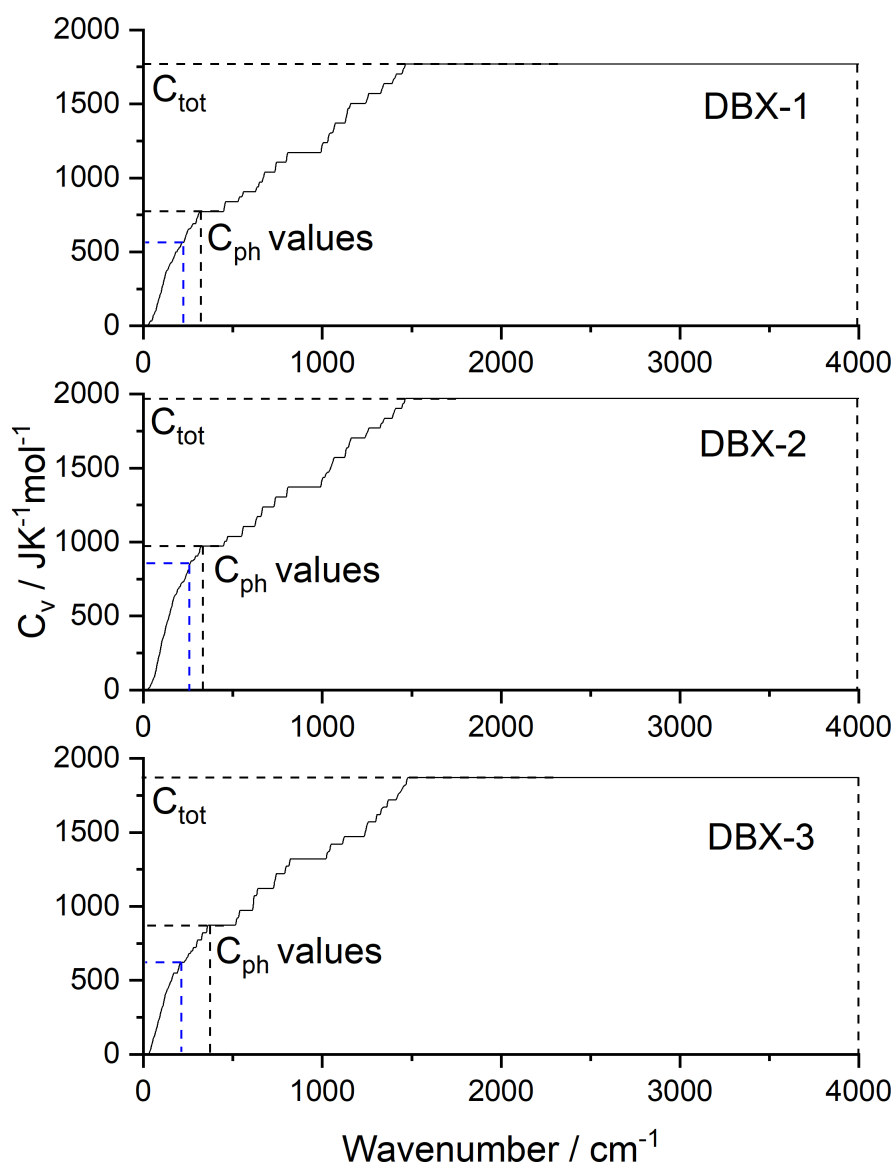
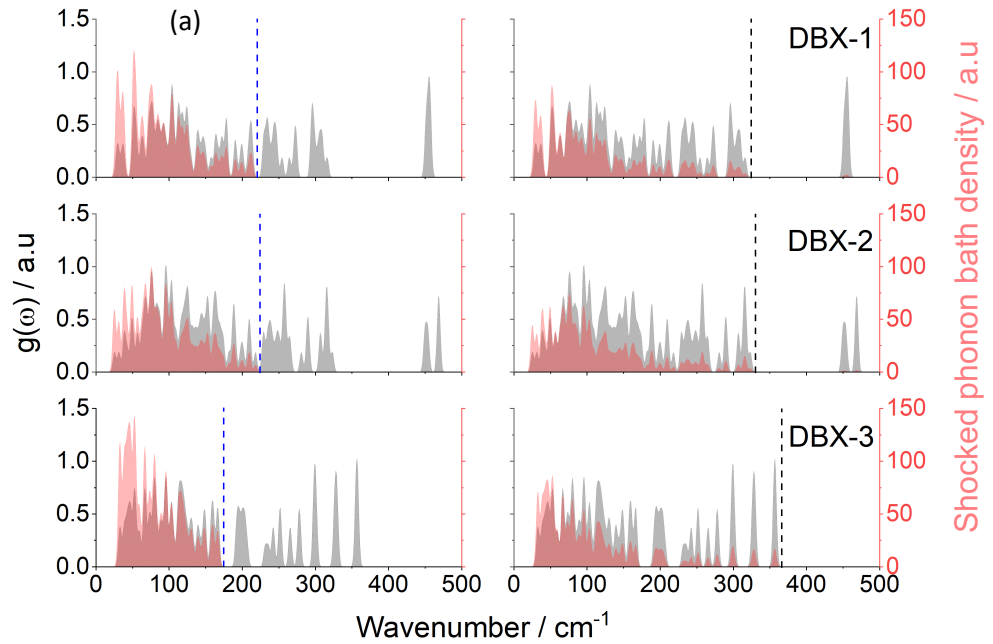


Figure 4.14: Shows the cumulative vibrational heat capacity for DBX-1, DBX-2 and DBX-3 with the locations of both C_{tot} and the two possible positions of C_{ph} marked (blue – lower, black – higher).

Table 4.3: Shows the ratio of $C_{\text{tot}}/C_{\text{ph}}$ alongside the associated T_{shock} values for each potential Ω_{max} value of each DBX material.

| EM | Ω_{max} | $C_{\text{tot}}/C_{\text{ph}}$ | $T_{\text{shock}} / \text{K}$ |
|-------|-----------------------|--------------------------------|-------------------------------|
| DBX-1 | 221 | 3.13 | 2052 |
| | 325 | 2.29 | 1501 |
| DBX-2 | 223 | 2.69 | 1764 |
| | 333 | 2.03 | 1331 |
| DBX-3 | 176 | 3.41 | 2236 |
| | 364 | 2.14 | 1403 |

The values of T_{shock} shown in Table 4.3 are lower than the values typically obtained for molecular EMs ($\sim 2\text{-}3000 \text{ K}$), which is due to the increased phonon bath contributions in these CP structures. With the values of T_{shock} calculated, the shocked phonon bath density can now be calculated (through the use of Equation 4.1), shown in Figure 4.15(a) and the shocked phonon bath density compared to the experimental impact sensitivity values; this is shown in Figure 4.15(b) alongside the molecular EMs (data previously quoted in Table 4.1). The normalisation scheme is expressed ‘per phonon bath mode, per molecule’, with the number of molecules in the unit cell once again being redefined by the parameter $Z_{\text{eff}} = 1$ due to the coordinated nature of each DBX structure.



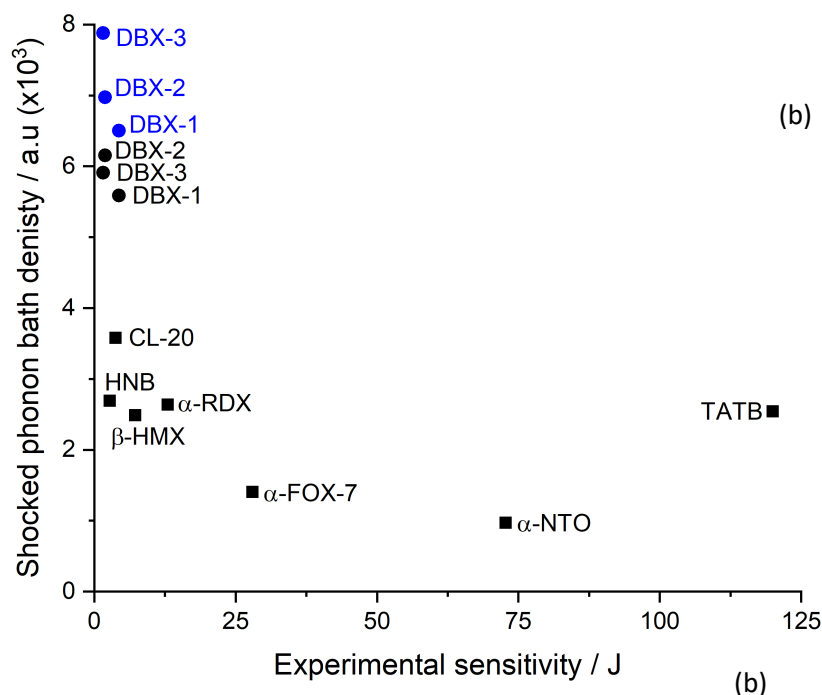


Figure 4.15: Shows the shocked phonon bath overlaid on the underlying $g(\omega)$ (a) and the shocked phonon bath density per molecule (from Equation 4.1) vs. experimental sensitivity for each of the DBX structures (circles) considered in this Section (b) alongside molecular EMs (squares). Blue points represent lower Ω_{\max} values and black represent larger Ω_{\max} values [4, 5, 9].

As can be seen from Figure 4.15, the shocked phonon bath densities of the three DBX materials are significantly larger than that of the well-studied molecular EMs, regardless of the location of Ω_{\max} . The black values represent the upper values, and hence have a greater probability of capturing more amalgamated mode behaviour, and therefore EM activation via target mode excitation. This data suggests that simple phonon bath heating correctly classifies these compounds as highly impact sensitive EMs, provided that C–NO₂ activation occurs. This will be probed further later in the chapter.

Turning now to the up-pumping model, the complete set of data parameters required for the three DBX compounds are listed in Table 4.4.

Table 4.4: Shows the input parameters for the vibrational up pumping procedure alongside the outputs for each of the DBX structures. Z_{eff} denotes the effective number of molecular units in each unit cell, Y is the number of amalgamated modes.

| EM | Ω_{max} | Z_{eff} | $Z(6+Y)$ | Y | $T_{\text{shock}} / \text{K}$ | Experimental IS / J | Shocked phonon bath density / a.u | Up-pumped density / a.u |
|-------|-----------------------|------------------|----------|-----|-------------------------------|---------------------|-----------------------------------|-------------------------|
| DBX-1 | 221 | 1 | 71 | 65 | 2052 | 4.4 | 6502 | 150215 |
| | 325 | | 96 | 90 | 1501 | | 5587 | 81283 |
| DBX-2 | 223 | 1 | 91 | 85 | 1764 | 1.9 | 6971 | 228267 |
| | 333 | | 120 | 114 | 1331 | | 6152 | 84068 |
| DBX-3 | 176 | 1 | 69 | 63 | 2236 | 1.6 | 7881 | 372255 |
| | 364 | | 102 | 96 | 1403 | | 5911 | 49249 |

Using the data in Table 4.4, the up-pumped density was calculated. The $g(\omega)$ spectra for each of the DBX structures along with the overlaid $\Omega^{(2)}$ for both possible values of Ω_{max} are shown in Figure 4.16 with both potential sets of Ω_{max} shown (black labels use the upper value, blue labels use the lower value).

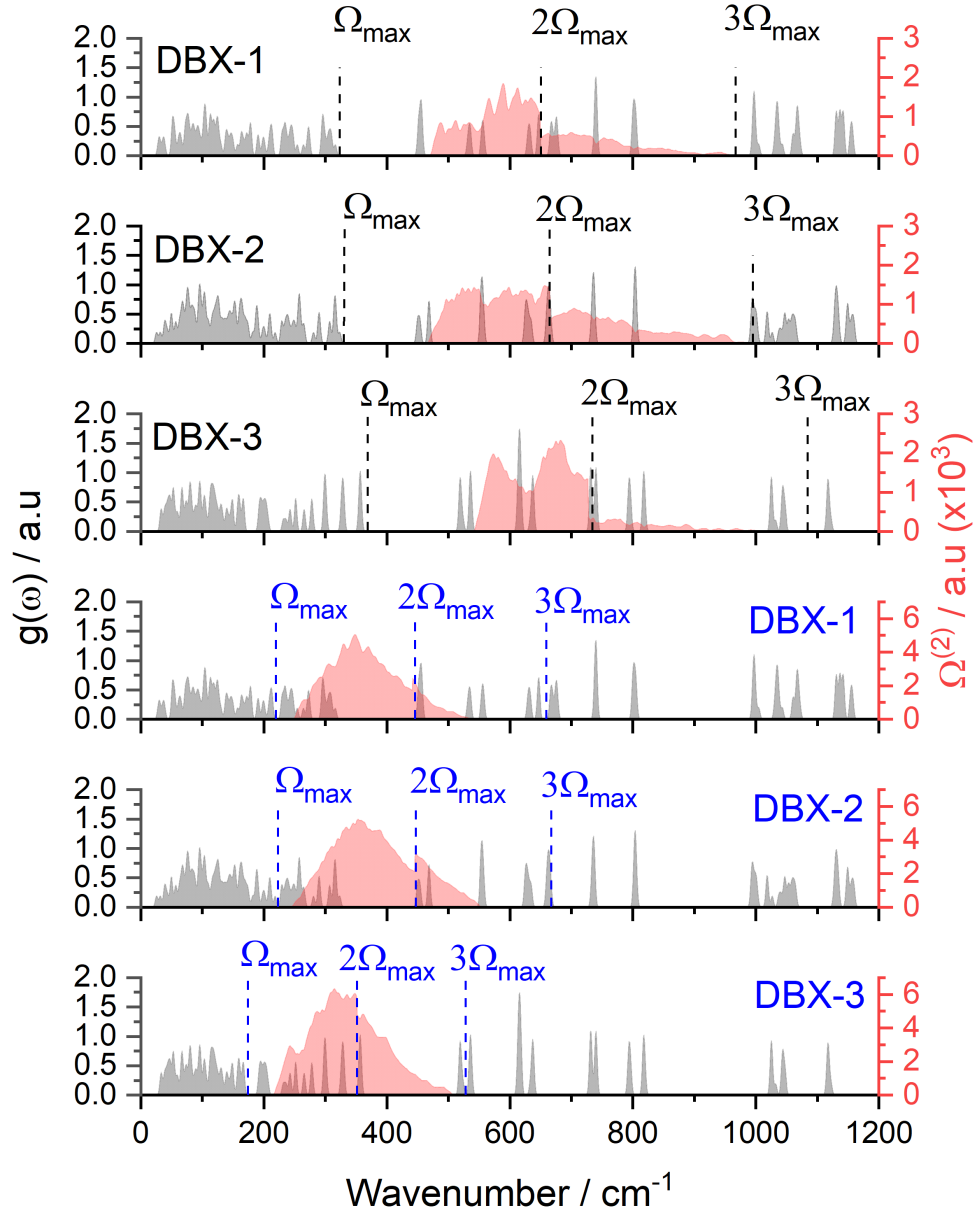


Figure 4.16: Shows the $g(\omega)$ and $\Omega^{(2)}$ of each DBX structure when the both potential values of Ω_{\max} is used (black signifying the larger, blue the lower).

As shown in Figure 4.16, the magnitude of the $\Omega^{(2)}$ for each EM is either comparable to or larger than that shown previously for LA (Figure 4.7). This indicates a more efficient channelling of energy (i.e. resonance states) into the higher energy vibrations, with an increased $\Omega^{(2)}$ intensity when the lower bound of Ω_{\max} is used as a result of phonon bath region modes being able to scatter with a more densely packed doorway region (1-2 Ω_{\max}). The resulting

integrations between the $\Omega^{(2)}$ and $g(\omega)$, for both values of Ω_{\max} gives the outcome shown in Figure 4.17.

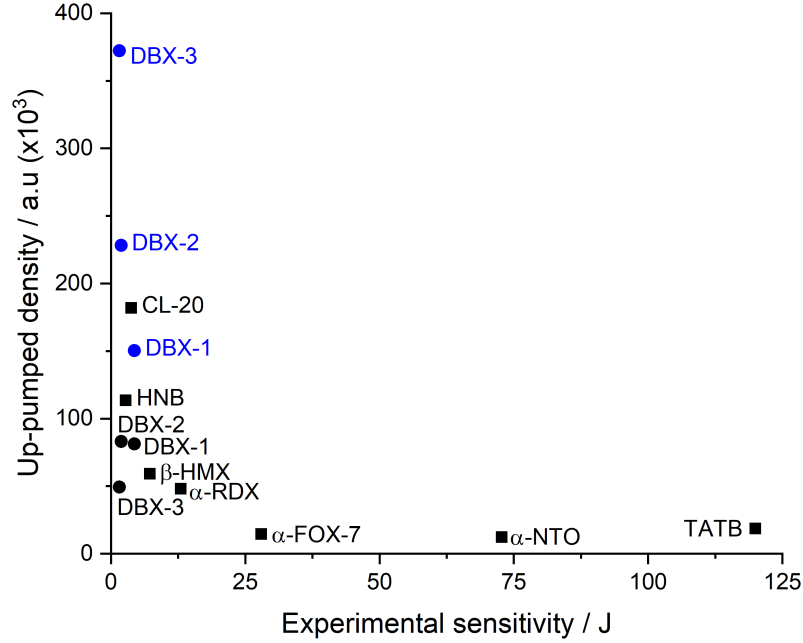


Figure 4.17: Shows the up-pumped density of a number of standard materials (taken from previous work, shown using square points) along with two values for each of the DBX materials with black points representing the upper bound of Ω_{\max} and blue the lower (shown using circular points) [4, 5, 9].

Figure 4.17 shows that the values of the up-pumped densities vary dramatically depending on the value of Ω_{\max} , with the lower value resulting in significantly higher predicted sensitivities (blue points) than the use of the larger value of Ω_{\max} (black points). The reason for this has already been noted in the discussion for Figure 4.16: a narrower phonon bath results in phonon scattering pathways that capture an increased density of doorway modes, which in turn both captures and boosts the $\Omega^{(2)}$ signal.

It is clear that the uncertainty around the placement of Ω_{\max} complicates the story for the DBX EMs. When the lower bound values of Ω_{\max} are taken the predicted sensitivities show clear primary EM behaviour, with sensitivities ranked in excellent agreement with experiment (DBX-3 > DBX-2 > DBX-1). This can largely be tracked to differences in the number of modes in the

doorway regions ($1-2 \Omega_{\max}$); modes here are involved in both scattering and capturing the $\Omega^{(2)}$ (see Table 4.5).

Table 4.5: Shows the two possible Ω_{\max} locations for each of the DBX materials alongside the experimental sensitivity as well as the associated number of doorway modes per molecular unit alongside well-studied molecular EMs [4].

| EM | Ω_{\max} | Experimental sensitivity / J | Number of doorway modes per molecular unit |
|-----------------|-----------------|------------------------------|--|
| DBX-1 | 221 | 4.4 | 25 |
| | 325 | | 24 |
| DBX-2 | 223 | 1.9 | 29 |
| | 333 | | 32 |
| DBX-3 | 176 | 1.6 | 36 |
| | 364 | | 30 |
| HNB | 155 | 2.75 | 12 |
| CL-20 | 222 | 3.75 | 12 |
| β -HMX | 200 | 7.25 | 7 |
| α -RDX | 164 | 13 | 6 |
| α -FOX-7 | 180 | 28 | 3 |
| α -NTO | 216 | 72.75 | 3 |
| TATB | 151 | 122 | 3 |

Table 4.5 shows that the number of doorway modes for each of the DBX structures (derived using Z_{eff} as the number of molecules) are significantly larger than for the molecular EMs. Interestingly, the number of doorway modes follow the trend in reported experimental sensitivities (DBX-3 > DBX-2 > DBX-1) when the smaller value of Ω_{\max} is used, suggesting a correlation between the doorway region vibrations and impact sensitivities, an observation that was noted in the previous Chapter. Using this value of Ω_{\max} also results in the same ordering of predicted sensitivities. However, when the larger Ω_{\max} value is taken the number of modes in the doorway region of DBX-2 exceeds that of DBX-3 (by 2), but it should be noted that both are larger than the number of modes in molecular materials and that the up-pumped density values follow a weaker trend in this regime also.

It is clear from the data presented in this Section that both methods, the shocked phonon bath density and vibrational up-pumping, generate predicted sensitivities for CP EMs with reasonable predictive accuracy. The primary consideration in the decision between the two methods should be the probability that target frequencies are activated, but this discussion is further complicated for the DBX compounds as the nature of these vibrational modes

are unknown. However, given that it is generally accepted that probable target modes for more complicated EMs are rooted in the breakage of weak trigger bonds in the molecule (most likely C–NO₂ for these compounds), the change in this bond length across the calculated eigenvectors was pursued next, and shown in Figure 4.18 [24, 25, 26]. Note values are normalised (to unity) with respect to the most significant C–N bond length variation. Values are shown for Ntet, DBX-1 and DBX-2 only (i.e., compounds constructed from the same molecular unit).

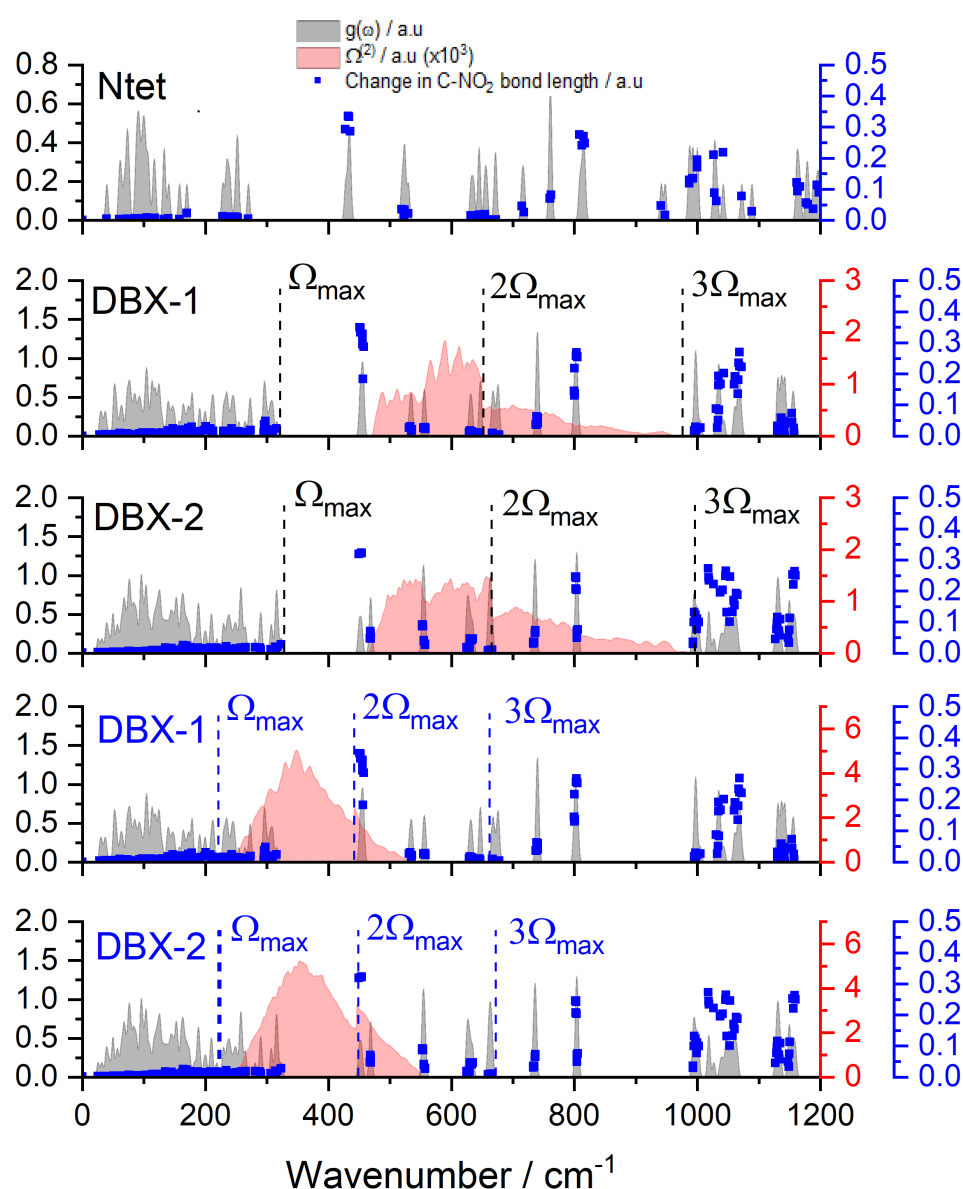


Figure 4.18: Shows the $g(\omega)$ (grey) with the average change in C–NO₂ bond length per vibrational mode overlaid (blue) for Ntet, DBX-1 and DBX-2. The $\Omega^{(2)}$ (red) is shown for both DBX-1 and DBX-2 for both large (black label) and small (blue label) Ω_{\max} locations.

Figure 4.18 shows clearly that the modes that exhibit the largest C–N bond distortion in the regions shown for Ntet, DBX-1 and DBX-2 occur at $\sim 450\text{ cm}^{-1}$ and $\sim 800\text{ cm}^{-1}$. Minimal excitation appears to occur in the phonon bath region, which in an argument analogous to that put forward for LA, suggests that phonon bath heating alone is not sufficient to elicit mechanical initiation, despite the presence of amalgamated modes. Thus, it would appear that, like LA, vibrational up-pumping is needed to activate the likely target vibrations present in DBX-1 and DBX-2. However, the question still remains as to whether the smaller or larger Ω_{max} value is the more appropriate for $\Omega^{(2)}$ generation.

The issue of Ω_{max} location can be further pursued through analysis Figure 4.18: when the larger value of Ω_{max} is taken, the resulting $\Omega^{(2)}$ trace in fact misses the vibrations at $\sim 450\text{ cm}^{-1}$, with the tail of trace capturing the higher vibrations at $\sim 800\text{ cm}^{-1}$. In contrast, the smaller value of Ω_{max} generates a $\Omega^{(2)}$ trace that does more comprehensively capture the $\sim 450\text{ cm}^{-1}$ vibrations. Thus, if these are the target modes for DBX-1 and DBX-2 this suggests that the lower value of Ω_{max} is the most appropriate choice.

While this argument provides a plausible account of the up-pumping windows for DBX-1 and DBX-2, it does not extend to DBX-3 as it is based on a different organic backbone. The analogous stretching modes for DBX-3 are shown in relation to the two possible $\Omega^{(2)}$ traces in Figure 4.19.

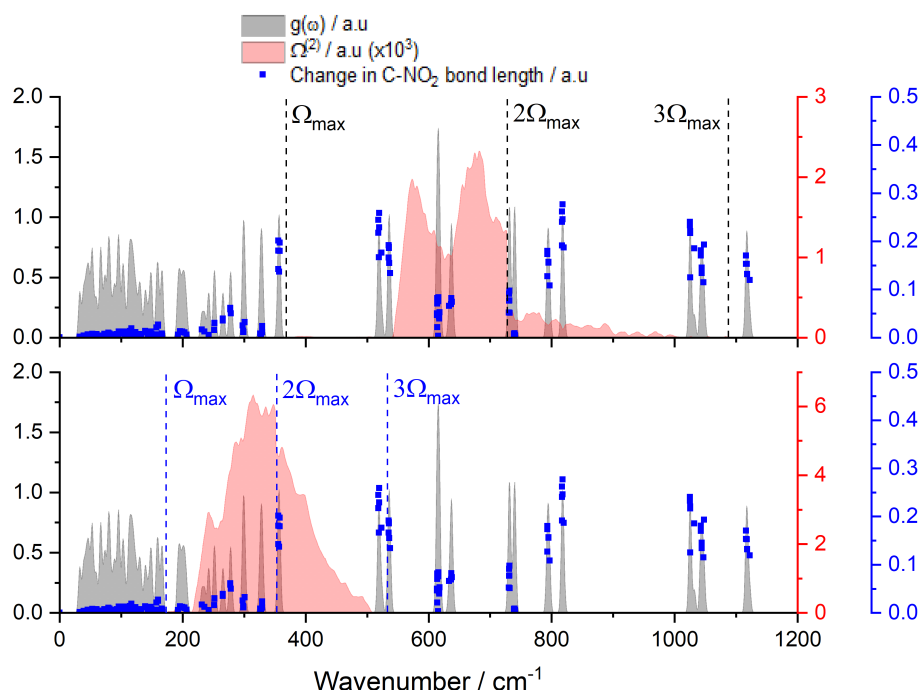


Figure 4.19: Shows the $g(\omega)$ (grey), $\Omega^{(2)}$ (red) and the average change in C-NO₂ bond length per vibrational mode overlaid (blue) for large (black label) and small (blue label) Ω_{\max} locations of DBX-3.

As can be seen from Figure 4.19, there is reasonable activation of C-NO₂ stretching motion in the modes at ~ 350 cm⁻¹, ~ 520 cm⁻¹ and ~ 800 cm⁻¹ which suggests that unlike in the case of DBX-1 and DBX-2 either potential value of Ω_{\max} has some merit. If either value is considered, vibrational up-pumping appears to miss the activation of the mode at ~ 520 cm⁻¹, with the larger value only resulting in slight activation of the modes at ~ 800 cm⁻¹. The activation of C-NO₂ is present within the phonon bath when the larger Ω_{\max} is taken, rendering consideration of the shocked phonon bath also an appropriate choice. Consideration of the lower value of Ω_{\max} results in the excitation of the same modes (~ 350 cm⁻¹) this time through vibrational up-pumping. This mirrors the effect seen with DBX-1 and DBX-2 as this is the first instance of weak bond activation and is present at roughly $2\Omega_{\max}$. When the structural similarity between the three CPs is taken into account it seems the most plausible that the lower value of Ω_{\max} is the most appropriate for DBX-3.

It should be noted that a more complicated trigger mechanism involving the C-NO₂ trigger unit (e.g. angle bend, torsion activation) is at work and the

location of the trigger bond explored in this Chapter was primarily used in order to give confidence in our definition of the phonon bath of such materials. At current, all modes within the up-pumping window are considered in the integration which is a significant simplification as these modes will inevitably contain a number of trigger and non-trigger motions. This simplification is a problem that must be addressed in future work.

Additionally, the issue regarding under-sampling the phonon bath, through the pursuit of only Γ -point phonons should be born in mind. As was alluded to in Section 4.3.3, under-sampling of the phonon bath may lead to an underprediction of the impact sensitivity and is an avenue of interest that should also be investigated in the future.

4.4.3 Conclusions

This work aimed to further explore the applicability of the vibrational up-pumping procedure when applied to predicting the impact sensitivity of coordinated primary energetics. The two conflicting proposals brought forward in the previous section questioned whether up-pumping of vibrational energy is required (or not), as sufficient molecular distortion may exist within the phonon bath. It has been shown that determining the location of Ω_{\max} is difficult by virtue of the coordinated nature of the materials, resulting in two potential locations being investigated (determined using the CoM script outlined in Chapter 2 – based on both the inclusion and exclusion of the acoustic vibrations to the normalisation process). Two of the structures considered in this work, DBX-1 and DBX-2 were compared to their organic parent compound (Ntet) suggesting the lower bound of Ω_{\max} was more appropriate. However, DBX-3 was unable to be compared in this way due to a lack of a molecular crystal structure, and as such the low value of Ω_{\max} was assumed to be located at the first meaningful break in the $g(\omega)$. This work has shown that both methods of consideration yield predictions in line with experimental findings, in that they are all predicted to be sensitivity primary energetics. Through consideration of the probable target modes (C-NO₂ stretching – tracked using the script outlined in Chapter 2) vibrational up-pumping based on the lower bound of Ω_{\max} was found to be the most appropriate approach for each DBX

material as this was the only way in which such modes could be activated through vibrational up-pumping. As such a workflow for the treatment of such EMs using the vibrational up-pumping methodology has been outlined.

4.5 A Copper Based Coordinated Energetic

4.5.1 Introduction

The previous Sections (4.3 and 4.4) have shown that the vibrational up-pumping procedure is a valid approach for CP EMs as well molecular EMs. One benefit of applying a common model to both classes of compounds is that the outputs can be compared on a common scale, allowing the predicted IS value for compounds to be ranked relative to one another. A final structure considered in this Chapter is that of Cu(ADNP), which provides a further interesting test case for exploration because this crystal structure contains metal-based coordination sites, in common with the DBX structures, but they pack as molecular-type entities, rather than extended coordination polymers (see Figure 4.20).

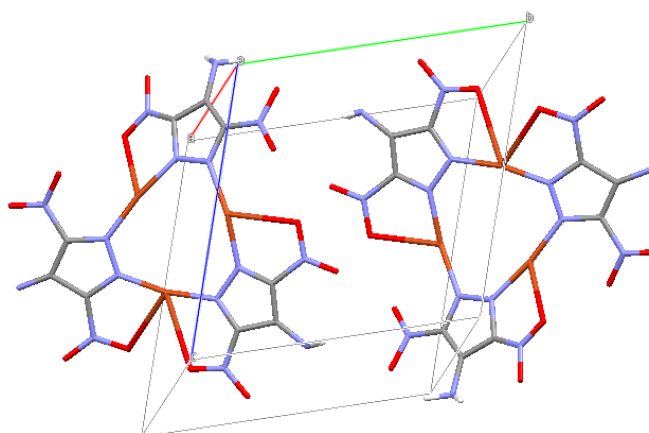


Figure 4.20: Shows the unit cell of Cu(ADNP) with Cu atoms show in orange, with missing and misplaced H atoms clearly present. The crystal structure (unpublished work) was provided by Dr. P. Portius, University of Sheffield [9].

Figure 4.20 shows that the repeating molecular unit consists of plate-like substructures containing three of the organic (ADNP) components connected by Cu atoms, with the unit cell containing two separate molecules. The hydrogen positions of Cu(ADNP) could not be determined through X-ray diffraction. For this reason, the computational modelling investigation began

with *ab initio* random structure searching (AIRSS) to locate the lowest energy hydrogen atom positions, prior to impact sensitivity prediction.

4.5.2 Results and Discussion

AIRSS V.0.9 simulations, run as a wrapper script around CASTEP, were performed to locate the hydrogen atoms in the crystal structure of Cu(ADNP) [27]. Initially, the hydrogen atoms that were poorly defined in the X-Ray crystal structure (twelve hydrogen atoms in total, reflecting the six nitrogen atoms of the -NH₂ groups) were removed. Two hydrogen atoms were then placed randomly on a sphere located 1 – 1.2 Å (i.e., the likely length range of N–H bond lengths) around the bare nitrogen atoms. In addition, the hydrogen atoms were constrained to lie at least 0.9 Å apart, in order to prevent the erroneous formation of molecular hydrogen within the crystal structure. The resulting structure was then subject to a geometry optimisation (atom only minimisation) with loose convergent criteria (CASTEP default for 30 cycles of optimisation), in order to focus on high throughput rather than calculation accuracy. This process was repeated 15 times for Cu(ADNP), resulting in 15 output structures which when overlaid produce very similar –NH₂ geometries (i.e. planar and exhibiting hydrogen bonding interactions with neighbouring –NO₂ groups). An overlay of each of the 15 Cu(ADNP) structures is shown in Figure 4.21 alongside a plot showing the relative energy of each structure. The energy range of structures obtained is extremely small (covering just 0.5 kJmol⁻¹), with the variation likely representing numerical variation in meeting the loose convergence criteria. The results obtained can allow the hydrogen atom positions to be assigned with confidence.

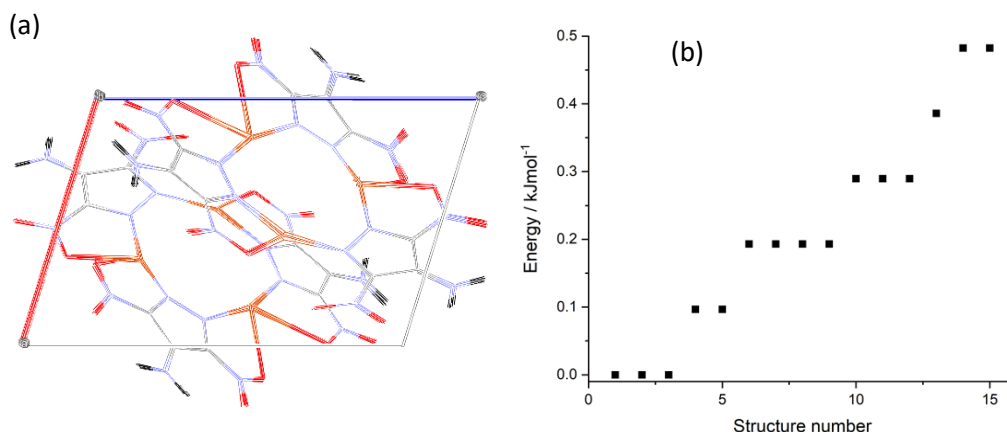


Figure 4.21: Shows the 15 optimised unit cells of Cu(ADNP) overlaid with the newly located H atoms shown in black (a). The energies of the structures relative to one another are shown in (b) with the lowest energy structure being set to 0 kJmol⁻¹.

With the crystal structure now completed, full geometry optimisation (atomic positions and unit cell vectors, using the stringent convergent criteria outlined in Section 4.2) was undertaken, with the favourable outcome recorded in Table A2 in Appendix A [20]. Following geometry optimisation, a Γ -point vibrational frequency calculation was performed which resulted in 3N real vibrational frequencies, suggesting that both the structure determined from the AIRSS calculation was reasonable and that the subsequent optimisation was a success.

Determining the value of Ω_{\max} for Cu(ADNP) was more straightforward than for LA and the DBX structures, as this crystal structure comprises two separate pseudo-molecular units, and the CoM of each can be tracked separately. This will allow the switch-over in eigenvector behaviour between external (large CoM distortion) and internal (low CoM distortion) to be more easily recognised. The results are shown in Figure 4.22, with the probable location of Ω_{\max} marked. The degree of distortion is normalised with respect to the acoustic modes.

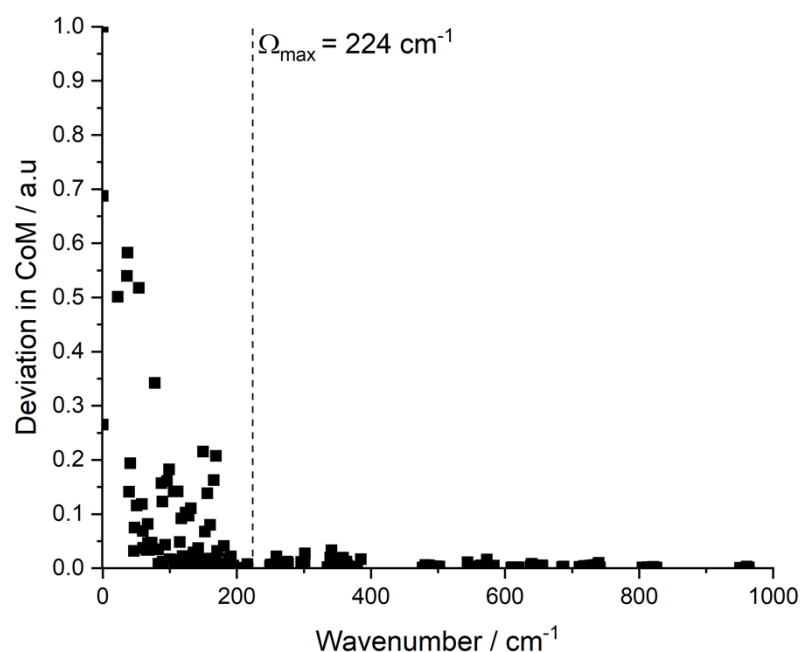


Figure 4.22: Shows the average deviation in CoM (normalised to unity) for the molecular units in the crystal structure of Cu(ADNP) with respect to wavenumber. The probable location of Ω_{\max} is denoted using a dashed line.

Figure 4.22 shows a significant drop off in the deviation of the CoM of the molecular units as the vibrational frequencies progress beyond 200 cm^{-1} . The numerical value of Ω_{\max} was then determined from the corresponding $g(\omega)$, plotted with a Gaussian smearing function of 5 cm^{-1} ; this gave a value of 224 cm^{-1} . The $g(\omega)$ spectrum of Cu(ADNP), with multiples of Ω_{\max} marked with dashed lines, is shown in Figure 4.23.

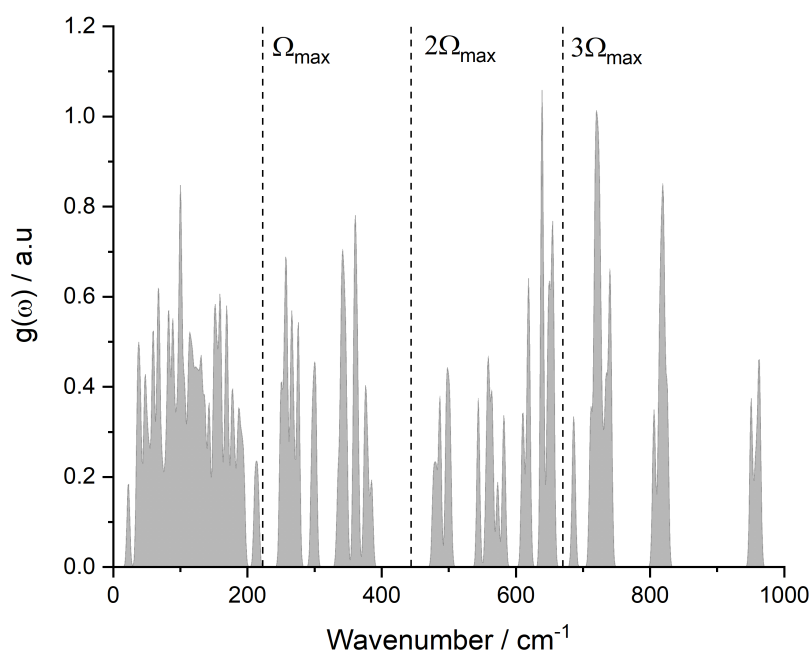


Figure 4.23: Shows the vibrational $g(\omega)$ spectrum of Cu(ADNP) with multiples of Ω_{\max} marked using dashed lines.

As can be seen from a combination of Figure 4.22 and 4.23 the location of Ω_{\max} also coincides with a notable gap in the $g(\omega)$ spectrum. In Section 4.4 the calculated $g(\omega)$ spectra for DBX-1 and DBX-2 were compared to the $g(\omega)$ of the crystal structure of the organic ligand from which these structures were derived from, in order to provide further insight to help locate Ω_{\max} for these complicated structures. In this case there is only one clear value of Ω_{\max} , allowing for a unique chance to study the effect of forming a Cu-based salt on the vibrational character and thus the impact sensitivity of the organic conformer, ADNP (formally, 4-amino-3,5-dinitro-1H-pyrazole) the crystal structure of which is shown in Figure 4.24.

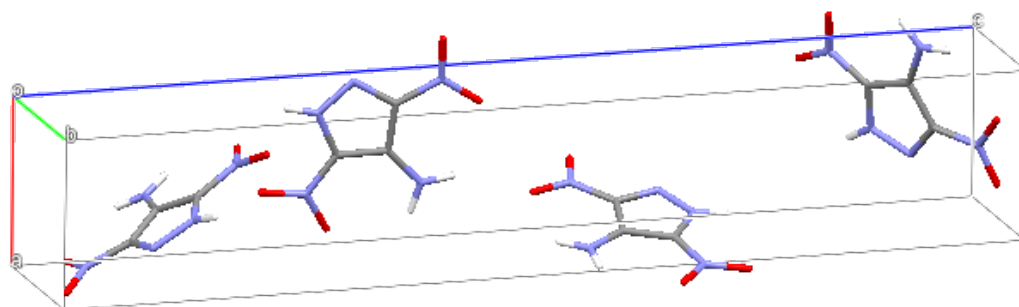


Figure 4.24: Shows the unit cell of the crystal structure of ADNP taken from Reference [28].

Geometry optimisation and zone-centre vibrational frequency calculations were therefore completed for ADNP, according to the procedure in Section 4.2, to allow comparison to Cu(ADNP). The experimental and calculated cell parameters for ADNP are shown in Table A2 in Appendix A. The small change in unit cell volume, combined with the return of 3N real vibrational frequencies all gave credence to a reliable simulation result having been obtained. Analysis of the change in CoM per vibrational mode, alongside the resulting vibrational $g(\omega)$ for ADNP is shown below in Figure 4.25.

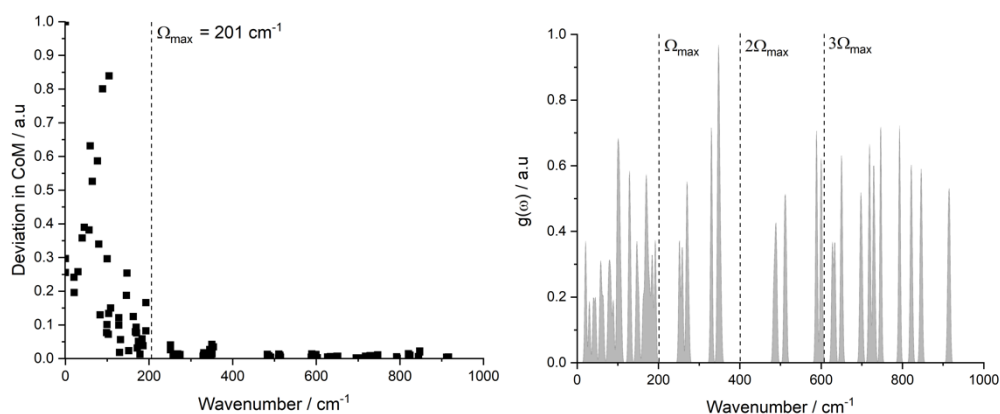


Figure 4.25: Shows the deviation in CoM (normalised to unity) per vibrational mode of ADNP (left) with the Ω_{\max} location shown using a dashed line and the vibrational $g(\omega)$ spectrum (right) with multiples of Ω_{\max} marked.

As can be seen from Figure 4.25, the value of Ω_{\max} of the organic component of Cu(ADNP) is very similar to that of the metal-containing EM. The $g(\omega)$ of Cu(ADNP) and ADNP (shown in a stack plot in Figure 4.26) share some similarities beyond Ω_{\max} , which is to be expected as they share an organic

component. There are some notable differences, however, with the copper salt having peaks at ca. 210 cm^{-1} and 300 cm^{-1} that are absent in the $g(\omega)$ for ADNP. Additionally, the phonon bath of the copper salt is more continuous, which can be explained by the presence of more vibrations (72 as opposed to 40), which will be dominated by a contribution from the heavy copper ions. As with DBX-1 and DBX-2, the target modes are assumed to be those that induce stretching of the weak C–NO₂ bonds. Tracking the average change in this bond length across the low energy modes for both compounds is shown below in Figure 4.26.

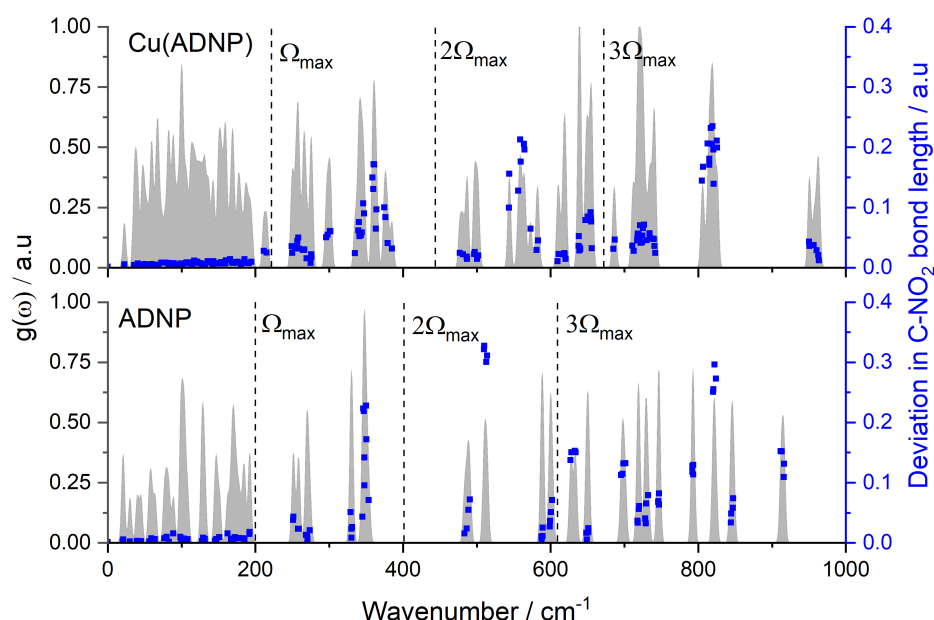


Figure 4.26: Shows the $g(\omega)$ (grey) with the average change in C–NO₂ bond length per vibrational mode overlaid (blue) for both Cu(ADNP) and ADNP with multiples of Ω_{max} denoted using dashed lines for each.

Figure 4.26 shows that activation of the assumed target modes can only be achieved through up-pumping of energy, as significant C–NO₂ bond deviation only occurs in the modes of vibration expressed beyond 200 cm^{-1} (i.e. outside the phonon bath). This is the same argument as used for LA and the DBX structures, confirming that consideration of the shocked phonon bath density is not necessary and vibrational up-pumping should instead be explored.

The shock temperature, T_{shock} , an important parameter needed for the up-pumping process, was determined in the usual way from the cumulative contributions to the heat capacity from the vibrational modes (see Figure 4.27); the ratios of $C_{\text{tot}}/C_{\text{ph}}$ (3.66 and 4.78) corresponding to $T_{\text{shock}} = 2400$ K and 3134 K for Cu(ADNP) and ADNP respectively (assuming $C_{\text{tot}}/C_{\text{ph}} = 5.22$ equates to $T_{\text{shock}} = 3423$ K). The resulting vibrational up-pumping parameters are summarised in Table 4.6 [4].

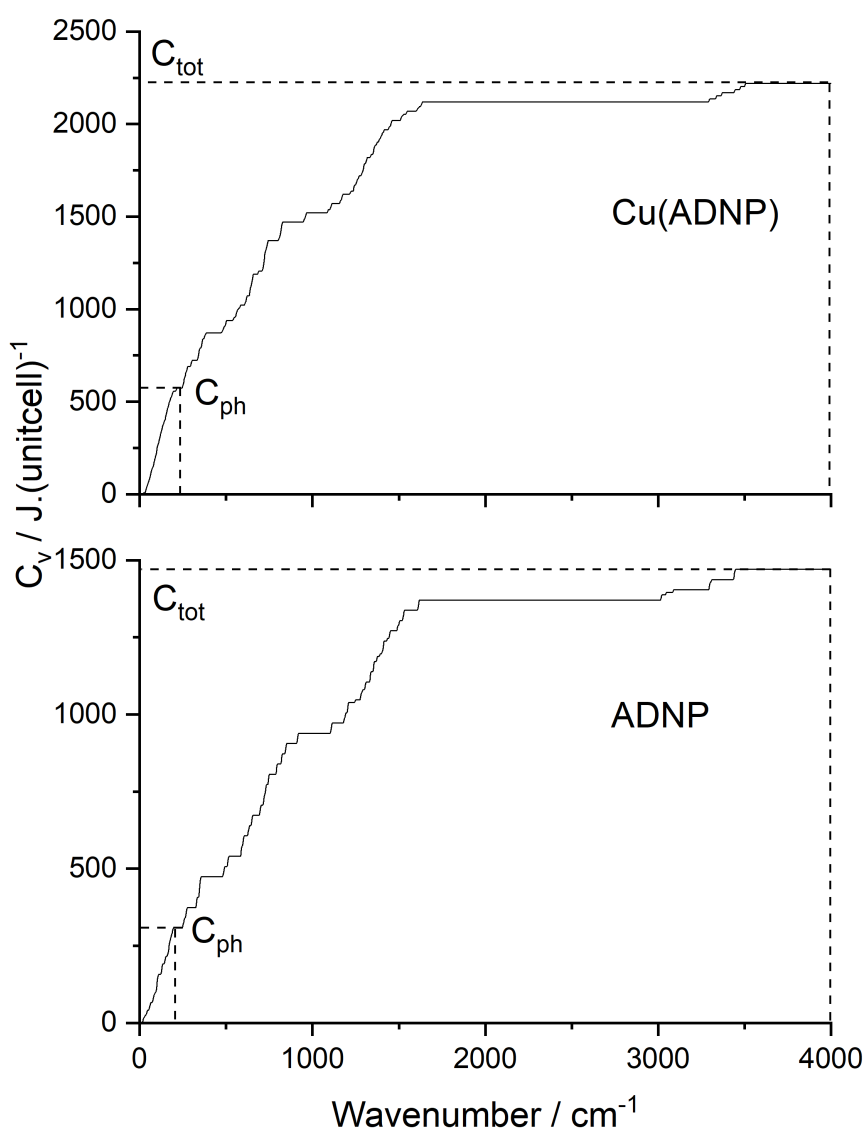


Figure 4.27: Shows the contribution to the heat capacity from each of the vibrational modes of Cu(ADNP) and ADNP with the values of C_{tot} and C_{ph} marked with dashed lines.

Table 4.6: Shows input parameters for the vibrational up-pumping procedure for Cu(ADNP), alongside the measured impact sensitivity value. Z denotes the number of molecular units contained in the unit cell, and Y the number of amalgamated modes that are present in the phonon bath [4, 28].

| EM | Ω_{\max} | Z | Z(6+Y) | Y | $T_{\text{shock}} / \text{K}$ | Experimental IS / J | Up-pumped density / a.u |
|----------|-----------------|---|--------|----|-------------------------------|---------------------|-------------------------|
| Cu(ADNP) | 224 | 2 | 72 | 30 | 2400 | 2.5 | 205347 |
| ADNP | 201 | 4 | 40 | 4 | 3134 | 41 | 27510 |

The parameters recorded in Table 4.6 indicate that Cu(ADNP) is treated as a molecular material for the vibrational up-pumping model (that is, the unit cell contains two discrete molecules ($Z = 2$), in contrast to the DBX structures that were treated as $Z_{\text{eff}} = 1$). The value of Ω_{\max} resembles that typically seen for a molecular material, but the value of T_{shock} is a little lower (molecular materials typically present T_{shock} values of around 3000 K). This is a reflection of the substantial contribution that the phonon bath region of Cu(ADNP) makes to the overall $g(\omega)$. The resulting $\Omega^{(2)}$ is shown overlaid on the $g(\omega)$ for both Cu(ADNP) and ADNP in Figure 4.28.

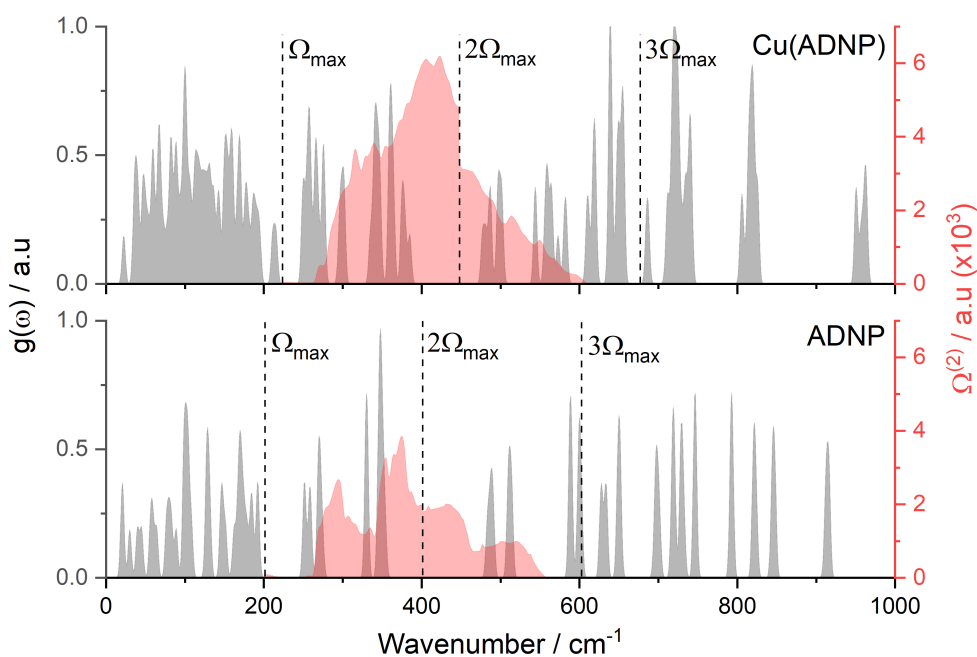


Figure 4.28: Shows the $g(\omega)$ spectrum (grey) with the $\Omega^{(2)}$ (red) for Cu(ADNP) and ADNP, with multiples of Ω_{\max} marked.

Comparing Figure 4.28 back to Figure 4.26 suggests that for both Cu(ADNP) and ADNP, eigenvalues capturing significant C–NO₂ motion fall comfortably within both up-pumping window regions.

The resulting total up-pumped density (per molecular unit, normalised to per phonon mode) plotted against the experimental sensitivity is shown in Figure 4.29 alongside the standard molecular EM test set.

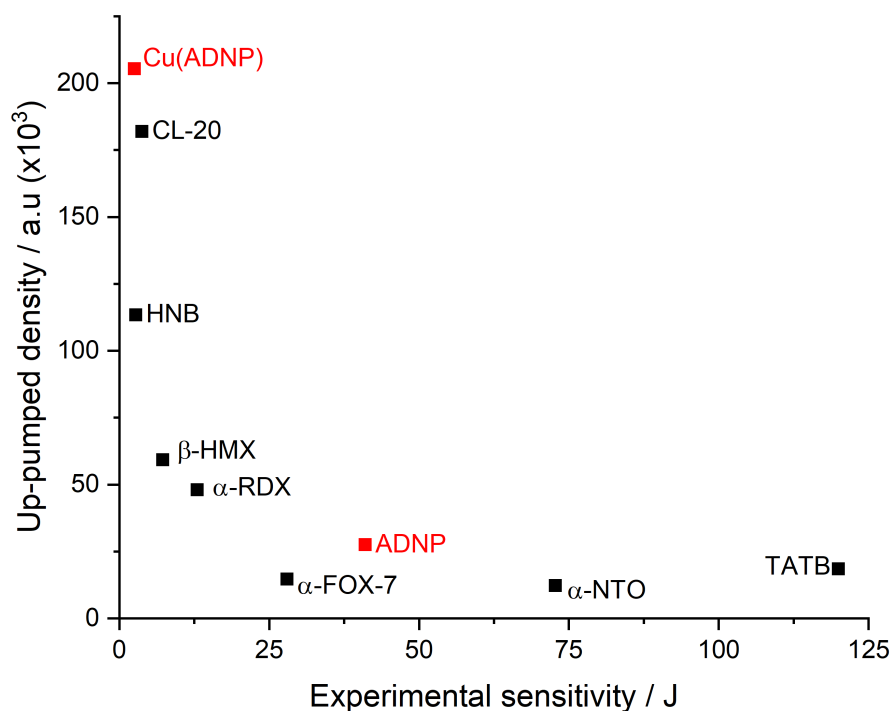


Figure 4.29: Shows the up-pumped density vs. the experimental sensitivity values for Cu(ADNP) and ADNP are shown in red alongside a number of previously well-studied materials [4, 5, 9, 28].

The up-pumped density calculated for Cu(ADNP) was found to be in good agreement with the experimental sensitivity value of 2.5 J, sitting close to the common decay line observed across the data set. It is clearly predicted to be more sensitive than a number of well-known primary EMs, including CL-20. Considering the $g(\omega)$ more closely, the leading reasons for the high sensitivity prediction are a densely packed phonon bath, combined with a densely packed doorway region (see Table 4.7); a clear correlation is readily apparent.

Table 4.7: Shows the number of doorway modes per molecular unit for Cu(ADNP) and ADNP as well as a number of well-studied molecular materials [4, 9, 28].

| EM | Ω_{\max} | Experimental sensitivity / J | Number of phonon bath modes per molecular unit | Number of doorway modes per molecular unit |
|-----------------|-----------------|------------------------------|--|--|
| Cu(ADNP) | 224 | 2.5 | 36 | 18 |
| HNB | 155 | 2.75 | 15 | 12 |
| CL-20 | 222 | 3.75 | 22 | 12 |
| β -HMX | 200 | 7.25 | 17 | 7 |
| α -RDX | 164 | 13 | 12 | 6 |
| α -FOX-7 | 180 | 28 | 9 | 3 |
| ADNP | 201 | 41 | 10 | 5 |
| α -NTO | 216 | 72.75 | 8 | 3 |
| TATB | 151 | 122 | 12 | 3 |

Table 4.7 shows that the number of phonon bath and doorway modes per molecular unit of Cu(ADNP) (of which there are 2, both made up of 3 ADNP moieties each bonded to a Cu atom) are significantly larger than those of the other molecular EMs, including ADNP itself, which also falls acceptably on the prediction line (ADNP experimental IS = 41 J) [25]. Given that the up-pumping model correctly ranks both compounds in relation to each other, and as part of the broader set of EMs, it suggests that the pattern of vibrational modes, and the resonance states that arise from their combination through the permitted up-pumping scattering routes, must provide a possible explanation for the increase in mechanical impact sensitivity for ADNP upon formation of the copper salt. To this end the doorway modes were considered more closely, by mapping the eigenvalues across the two spectra according to their visual similarity (Figure 4.30).

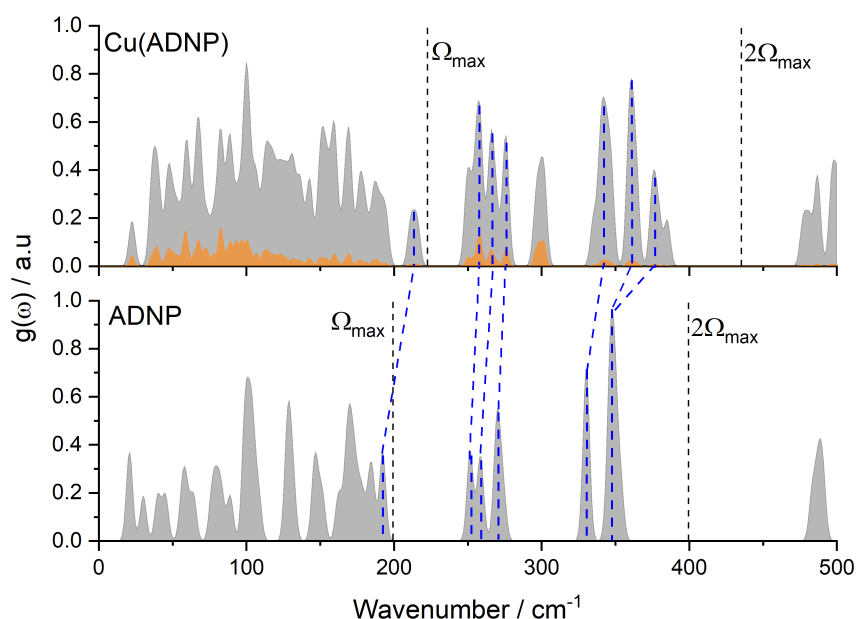


Figure 4.30: Shows the $g(\omega)$ spectrum (grey) for Cu(ADNP) and ADNP with the partial $g(\omega)$ with respect to the Cu atom overlaid for Cu(ADNP) (orange) and blue lines linking analogous modes.

The analysis shown in Figure 4.30 indicates that the eigenvectors of all five of the doorway modes per molecule in ADNP are present in the doorway region of Cu(ADNP). As the molecular unit of Cu(ADNP) is comprised of three Cu-ADNP units bound in a ring, 15 of the 18 doorway modes have thus been accounted for. The remaining three doorway modes present in Cu(ADNP) account for the peak observed at 300 cm^{-1} that is absent in the $g(\omega)$ for ADNP. The eigenvectors for this peak resemble those of the vibrational mode at 276 cm^{-1} in ADNP (which are mapped onto Cu(ADNP) modes at ca. 280 cm^{-1}), however there is also significant motion of the copper ions in these eigenvectors (25 % of the total motion of the mode), which has resulted in a mode hardening effect. This mode hardening is actually reflected across a number of the doorway modes, which suggests that complexation with the copper ions has resulted in an increase in the structural rigidity of the molecular units. This not only increases the scattering potential of the doorway region (as there is a greater diversity in mode frequency for phonon scattering combination), it also pushes the $\Omega^{(2)}$ envelope out to higher wavenumbers. This, combined with the more continuous phonon bath region provided by the

presence of the heavy Cu atoms creates a two-fold effect on the $\Omega^{(2)}$ to dramatically shift the mechanical impact sensitivity of Cu(ADNP) compared to ADNP.

4.5.3 Conclusions

To conclude this section, the primary EM Cu(ADNP) was subjected to a computational investigation to first complete its crystal structure by locating the missing hydrogen atoms through *ab initio* random structure searching, and second, to predict its mechanical impact sensitivity. A successful outcome then allowed exploration of structure/property relationships in order to rationalise why such a marked change in experimentally determined impact sensitivity arose.

The study yielded a global minimum structure with a high degree of confidence, and further geometry optimisation and vibrational frequency calculation provided the input data for the vibrational up-pumping procedure to predict its impact sensitivity. The parent molecular crystal ADNP was subjected to the same treatment, and the outcome ranked both compounds satisfactorily alongside a range of other molecular EMs. The up-pumping model therefore suggests that the pattern of vibrational mode distribution, and the resonance effects that arise through the permitted phonon scattering pathways inherent to the model, provide a route to rationalise why ADNP becomes a primary EM upon formation of a copper salt. The study suggested that the introduction of copper ions into the crystal lattice both contributed to a more continuous phonon bath, as well as to broadening out the doorway region through increasing the structural rigidity of the molecular units. Moreover the addition of vibrations with a high degree of copper motion within the up-pumping window of Cu(ADNP) when compared to ADNP show that it is more vibrationally active within the key range of 1-3 Ω_{max} . The combination of these effects leads to improved phonon scattering and energy transfer into molecular vibrations associated with C–NO₂ bond stretching character, i.e., the trigger or target frequencies likely to be involved in the initiation pathway.

4.6 Overall Conclusions

The work outlined in this Chapter was undertaken to determine whether or not the vibrational up-pumping procedure is a suitable approach for the impact sensitivity prediction of metal-containing CP EMs. In addition to the two-phonon scattering model, a simple phonon bath shock model (i.e., no phonon scattering) was also pursued. The simpler model was ultimately ruled out for all CP EMs investigated in this Chapter as, while good overall sensitivity prediction curves were generated, on closer inspection of the underlying physical models, all failed to transfer energy into the molecular vibrations most likely associated with triggering the initiation pathway.

In general terms, the up-pumping model was able to correctly rank all four CPs (LA, and DBX-1, -2 and -3) as primary energetics, however it was clear that a significant challenge exists with applying the methodology. This concerns locating the top of the phonon bath, denoted by the parameter Ω_{\max} . Separating the phonon density of states into external and internal vibrations is an inherent part of the vibrational up-pumping model. While this could be reliably located for LA, the same did not hold for the DBX series, as the CoM analysis suggested two potential locations for Ω_{\max} , one derived from the consideration of the acoustic vibrations, and the other from the consideration of mode with the largest CoM displacement this time excluding the acoustics. Consideration of the lower value of Ω_{\max} (resulting from exclusion of the acoustic modes in the normalisation process) gave predicted sensitivities in excellent alignment with experimental expectations, each EM was predicted to be a primary EM. On closer analysis of the nature of the vibrations within the up-pumping window, it was clear that the $\Omega^{(2)}$ envelopes (generated from the lower Ω_{\max}) fell over molecular modes that involved likely trigger mode C–NO₂ bond stretching character for DBX-1, -2 and -3, suggesting that such an approach was physically realistic. The likely trigger mode in DBX-3 was also found to be present within the larger phonon bath however, suggesting that consideration of the shocked phonon bath density is reasonable, but the similarities to DBX-1 and -2 and in the absence of organic substructure to compare to (to gain confidence in Ω_{\max}) resulted in the lower bound being

considered the most likely. The process outlined in this Section can also be applied as a guideline workflow to predict the impact sensitivity of metal containing CP EMs developed in the future.

The final compound studied in this Chapter, Cu(ADNP), provided a middle ground between the molecular and CP EMs. Through comparison with the predicted impact sensitivity for its parent molecular EM, ADNP, the vibrational up-pumping model was able to correctly rank both compounds alongside a broad class of other molecular EMs. This then allowed structure/property relationships to be probed, and a hypothesis, based on an enhanced phonon bath and doorway region, which can be attributed to the addition of low-lying copper-based vibrations and an enhancement in structural rigidity, respectively, has been put forward. Thus, a change in a material property has been traced back to the atomic level.

Each of the five structures studied in this work were correctly predicted to be highly sensitive primary EMs, and while the theoretical ranking is not perfect (or if it looks perfect, it is likely to be for flawed reasoning), overall, there are grounds for optimism in the application of the up-pumping model to predict the safe-handling properties of these dangerous materials.

4.7 References

1. A. A. Michalchuk, P. T. Fincham, P. Portius, C. R. Pulham and C. A. Morrison, *A Pathway to the Athermal Impact Initiation of Energetic Azides*, *J. Phys. Chem. C.*, 2018, **122**, 19395 – 19408.
2. A. A. L. Michalchuk, S. Rudic, C. R. Pulham and C. A. Morrison, *Vibrationally Induced Metallisation of the Energetic Azide α -NaN₃*, *Phys. Chem. Chem. Phys.*, 2018, **20**, 29061-29069.
3. A. A. Michalchuk, M. Trestman, S. Rudic, P. Portius, P. T. Fincham, C. R. Pulham and C. Morrison, *Predicting the reactivity of energetic materials: an ab initio multi-phonon approach*, *J. Mat. Chem. A*, 2019, **7**, 19539–19553.
4. A. A. L. Michalchuk, J. Hemingway and C. A. Morrison, *Predicting the impact sensitivities of energetic materials through zone-center phonon up-pumping*, *J. Chem. Phys.*, 2021, **154**, 064105.
5. I. L. Christopher, C. R. Pulham, A. A. L. Michalchuk and C. A. Morrison, *Is the impact sensitivity of RDX polymorph dependant?*, *J. Chem. Phys.*, 2023, **158**, 124115.

6. D. M. Badgujar, M. B Talawar, S. N. Asthana and P. P. Mahulikar, *Advances in science and technology of modern energetic materials: An overview*, *JHM Letters*, 2008, **151**, 289-305.
7. F. A. Mauer, C. R. Hubbard, T. A. Hahn, *Anisotropic thermal expansion of α -Pb(N₃)₂*, *J. Chem. Phys.*, 1974, **60**, 1341-1344.
8. J. W. Fronabarger, M. D. Williams, W. B. Sanborn, J. G. Bragg, D. A. Parrish and M. Bichay, *DBX-1 A Lead Free Replacement for Lead Azide*, *Propellants Explos. Pyrotech.*, 2011, **36**, 541-550.
9. Dr P. Portius, Personal Communication, University of Sheffield, 2020 – 2023.
10. T. M. Klapötke, *Chemistry of High-Energy Materials*, *De Gruyter*, Berlin, 5th edn., 2019.
11. S. J. Clark, M. D. Segall, C. J. Pickard, P. J. Hasnip, M. J. Probert, K. Refson and M. Payne, *First principles methods using CASTEP*, *Z. Kristall.*, 2005, **220**, 567–570.
12. B. G. Pfrommer, M. Cote, S. G. Louie and M. L. Cohen, *Relaxation of Crystals with the Quasi-Newton Method*, *J. Comput. Phys.*, 1997, **131**, 233–240.
13. F. Herman, J. P. Van Dyke and I. B. Ortenburger, *Improved statistical exchange approximation for inhomogeneous many-electron systems*, *Phys. Rev. Lett.*, 1969, **22**, 807–811.
14. Tkatchenko and M. Scheffler, *Accurate molecular van der Waals interactions from ground-state electron density and free-atom reference data*, *Phys. Rev. Lett.*, 2009, **102**, 073005 1–4
15. S. Baroni, S. D. Gironcoli, A. D. Corso and P. Giannozzi, *Phonons and related crystal properties from density-functional perturbation theory*, 2001 73, 516-557.
16. J. Akhavan, *The Chemistry of Explosives*, *Royal Society of Chemistry*, Cambridge, 2nd edn., 2004, p.11-14.
17. J. J. Sabatini and K. D. Oyler, *Recent Advances in the Synthesis of High Explosive Materials*, *Crystals*, 2016, **6**, 5.
18. M. H. V. Huynh, M. A. Hiskey, T. J. Meyer and M. Wetzler, *Green primaries: Environmentally friendly energetic complexes*, *Proc. Natl. Acad. Sci. U.S.A.*, 2006, **103**, 5409-5412.
19. R. Matyas and J. Pachman, *Primary Explosives*, *Springer Berlin*, Heidelberg, 2013, p.71-129.
20. J. Binns, M. R. Healy, S. Parsons and C. A. Morrison, *Assessing the performance of density functional theory in optimizing molecular crystal structure parameters*, *Acta Cryst.*, 2014, **B70**, 259–267.
21. J. P. Agrawal, *High Energy Materials: Propellants, Explosives and Pyrotechnics*, *John Wiley & Sons*, New Jersey U.S., 2010.
22. <https://ila-reach.org/> (Date accessed 07/06/2023)

23. T. M. Klapotke, C. M. Sabate and J. Stierstorfer, *Neutral 5-nitrotetrazoles: easy initiation with low pollution*, *New J. Chem.*, 2009, **33**, 136-147.
24. T. B. Brill and K. J. James, *Kinetics and Mechanisms of Thermal Decomposition of Nitroaromatic explosives*, *Chem. Rev.* 1993, **93**, 2667-2692.
25. P. Politzer and J. S. Murray, *Energetic Materials Part 2. Detonation, Combustion*, Elsevier, Amsterdam, 2003.
26. T. L. Jensen, J. F. Moxnes, E. Unneberg and D. Christensen, *Models for predicting impact sensitivity of energetic materials based on the trigger linkage hypothesis and Arrhenius kinetics*, *J. Mol. Model.*, 2020, **26**, 65.
27. C. J. Pickard and R. J. Needs, *Ab initio random structure searching*, *J. Phys. Condens. Matter*, 2011, **23**, 053201.
28. R. D. Schmidt, G. S. Lee, P. F. Pagoria and A. R. Mitchell, *Synthesis of 4-Amino-3,5-dinitro-1H-pyrazole Using Vicarious Nucleophilic Substitution of Hydrogen*, *J. Heterocyclic Chem.*, 2001, **38**, 1227 – 1230.

Chapter 5: Towards Developing Structure/Property Relationships for the Prediction of Impact Sensitivities in EMs

5.1 Introduction

In the previous two Chapters, the vibrational up-pumping methodology was applied to study two different structural modifications, co-crystallisation and polymorphism, as well as coordination polymers, which presented a different class of materials to which the method originally set out to explore. The predicted sensitivities were generally found to be in good agreement with experimental sensitivity trends, showing that the vibrational up-pumping procedure is capable of predicting the sensitivity of a broad class of energetic material structure types [1, 2, 3, 4, 5, 6]. The purpose of this Chapter is slightly different, in that it sets out to apply the model to perform a comprehensive structure/property relationship study on a large number of compounds. For this, three common chemical families of EMs were selected, namely pyrazoles, tetrazoles and nitrate esters [7]. Examples of compounds were chosen to present a wide spread of impact sensitivity responses while presenting common structural features, such that e.g., the positioning or number of $-\text{NO}_2$ groups on aromatic rings, could be assessed. The aim of this work is therefore to develop simple chemical descriptors that are synonymous with controlling impact sensitivity which can be employed in the design process to yield novel materials with tailored properties.

5.2 Computational Methodology

For each of the EMs considered in this Chapter, a geometry optimisation calculation was completed using the BFGS optimisation method as implemented in CASTEP V.16.11 using the generalised gradient approximation (GGA) functional PBE with the TS dispersion correction scheme, alongside plane wave basis set expressed to at least 800 eV [8, 9, 10, 11]. Additionally, the model was supplemented with norm-conserving pseudopotentials that represented the core electrons. The following

convergence criteria were used for each of the geometry optimisation calculations: residual atomic forces ≤ 0.005 eVÅ, atomic displacements $\leq 5 \times 10^{-4}$ Å, wavefunction self-consistency $\leq 5 \times 10^{-6}$ eV and lattice vector stresses ≤ 0.01 GPa. A grid scale and fine grid scale of at least 2.0 was used for each of the EMs. These tight convergence criteria were enforced in order to minimise the probability of calculating imaginary frequencies (Γ -point only, calculated by the DFPT method) [12]. The resulting vibrational frequencies were used to generate a vibrational density of states, $g(\omega)$, using the script outlined in Chapter 2. To determine gas phase bond strengths for each EM, LModeA V.2.0.0 was used based on the output of gas phase optimisation and frequency calculations completed using Gaussian V.16 (B3LYP with a 6-31g* basis set) [13, 14, 15, 16]. Kier molecular flexibility values for each of the molecules considered in this work which represents the extent of a molecules ability to rearrange, were calculated through the use of Equation 5.1 using a Python 3 script which implements the RDKit package, following the methodology outlined by Kier [17, 18].

$$KMF = \frac{\kappa_1^\alpha \kappa_2^\alpha}{N} \quad \text{Equation 5.1}$$

The KMF is a based on the molecular graph (2-dimensional) with the two parameters κ_1^α and κ_2^α representing the relative cyclicity of the molecule and the relative spatial density of the molecule comprised of N atoms.

5.3 Pyrazole Investigation

5.3.1 Introduction

Pyrazoles are a common class of EM, as their high nitrogen content promotes an exothermic reaction on initiation due to the generation of large amounts of nitrogen gas [7, 19]. Moreover, the heterocyclic ring readily undergoes nitration reactions, resulting in a broad number of possible derivatives being synthetically accessible. This opens the door to a vast number of potential EMs which will each have different performance and safety properties. This provides a good opportunity to explore the effect of differing degrees of substitution on the measured ISfor a series of polysubstituted pyrazole EMs. The compounds considered in this work were: 3,4,5-trinitro-1H-pyrazole (TNP,

IS = 17 J), 3,5-dinitro-1H-pyrazole (3,5-DNP, IS = 25 J), 3,4-dinitro-1H-pyrazole (3,4-DNP, IS = 40 J), 1,3-dinitro-1H-pyrazole (1,3-DNP, IS = 25 J), 3-nitro-1H-pyrazole (3-NP, IS > 100 J), 1-nitro-3-(trinitromethyl)-1H-pyrazole (1-N-3-TNMP, IS = 2.5 J), 5-amino-3,4-dinitro-1H-pyrazole (5-ADNP, IS = 23 J), 4-amino-3,5-dinitro-1H-pyrazole (4-ADNP, IS = 40 J), 3,5-dinitro-1H-pyrazole-1,4-diamino (1,4-DADNP, IS = 41 J), 3,3',5,5'-tetranitro-1H,1'H-4,4'-bipyrazole (BP-1, IS = 4.5 J), 3,3',5-trinitro-1H,1'H-4,4'-bipyrazole (BP-2, IS = 20 J) and 3,3'-dinitro-1H,1'H-4,4'-bipyrazole (BP-3, IS = 30 J) [20 - 30]. The molecular structures alongside the crystallographic unit cells of each pyrazole EM investigated in this work is shown in Figure 5.1.

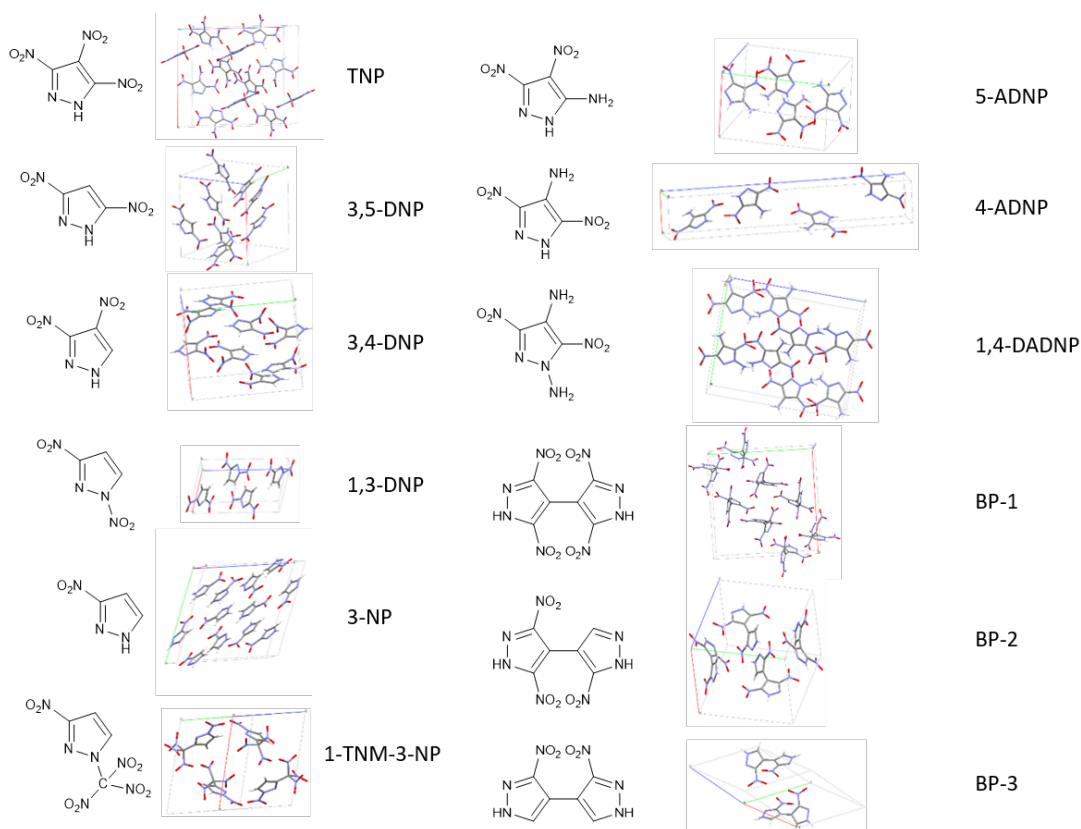


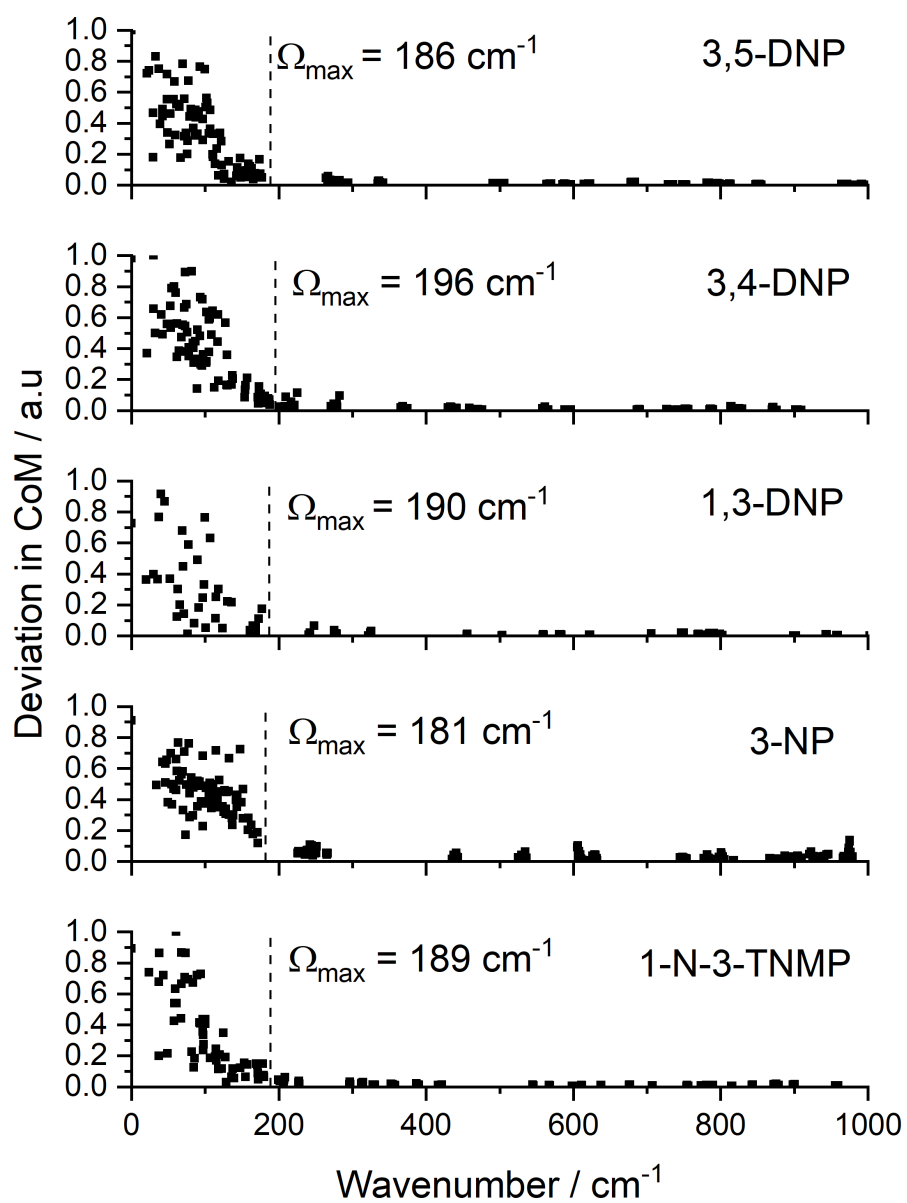
Figure 5.1: Shows the molecular structure, primitive crystallographic unit cell and abbreviated name which will be used in this work for each of the pyrazole EMs considered [20-28].

As can be seen from Figure 5.1, the EMs share common structural features, such that a systematic study could start to link material properties to molecular structure. This therefore represents a good test for using the up-pumping model to rationalise the predicted outcomes back to the molecular, and therefore the design, level.

5.3.2 Results and Discussion

Geometry optimisation calculations for each of the pyrazole-based EMs considered in this work were completed to the specifications outlined in Section 5.2. Comparison between experimental and calculated unit cell parameters are shown in Table A3 in Appendix A, with percentage change in unit cell volume included. Each of the structures considered in this work (including TNP and 4-ADNP which have been outlined in previous Chapters – 4-ADNP is referred to as simply ADNP in Chapter 4) have been optimised to a suitable standard, as can be seen by the small percentage change in volume (less than 6 % which is not too dissimilar to that of the ideal change in volume of roughly 5 %) [31]. It should be noted that the unit cell parameters outlined for BP-3 are those of the conventional cell, but the $g(\omega)$ and subsequent predicted sensitivity is based on the primitive cell in the interest of compute time. This difference will be accounted for in the normalisation process of the vibrational up-pumping procedure [4]. The resulting optimised geometries were then used as the input for subsequent zone centre (Γ -point) vibrational frequency calculations which resulted in 3N real vibrations in all cases. This suggests that the geometry optimisation convergence criteria were appropriate to result in location of the global minimum of the potential energy surface.

As has been shown in previous Chapters, a key material property required to predict the impact sensitivity through vibrational up-pumping is the location of Ω_{\max} which can be determined with help from the CoM script outlined in Chapter 2. Plots outlining the change in CoM for each of the eigenvectors of each of the pyrazole EM groups considered (excluding those presented in previous Chapters) in this work are shown in Figure 5.2.



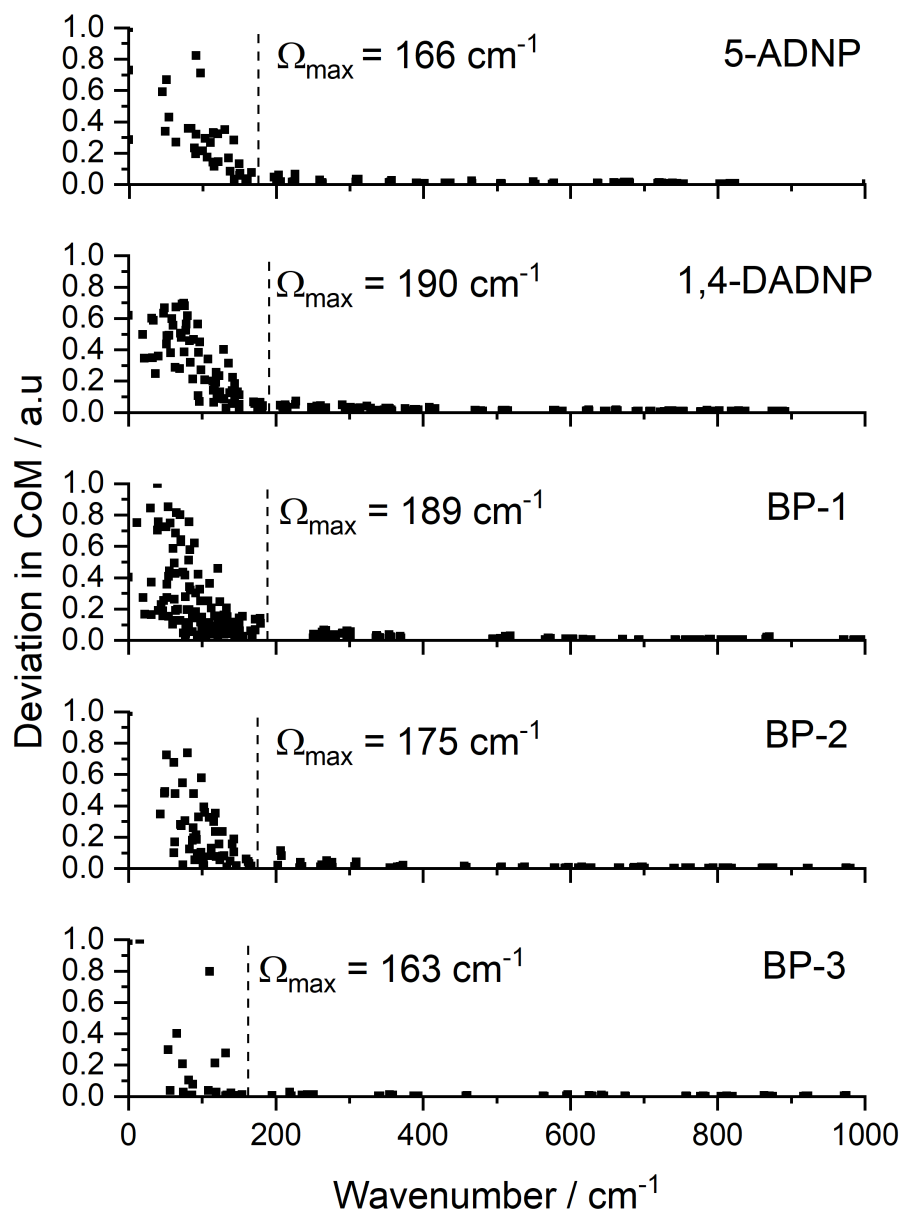
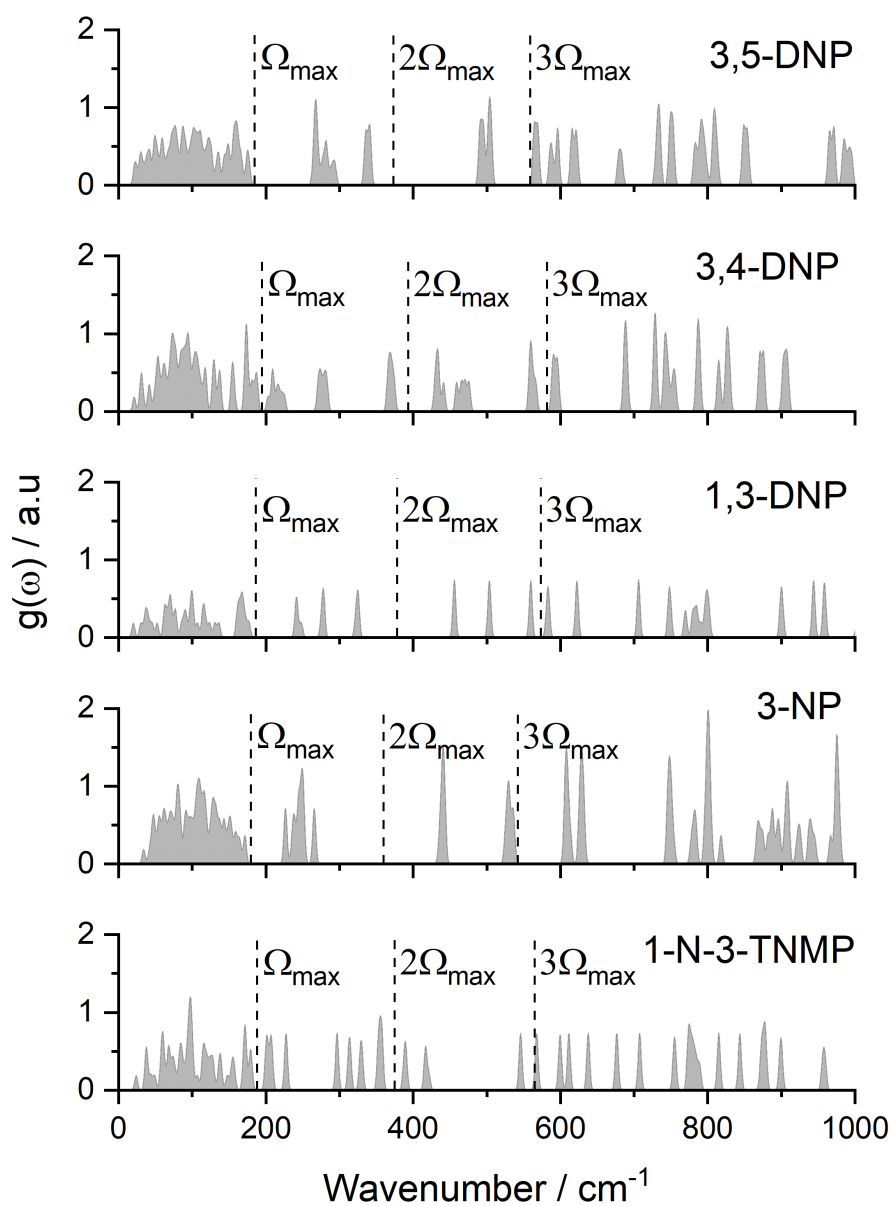


Figure 5.2: Shows the deviation in CoM (normalised to unity) for each vibrational mode of the pyrazole EMs considered in this work with Ω_{\max} marked by a dashed line.

It is clear from Figure 5.2 that the expected dramatic drop off in CoM deviation as the vibrational mode frequency increases was observed in all cases close to the expected value of $\sim 200 \text{ cm}^{-1}$ for molecular materials. The accurate numerical value of Ω_{\max} could only be obtained through consideration of the vibrational density of states ($g(\omega)$, generated using the script outlined in Chapter 2) such that the Gaussian smearing (5 cm^{-1}) is accounted for. The

$g(\omega)$ spectra for the pyrazole EMs considered in this work are shown in Figure 5.3 with multiples of Ω_{\max} marked using dashed lines.



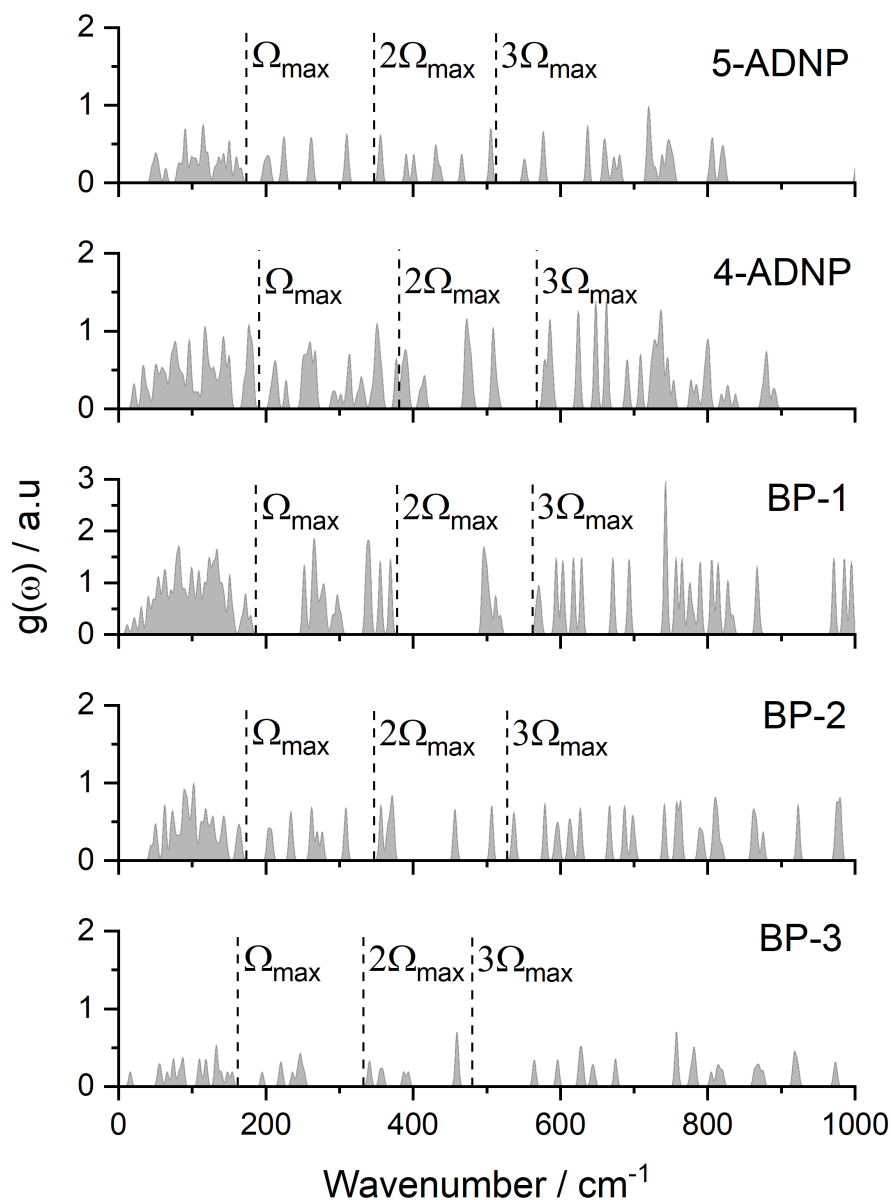
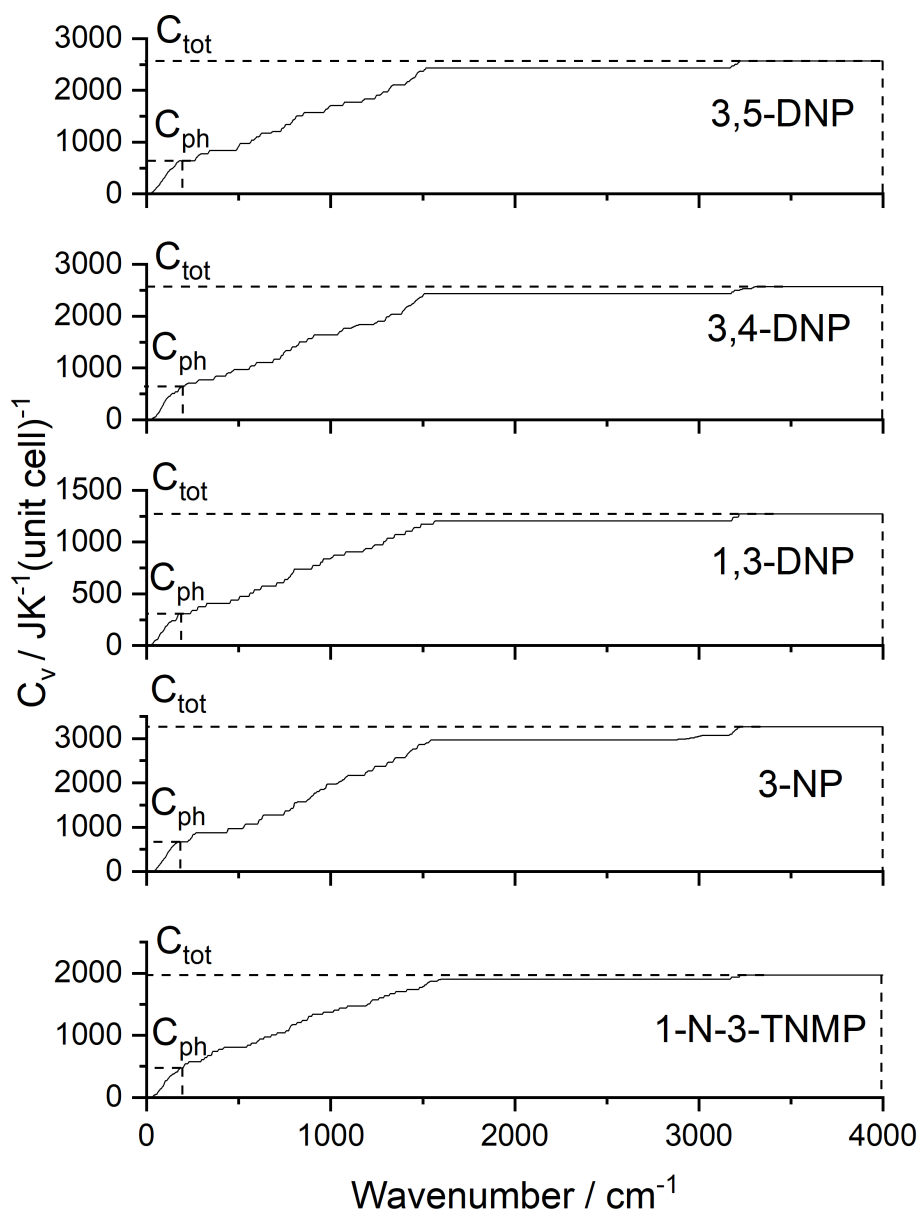


Figure 5.3: Shows the $g(\omega)$ for each of the pyrazoles considered in this work with multiples of Ω_{\max} marked by dashed lines.

As can be seen from Figure 5.3 despite the structural similarity of the various materials, their vibrational landscapes (between 0-1000 cm^{-1}) are quite different, suggesting that there is a big contribution from the variety of functional groups to this region and associated changes in intermolecular interactions. The number of molecules in the unit cell (Z) also varies across the test set, which results in a wide range of y-axis ($g(\omega)$) heights; this is accounted for in the normalisation process of the vibrational up-pumping procedure.

A final variable that must be calculated prior to the sensitivity prediction is the shock temperature (T_{shock}) such that vibrational heating on impact can be estimated. This is completed using the ratio of the total heat capacity (C_{tot}) and the contribution to the total provided by the phonon bath (C_{ph}), benchmarked against 3423 K corresponding to a ratio of 5.22 based on prior work [4]. The cumulative heat capacity for each of the pyrazole EMs is shown plotted against wavenumber in Figure 5.4.



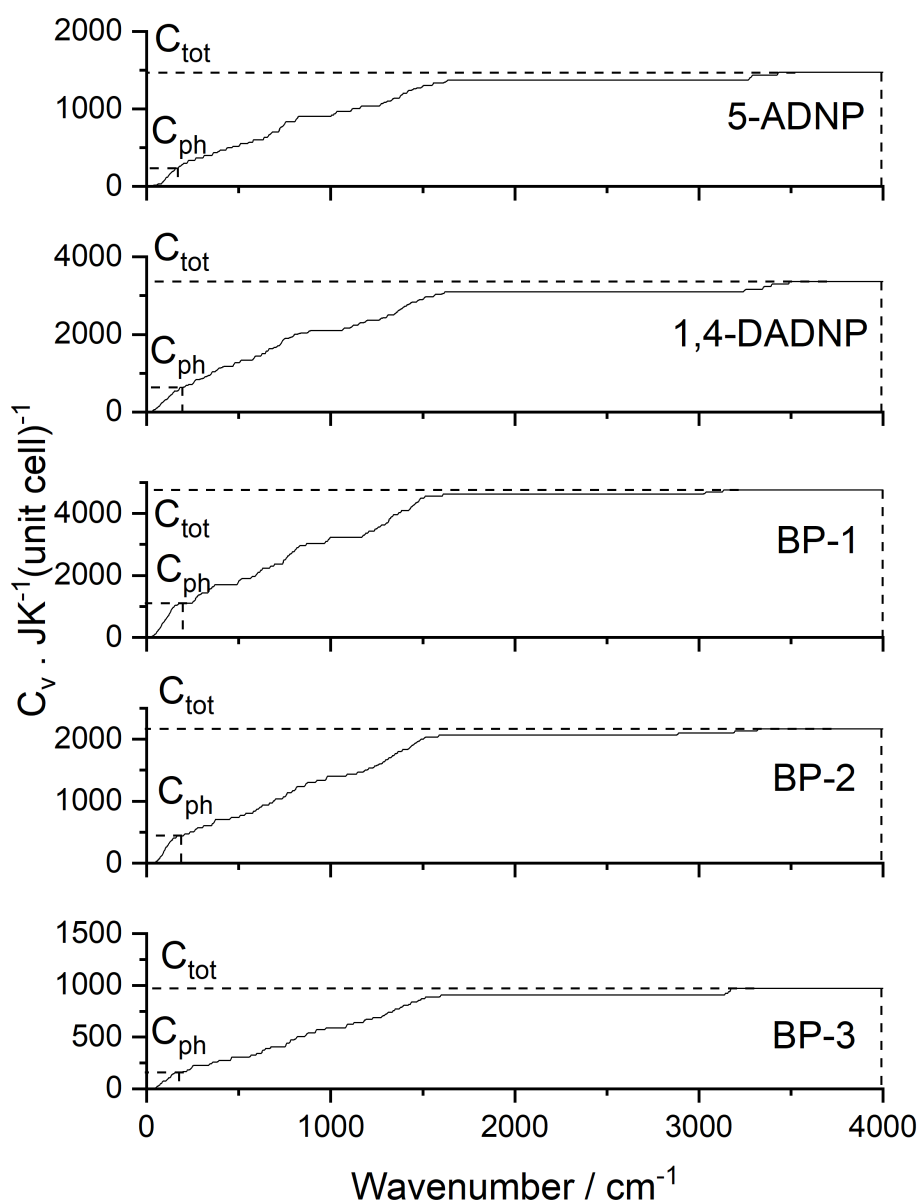


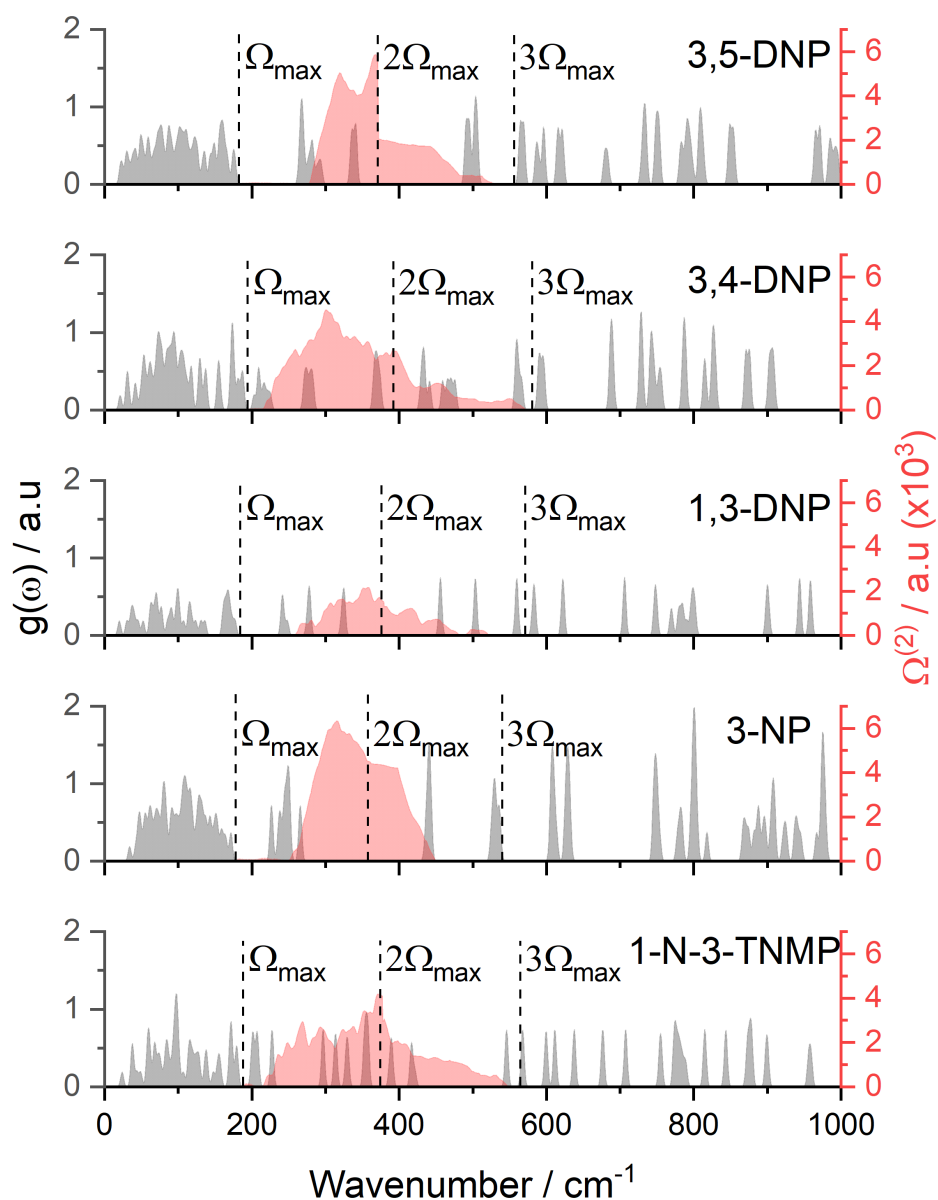
Figure 5.4: Shows the cumulative heat capacity for each of the pyrazole EMs considered with their respective C_{tot} and C_{ph} values marked using dashed lines.

Figure 5.4 shows how the ratio of $C_{\text{tot}}/C_{\text{ph}}$ was determined, their numerical values alongside the associated values of T_{shock} are shown in Table 5.1 alongside the final key input parameter for the vibrational up-pumping procedure, which is the number of phonon bath modes given by $(Z(6+Y))$, where Y denotes the number of amalgamated modes, which are molecular based vibrations that fall into the phonon bath region and Z the number of molecules in the unit cell; both of these metrics are required for the up-pumping normalisation scheme.

Table 5.1: Outlines the input parameters for the vibrational up-pumping procedure alongside the experimental sensitivity for each of the pyrazoles considered in this work as well as the two presented in previous Chapters for completeness [20-30]. The provided references correspond to the publication of both the crystal structure and experimental impact sensitivity of the EMs.

| EM | Ω_{\max} | Z | Z(6+Y) | Y | $C_{\text{tot}}/C_{\text{ph}}$ | $T_{\text{shock}} / \text{K}$ | Experimental IS / J | Relative up-pumped density / a.u | Ref |
|------------|-----------------|----|--------|----|--------------------------------|-------------------------------|---------------------|----------------------------------|--------|
| TNP | 214 | 12 | 156 | 7 | 3.49 | 2288 | 17 | 31931 | 20, 21 |
| 3,5-DNP | 186 | 8 | 80 | 4 | 4.01 | 2630 | 25 | 14744 | 22, 29 |
| 3,4-DNP | 196 | 8 | 80 | 4 | 3.64 | 2387 | 40 | 22898 | 23, 29 |
| 1,3-DNP | 190 | 4 | 40 | 4 | 4.13 | 2708 | 25 | 13087 | 22 |
| 3-NP | 181 | 12 | 84 | 1 | 4.85 | 3180 | 100 | 2532 | 24, 30 |
| 1-N-3-TNMP | 189 | 4 | 60 | 9 | 4.16 | 2728 | 2.5 | 54921 | 25 |
| 5-ADNP | 166 | 4 | 36 | 3 | 6.29 | 4124 | 23 | 51549 | 21 |
| 4-ADNP | 201 | 4 | 40 | 4 | 4.78 | 3134 | 41 | 27510 | 26 |
| 1,4-DADNP | 190 | 8 | 80 | 4 | 5.26 | 3449 | 40 | 147966 | 27 |
| BP-1 | 189 | 8 | 136 | 11 | 4.31 | 2826 | 4.5 | 105202 | 28 |
| BP-2 | 175 | 4 | 56 | 8 | 4.92 | 3226 | 20 | 51601 | 28 |
| BP-3 | 163 | 2 | 22 | 5 | 6.16 | 4039 | 30 | 41753 | 28 |

Using the information outlined in Table 5.1, the two-phonon density of states ($\Omega^{(2)}$) was generated using the vibrational up-pumping methodology. The resulting $\Omega^{(2)}$ trace is shown overlaid on the underlying $g(\omega)$ spectrum for each of the pyrazole EMs in Figure 5.5.



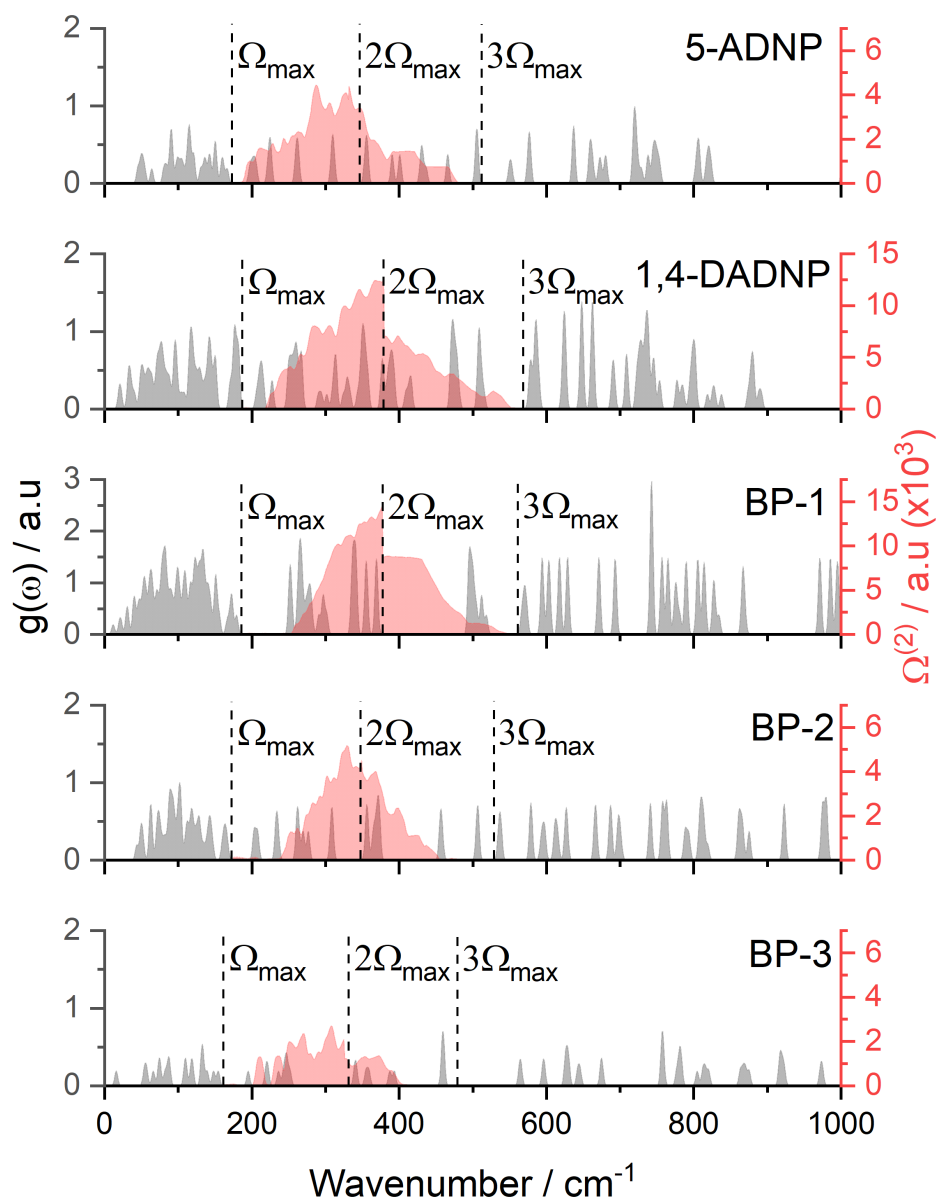


Figure 5.5: Shows the $g(\omega)$ (grey) for each of the pyrazoles considered in this work with the $\Omega^{(2)}$ trace (red) overlaid with multiples of Ω_{\max} marked by dashed lines.

As can be seen from Figure 5.5, there is a large spread in the magnitudes of the $\Omega^{(2)}$ traces displayed by the EMs considered, both in terms of their intensities and their distributions. Two notable traces are worth discussion. The first is 3-NP, which is experimentally insensitive but produces an $\Omega^{(2)}$ trace of comparable height to the more impact sensitive compounds 3,5-DNP and 3,4-DNP. Despite this there is almost no vibrational motion for this energy to excite as 3-NP is vibrationally sparse in the 1-3 Ω_{\max} region. The second is 1,4-DADNP which generated the most intense $\Omega^{(2)}$ trace which encapsulates many vibrational states in the up-pumping window despite only being moderately

sensitive to impact (40 J) [27]. The up-pumped densities of the pyrazole EMs compared to the experimental sensitivities are shown in Figure 5.6 alongside previously reported predictions by the same up-pumping model for a number of well-known EMs.

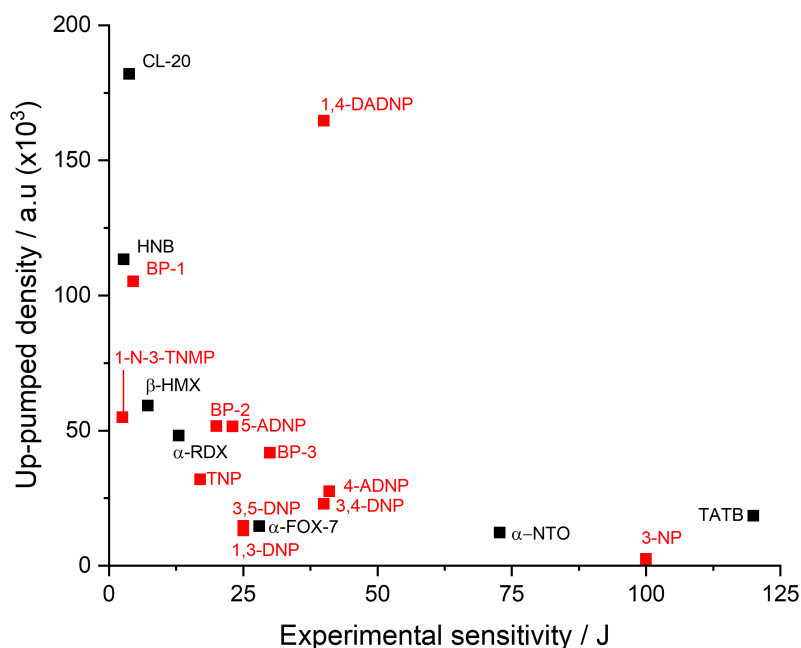


Figure 5.6: Shows the up-pumped density of the pyrazole EMs considered in this work (red) plotted against the experimental sensitivity with a number of previously reported EMs shown alongside (black) [4, 6].

As can be seen from Figure 5.6, the pyrazole EMs follow a good trend of increasing up-pumped density with decreasing experimental sensitivity and compare reasonably well alongside the previously studied materials with the exception of 1,4-DADNP, which is dramatically over-predicted. The extent of over-prediction places 1,4-DADNP almost to level of CL-20, which is exceptionally sensitive and clearly not reinforced from the experimental measurement. The structure of 1,4-DADNP is comprised of a tetra-substituted pyrazole ring with alternating amino and nitro groups. It is likely that only vibrations involving significant contribution from the nitro groups will result in any energetic performance, as nitro groups are often synonymous with energetic character [32]. As such partial $g(\omega)$ plots with respect to both nitro and amino groups of 1,4-DADNP were calculated, in order to further probe the

nature of the vibrations that fall within the up-pumping window. Similar plots were also completed for the other two amino-pyrazoles, 4-ADNP and 5-ADNP, both of which fell on the predicted trend line, for comparison. The respective nitro and amino partial $g(\omega)$ plots overlaid on the complete $g(\omega)$ for each of the three EMs are shown in Figure 5.7.

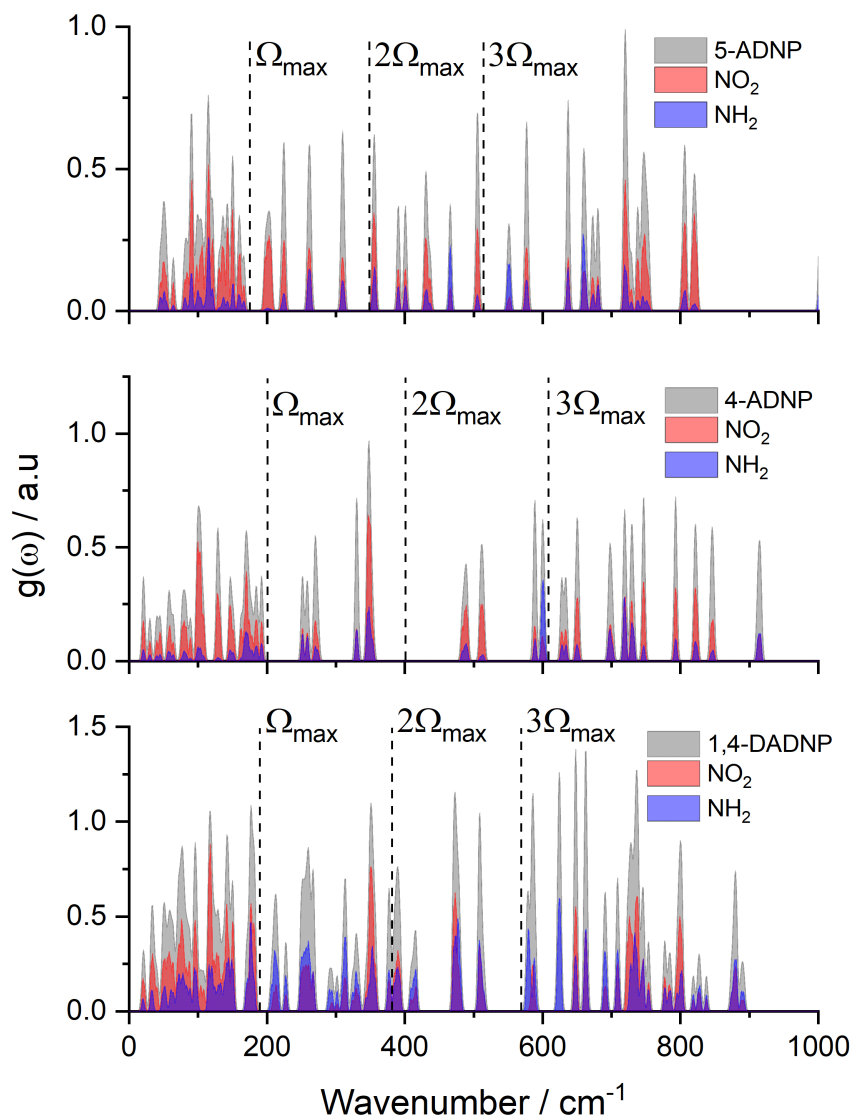


Figure 5.7: Shows the partial $g(\omega)$ with respect to nitro groups (red) and amino groups (blue) overlaid on the complete $g(\omega)$ (grey) for 5-ADNP, 4-ADNP and 1,4-DADNP.

As can be seen from Figure 5.7, the up-pumping windows of both 4-ADNP and 5-ADNP contain vibrational modes that have more nitro group character than amino group, as indicated by the increased height of the red peaks compared to the blue. This, however, is not the case for 1,4-DADNP, where all bar three

vibrations contain more amino group motion. Since it is likely that it is the vibrations involving significant nitro group movement that results in energetic character, projecting onto all modes (particularly those with significantly more amino character than nitro) will likely result in an over prediction of the impact sensitivity of 1,4-DADNP, as exciting these modes will be unlikely to result in bond rupture. In an attempt to rationalise the extent of over prediction that this causes, the integral of the $\Omega^{(2)}$ trace was again rationalised when projected only onto modes in which the partial $g(\omega)$ of nitro group character exceeds that of the amino groups. This process was completed for the three pyrazole EMs shown in Figure 5.7, resulting in a change in up-pumped density from 51549 to 49745 and 164655 to 56875 a.u. for 5-ADNP and 1,4-DADNP respectively, with 4-ADNP remaining unchanged. An updated version of Figure 5.6 is shown in Figure 5.8 where 4-ADNP and 5-ADNP appear essentially unchanged and the lower value of 1,4-DADNP is labelled with an asterisk (*). While still somewhat over-predicted, it does now sit much closer to the general trend line.

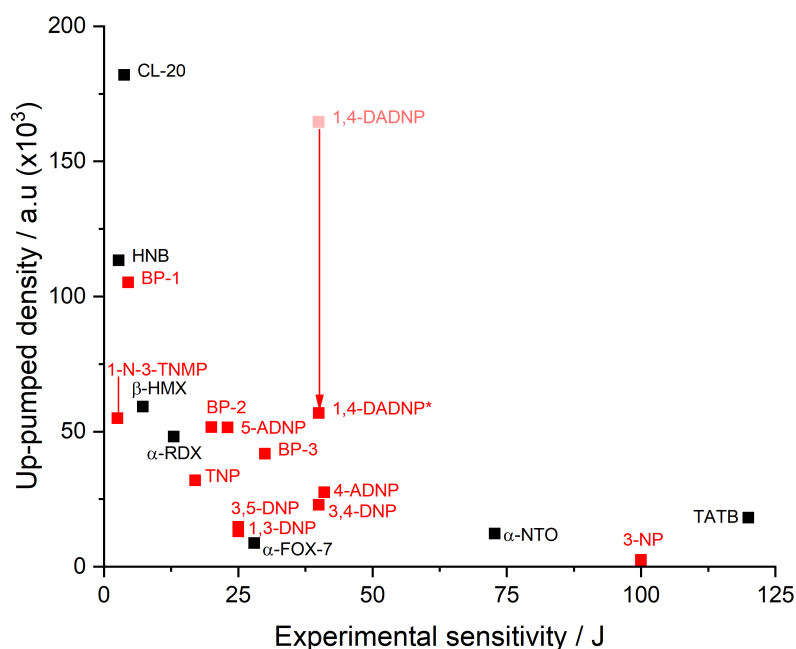


Figure 5.8: Shows the up-pumped density of the pyrazole EMs considered in this work (red) alongside well-studied EMs (black), with an arrow indicating the dramatic change in placement of 1,4-DADNP [4, 6].

The correction applied to 1,4-DADNP is a very crude approach based on the understanding that a particular trigger motion is the root cause of initiation and, while not a trigger vibration explicitly, the partial $g(\omega)$ does give an indication as to the amount of potential nitro-based vibrations that are present. It should be noted that materials such as TATB and FOX-7 also contain both nitro and amino groups and would likely also see some reduction in up-pumped density if subjected to the same treatment. However, this is not pursued here, as a more robust examination into $\Omega^{(2)}$ projection onto probable target mode frequencies is outlined later in this work; Figure 5.8 is merely used to show the possible extent of change as a result of the method on 1,4-DADNP.

The structural similarity of the pyrazole EMs and the incremental structural changes between them, combined with the relative success of the up-pumping method, allow for an in-depth investigation into structure/property relationships for these compounds. This can be explored through examination of two key properties that a material must have in order to be an impact sensitive EM:

- Having the propensity to efficiently up-pump impact energy into higher energy modes.
- Possessing the underlying vibrational structure to capture the up-pumped energy and transfer it into an energetic response.

As in previous Chapters, the number of doorway modes per molecule provides a simple metric to roughly quantify the up-pumping capacity of the material, as the doorway modes (in conjunction with the phonon bath modes) are able to scatter energy upwards. The relationship between the number of doorway modes and the up-pumped density is shown graphically in Figure 5.9.

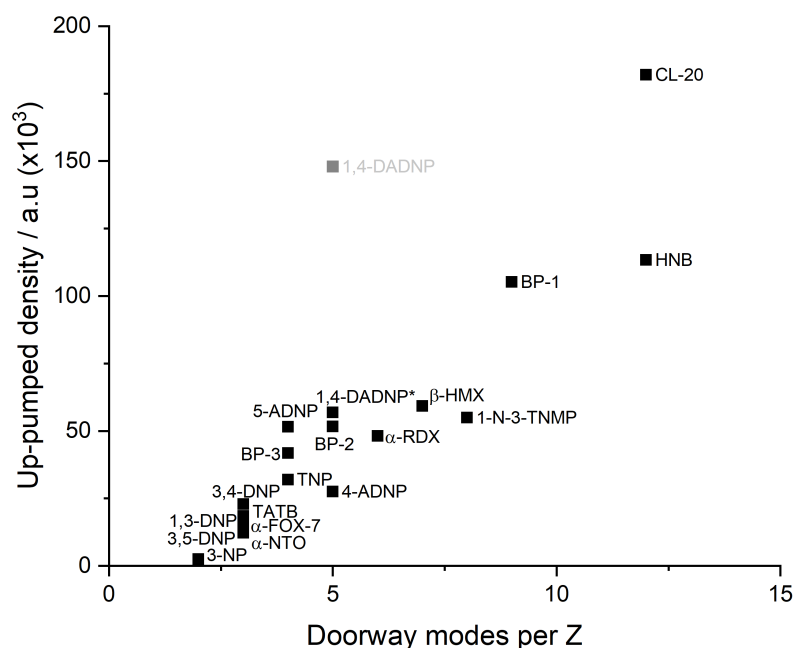


Figure 5.9: Shows the relationship between the number of doorway modes per molecule and the up-pumped density of both pyrazole EMs and the well-studied baseline EMs [4, 6]. Both up-pumped density values for 1,4-DADNP are shown with the complete up-pumped density shown by a faded point and when projected onto nitro group density denoted by an asterisk.

As can be seen from Figure 5.9, there is a strong trend between the number of doorway modes per molecule and the predicted up-pumped density. It should be noted that 1,4-DADNP sits significantly above the trend (shown as a transparent point) as was shown in Figure 5.6, but when the up-pumped energy is projected onto the nitro containing modes only (the data point marked with the asterisk) it sits nicely in the trend. This heavily implies that the over prediction of 1,4-DADNP is based on an over capture of up-pumped energy, rather than an erroneously large up-pumping capacity.

To study the trend highlighted in Figure 5.9 in more detail, the number of doorway modes and the number of bound functional groups ($-\text{NO}_2$, $-\text{NH}_2$ and $-\text{C}(\text{NO}_2)_3$) are quoted in Table 5.2 and plotted in Figure 5.10(a), alongside the data points for the previously reported standard EM dataset. Clearly as the number of functional groups attached to the base pyrazole skeleton is increased, there is an increase in the number of doorway modes per molecule.

A potentially more robust measure of a material's capability to exhibit doorway mode character is through consideration of molecular flexibility. This is represented by the Kier Molecular Flexibility index (KMF), a metric that is based on the molecular graph and accounts for the type of atoms and their relative spatial density, the formula for its calculation is given by Equation 5.1 [18]. KMF is a very simple metric to calculate, as the only required input into an in-house Python script is a SMILES string of the molecular structure. The value for each of the pyrazole EMs is shown in Table 5.2 [18].

Table 5.2: Outlines both the experimental sensitivity and the up-pumped density, the number of rotatable groups and doorway modes per molecule and their KMF values [20-30].

| EM | Experimental IS / J | Up-pumped density / a.u | # rotatable groups per Z | # Doorway modes per Z | KMF |
|------------|------------------------|----------------------------|--------------------------------|-----------------------------|-------|
| TNP | 17 | 31931 | 3 | 4 | 28.88 |
| 3,5-DNP | 25 | 14744 | 2 | 3 | 16.56 |
| 3,4-DNP | 40 | 22898 | 2 | 3 | 16.56 |
| 1,3-DNP | 25 | 13087 | 2 | 3 | 16.56 |
| 3-NP | 100 | 2532 | 1 | 2 | 7.66 |
| 1-N-3-TNMP | 2.5 | 54921 | 5 | 8 | 51.48 |
| 5-ADNP | 23 | 51549 | 3 | 4 | 19.38 |
| 4-ADNP | 41 | 27510 | 3 | 5 | 19.38 |
| 1,4-DADNP | 40 | 164655 | 4 | 5 | 22.48 |
| 1,4-DADNP* | 40 | 56875 | 4 | 5 | 22.48 |
| BP-1 | 4.5 | 105202 | 5 | 9 | 69.94 |
| BP-2 | 20 | 51601 | 4 | 5 | 49.94 |
| BP-3 | 30 | 41753 | 3 | 4 | 33.53 |

Table 5.2 shows that there is a clear trend between both the number of rotatable groups and the KMF of a molecule when compared to the number of doorway modes; this data is shown graphically in Figures 5.10 (a and b).

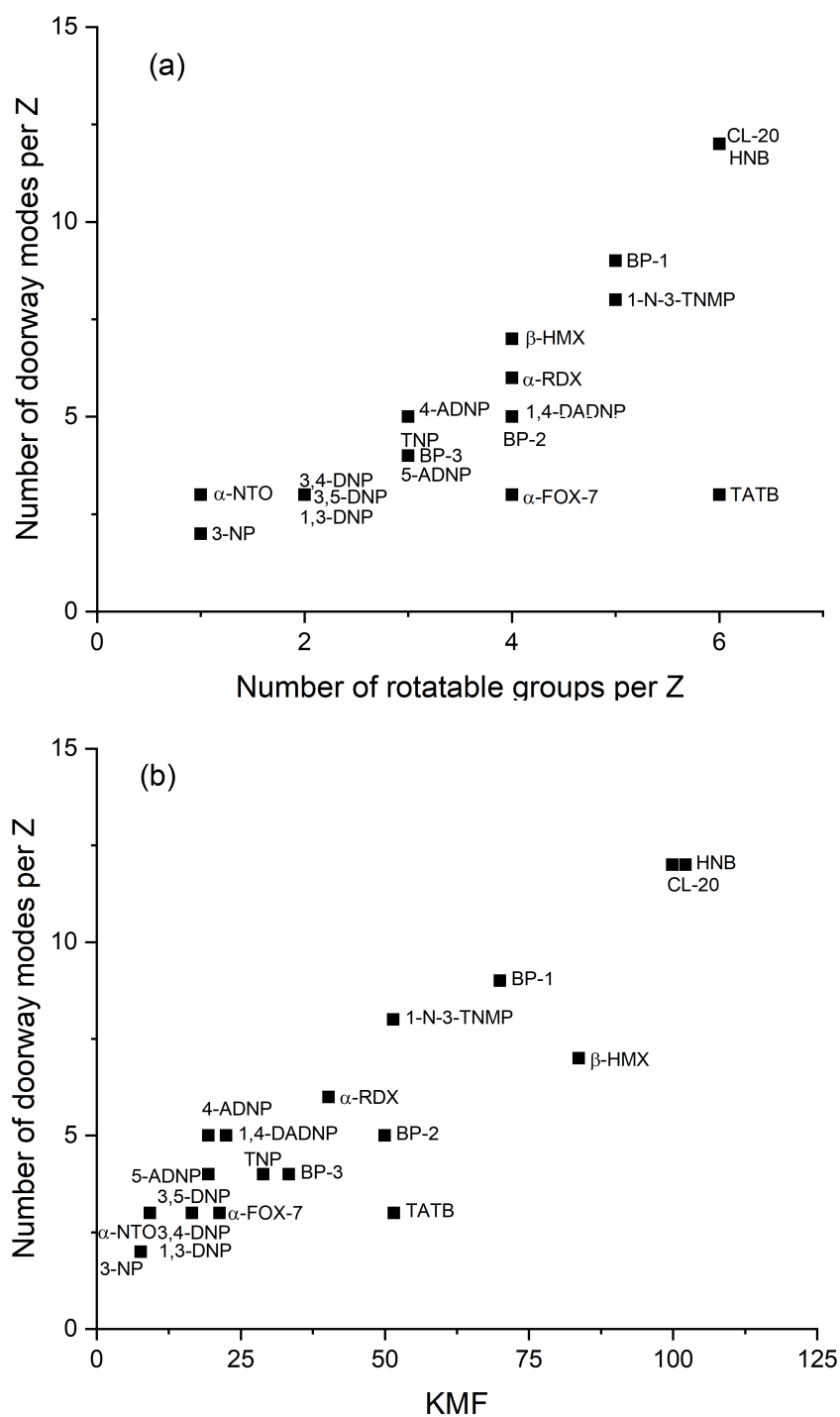


Figure 5.10: Shows how the number of functional groups influences the number of doorway modes (a) and how the KMF influences the number of doorway modes per Z (b) [4, 6].

Figure 5.10 (a) shows that an increasing number of functional groups per molecule leads to an increase in the number of doorway modes attributed to that molecule. The number of doorway modes exhibited by α -FOX-7 and TATB sit lower than would be expected based on their number of functional groups.

This is likely as a result of the increased amount of intramolecular hydrogen bonding exhibited between the functional groups (amino and nitro) resulting in them being 'locked in' and unable to rotate. This blocking of the librational motion will result in a direct decrease in the vibrational character present within the doorway region.

This deviation from the trend is rectified in the case of α -FOX-7 when KMF is considered rather than a simple functional group count. Now TATB and β -HMX are the only real outliers from the general trend. This can be rationalised in the case of β -HMX as the ring structure is incredibly flexible (as it is comprised of purely single bonds), which will contribute to a high KMF value. In the case of TATB, there is likely very little molecular motion contributing to doorway modes due to each of the functional groups being involved in strong intramolecular interactions on each side. This is not observed for α -FOX-7, which also possess amino and nitro groups, as the inter/intramolecular bonding regime is less rigid and as such librational motion can still occur.

In an attempt to explore the effectiveness of KMF as an indicator for sensitivity, the relationship between the up-pumped density and KMF is explored in Figure 5.11.

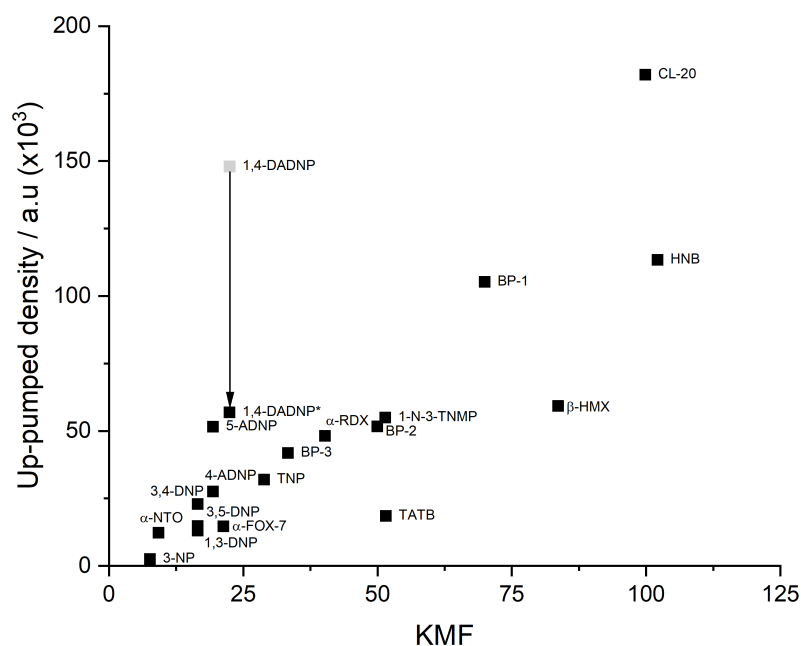


Figure 5.11: Shows the relationship between the up-pumped density and the KMF of the molecular structure [4, 6]. Both the complete and nitro projected (*) up-pumped densities of 1,4-DADNP are shown.

Figure 5.11 indicates that there is a good relationship between the predicted sensitivity and KMF, likely as result of increased up-pumping of energy as a result of increased low energy vibrational character. While the KMF of the structure appears to allow for a good understanding of the origin of the magnitude of the $\Omega^{(2)}$ and as such the up-pumped density, it does not give insight into the nature of the target modes or the actual physical basis of the initiation.

As was discussed in Chapter 4, the likely cause of initiation in nitrated EMs is the cleavage of the weakest bond in the molecule (most often C-NO₂ or N-NO₂), resulting in rapid decomposition of the structure and release of chemical energy [33, 34, 35]. In order to probe the relative bond strengths of each of the pyrazole EMs (to check that the bonds involving nitro groups are in fact the weakest in the molecules, and if so, how much weaker), the strength of each bond in the molecule was calculated using local mode analysis (according to Section 5.2) [13]. This analysis was performed on isolated (gas phase) structures, and while the resulting values are not truly representative of the

solid state, where intermolecular interactions will weaken and strengthen some bonds, it is likely that the weakest bonds will remain regardless of the state of matter.

The local mode analysis yielded comparable strengths for each analogous bond for the pyrazole data set. The weakest bonds were confirmed to be the C-NO₂ or N-NO₂ bonds for each structure, which fell typically around 4.5 ± 0.5 , and $2.8 \text{ mDyn}\text{\AA}^{-1}$, respectively (see Figure 5.12). The two exceptions to this finding were 1,4-DADNP, which showed stronger C-NO₂ bonds, such that the N-NH₂ bond presents as the weakest bond in this structure ($4.747 \text{ mDyn}\text{\AA}^{-1}$, note these bond types for the structures shown in Figure 5.12 were typically $5.5 \pm 0.2 \text{ mDyn}\text{\AA}^{-1}$). This suggests that projecting onto only nitro motion, as discussed above, is potentially incorrect. The other exception is 1-N-3-TNMP, for which the aliphatic C-NO₂ bonds, present as exceptionally weak ($1.9\text{--}2.2 \text{ mDyn}\text{\AA}^{-1}$). Interestingly, Figure 5.13 shows the following trends structures:

1. Positioning multiple neighbouring C-NO₂ groups around a ring structure in close proximity generally weakens the bond force constants. This can clearly be observed through consideration of the change in force constant of the C-NO₂ bond at the 3-position on the pyrazole ring of 3-NP which decreases from $4.305 \text{ mDyn}\text{\AA}^{-1}$ to 3.990 and $4.214 \text{ mDyn}\text{\AA}^{-1}$ when further nitrated to 3,4 and 3,5-DNP respectively. This can be seen even more clearly through consideration of the 4-position of TNP, which is repelled from either side resulting in a C-NO₂ bond strength of $3.962 \text{ mDyn}\text{\AA}^{-1}$. The same effect is also observed for HNB. This effect is presumably due to repulsion between closely positioned -NO₂ groups.
2. Positioning a C-NH₂ group adjacent to a C-NO₂ group in a ring structure strengthens the force constant of the latter. Exemplified by 3,5-DNP, 4-ADNP and 1,4-DADNP where introduction of an -NH₂ group at the four position increases the strength of the 3-position C-NO₂ bond from 4.214 to 4.574 and $4.796 \text{ mDyn}\text{\AA}^{-1}$ respectively and the 5 position C-NO₂ bond from 4.493 to 5.232 and $5.202 \text{ mDyn}\text{\AA}^{-1}$

respectively. The same trend is shown for the 3-position nitro group of 1,3-DNP. An additional pair of structures which exhibit this is 3,4-DNP and 5-ADNP, as the strength of the C-NO₂ group is increased from 4.333 to 4.767 mDynÅ⁻¹ when the -NH₂ group is introduced. This effect is also seen between HNB and TATB and can be attributed to intramolecular hydrogen bonding. It should be noted that the -NH₂ group at the 1 position of 1,4-DADNP is pyramidalised and therefore likely cannot lock the 5 position -NO₂ group as efficiently as the H atom present on 4-ADNP resulting in a slightly weaker C-NO₂ than may be expected.

3. For the pyrazole structures, C-NO₂ bonds in the 5-position are stronger than C-NO₂ bonds in the 3-position. This is apparent in each structure that has a C-NO₂ bond at both of these positions (3,5-DNP, TNP, 4-ADNP, BP-1 and BP-2). This is once again likely as a result of H-bonding interactions between the hydrogen atom and the -NO₂ group in the 5-position somewhat restricting its rotation. It should again be noted that this trend is observed for 1,4-DADNP but more than likely as a result of the 4-position -NH₂ group as the pyramidalised nature of the other NH₂ will likely not interact with the NO₂ as efficiently.

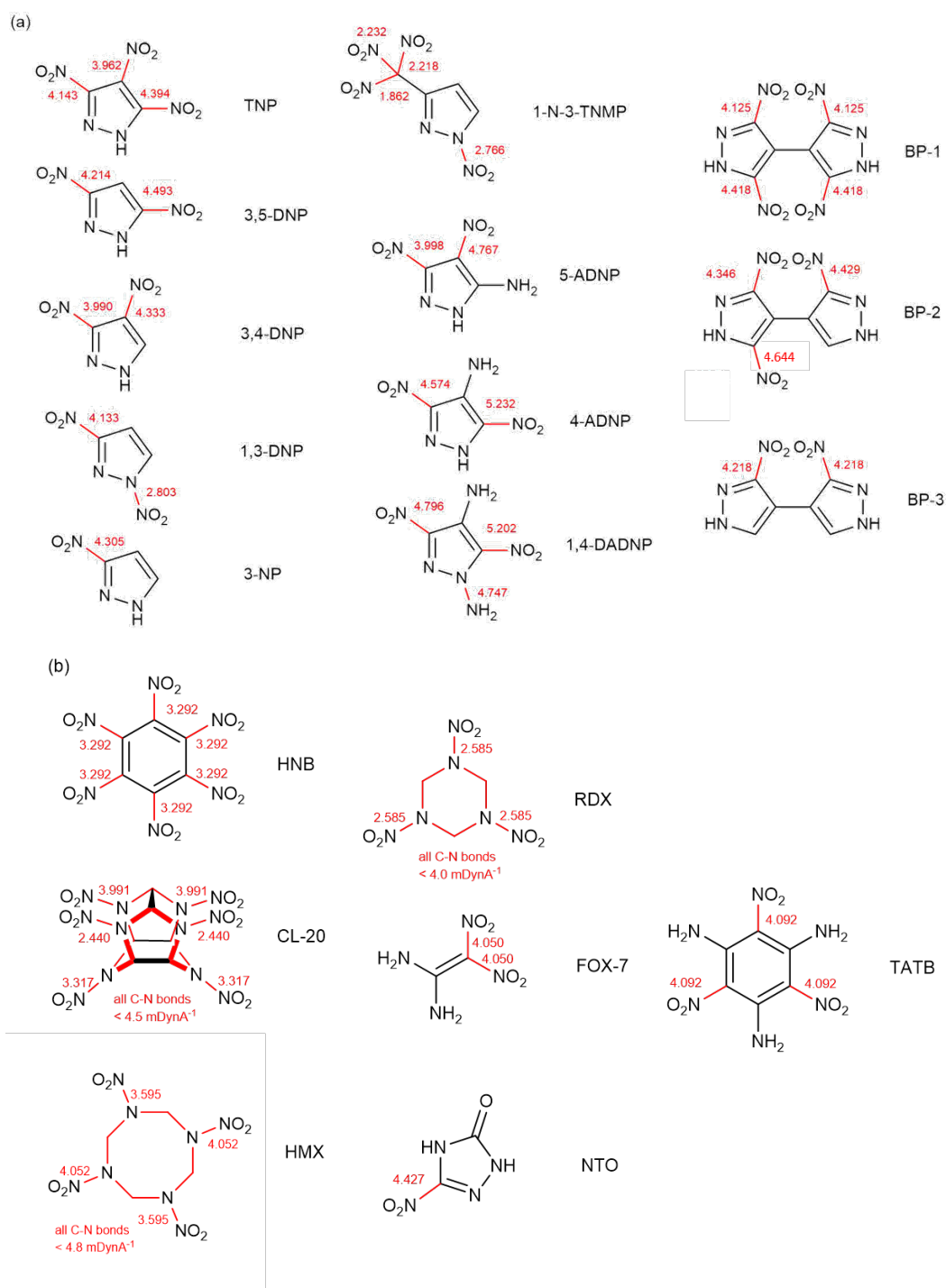
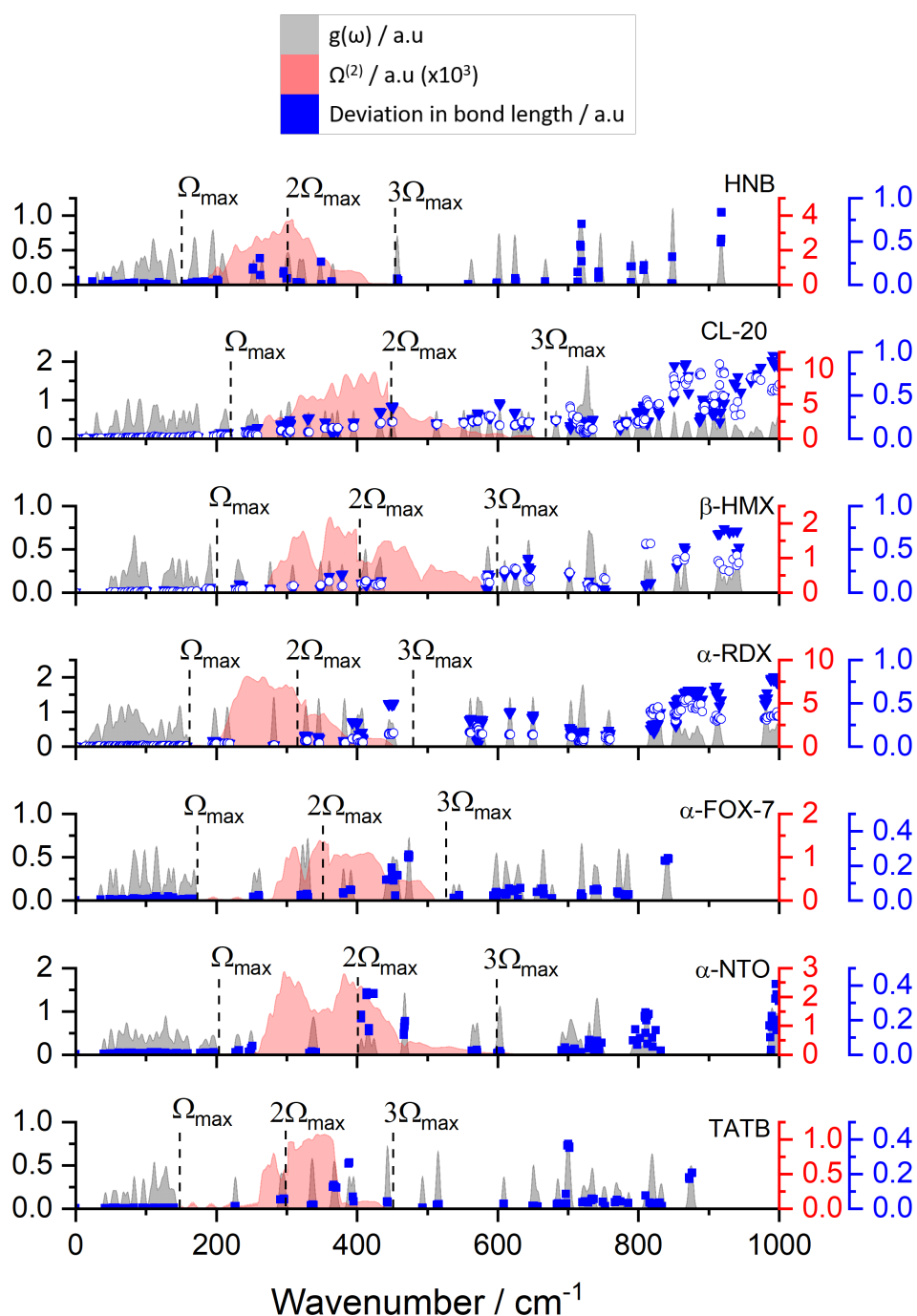


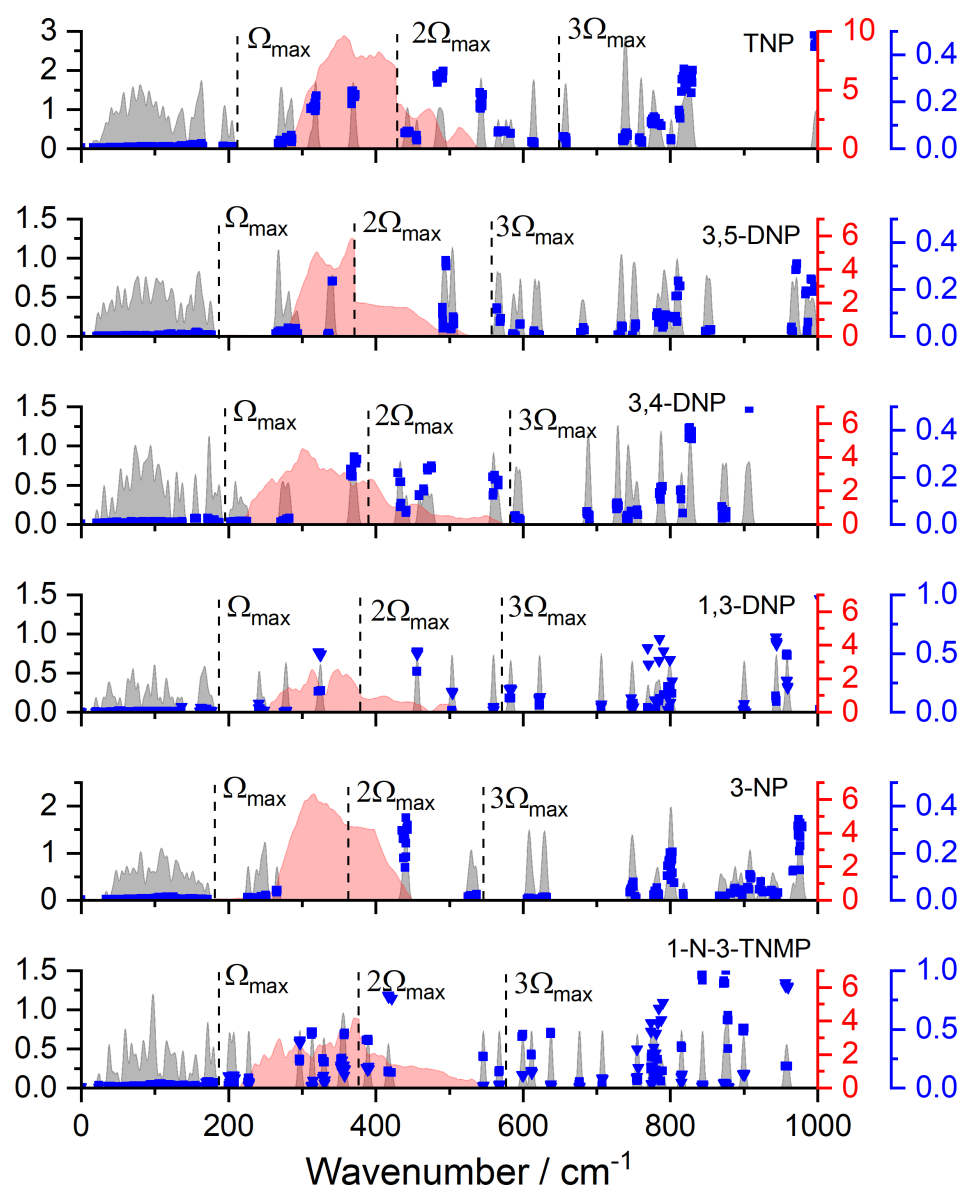
Figure 5.12: Shows the structures of the pyrazole EMs (a) and well-studied materials (b) with their respective weak bonds shown in red with their relative strengths alongside (units $\text{mDyn}\text{\AA}^{-1}$ – calculated using LModeA) [13]. Bonds drawn in black have local force constants $> 5.0 \text{ mDyn}\text{\AA}^{-1}$.

The stretching motion of the weak bonds (those denoted in red in Figure 5.12) were tracked for each vibrational mode in the pyrazole EMs as well as for the previously studied molecular EMs using the code discussed in Section 2.4.

Despite C-NO₂ bonds in the 5-position of 5-ADNP and 1,4-DADNP being unexpectedly strong they were still tracked as they are believed to be the trigger bond.

Here the average change in the weakest bond geometries, normalised with respect to the eigenvector presenting with the largest bond stretch motion, is overlaid on the $g(\omega)$ and $\Omega^{(2)}$ for each of the EMs considered in this work (see Figure 5.13).





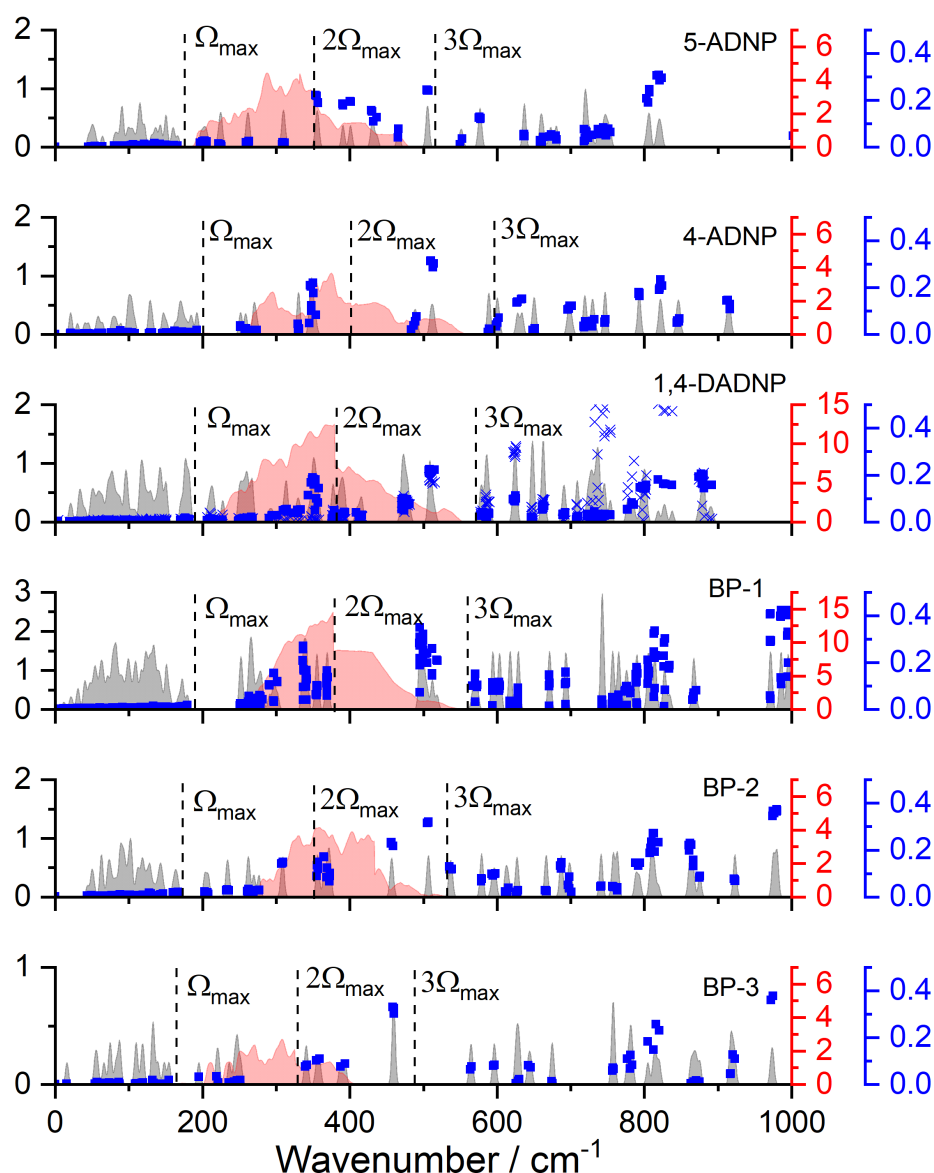


Figure 5.13: Shows the change in C-NO₂ (blue squares), C-N bonds (open blue circles), N-NO₂ (solid blue triangles) and N-NH₂ (blue crosses) bond lengths for the weakest bonds averaged over each molecule, with respect to each vibrational mode, overlaid on the $g(\omega)$ and $\Omega^{(2)}$ for a number of well-studied EMs as well as the pyrazole EMs considered in this work.

It is clear from Figure 5.13 that there is at least some activation of the weak C-NO₂/N-NO₂ bonds within the up-pumping window for each of the EMs shown. Since this bond activation likely acts as an initiation trigger, the up-pumped density was re-evaluated when projected onto only modes containing this vibration (modes are deemed to contain sufficient bond activation if the eigenvector motion resulted in a deviation in the bond length that was $> 10\%$ of the pure stretching mode, which is normalised to 1.0). This simplification,

while crude, essentially represents the capture of only the energy which can directly lead to energetic performance, assuming the weak bond stretching is the trigger motion. For particularly sensitive EMs, a vast majority, if not all of the modes within the up-pumping window, contain structure deformation of the weak bonds, while less is present for less sensitive materials. The case of 1,4-DADNP shows that only three groups of frequencies show pronounced C-NO₂ activation, at ca. 350, 480 and 510 cm⁻¹; the latter two also show pronounced N-NH₂ activation, which was previously highlighted as a weak bond. This is in agreement with the previous partial $g(\omega)$ investigation. A large contribution to the vibrations removed below 380 cm⁻¹ comprise of wag, rock and twisting motions of the -NH₂ groups, primarily the group located at the 1-position on the pyrazole ring. Additionally, vibrations present at roughly 410 cm⁻¹ are almost exclusively twisting of the 1-position -NH₂ group. Re-evaluating the up-pumped density to just capture the modes associated with weak bond activation gives the plot shown in Figure 5.14.

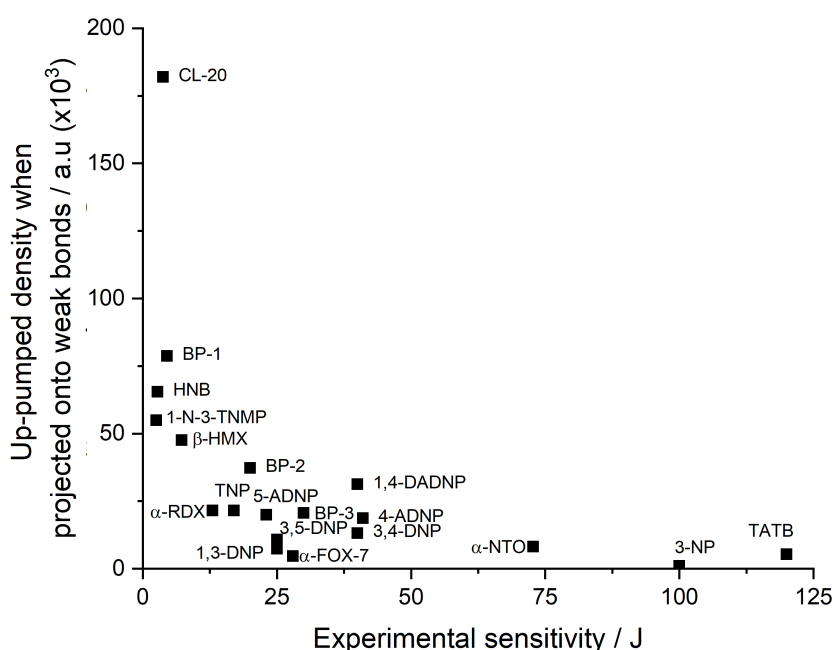


Figure 5.14: Shows the up-pumped density projected onto modes showing bond stretching behaviour for the weak bonds highlighted in red in Figure 5.12 vs. experimental sensitivity.

The relationship outlined in Figure 5.14 is very similar to that shown in Figure 5.8 with two key differences. Firstly, 1,4-DADNP now appears to fall in a more expected place while being treated consistently with the other data points. Despite this, it is still slightly over predicted with respect to the general trend. Secondly, all materials have a decreased up-pumped density on account of the projection being counted onto fewer modes; the one exception here is CL-20, as all modes within the up-pumping window contain activation of the weak bonds its position is unchanged.

Since the strong trend outlined in Figure 5.8 is actually improved upon through consideration weak bond stretches, this suggests that the vibrational up-pumped density can be used to assess structural features that are attributed with high sensitivity. As such the Figure 5.11 has been replotted for the pyrazoles only (such that structure/property relationships can be developed for the EM skeleton), this time with the up-pumped density projected onto weak bonds. The points are coloured to represent the number of weak bonds on the structure, shown in Figure 5.15 (4 - red, 3 – yellow, 2 – green and 1 – blue).

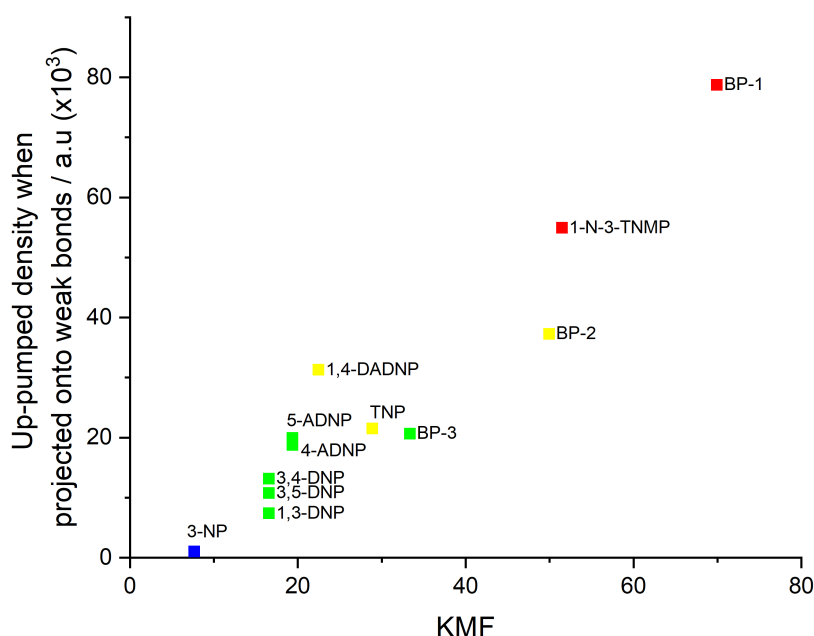


Figure 5.15: Shows the up-pumped density projected onto modes showing bond stretching behaviour for the weak bonds vs. experimental sensitivity. Colours represent the number of weak bonds in the structure (warmer colours signify an increased number of weak bonds).

Figure 5.15 clearly indicates that with an increase in number of weak bonds, an associated increase in the predicted sensitivity is noted. Additionally, an increase in KMF is associated with both increased predicted sensitivity and weak bond count. The EMs with an increased number of weak bonds in their structure also have increased numbers of -NO₂ groups (as a direct result of C – NO₂ bond commonly being weakest bond). The primary outlier to this trend is BP-3, which is slightly more flexible than TNP and 1,4-DADNP whilst having one less weak bond than both, despite this it is predicted to be slightly less sensitive than both. While it is commonly known that the -NO₂ group is an explosophoric group and increasing the number present in the molecular structure results in a general increase in sensitivity, this data presents a quantitative validation to a previously unquantified observation. Namely that the increase in number of nitro groups leads to both an increased number of low energy doorway modes which mediate up-pumping of energy (through an increase in KMF) and an increase in activation of weak bonds within the up-pumping window.

From this, a number of structure/property relationships can be developed for the impact sensitivity of pyrazole-based EMs.

1. An increased KMF (through addition of flexible/rotational groups) results in increased up-pumping capacity of the EM.
2. Addition of weakly bound explosophoric functional groups (most commonly -NO₂) results in increased target mode behaviour in the up-pumping window (as well as an associated increase in up-pumping capacity through means of increasing KMF).
3. More sensitive pyrazole EMs have a greater extent of weak bond stretching in the up-pumping window.

5.3.3 Conclusions

In conclusion, a test set of pyrazole-based EMs that presented various structural chemistry trends and that encompassed a broad range of reported impact sensitivity values have been studied by the vibrational up-pumping model. The predicted impact sensitivity values were found to be largely in excellent agreement with reported experimental values, with the key exception

of 1,4-DADNP that was dramatically over predicted. It was found that a significant proportion of the vibrations within the up-pumping window of 1,4-DADNP were primarily comprised of motions based on the C-NH₂ groups, which are unlikely to be associated with an energetic response. As such the up-pumped density of 1,4-DADNP was re-evaluated to project only onto modes with pronounced C-NO₂ character. While crude, this approach resulted in a far better agreement with experimental sensitivity of 1,4-DADNP but was not readily applicable to other EMs considered. In order to rectify this, a more robust methodology in which only projection onto vibrations containing stretches of weak bonds (stretching character determined by the script outlined in Chapter 2, and bond force constants calculated using LModeA) was considered in the generation of the up-pumped density. This approach had the same effect for 1,4-DADNP, in that it dramatically lowered its predicted sensitivity to nearer what would be expected based on its experimental value. This same treatment reassuringly did not have too drastic an effect on the predictions for the other eighteen EMs, simply shifting all up-pumped density values to a lower number. Whilst almost certainly oversimplifying the problem of target mode determination, this approach shows that projecting onto particular modes does not break the observed trend and in fact enhances it. It is also worth noting that the general form of the prediction graph, which is based on Γ -point only $g(\omega)$ plots essentially only offers a distinction between the very sensitive EMs and the less sensitive EMs which this approach still achieved. Its ability to rank the IS ordering for the latter is particularly limited. An obvious next step is to repeat the process using $g(\omega)$ that more fully sample the Brillouin zone.

The primary motivation for the consideration of a series of structurally similar EMs (pyrazole based) was to develop meaningful structure/property relationships which can be used in the future to guide the material design process towards tailored energetic properties. There are two primary attributes that must be considered when attempting to understand the origin of a high predicted sensitivity (from vibrational up-pumping) which are the ability to channel energy into the higher wavenumber vibrations (up-pumping capacity) and the amount and nature of vibrations able to capture this energy. This work

has shown that there is an excellent agreement between the number of doorway modes per Z and the KMF – a measure of molecular flexibility, suggesting that flexibility of molecular structure allows for increased up-pumping capacity. Additionally, increasing the number of weak bonds in the system results in both an increase in KMF and capture potential. This work has therefore given credence to the long-observed notion of increased nitro group count leading to increased impact sensitivity.

5.4 Tetrazole Investigation

5.4.1 Introduction

Tetrazoles are a commonly used skeleton for a number of EMs due to their high nitrogen content, as well as the ability to substitute a variety of functional groups on to both the carbon and nitrogen atom positions, resulting in high structural diversity and resulting material properties [36, 37]. High nitrogen content is desirable as the thermodynamic driving force for the expulsion of nitrogen gas upon detonation is present leading to high amount of stored chemical energy within the structure [7].

To assess how the degree of substitution altered the impact sensitivity of substituted tetrazole EMs, a selection of six compounds were taken from Fischer et al [38]. A positive of taking all the EMs from the same body of work is that their experimental impact sensitivities were determined by the same group, likely ruling out a large amount of the user error and machine inconsistencies. As such a computational investigation to predict the sensitivity of the tetrazole EMs namely: 2,5-bis(2-nitro-2-azapropyl)-nitriminotetrazole (LUVPOI, IS = 2 J), 1-methyl-5-(2-nitro-2-azapropyl)-nitriminotetrazole (LUVNIA, IS = 5 J), 2-methyl-5-(2-nitro-2-azapropyl)-nitriminotetrazole (LUVPAU, IS = 8 J), 1-(2-nitro-2-azapropyl)-tetrazole (LUVPIC, IS = 15 J), 1-methyl-4-(2-nitro-2-azapropyl)-aminotetrazole (LUVPEY, IS = 40 J) and 1-(2-nitro-2-azapropyl)-5-aminotetrazole (LUVNAS, IS > 100 J) was completed [38]. Their molecular structure alongside the crystal structure, CSD identifier and experimental impact sensitivity values are outlined in Figure 5.16.

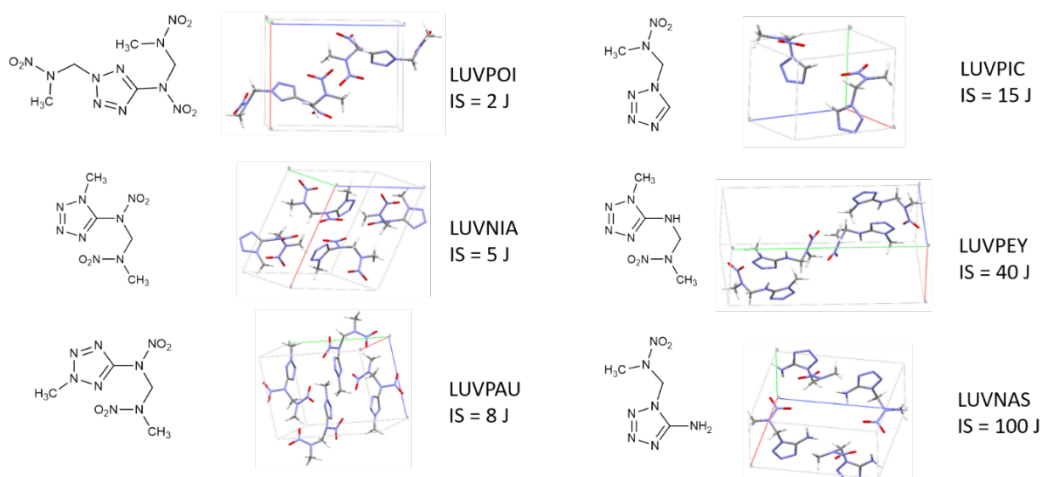


Figure 5.16: Shows the structure, primitive crystallographic unit cell and CSD identifier (which will be used to refer to the structures throughout) for each of the tetrazole EMs considered in this Section [38].

The CSD identifiers outlined in Figure 5.16 will be used throughout the Section to refer to the structures for clarity. It is clear to see that the structures of these materials are significantly more structurally complex than the pyrazoles considered previously as there are a number of polysubstituted N-alkyl chains with differing numbers of $-\text{NO}_2$, $-\text{CH}_3$ and $-\text{NH}_2$ groups whereas the pyrazoles were primarily nitrated. This provides an opportunity to explore the effect of additional functional group variation on the predicted sensitivity of the materials. Within the set of tetrazoles shown in Figure 5.16, there are a number of structures that differ by placement of one group, such as LUVNIA and LUVPAU which are comprised of the same atoms with only the location of the ring based $-\text{CH}_3$ group being different, and the resulting experimental impact sensitivities are similar (5 and 8 J, respectively). LUVPEY is also structurally similar to LUVNIA, with the only difference being the removal of the N-based NO_2 group on the N-alkyl chain, a structural modification that reduces the impact sensitivity from 5 to 15 J. Finally, both LUVPIC and LUVNAS only differ through the introduction of an amino group in the latter, which has caused a dramatic decrease in impact sensitivity (15 to 100 J).

These small structural changes alongside their wide span in experimental impact sensitivity values are the reason this test set was an attractive study case to further test the structure/property relationships that were observed in the pyrazole dataset.

5.4.2 Results and Discussion

Geometry optimisation and Γ -point frequency calculations were performed by masters project student Cian Byrne. Repeat of LUVNIA calculation (to remove an imaginary frequency) and all subsequent data processing was redone for this thesis.

Geometry optimisation calculations were performed using the convergence criteria outlined in Section 5.2 such that the geometry was sufficiently converged for successful frequency calculations to be completed. Comparison between the experimental and optimised unit cell parameters, as well as the percentage change in unit cell volume as a result of optimisation are shown in Table A3 in Appendix A. There is excellent agreement between the experimental and optimised unit cell parameters exemplified by the very small % change (significantly below the recommended change of less than 5 % in most cases) [30]. As such, the optimised geometries were used as the input structure for Γ -point vibrational frequency calculations. All of the structures returned 3N real vibrations suggesting that the geometry convergence criteria were sufficiently tight. Using the calculated vibrational modes, the locations of the top of the phonon bath (Ω_{\max}) were determined through examination of the CoM deviation per mode. This was completed using the script outlined in Chapter 2. The average deviation in CoM per molecule per vibrational mode with the location of Ω_{\max} marked is shown in Figure 5.17 for each of the six tetrazole based EMs.

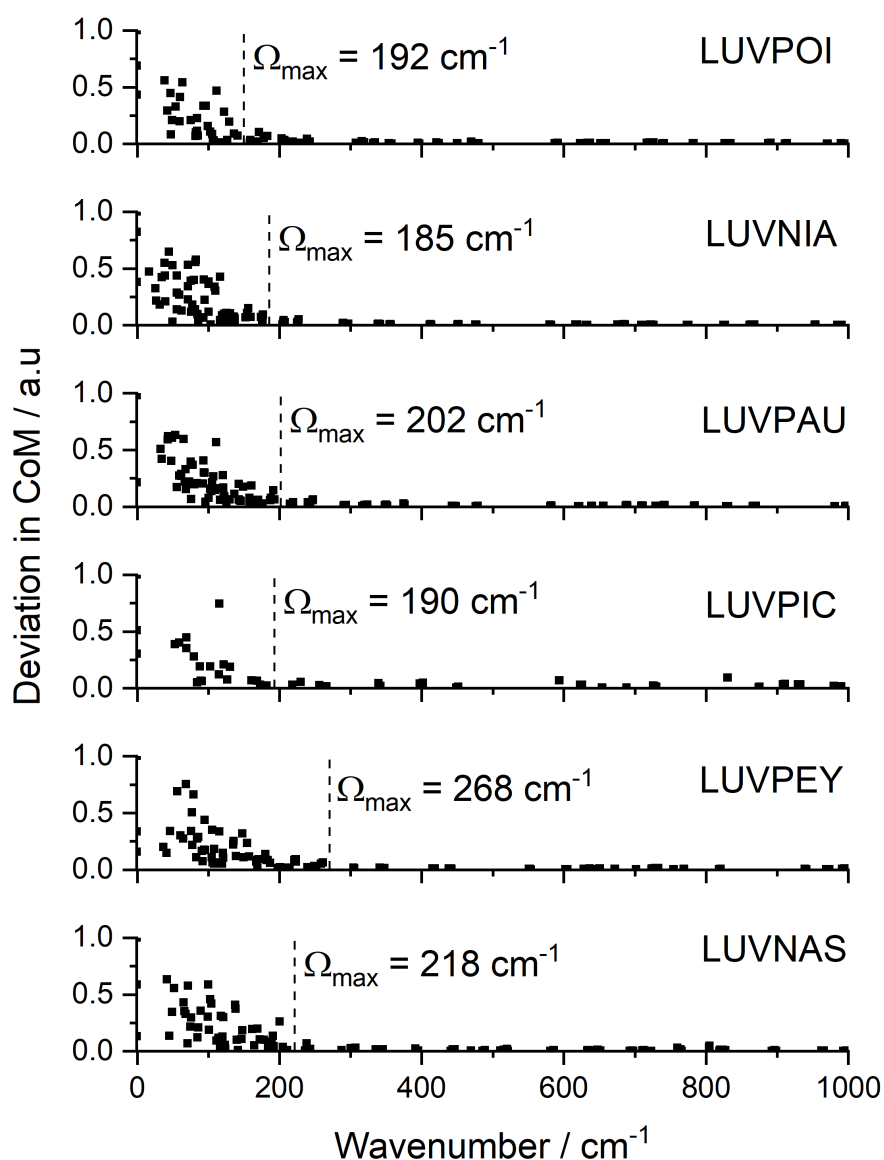


Figure 5.17: Shows the average deviation in CoM (normalised to unity) per molecule per vibrational mode of each of the tetrazole EMs considered in this work with Ω_{\max} denoted using a dashed line.

It is clear from Figure 5.17 that the expected decay in CoM motion is observed as the energy of the vibrational modes is increased, indicating localisation of vibrational motion into the molecular modes. The location of Ω_{\max} was determined from the plots shown in Figure 5.17, following the standard 5 cm^{-1} Gaussian smearing of the calculated peaks in the $g(\omega)$. This was done using the script outlined in Chapter 2, to give the output $g(\omega)$ plots in Figure 5.18.

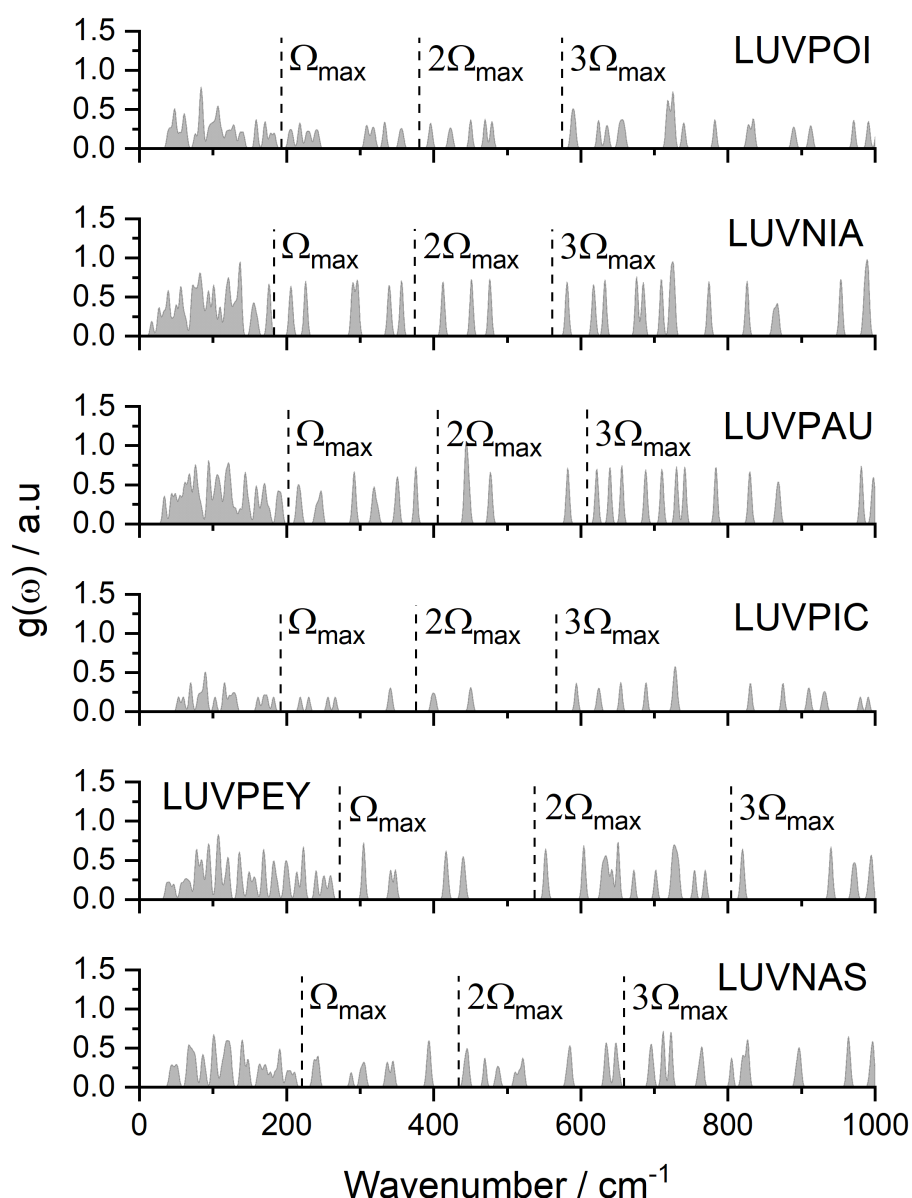


Figure 5.18: Shows the $g(\omega)$ spectrum (grey) for the six tetrazole-based EMs with a Gaussian smearing of 5 cm^{-1} applied, multiples of Ω_{max} are denoted using dashed lines.

As can be seen from Figure 5.18, the $g(\omega)$ spectra for the six tetrazoles are all distinct from one another, with LUVNIA and LUVPAU being the two with the most similar vibrational landscape which would be expected as they are isomers of one another. Comparison between the structures that differ by removal or addition of a functional group (LUVNIA and LUVPEY / LUVPIC and LUVNAS) show that such small changes can have a rather large effect on the doorway region of the $g(\omega)$. This is expected as such modes are often dominated by librational motion of functional groups – meaning a change in

the number will have a dramatic effect on the spectral composition and potentially the crystal up-pumping capacity.

In order for the impact sensitivity to be predicted using the vibrational up-pumping procedure the shock temperature needs to be calculated through consideration of the ratio of $C_{\text{tot}}/C_{\text{ph}}$. The contributions of each vibrational mode to the heat capacity for each of the tetrazoles are shown in Figure 5.19.

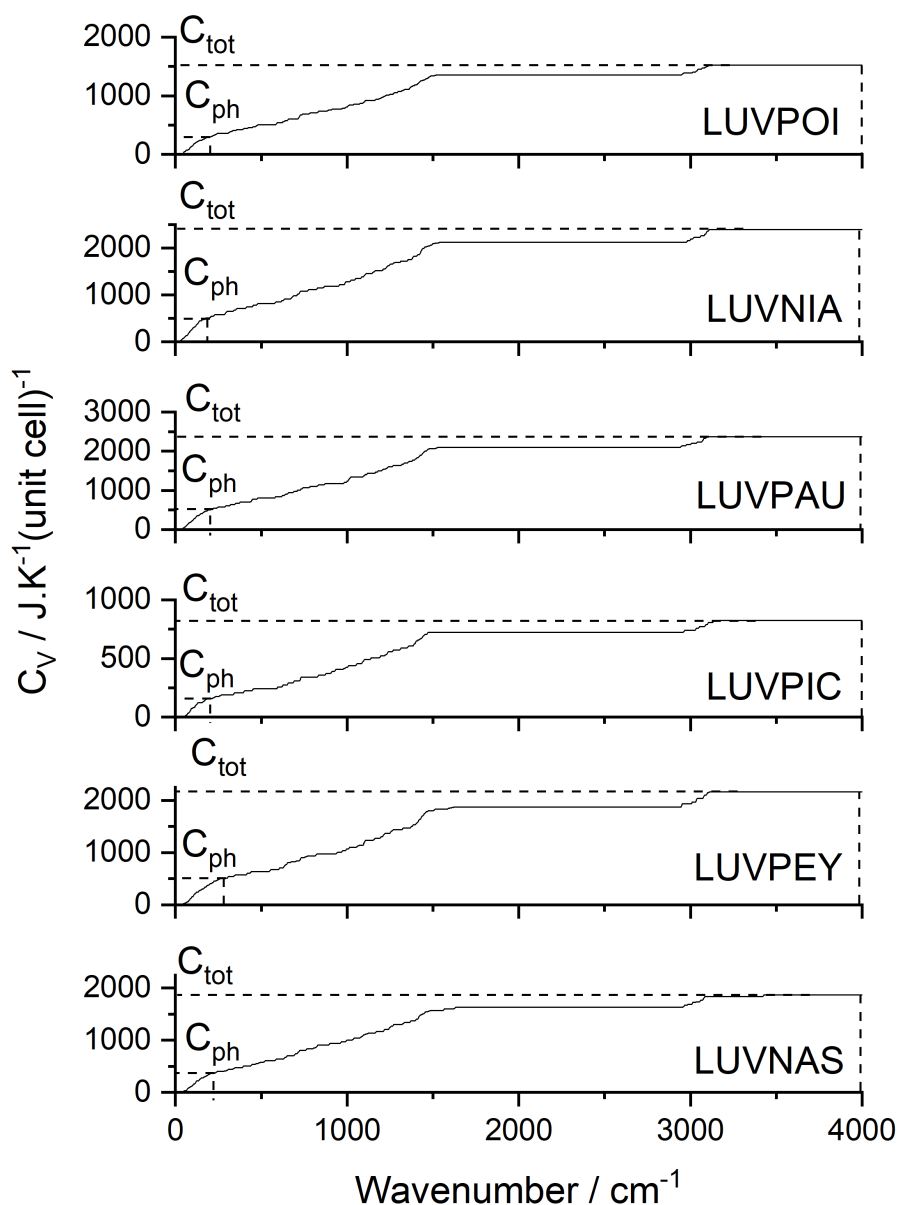


Figure 5.19: Shows the contributions of each vibrational mode to the cumulative heat capacity with both C_{tot} and C_{ph} marked using dashed lines.

Using the ratio of $C_{\text{tot}}/C_{\text{ph}}$ (based on $C_{\text{tot}}/C_{\text{ph}} = 5.22$ equates to a shock temperature of 3423 K) the shock temperature was calculated for each of the

tetrazole EMs [4]. With this step complete, all the input parameters required for predicting the sensitivity through vibrational up-pumping have been determined and are outlined in Table 5.3.

Table 5.3: Outlines the input parameters for the vibrational up-pumping procedure alongside the experimental sensitivity and the up-pumped density for each of the tetrazole EMs considered in this Section. Experimental IS values are taken from Reference [38].

| EM | Ω_{\max} | Z | Z(6+Y) | Y | $C_{\text{tot}}/C_{\text{ph}}$ | $T_{\text{shock}} / \text{K}$ | Experimental IS / J | Up-pumped density / a.u |
|--------|-----------------|---|--------|----|--------------------------------|-------------------------------|---------------------|-------------------------|
| LUVPOI | 192 | 2 | 38 | 13 | 5.23 | 3430 | 2 | 103468 |
| LUVNIA | 185 | 4 | 64 | 10 | 4.67 | 3062 | 5 | 49309 |
| LUVPAU | 202 | 4 | 64 | 10 | 4.67 | 3062 | 8 | 67298 |
| LUVPIC | 190 | 2 | 22 | 5 | 5.21 | 3416 | 15 | 19744 |
| LUVPEY | 268 | 4 | 60 | 11 | 4.28 | 2807 | 40 | 24335 |
| LUVNAS | 218 | 4 | 48 | 6 | 5.00 | 3279 | 100 | 47694 |

The data outlined shows the input parameters for the vibrational up-pumping procedure meaning that the impact sensitivity was able to be predicted, the generated $\Omega^{(2)}$ for each structure overlaid on the underlying $g(\omega)$ for each of the tetrazole-based structures is shown in Figure 5.20.

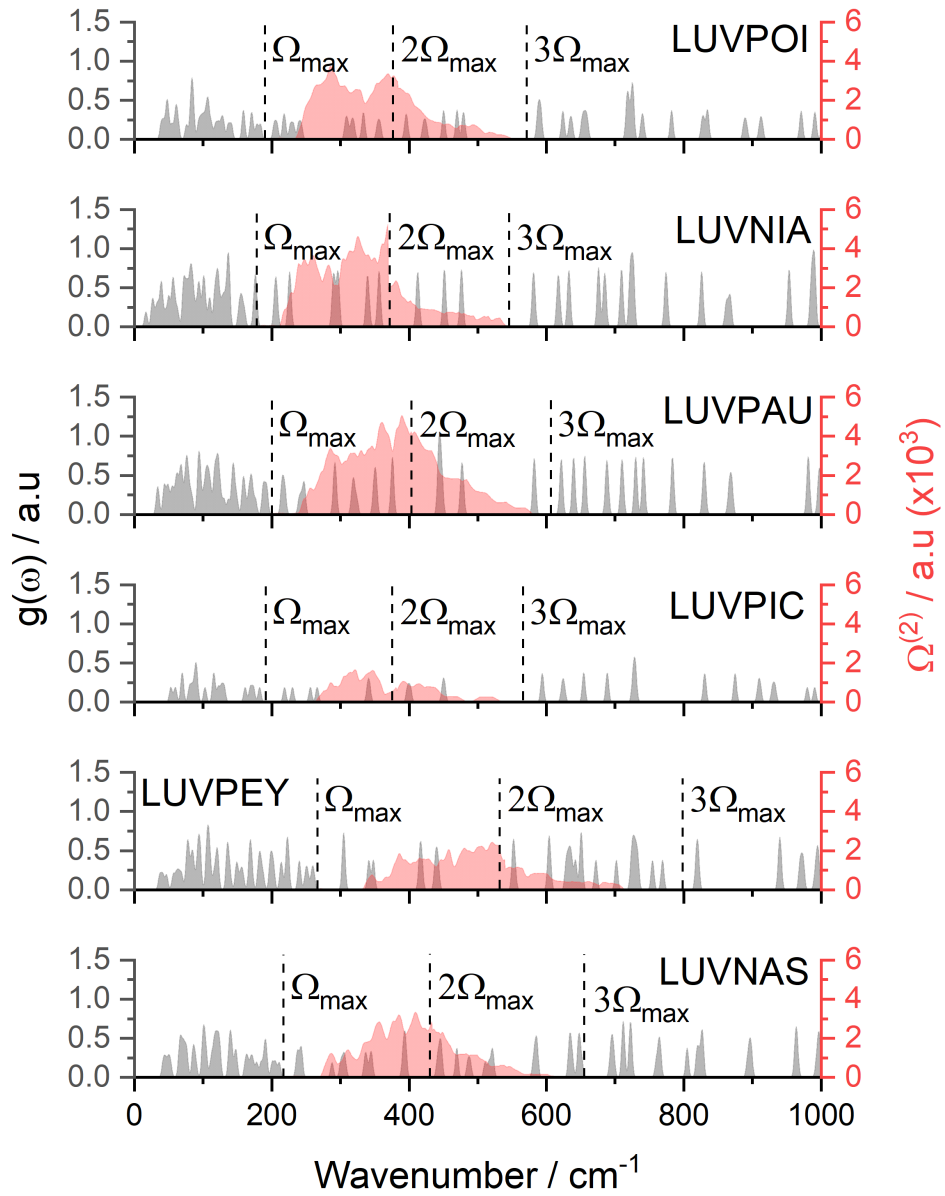


Figure 5.20: Shows the $\Omega^{(2)}$ (red) overlaid on top of the $g(\omega)$ (grey) with multiples of Ω_{\max} denoted using dashed lines.

The compound ordering in Figure 5.20 is ranked from most to least sensitive, and shows that the magnitude of the $\Omega^{(2)}$ is generally larger for the more sensitive EMs. The primary exception to this observation is LUVNAS, which appears to have a larger $\Omega^{(2)}$ trace than the more impact sensitive LUVPIC and LUVPEY. In order to generate a predicted sensitivity the integral of $\Omega^{(2)}$ projected onto the modes in the underlying $g(\omega)$ was determined. This yielded the up-pumped density which was the plotted against the experimental sensitivity and compared to a number of well-studied structures. This is shown in Figure 5.21.

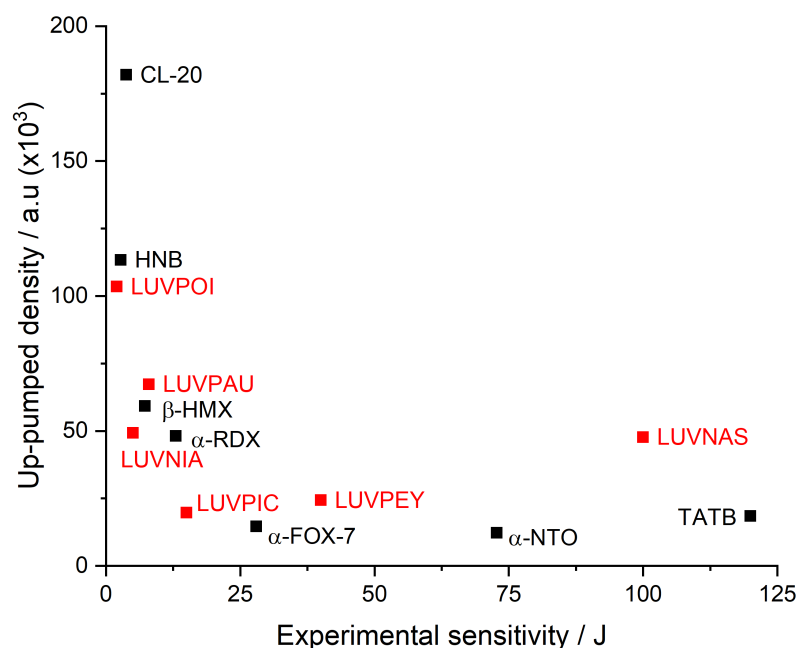


Figure 5.21: Shows the up-pumped densities of the tetrazoles considered in this section (red) ranked alongside a number of well-studied molecular EMs (black) [4, 6].

As can be seen in Figure 5.21, there is a reasonable correlation shown albeit with a number of small inconsistencies with the experimental sensitivity value ranking. Reassuringly, LUVPOI is predicted to be the most sensitive EM in this group, and LUVPAU sits slightly above β -HMX which has a very similar experimental sensitivity. LUVNIA appears to be slightly under predicted with respect to its experimental sensitivity, with a calculated value similar to α -RDX. LUVPIC and LUVPEY both appear to be in good agreement with experimental sensitivity; the apparent reverse order ranking is likely an artefact of the loss of differentiation in prediction order ranking seen throughout the work presented in this thesis when Γ -point only $g(\omega)$ are used for up-pumping. Finally, LUVNAS appears to be over predicted compared to its experimental impact sensitivity value of 100 J. Attempts to explore this via $\Omega^{(2)}$ projection onto molecular modes associated with bond stretching character of weak bonds, as developed for the pyrazoles, will be explored latter on in this section.

The origin of the sensitivity of the tetrazole EMs will once again be investigated through consideration of two primary material characteristics: firstly, the up-

pumping capacity, i.e., the ability for the material to channel energy upwards into higher energy vibrational modes, and secondly the consideration of the amount of probable target mode activation within the up-pumping window.

As with the pyrazole EMs, the former metric was investigated through a count of the number of doorway modes per Z with increasing structure complexity, as well as comparison to the Keir molecular flexibility (KMF) metric [18]. Results are shown in Table 5.4.

Table 5.4: Outlines the input parameters for the vibrational up-pumping procedure alongside the experimental sensitivity, number of doorway modes and the KMF (calculated by Equation 5.1) for each of the tetrazole EMs considered in this Section.

| EM | Experimental IS / J | Up-pumped density / a.u | # Doorway modes per Z | KMF |
|--------|------------------------|-------------------------------|-----------------------------|-------|
| LUVPOI | 2 | 103468 | 8 | 97.69 |
| LUVNIA | 5 | 49309 | 6 | 49.96 |
| LUVPAU | 8 | 67298 | 6 | 49.96 |
| LUVPIC | 15 | 19744 | 3 | 21.41 |
| LUVPEY | 40 | 24335 | 4 | 33.41 |
| LUVNAS | 100 | 47694 | 4 | 24.38 |

As can be seen from Table 5.4, the general trend of more sensitive materials having increased numbers of doorway modes and KMF values are held, with the primary exception being LUVPIC which appears to have lower values for both metrics compared to those obtained for the rest of the data set. It should also be noted that LUVPIC is slightly under predicted by the vibrational up-pumping model. The relationship between the up-pumped density and the number of doorway modes per Z is shown graphically in Figure 5.22.

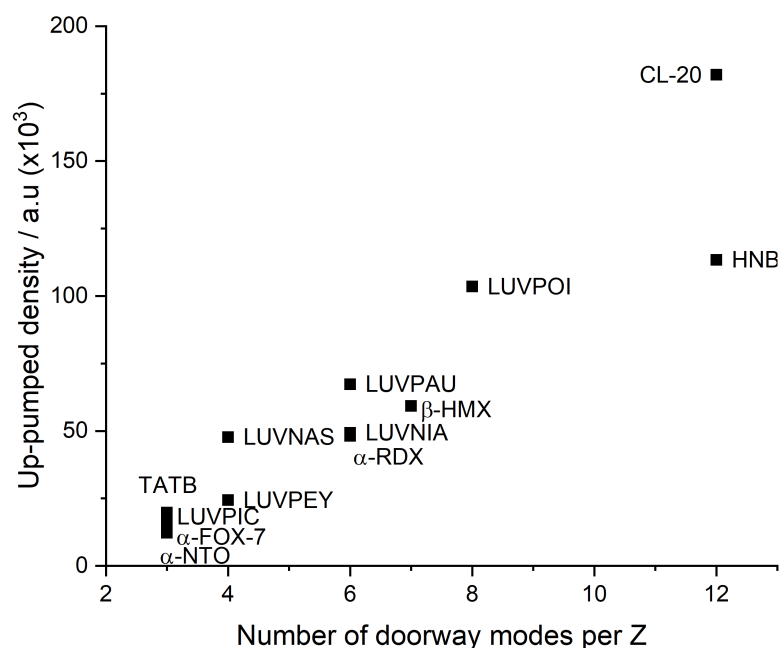


Figure 5.22: Shows the relationship between the up-pumped density and number of doorway modes per Z for the tetrazole EMs and a number of previously studied EMs [4, 6].

Figure 5.22 shows that as the number of doorway modes per Z increases, there is a general increase in up-pumped density. The reason for this is once again that an increased number of vibrational modes in the doorway region symbolises an increased number of vibrations that are able to scatter energy upwards, resulting in a more pronounced $\Omega^{(2)}$. As was stated previously, the magnitude of the $\Omega^{(2)}$ does not directly lead to sensitivity as this energy must still be captured by vibrational modes with energetic character. The character of doorway vibrational modes are generally comprised of librational motion of the functional groups, suggesting that those with lower energy barriers to this motion (i.e. increased flexibility) are likely to have more doorway modes. For this reason, KMF was compared to the number of doorway modes per Z; as well as the relative up-pumped density this is shown graphically in Figure 5.23 (a and b respectively).

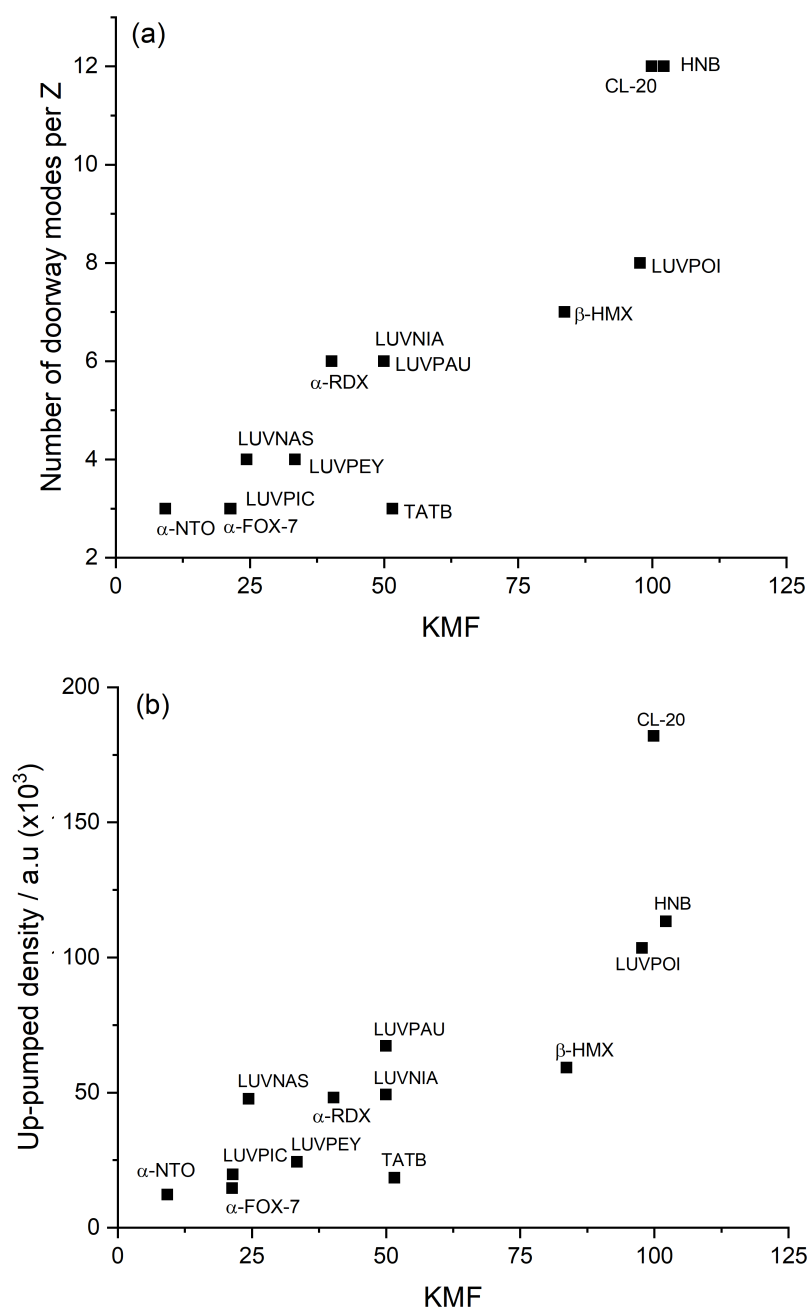


Figure 5.23: Shows the relationship between KMF and the number of doorway modes per Z (a) and the up-pumped density (b) for the tetrazole EMs as well as other well-studied molecular EMs [4, 6].

As the molecular flexibility of the EMs increases it is clear that there is a rough increase in the number of doorway modes per Z, which likely arises due to an increased prevalence of librational motion of functional groups which falls in this region of the vibrational spectrum. The number of doorway modes per Z is slightly smaller for LUVPOI than its KMF value would suggest; however, it still has a larger number of doorway modes than β -HMX and is predicted to be

a primary as the experimental work would suggest, so this is not too concerning. This increase in motion is then attributed with an increased phonon scattering potential, and thus the larger $\Omega^{(2)}$ trace, as previously discussed. This argument is in agreement with the general findings reported earlier in this Chapter. This, alongside the pyrazole study in the previous Section, suggests that it could be used as a preliminary scouting tool for the sensitivity of novel EMs to be quickly (and crudely) ascertained based purely on its molecular structure, a prediction that is available in seconds. The differences between LUVNIA and LUVPEY, for instance, which is just the addition of a substituent -NO₂ group on the compound side chain, is quite stark.

While KMF appears to be able to account for the ability of a material to generate a large $\Omega^{(2)}$ trace, it yields no information regarding the number of capture states across the up-pumping window and whether the nature of those states would elicit an energetic response. For this reason, consideration of the weakest bonds in the tetrazole EMs and the ability of those bonds to be activated by the modes present in the up-pumping window (i.e., trigger modes) was explored next. The up-pumped density would then be re-evaluated when projected only onto such vibrational modes [33, 34, 35]. In the case of the pyrazole EMs, the C-NO₂ and N-NO₂ bonds were found to be weakest bonds, however for the tetrazole EMs, local mode analysis showed that while the N-NO₂ bonds are very weak, the chain-based C-N bonds were also found to be comparably weak. Figure 5.24 shows the structures drawn with their weakest bonds highlighted in red, alongside the associated local force constants.

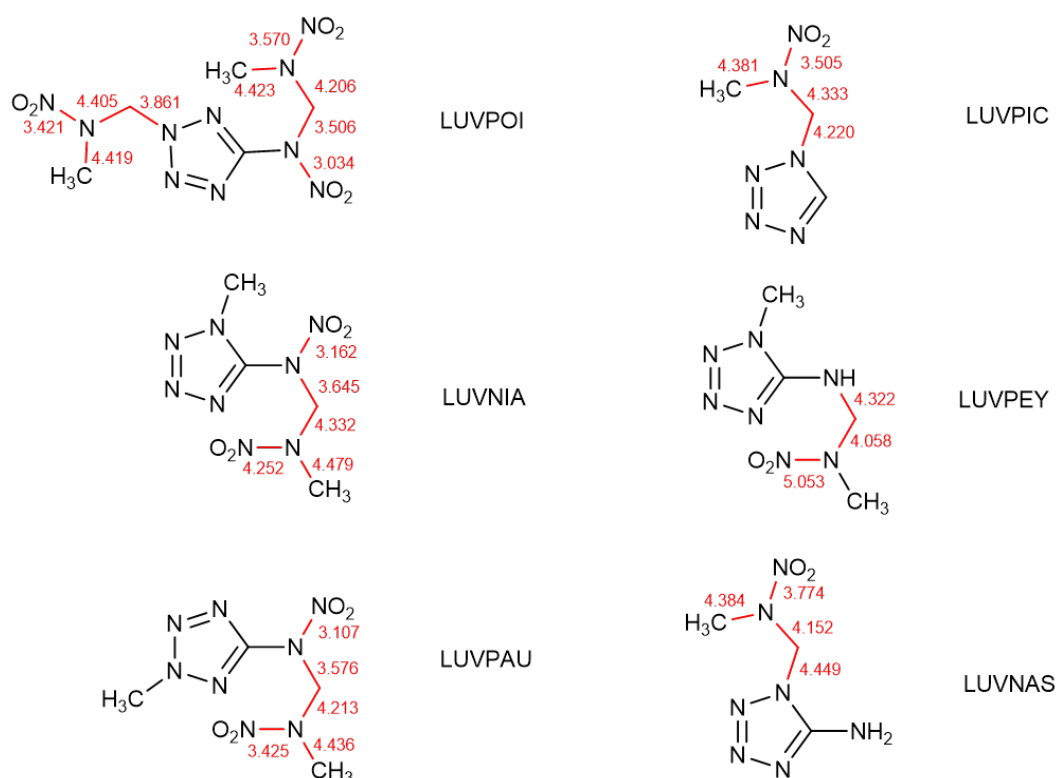


Figure 5.24: Shows the six tetrazole structures considered in this Section with weak bonds outlined in red with their relative bond strengths shown alongside them. Bonds shown in black have local force constants above $4.5 \text{ mDyn}\text{\AA}^{-1}$ except for the N-NO₂ bond in LUVPEY. The force constants were calculated using local mode analysis as implemented in LModeA [13].

The data obtained from the local force constant analysis can be summarised by the following key observations:

1. The weakest bond for each of the structures is the N-NO₂ bond, with LUVPEY being the only exception, where it is surprisingly strong. The three most sensitive energetics (LUVPOI, LUVNIA and LUVPAU) present the weakest N-NO₂ bonds, each being $< 3.5 \text{ mDyn}\text{\AA}^{-1}$.
2. All structures also present relatively weak C-N bonds in the substituent chains.
3. The position of the methyl group on the ring notably weakens the N-NO₂ bonds on the long-chain substituents, this can be seen through comparison of LUVNIA and LUVPAU. In LUVNIA, the methyl group is

located in the alpha-position with respect to the long chain, whereas in LUVPAU it is located at the beta-position, resulting in weaker N-NO₂ bonds (the largest change is observed for the terminal N-NO₂ bond). The weakening of the N-NO₂ bond nearest the ring is likely as a result of removal the H-bond between the -NO₂ and -CH₃ groups. The dramatic weakening of the terminal N-NO₂ bond on the other hand is potentially as a result of steric clash with the newly positioned -CH₃ group.

4. The addition of a second N-NO₂ group on the substituent chain close to the aromatic ring weakens the terminal N-NO₂ bond as can be seen for the comparison between LUVPEY and LUVNIA (5.053 to 4.242 mDynÅ⁻¹ respectively).

The deviation in N-NO₂ and C-N bond lengths (i.e., those marked in red in Figure 5.24) were tracked across the eigenvector motions and normalised (i.e., the most pronounced deviation scaled to one) using the script outlined in Chapter 2. The output is shown alongside the $g(\omega)$ and $\Omega^{(2)}$ traces in Figure 5.25.

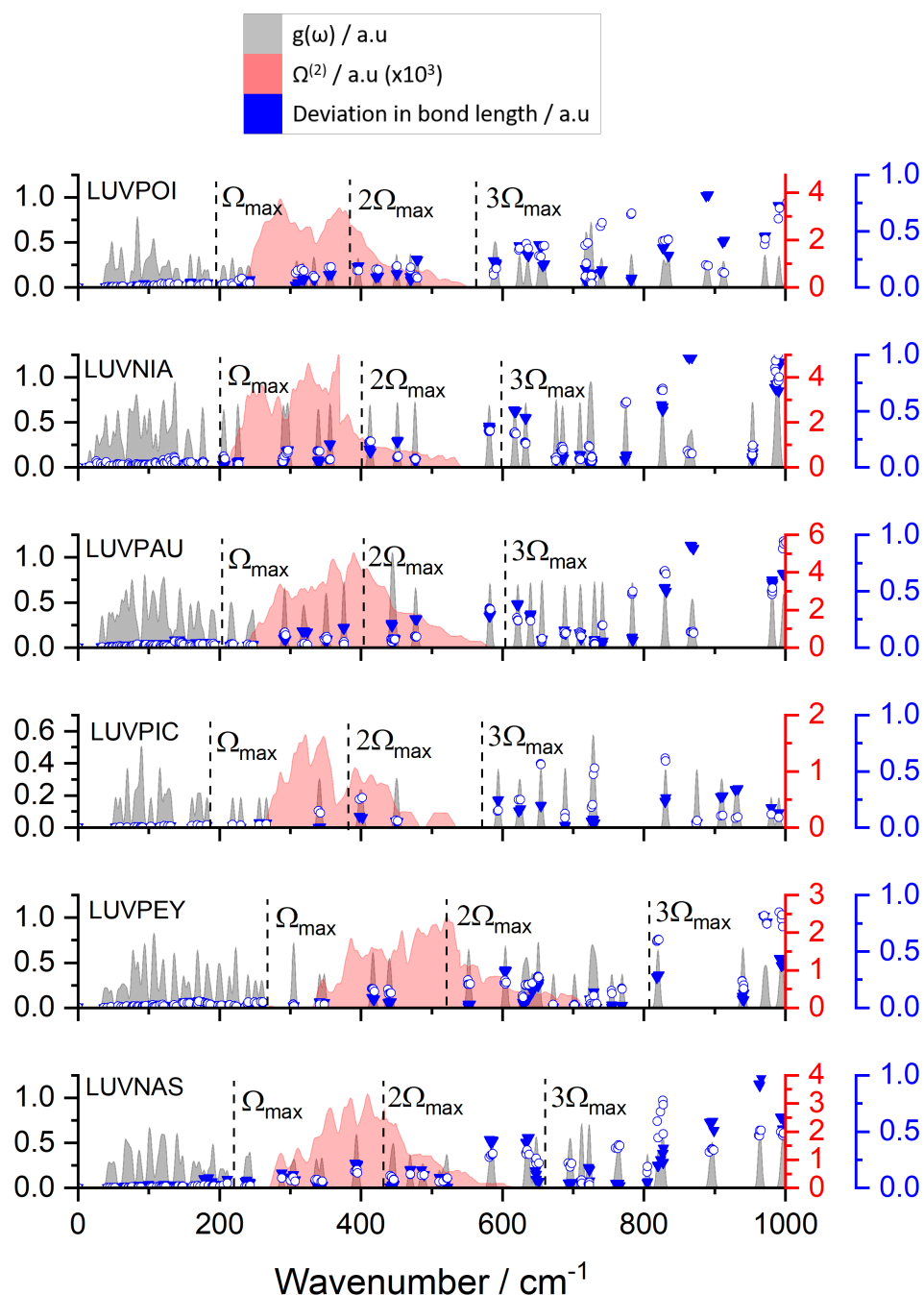


Figure 5.25: Shows the average change in C-N (blue open circles) and N-NO₂ (blue triangles) bond lengths for each vibrational mode overlaid on the $g(\omega)$ (grey) and $\Omega^{(2)}$ (red) for the tetrazole EMs considered in this Section.

As can be seen from Figure 5.25, there is slight activation of both the N-NO₂ and C-N bonds in each of the EMs within the up-pumping window, suggesting that impact energy will be directly transferred into bond stretching motion. Once again the up-pumped density was re-evaluated by projecting the $\Omega^{(2)}$ onto only vibrational modes which result in a change in weak bond length > 10 % of the pure stretching frequency. The re-evaluated up-pumped density

values plotted against those of the well-studied materials (outlined alongside the pyrazole EMs in the previous Section) are shown below in Figure 5.26.

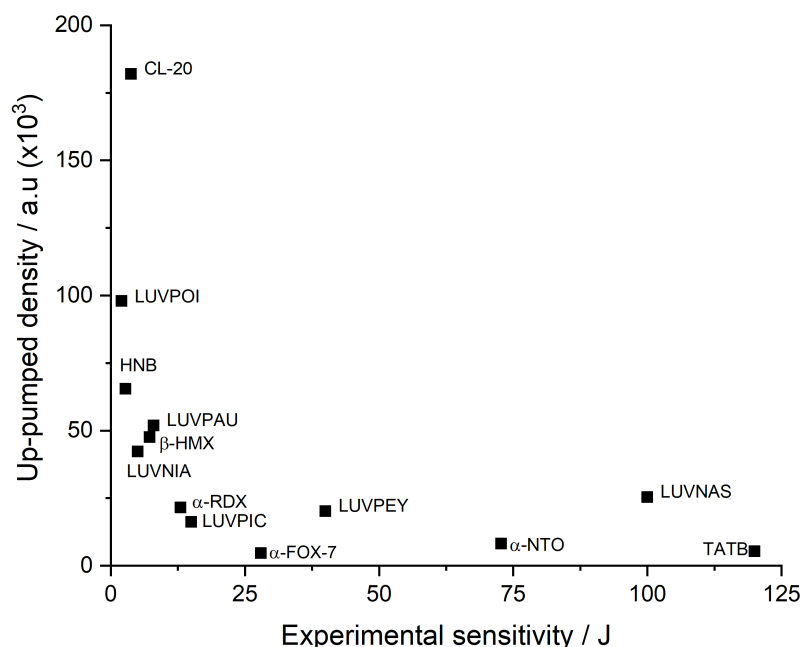


Figure 5.26: Shows the relationship between the up-pumped densities (when projected onto weak bond partial stretch modes) and the experimental sensitivity for the tetrazoles considered in this Section and the previously studied EMs [4, 6].

As can be seen from Figure 5.26, the trend outline is very similar to that obtained for the pyrazole study. There is good agreement between predicted and experimental sensitivity for all tetrazoles considered. LUVPEY and LUVNAS are slightly over predicted with respect to materials of similar sensitivity, while LUVPAU and LUVNIA are in the right ballpark but are the wrong way round. Despite these issues, there is good distinction between predicted primary and secondary EMs (with β -HMX marking the distinction between the two material classifications). As was done for the pyrazole EMs the up-pumped density when projected onto the weak bonds was plotted against the KMF with colour coded points referring to the number of weak bonds in the structure is shown in Figure 5.27 (with warmer colours representing an increased number of weak bonds; red – 9, yellow – 5, blue – 4 and green – 3).

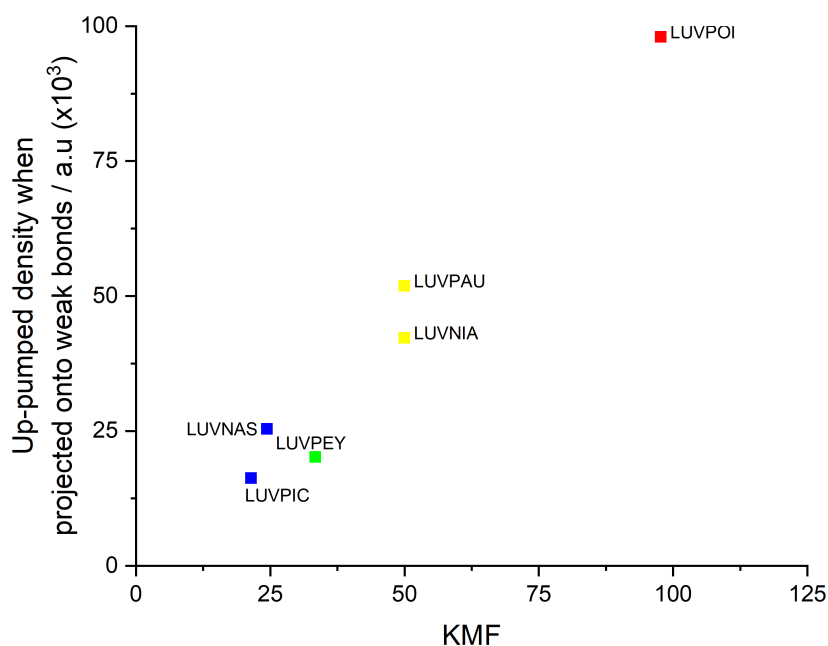


Figure 5.27: Shows the up-pumped density when projected onto probable target modes (stretching of weak bonds) vs. KMF, with colours representing the number of weak bonds in the structure (warmer colours representing an increased number of bonds).

As can be seen from Figure 5.27 there is a good relationship between the up-pumped density from projection onto the weak bond stretch modes and the KMF. Additionally, an increase in both KMF and predicted sensitivity are present for the structures with a higher number of weak bonds with the exception of LUVPEY. It should be noted that both LUVPEY and LUVNAS were over predicted using the current model as was outlined previously. The reason LUVPEY has an increased KMF when compared to both LUVNAS and LUVPIC is the addition of a $-\text{CH}_3$ group to ring, increasing flexibility without introducing another weak bond. Similarly, to the pyrazole work, a series of structure/property relationships can be extracted from the data above.

1. Increasing the KMF of the molecules through addition of functional groups increased the up-pumping capacity of the material.
2. Increasing the number of weak bonds within the molecule increases the predicted sensitivity.

3. The number of weak bonds can be increased through addition of NO₂ groups, or through addition of weak C-N bonds in attached alkyl chains.

5.4.3 Conclusions

To conclude, the impact sensitivity of six tetrazole based EMs was predicted through the use of the vibrational up-pumping methodology and were found to be in reasonable agreement with the experimental sensitivity values, with slight overprediction of LUVNAS and underprediction of LUVNIA. The predicted sensitivities were rationalised through consideration of two material properties, namely the up-pumping capacity and the ability to capture up-pumped energy. The capacity of a material to up-pump energy into higher energy vibrations was found to correlate very well with the KMF (similar to the pyrazole study), which is attributed to an increased number of librational modes within the doorway region of more flexible EMs. Increased doorway region character allows for the generation of a more intense $\Omega^{(2)}$ trace. In an attempt to focus on the ability of an EM to capture up-pumped energy, the nature of the vibrational modes were explored to locate those which may elicit an energetic response. The bonds within the tetrazole EMs were investigated using gas phase LModeA calculations, resulting in bond strength information (mass decoupled force constants). The up-pumped density was then re-evaluated projecting only onto vibrational modes that result in change in the length of weak bonds (such modes were identified using the local mode script developed in this work – Chapter 2) with a similar degree of success (slight over prediction of LUVPEY and LUVNAS but improvement in the placement of LUVNIA). From this, as was the case for pyrazole EMs, it was determined that an increase in molecular KMF and the number of weak bonds in a structure results in increased sensitivity through mediating both increased energy transfer into higher energy modes and increased energy capture.

5.5 Nitrate Ester Investigation

5.5.1 Introduction

Nitrate esters are a common family of EMs derived from nitration of various naturally occurring sugars and polymers such as glycerine and cellulose. There are a number of both primary and secondary nitrate ester EMs which are generally very sensitive to both impact and friction [39]. One of the most well-known nitrate ester EM is PETN (pentaerythritol tetranitrate) which is highly sensitive and has very high energetic performance [7]. First synthesised in the early 1900s it has commonly been used in a number of industrial/commercial applications such as blasting caps and detonation chords. More recently the material properties of PETN have been found to be altered when mixed with plasticisers and additional EMs (such as RDX), resulting in the mouldable and relatively safe to handle military explosive Semtex [40, 41]. Moreover, PETN has a number of medical uses such as in the treatment of angina (lack of blood flow to the heart muscle) in which it acts as a vasodilator [41]. Due to the vast number of uses of PETN a large number of structural analogues have been synthesised with a view to improving the safety and performance of the EM. A number of such structures are found to be exceptionally sensitive to impact, to such a degree that without the introduction of plasticisers they are commercially unviable.

Manner et al. reported an experimental IS study on a series of PETN derivatives that are all based on the substitution of a single side chain [43]. This work suggested that the liquid and solid-state impact sensitivity values differed for the materials, with the liquid state being more sensitive.

An additional nitrate ester EM which is widely studied is nitroglycerin (1,2,3-propanetriol trinitrate, hereafter NG), the fully nitrated analogue of glycerol which is exceptionally sensitive [44]. Despite this it is often used to treat angina, much like PETN [45]. Interestingly NG is far more sensitive in its liquid form than in the solid-state (0.2 J compared to 14 J) which is the same trend observed by Manner et al. for the PETN derivatives [46].

Recent vibrational up-pumping work conducted by Bernstein, based on the overtone model (discussed in Chapter 1), gave promising results for the prediction of the impact sensitivity of PETN, predicting it to be a primary [47]. Jensen et al., have noted that using the assumed trigger linkage dissociation energy divided by the heat of detonation gives a good prediction of impact sensitivity for a number of solid EMs including nitrate esters. However, this does not give a good predictive measure for liquid sensitivities [35]. Both of these bodies of work appear to suggest that solid-state nitrate ester sensitivities are able to be reliably predicted to a reasonable standard.

The vibrational up-pumping methodology as used in this work has shown its ability to reproduce the experimental sensitivity values of a number of solid-state EMs, however, to date nitrate esters have not been looked into. As such, a computational investigation into four nitrate ester-based EMs was conducted, referred to as PETN, PO-PETN, CH-PETN (both of which are structural analogues of PETN with one of the side groups (-CH₂ONO₂) replaced with P=O and CH respectively – taken from Manner et al.,) and NG [43, 48, 49]. The molecular structures, alongside the corresponding crystallographic unit cells, are shown in Figure 5.28.

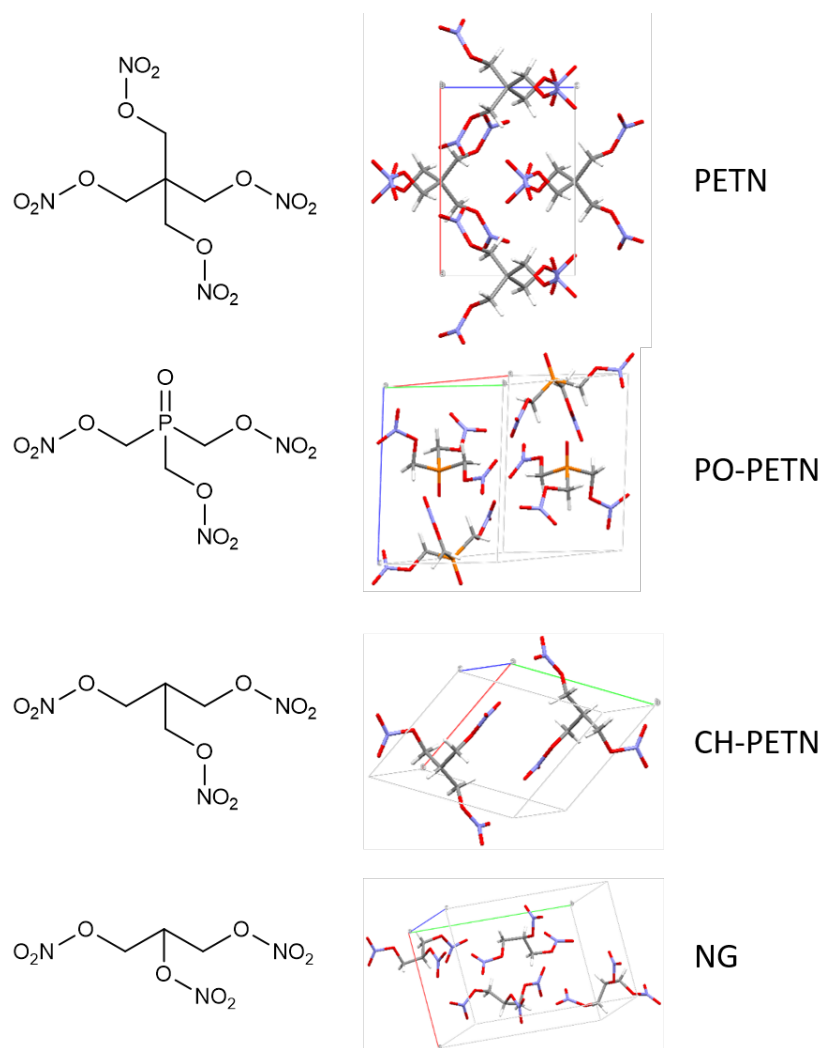


Figure 5.28: Shows the molecular structures and crystallographic unit cells of the nitrate ester EMs considered in this work.

The solid-state experimental impact sensitivities of the nitrate esters are as follows; PETN – 3 J, PO-PETN – 2 J, CH-PETN – 6 J and NG - 14 J [43, 46]. The main question to be addressed in this work is whether the vibrational up-pumping methodology is able to reproduce the experimental sensitivities of the solid-state nitrate esters and if so, could the origin of the sensitivity ordering be discovered through development of structure/property relationships.

5.5.2 Results and Discussion

Initially geometry optimisation calculations were completed using the calculation parameters outlined in Section 5.2 such that the geometry is sufficiently converged for a vibrational frequency calculation to be completed. Comparison between the experimental and optimised unit cell parameters

alongside the % change in the unit cell volume experienced throughout the optimisation process are shown in Table A3 in Appendix A. It should be noted that the reported crystal structure determinations of PO-PETN and CH-PETN had R factors of 8.02 and 7.38, respectively, which are quite large, indicating aspects of the crystal structure are poorly defined. Both PETN and CH-PETN appear to have acceptable changes in unit cell volume as a result of the optimisation process (less than 5 % change) [30]. The same cannot be said for the optimisations of PO-PETN and NG, however, where there is a significantly larger change in the percentage volume, particularly in the case of PO-PETN. Despite this, Γ -point (Brillouin Zone centre) vibrational frequency calculations were completed for each of the four nitrate ester structures, and each resulted in 3N real vibrations with an acoustic mode along each of the coordinate axes. This suggests that the geometry optimisation process was successful at locating the global minimum for each of the structures.

With vibrational frequency calculations complete, the impact event can be simulated using the vibrational up-pumping procedure once a number of material properties are determined. As before the location of Ω_{\max} was determined through the standard CoM analysis, with data shown in Figure 5.29.

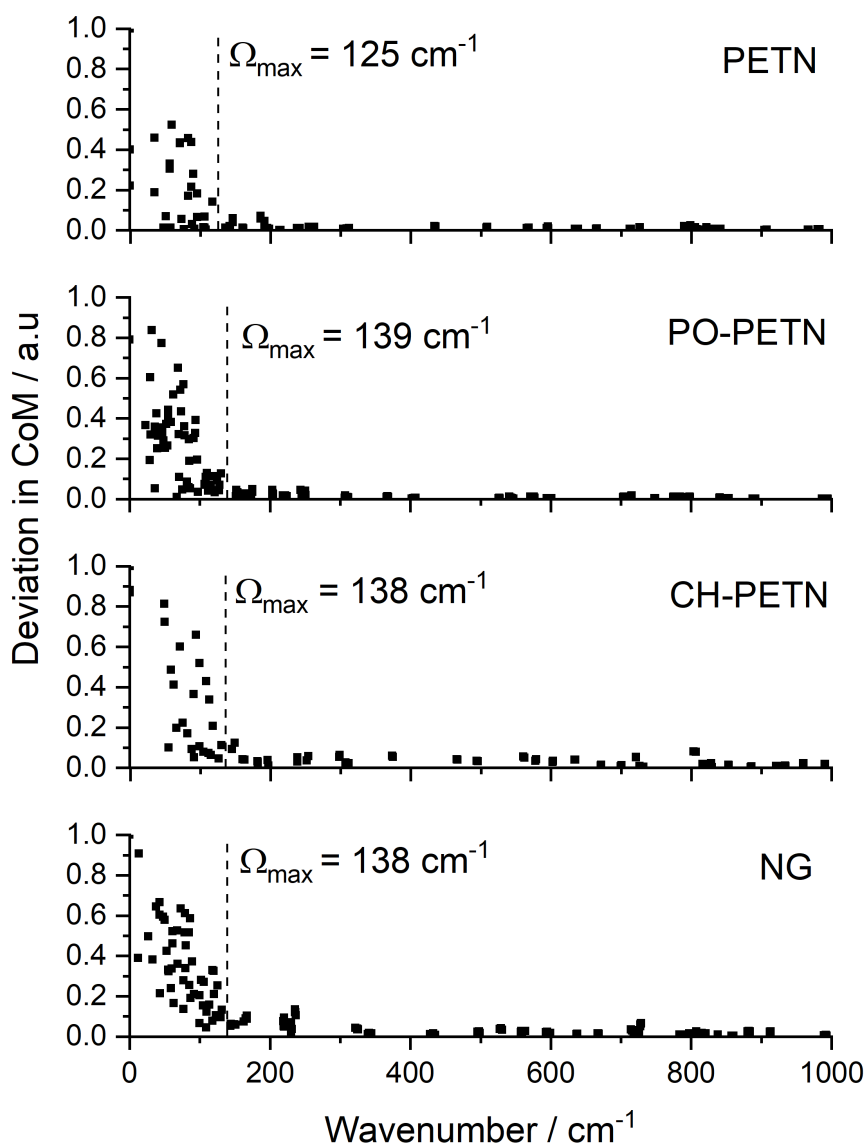


Figure 5.29: Shows the average deviation in CoM (normalised to unity) per molecule of the four nitrate ester EMs considered in this work.

There is a dramatic drop off in the deviation in CoM for each of the materials as the vibrational frequency is increased. The location of Ω_{\max} for the nitrate esters is clear cut as it is placed immediately following the plateau of CoM deviation. This results in lower than typical values (ca. 200 cm⁻¹); short phonon baths are a likely indication of weak intermolecular interactions (contrast with the broad phonon baths observed in Chapter 4 for the coordination polymers), which is in keeping with the low melting points expressed by these compounds. The $g(\omega)$ plots, shown with the standard Gaussian smearing width (5 cm⁻¹), with the limits of the up-pumping windows drawn are given in Figure 5.30.

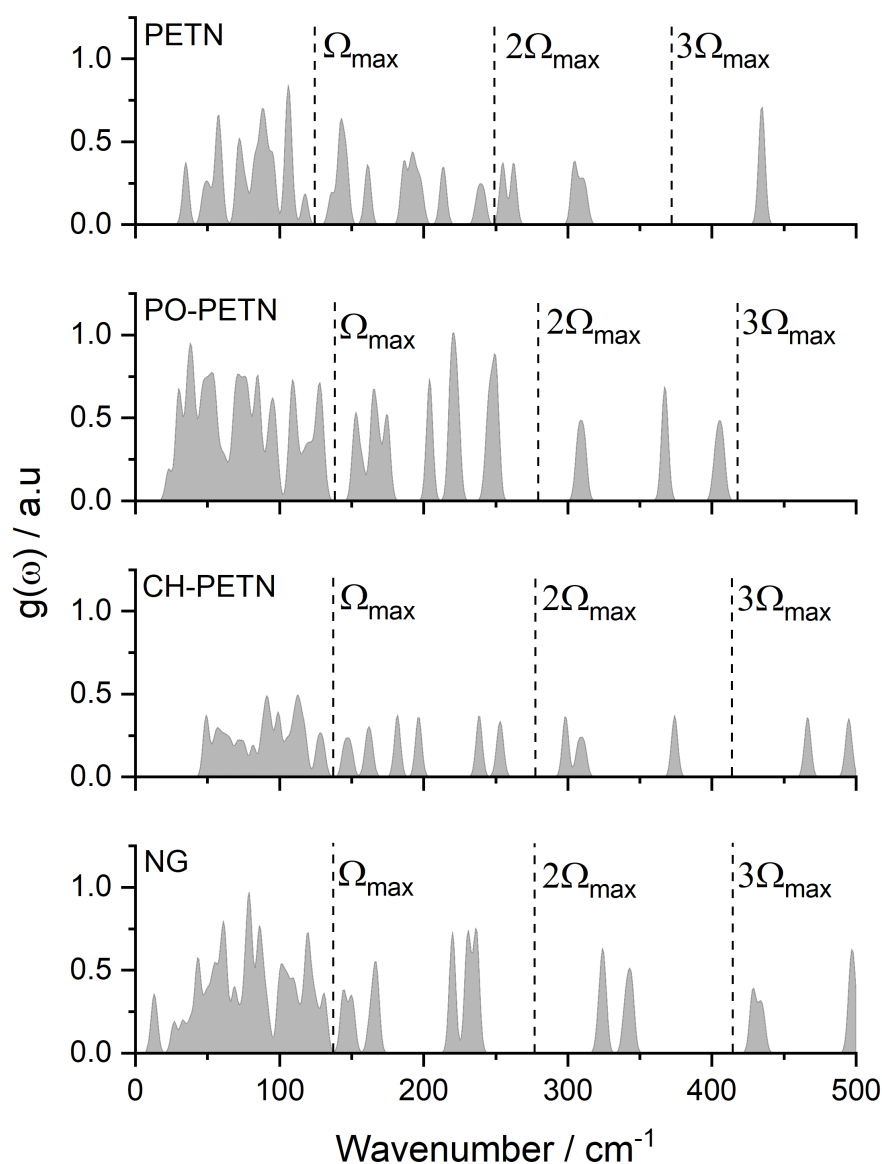


Figure 5.30: Shows the $g(\omega)$ spectra for the nitrate ester EMs with multiples of Ω_{\max} denoted using dashed lines.

From the $g(\omega)$ plots shown in the plot above it is clear that all compounds present a large amount of vibrational character within their respective doorway regions ($1-2 \Omega_{\max}$), which has been highlighted in the two preceding Sections in this Chapter as being associated with a high impact sensitivity response. This is a promising early indication that these materials are therefore likely to return high vibrational up-pumping integrations.

The T_{shock} values for each material were determined in the standard way through consideration of the ratio of $C_{\text{tot}}/C_{\text{ph}}$ (based on $C_{\text{tot}}/C_{\text{ph}} = 5.22$ equating

to a T_{shock} value of 3423 K) [4]. The location of each variable is shown graphically for each nitrate ester in Figure 5.31.

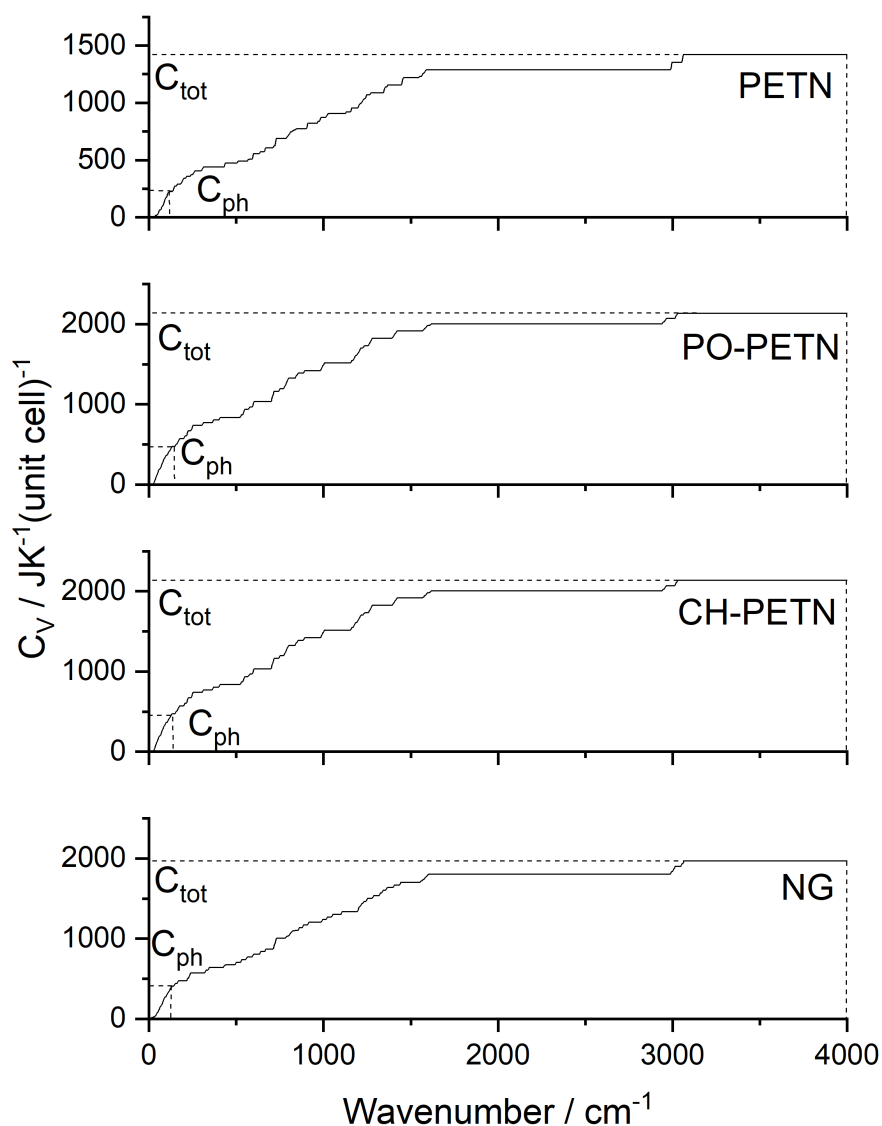


Figure 5.31: Shows the cumulative contributions to the heat capacity from each vibrational mode for each of the nitrate esters considered in this work with C_{tot} and C_{ph} denoted using dashed lines.

The complete set of input parameters for the vibrational up-pumping alongside the experimental sensitivities and up-pumped densities are outlined in Table 5.5.

Table 5.5: Shows the input parameters used for the vibrational up-pumping procedure as well as the experimental sensitivity and up-pumped densities of each of the nitrate ester EMs.

| EM | Ω_{\max} | Z | Z(6+Y) | Y | $C_{\text{tot}}/C_{\text{ph}}$ | T_{shock} / K | Experimental IS / J | Up-pumped density / a.u |
|---------|-----------------|---|--------|---|--------------------------------|------------------------|---------------------|-------------------------|
| PETN | 125 | 2 | 30 | 9 | 6.33 | 4147 | 3 | 176775 |
| PO-PETN | 139 | 4 | 60 | 9 | 4.51 | 2963 | 2 | 104864 |
| CH-PETN | 138 | 2 | 26 | 7 | 4.51 | 2956 | 6 | 66364 |
| NG | 138 | 4 | 52 | 7 | 4.84 | 3168 | 14 | 64273 |

As can be seen from Table 5.5, each of the nitrate ester materials are particularly sensitive to mechanical impact, with each requiring less than 15 J of energy to initiate. The up-pumped density values are also shown, which were determined through rationalisation of the integral of the $\Omega^{(2)}$ when projected onto the underlying $g(\omega)$, both of which are shown in Figure 5.32.

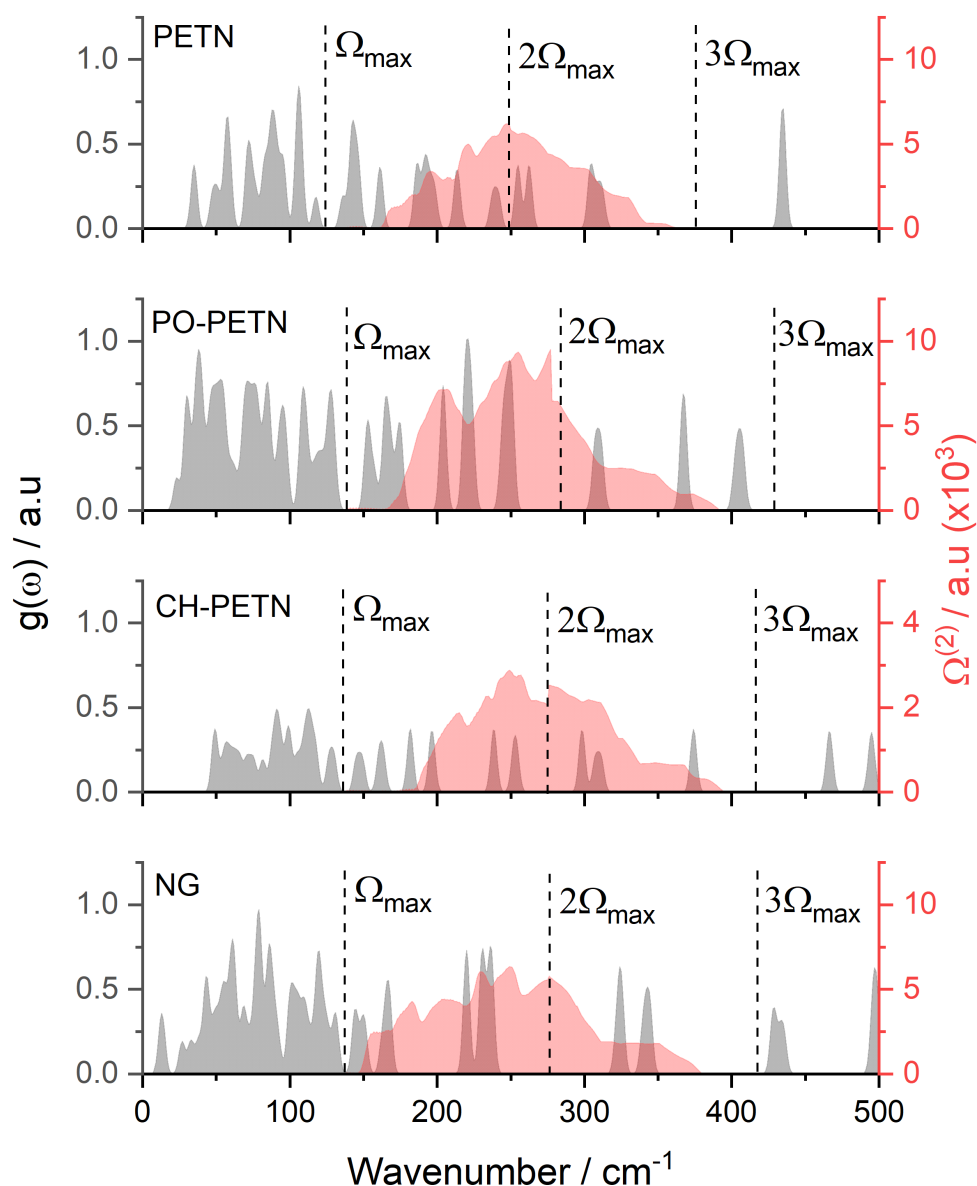


Figure 5.32: Shows the $\Omega^{(2)}$ trace (red) overlaid on the $g(\omega)$ (grey) with multiples of Ω_{\max} denoted using dashed lines.

The $\Omega^{(2)}$ traces shown in Figure 5.32 are all very similar in terms of shape and size, with the exception of CH-PETN which is roughly half as intense (due to having less molecules than PO-PETN and NG and a smaller phonon bath than PETN). It is also clear that the amount of vibrational character present beneath the $\Omega^{(2)}$ trace is high for both PETN and PO-PETN, suggesting that the energy will be more efficiently captured in these materials. The up-pumped density plotted against the experimental sensitivities of the nitrate ester materials compared to the well-studied molecular EMs are shown in Figure 5.33.

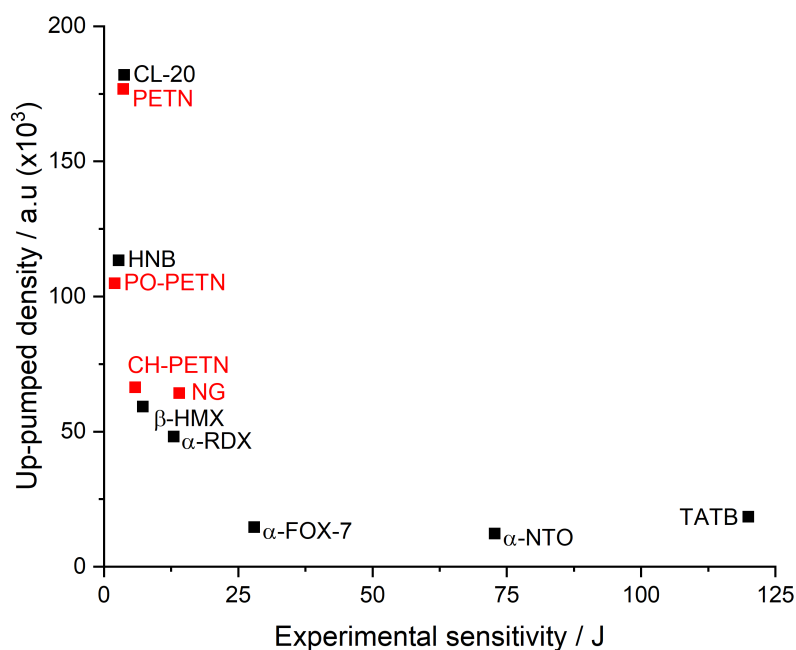


Figure 5.33: Shows the relationship between the up-pumped density and the experimental sensitivity of the nitrate ester EMs (red) compared with a number of well understood molecular EMs (black) [4, 6].

It is clear from Figure 5.33 that each of the nitrate ester EMs is correctly predicted to be a primary energetic, as each fall above β -HMX (often regarded as representing the border between primary and secondary energetic behaviour) [50]. When considering the relative ranking it appears that PETN and PO-PETN are ranked incorrectly with respect to one another (as are HNB and CL-20) but are both predicted to be exceptionally sensitive so that is not too concerning. CH-PETN is ranked similarly to NG. The impact sensitivity of CH-PETN was measured for both states of matter by Manner et al., (the same work as crystal structures in this investigation were taken from) where it was shown that the liquid is three times more sensitive than that of the solid form [43]. The same conclusion has been made regarding NG by Jones et al., who tested both solid and liquid NG and found the liquid state to be exceptionally sensitive (<1 J) [46].

In a similar vein as the work in the previous Sections of this Chapter, the origin of the sensitivity to impact for the nitrate ester EMs was rationalised through consideration of their efficiency of energy up-pumping as well as their capacity

to capture up-pumped energy into modes that directly lead to material decomposition.

Firstly, the capacity for up-pumping was investigated through analysis of the number of doorway modes and the relationship between this and molecular flexibility (KMF), the logic being that increased molecular flexibility leads to an increase in the number of low energy vibrational modes that are dominated by librational motion of terminal functional groups (-NO₂). The number of doorway modes per molecule in the unit cell with the KMF and both experimental and predicted sensitivities are shown in Table 5.6 [18].

Table 5.6: Shows the experimental sensitivities alongside the up-pumped densities, number of doorway modes per molecule and the KMF (calculated by Equation 5.1) of the nitrate ester EMs considered in this Section [18].

| EM | Experimental IS / J | Up-pumped density / a.u | # Doorway modes per Z | KMF |
|---------|------------------------|-------------------------------|-----------------------------|--------|
| PETN | 3 | 176775 | 9 | 143.61 |
| PO-PETN | 2 | 104864 | 8 | 95.22 |
| CH-PETN | 6 | 66364 | 6 | 94.75 |
| NG | 14 | 64273 | 10 | 77.04 |

Table 5.6 shows the expected correlation with IS and the number of doorway modes and KMF, with the exception of NG, which presents a surprisingly large number of doorway modes. However, it is clear from the $g(\omega)$ plot in Figure 5.30 that several of the peaks must be close to degenerate (i.e. overlapping), as the number of distinct peaks presented on the $g(\omega)$ is fewer than on the other plots. This will act to reduce the intensity of the $\Omega^{(2)}$ trace that is captured thereby bringing the up-pumped density down. Comparison between the number of doorway modes per Z and the up-pumped density is shown in Figure 5.34 for the nitrate ester EMs, alongside other molecular EMs. A similar trend as observed for the compounds presented in the previous two Sections is readily apparent. The two outliers are NG (which has been accounted for above) and PETN. The reason the latter sits higher on the graph is the same reason why the former sits lower: the doorway modes in PETN are spread out, in contrast to those for NG being bunched together. As a result, the PETN up-pumping signal generation is boosted more of it is captured.

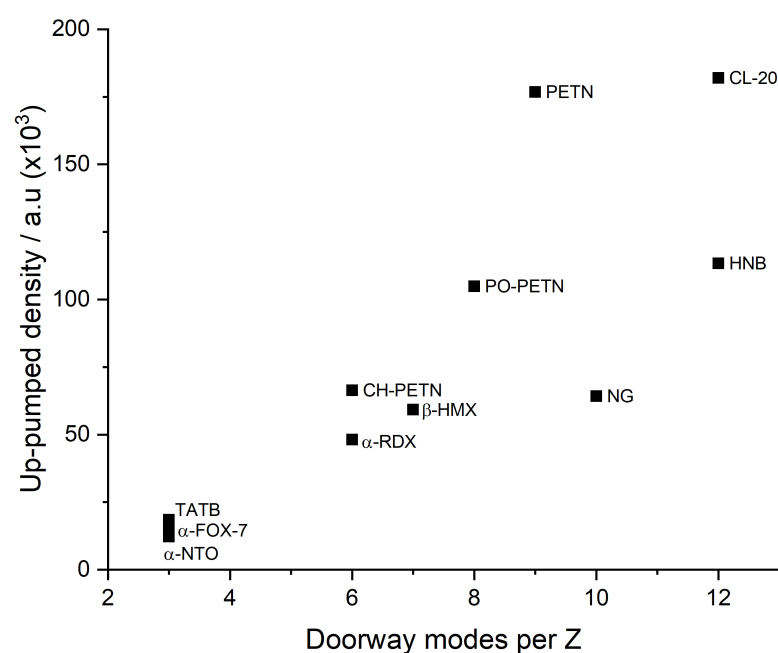


Figure 5.34: Shows the relationship between the number of doorway modes per Z and the up-pumped density for the four nitrate ester EMs considered alongside a number of well-studied EMs [4, 6].

The plot of up-pumped density against the molecular flexibility index in Figure 5.35. A good correlation is observed here, suggesting a clear link between molecular flexibility and impact sensitivity exists.

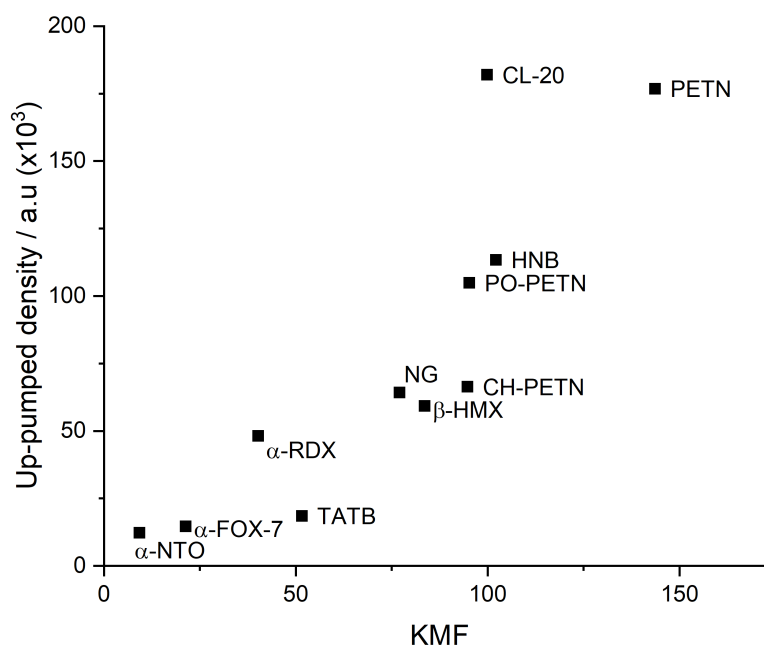


Figure 5.35: Shows the relationship between the up-pumped density and Kier molecular flexibility (KMF) for the four nitrate esters considered in this work alongside a number of well-studied EMs [4, 6].

In an attempt to assess the extent of energetic character activated through the vibrational up-pumping of impact energy, the weak bonds of the nitrate ester materials were once again investigated.

Manner et al. conducted a molecular dynamics simulation in an attempt to understand how the impact event leads to initiation of a liquid sample of PETN type materials. It was found that a common route of molecular decomposition was initiated through cleavage of a terminal CO–NO₂ bond, which results in subsequent cleavage of the C–C bond on the same ‘arm’ as the initial group, to result in the complete removal of one of the nitrate ester groups. Following this, cleavage of a C–O bond on a neighbouring nitrate ester ‘arm’ group is observed. It was noted that these reactions occurred on an incredibly fast timescale (less than 10 fs). An additional competing reaction was the removal of HONO from the system through cleavage of the O–N bond once again. This work exemplified that cleavage of any number of bonds in the nitrate ester structure is a key step towards the initiation of the liquid phase of the EMs. While such mechanisms do not directly translate to the solid-state material, it

is likely initiation is still tied to the cleavage of one or more of these weak bonds. As such, an LModeA analysis was completed for each of the four nitrate esters considered in this work to assess the relative bond strengths and determine which are likely to play a role in the initiation process. The structure of the nitrate esters are shown in Figure 5.36, with weak bonds denoted in red and their force constants (in mDynÅ⁻¹) shown alongside.

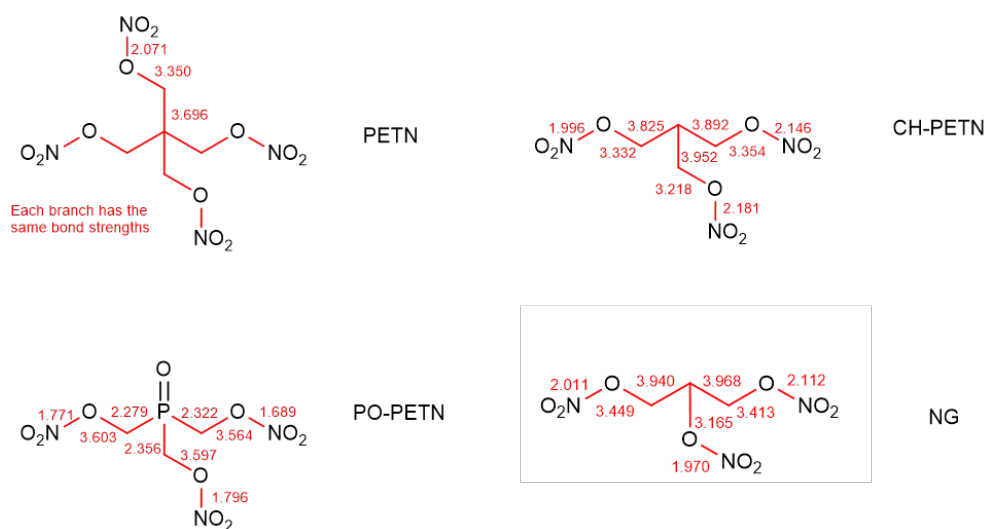


Figure 5.36: Shows the structure of the nitrate ester EMs considered in this work with weak bonds shown in red with force constants (in mDynÅ⁻¹ calculated using LModeA) shown alongside [13].

From Figure 5.36, the following trends can be observed for each of the nitrate ester EMs.

1. The local force constants determined for the materials show that the bonds observed to be broken in the molecular dynamics simulation conducted by Manner et al., are all comparable in strength to the weak bonds considered in previous Sections.
2. The terminal O-NO₂ bonds are the weakest bonds in each of the four structures.
3. The C-P bonds of PO-PETN are much weaker than the analogous C-C bonds in the three remaining structures (~ 2.3 compared to 3.7 – 3.9 mDynÅ⁻¹).

4. With the exception of PO-PETN, the bonds increase in strength as the centre of the molecule is approached.

The deviations in the length of the weak bonds were once again tracked through the eigenvectors for each of the nitrate esters in order to assess the extent of deviation exhibited within the up-pumping window, and to gauge whether or not cleavage of a weak bond is feasible through vibrational up-pumping. The stretching motion contributions in each vibrational mode, for each weak bond type, are shown overlaid on the $g(\omega)$ and $\Omega^{(2)}$ traces for each material in Figure 5.37.

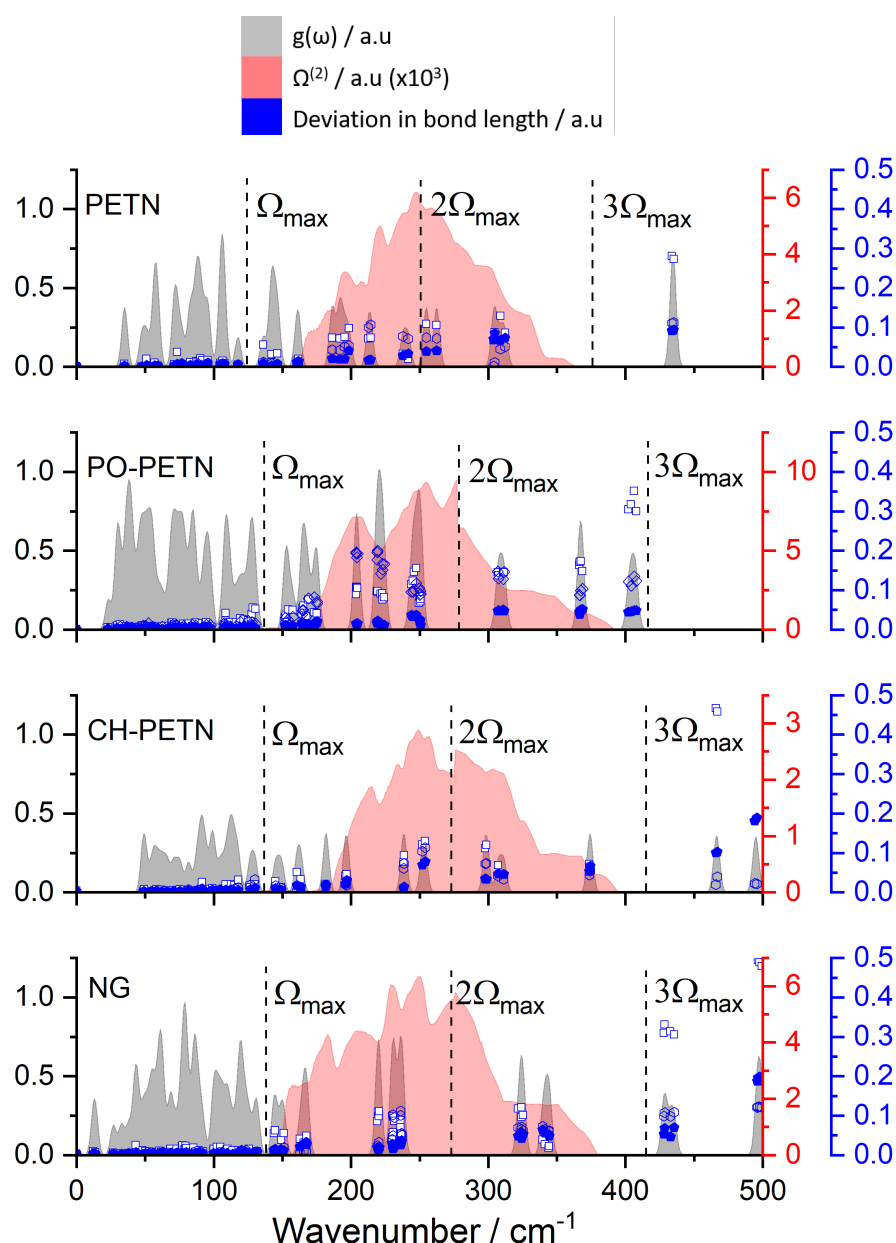


Figure 5.37: Shows the deviation in O–N (white filled, open blue squares), C–O (solid blue pentagons), C–C (open blue hexagons) and C–P (open blue diamonds) bond lengths overlaid on the $g(\omega)$ (grey) and $\Omega^{(2)}$ (red) for the four nitrate EMs considered in this work.

It is clear from Figure 5.37 that there is some weak bond stretching present in the up-pumping window of each of the nitrate ester EMs considered in this work, suggesting that impact energy will efficiently be channelled into vibrational modes that result in activation of weak bond stretching motion. This stretching is likely sufficiently excited to result in bond cleavage and molecular breakdown. In keeping with the previous two Sections, the up-pumping

projections were kept for all frequencies that result in > 10 % weak bond stretching character (marked with asterisks in Figure 5.33). This gives the plot shown in Figure 5.38.

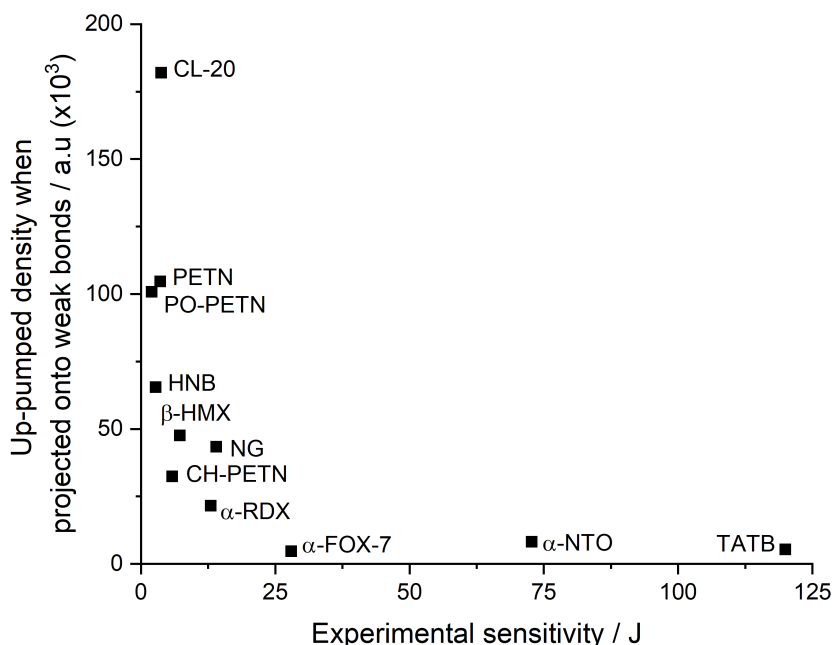


Figure 5.38: Shows the up-pumped density projected onto modes containing weak bond stretching compared to experimental sensitivity for each of the four nitrate ester EMs considered in this Section alongside a number of previously well-studied EMs [4, 6].

The relationship between experimental sensitivity and both the complete up-pumped density and when it is projected onto weak bonds are very similar, with good agreement seen for the nitrate ester EMs. The primary difference between Figures 5.33 and 5.38 is that the predicted sensitivity for all materials (with the exception of CL-20) has decreased as a result of projecting onto less vibrational modes. This is most notable in the case of PETN, which has fallen to be comparable to PO-PETN (roughly 70×10^3 y-axis units), which brings their predictions closer in alignment with their similar experimental IS values. CH-PETN is (incorrectly) assigned as a secondary EM, as it sits below β -HMX. This is the only significant worrisome feature of Figure 5.38. Otherwise, it is clear that the relative sensitivity responses for the nitrate ester EMs can be simply explained in terms of their molecular flexibility as they are almost

entirely comprised of weak bonds. This is exemplified clearly by the comparison between PETN and the 3 other nitrate ester EMs, where the loss of an organic side chain results in a decrease in flexibility, weak bond count and predicted impact sensitivity.

5.5.3 Conclusions

In this section a number of highly sensitivity nitrate ester EMs had their impact sensitivities predicted using the vibrational up-pumping procedure after comprehensive geometry optimisation and Γ -point vibrational frequency calculation. Predicted values were found to be in excellent agreement with experimental sensitivities, outlining that the vibrational up-pumping methodology is a suitable approach for the sensitivity prediction of nitrate esters. Additionally, this work provided validation of the observation that NG is less sensitive as a solid than it is as a liquid (14 J as opposed to < 0.2 J) as NG was found to have an up-pumped density comparable to β -HMX. It was found that there is a good relationship between the up-pumped density and the molecular flexibility (KMF), with increasing flexibility resulting in increased sensitivity. The number of doorway modes per molecule as well as their distribution within the window were found to be important factors that also influence the sensitivity for example, NG has a larger number of doorway modes than would be expected for its sensitivity, however, a number of modes are near degenerate (present at very similar frequency values) resulting in reduced capture capacity. Moreover, the probable trigger modes (stretches of weak bonds – determined using the local mode tracking script detailed in Chapter 2) were considered in isolation from non-trigger modes in an attempt to rationalise the amount of energy that is directly able to cause an energetic response. Projection up-pumped energy solely onto the probable target modes resulted in a very similar trend to projecting over the whole up-pumping window, with the slight underprediction of the sensitivity of CH-PETN. Despite this, the values in general show great agreement with experimentally derived values, suggesting that consideration of target modes is a promising route for driving the methodology forwards.

5.6 Overall Conclusions

To conclude, a large number of EMs from three structural families, namely pyrazoles, tetrazoles and nitrate esters had their impact sensitivities predicted computationally through use of the vibrational up-pumping methodology. It was found that predicted sensitivities were generally in excellent agreement with experimental values across the three families, with a significant outlier in the over prediction of 1,4-DADNP which was mitigated when up-pumped energy was projected only onto probable target modes. A key takeaway from this work is that the predicted sensitivity values of the solid-state nitrate ester EMs were found to be in excellent agreement with experimental values, as they had previously not been studied using the vibrational up-pumping methodology.

In an attempt to develop structure/property relationships two primary material properties were investigated, namely, the up-pumping capacity (ability to transfer impact energy into higher energy modes attributed to energetic performance) as well as the capture capacity (degree of target mode behaviour within the up-pumping window).

It was noted that the more sensitive materials are generally more substituted structures (especially containing nitro groups) and it was shown that an increase in the number of functional groups results in increased vibrational character (librational motion) just above the phonon bath region. These doorway modes are able to take part in subsequent scattering of energy upwards as well as capture up-pumped energy, significantly increasing the magnitude of the $\Omega^{(2)}$. While this showed some promise, a more comprehensive metric was used to quantify the flexibility of the material, the Kier molecular flexibility index (KMF). There was found to be good agreement between the KMF of the molecular structure and the up-pumped density, suggesting that the more flexible the molecular structure, the larger the up-pumping capacity. Clearly this does not account for a variety of solid-state phenomena such as intermolecular interactions but provides a very quick and simple metric to get a rough idea of the sensitivity of a novel material based solely on the molecular structure.

With a metric to define the up-pumping capacity outlined, whether or not each vibrational mode within the up-pumping window can result in energetic performance was investigated. It is generally accepted that cleavage of weak ‘trigger’ bonds acts as the first step towards energetic performance, as such the bond strengths for each of the EMs considered were calculated using gas-phase LModeA calculations. The up-pumped density was re-evaluated projected onto the vibrations in which the weakest bonds in the structure are stretched. This resulted in a very similar decay trace as was determined when the complete up-pumping window was projected onto, with the primary difference being a dramatic decrease in the predicted sensitivity of 1,4-DADNP which was previously vastly over predicted. Projection solely onto probable target modes provides a potential route for further development of the vibrational up-pumping procedure as a whole. This work was only made possible by development of the local mode tracking script outlined in Chapter 2, as without this it would not be possible to know which modes produced a significant enough deviation in weak bonds to be considered as target modes.

This work has shown that increasing both the KMF and the number of weak bonds in the system (which may be achieved through addition of nitro groups) results in increased predicted sensitivity. While crude, this approach shows quantitatively that a direct increase in the number of nitro groups/weak bonds results in increased low energy vibrational character and as such increased sensitivity for EMs from a variety of structural types.

Finally it should be noted that this study was, once again, completed using Γ -point vibrational frequencies (in the interest of compute time/cost) which result in systematic under sampling of the phonon bath region and as such causes a significantly smaller $\Omega^{(2)}$ trace to be generated in up-pumping. A direct result of this is that the general trend of predicted vs experimental sensitivities resembles a decay curve rather than a more linear relationship, this loss in data is compounded when projected on a subset of vibrational modes. As such repeating the analysis with full BZ sampling either at greater computational cost or through parametrised methods such as DFTB/GNF2-xTB is of top priority as the differences between high and low sensitivity materials will likely

be much more apparent. Potentially leading to improved structure/property metrics being visible.

5.7 References

1. A. A. Michalchuk, P. T. Fincham, P. Portius, C. R. Pulham and C. A. Morrison, *A Pathway to the Athermal Impact Initiation of Energetic Azides*, *J. Phys. Chem. C.*, 2018, **122**, 19395 – 19408.
2. A. A. L. Michalchuk, S. Rudic, C. R. Pulham and C. A. Morrison, *Vibrationally Induced Metallisation of the Energetic Azide α -NaN₃*, *Phys. Chem. Chem. Phys.*, 2018, **20**, 29061-29069.
3. A. A. Michalchuk, M. Trestman, S. Rudic, P. Portius, P. T. Fincham, C. R. Pulham and C. Morrison, *Predicting the reactivity of energetic materials: an ab initio multi-phonon approach*, *J. Mat. Chem. A*, 2019, **7**, 19539–19553.
4. A. A. L. Michalchuk, J. Hemingway and C. A. Morrison, *Predicting the impact sensitivities of energetic materials through zone-center phonon up-pumping*, *J. Chem. Phys.*, 2021, **154**, 064105.
5. A. A. L. Michalchuk, S. Rudic, C. R. Pulham and C. A. Morrison, *Predicting the impact sensitivity of a polymorphic high explosive: the curious case of FOX-7*, *Chem. Commun.*, 2021, **57**, 11213.
6. I. L. Christopher, C. R. Pulham, A. A. L. Michalchuk and C. A. Morrison, *Is the impact sensitivity of RDX polymorph dependant?*, *J. Chem. Phys.*, 2023, **158**, 124115.
7. T. M. Klapötke, *Chemistry of High-Energy Materials*, De Gruyter, Berlin, 5th edn., 2019.
8. S. J. Clark, M. D. Segall, C. J. Pickard, P. J. Hasnip, M. J. Probert, K. Refson and M. Payne, *First principles methods using CASTEP*, *Z. Kristall.*, 2005, **220**, 567–570.
9. B. G. Pfrommer, M. Cote, S. G. Louie and M. L. Cohen, *Relaxation of Crystals with the Quasi-Newton Method*, *J. Comput. Phys.*, 1997, **131**, 233–240.
10. F. Herman, J. P. Van Dyke and I. B. Ortenburger, *Improved statistical exchange approximation for inhomogeneous many-electron systems*, *Phys. Rev. Lett.*, 1969, **22**, 807–811.
11. Tkatchenko and M. Scheffler, *Accurate molecular van der Waals interactions from ground-state electron density and free-atom reference data*, *Phys. Rev. Lett.*, 2009, **102**, 073005 1–4
12. S. Baroni, S. D. Gironcoli, A. D. Corso and P. Giannozzi, *Phonons and related crystal properties from density-functional perturbation theory*, 2001 73, 516-557.

13. Y. Tao, W. Zou, M. Friendorf, M. Makos, N. Verma and E. Kraka, *Local vibrational mode analysis, Program LMODEA(F90), Ver. 2.0.0, Computational and Theoretical Chemistry Group (CATCO), SMU, Dallas, Texas 75275 USA, 2020.*
14. M. J. Frisch et al., *Gaussian 16, Revision A.03*, Gaussian, Inc., Wallingford CT, 2016.
15. A. D. Becke, *Density-functional exchange-energy approximation with correct asymptotic behaviour*, *Phys. Rev. A*, 1988, **38** (6), 3098–3100
16. C. Lee, W. Yang, R. G. Parr, *Development of the Colle-Salvetti correlation-energy formula into a functional of the electron density*, *Phys. Rev., B*, 1988, **37** (2), 785–789
17. G. Van Rossum and F. L. Drake, *Python 3 Reference Manual*, Scotts Valley, CA: CreateSpace, 2009.
18. L. B. Kier, *An Index of Molecular Flexibility from Kappa Shape Attributes*, *Mol. Inform.*, 1989, **8**, 221-224.
19. P. Yin and J. M. Shreeve, *Chapter Four – Nitrogen-Rich Azoles as High Density Energy Materials: Reviewing the Energetic Footprints of Heterocycles*, *Adv. Heterocycl. Chem.*, 2017, **121**, 89-131.
20. Y. V. Nelyubina, I. L. Dalinger, K. A. Lyssenko, *Pseudosymmetry in Trinitropyrazole: The Cost of Error in Space-Group Determination*, *Angew Chem.*, 2011, 50, 2892-2894
21. G. Herve, C. Roussel, H. Graindorge, *Selective Preparation of 3,4,5-Trinitro-1H-Pyrazole: A Stable All-Carbon-Nitrated Arene*, *Angew. Chem. Int. Ed.*, 2010, 49, 3177-3181.
22. M. F. Bölter, A. Harter, T. M. Klapötke and J. Stierstorfer, *Isomers of Dinitropyrazoles: Synthesis, Comparison and Tuning of their Physicochemical Properties*, *ChemPlusChem*, 2018, **83**, 804-811.
23. C. Lizhen, S. Liang, C. Duanlin and W. Jianlong, *Crystal structure of 3,4-dinitropyrazole C₃H₂N₄O₄*, *Z. Kristall.*, 2016, **231**, 1099-1100.
24. C. Foces-Foces, A. L. Llamas-saiz, M. Menendez, N. Jagerovic and J. Elguero, *Structure of 3-nitropyrazole in solution and in the solid state*, *J. Phys. Org. Chem.*, 1998, **10**, 637-645.
25. Y. Zhang, Y. Li, J. Hu, Z. Ge, C. Sun and S. Pang, *Energetic C-trinitromethyl substituted pyrazoles: synthesis and characterisation*, *Dalton Trans.*, 2019, **48**, 1524.
26. R. D. Schmidt, G. S. Lee, P. F. Pagoria, A. R. Mitchell and R. Gilardi, *Synthesis of 4-amino-3,5-dinitro-1H-pyrazole, using vicarious nucleophilic substitution of hydrogen*, *J. Heterocycl. Chem.*, 2009, **38**, 1227-1230.
27. C. He, J. Zhang, D. A. Parrish, J. M. Shreeve, *4-Chloro-3,5-dinitropyrazole: a precursor for promising insensitive energetic compounds*, *J. Mat. Chem. A*, 2013, **1**, 2863.

28. K. V. Domasevitch, I. Gispodinov, H. Krautsheid, T. M. Klapötke and J. Stierstorfer, *Facile and selective polynitrations at the 4-pyrazolyl dual backbone: straightforward access to a series of high-density energetic materials*, *New J. Chem.*, 2019, **43**, 1305.
29. V. A. Kuehl, A. H. Cleveland, C. J. Snyder and D. E. Chavez, *Synthesis and Energetic Properties of N-Substituted 3,4- and 3,5-dinitropyrazoles*, *ACS Omega*, 2023, **8**, 18408-18413.
30. S. Zhang, Z. Gao, D. Lan, Q. Jia, N. Liu, J. Zhang and K. Kou, *Recent Advances in Synthesis and Properties of Nitrated-Pyrazoles Based Energetic Compounds*, *Molecules*, 2020, **25**, 3475.
31. J. Binns, M. R. Healy, S. Parsons and C. A. Morrison, *Assessing the performance of density functional theory in optimizing molecular crystal structure parameters*, *Acta Cryst.*, 2014, **B70**, 259–267.
32. Y. Luo, W. Zheng, X. Wang and F. Shen, *Nitrification Progress of Nitrogen-Rich Heterocyclic Energetic Compounds: A Review*, *Molecules*, 2022, **27**, 1465.
33. T. B. Brill and K. J. James, *Kinetics and Mechanisms of Thermal Decomposition of Nitroaromatic explosives*, *Chem. Rev.* 1993, **93**, 2667-2692.
34. P. Politzer and J. S. Murray, *Energetic Materials Part 2. Detonation, Combustion*, Elsevier, Amsterdam, 2003.
35. T. L. Jensen, J. F. Moxnes, E. Unneberg and D. Christensen, *Models for predicting impact sensitivity of energetic materials based on the trigger linkage hypothesis and Arrhenius kinetics*, *J. Mol. Model*, 2020, **26**, 65.
36. J. C. Gamekkanda, A. S. Sinha and C. B Aakeröy, *Cocrystals and Salts of Tetrazole-based Energetic Materials*, *Cryst. Growth Des.*, 2020, **20**, 2432-2439.
37. G. da Silva and J. W. Bozzelli, *Retro-[3 + 2]-Cycloaddition Reactions in the Decomposition of Five-Membered Nitrogen-Containing Heterocycles*, *J. Org. Chem.*, 2008, **73**, 1343-1353.
38. N. Fischer, K. Karaghiosoff, T. M. Klapötke and J. Stierstorfer, *New Energetic Materials featuring Tetrazoles and Nitramines – Synthesis, Characterization and Properties*, *Z.Kristall.*, 2010, **636**, 735-749.
39. J. J. Sabatini and E. C. Johnson, *A Short Review of Nitric Esters and Their Role in Energetic Materials*, *ACS Omega*, 2021, **6**, 11813-11821.
40. Gibbs, T.R.; Popolato, A. *LASL Explosive Property Data*; University of California, Berkeley, CA, USA, 1980
41. S. Moore, M. Schantz and W. MacCrehan, *Characterization of Three Types of Semtex (H, 1A, and 10)*, *Propellants Explos. Pyrotech.*, 2009, **35**, 540-549.
42. T. Münzel, T. Meinertz, U. Tebbe, H. T. Schneider, D. Stalleicken, M. Wargenau, T. Gori and I. Klingmann, *Efficacy of the long-acting nitro vasodilator pentaerithryl*

- tetranitrate in patients with chronic angina pectoris receiving anti-anginal background therapy with beta-blockers: a 12-week, randomized, double blind, placebo-controlled trial*, *Eur. Heart J.*, 2014, **35**, 895-903.
43. V. W. Manner, M. J. Cawkwell, E. M. Kober, T. W. Myers, G. W. Brown, H. Tian, C. J. Snyder, R. Perriot and D. N. Preston, *Examining the chemical and structural properties that influence the sensitivity of energetic nitrate esters*, *Chem. Sci.*, 2018, **9**, 3649-3663.
 44. D. E. Chavez, M. A. Hiskey, D. L. Naud and D. Parrish, *Synthesis of an Energetic Nitrate Ester*, *Angew. Chem.*, 2008, **47**, 8307-8309.
 45. L. J. Ignarro, *After 130 years, the molecular mechanism of action of nitroglycerin is revealed*, *Proc. Natl. Acad. Sci. USA*, 2002, **12**, 7816-7817
 46. M. L. Jones, and E. Lee, *Impact sensitivity of nitroglycerin*, *J. Energ. Mater.*, 2006, **15**, 193-204.
 47. J. Bernstein, *Ab initio study of energy transfer rates and impact sensitivities of crystalline explosives*, *J. Chem. Phys.*, 2018, **148**, 084502
 48. M. Nieger, J. Lehman, CSD Communication, 2002.
 49. A. A. Espenbetov, M. Y. Antipin, Y. T. Struchkov, V. A. Philippov, V. G. Tsirel'son, R. P. Ozerov and B. S. Svetlov, *Structure of 1,2,3-propanetriol trinitrate (β modification), $C_3H_5N_3O_9$* , *Acta Cryst. C.*, 1984, **40**, 2096-2098.
 50. J. P. Agrawal, *High Energy Materials: Propellants, Explosives and Pyrotechnics*, John Wiley & Sons, New Jersey U.S., 2010.

Chapter 6: Conclusions and Future Outlook

6.1 Conclusions

The work in this thesis has explored the use and improvement of the vibrational up-pumping methodology to predict the mechanical impact sensitivities of a broad range of EMs. The method had originally been developed and tested on molecular-based materials, but its application to co-crystals and coordinated metal salts had previously not been explored. Performing these tests therefore formed a major strand of the work undertaken. In addition to the use of the model in a predictive sense, exploration into in-depth connections between structure and property were explored, in an effort to determine the physical basis of impact sensitivity, such that the model may potentially be used for material design. This formed the second significant strand of the work presented in this thesis.

A number of supplementary scripts have been developed throughout the course of this work to improve both the efficiency and applicability of the vibrational up-pumping methodology. One such script provides a unified method for the generation of the $g(\omega)$ and partial $g(\omega)$ to act as the primary source of input files for the procedure, whilst remaining comparable with previously studied materials. The $g(\omega)$ spectrum of each EM considered in this work was generated using this script, additionally, historic data that has been used for comparative purposes throughout this work was regenerated and shown to match previous methods of generation. In addition, a quantitative approach to assessing the location of Ω_{\max} was developed based on the consideration of molecular centre of mass (CoM), largely removing the reliance on visual eigenvector examination. This approach has also been applied to each EM considered in this work and allowed for a higher degree of confidence to be placed on the location of Ω_{\max} dramatically improving the efficiency of the overall up-pumping procedure. This script was particularly useful for the complex CP structures outlined in Chapter 4, as their interconnected nature blurred the line between delocalised and localised modes. Finally, a script to explore the deviation in local modes (bond stretches/angle bends) within the solid-state vibrational modes for discussion of target mode activation was

developed. This script has been readily applied to the EMs in this work to locate probable target vibrations, and in Chapter 5 used to project up-pumped energy onto a specific subset of vibrational modes. The work presented in this thesis would not have been possible without the development of these scripts.

Throughout this work 30 new EMs have had their impact sensitivity predicted using the vibrational up-pumping methodology and compared to experimental reports with a good trend between the two observed. The predicted sensitivities were generally in excellent agreement with experiment highlighting the ability of the vibrational up-pumping methodology capture the trend of sensitivities across a wide array of EMs of different structure types. This work therefore has shown that such an approach is applicable to a far more structures than the simple molecular EMs that it was initially designed for.

An in-depth exploration into the effect of crystal packing on impact sensitivity was conducted in Chapter 3. This investigation was prompted by the development of both a novel EM/non-EM co-crystal comprised of FOX-7 and p-phenylenediamine (PPD) and a high-pressure polymorph of TNP, both of which were found to be unexpectedly more impact sensitive than the parent compounds they were based on (FOX-7 and TNP respectively). In order to study an EM/non-EM co-crystal using the up-pumping method, a new workflow was needed, which also utilised the novel script to generate the partial $g(\omega)$. This took the form outlined below:

- Complete geometry optimisation and zone-centre vibrational frequency calculation for the co-crystal.
- Generate both the $g(\omega)$ and the partial $g(\omega)$ traces for both co-crystal components using the script outlined Chapter 2.
- Allow every vibration below $2\Omega_{\max}$ to take part in phonon-phonon collisions according to the allowed up-pumping collision pathways defined by the methodology.
- Only consider vibrations with sufficient (in this work > 10 %) EM contribution for energy capture.

- The normalisation process, and determination of the up-pumped density remains the same as for single component EMs.

In the case of FOX-7/PPD it was shown that this modified workflow, while also being physically sound, correctly ranked the sensitivity of the co-crystal compared to the parent EM. Further analysis noted that stronger hydrogen bonding interactions were present in the co-crystal compared to the parent EM. This led to an increase in amalgamated vibrational mode behaviour, causing the location of Ω_{\max} to shift to a higher frequency, and the creation of a broader up-pumping window for the co-crystal. This led to an increase in the number of doorway vibrational frequencies present in the co-crystal. This increase in phonon bath and doorway modes caused a two-fold increase in up-pumping capacity, resulting in increased energy transfer onto a greater number of modes that may result in energetic response.

Chapter 3 also reported the prediction of the impact sensitivity of TNP at ambient and high pressure, with predictions agreeing with experimental findings that exposure to pressure results in an increase in sensitivity. It was noted that TNP Form II (high pressure polymorph) exhibited an increased value of Ω_{\max} and subsequent larger up-pumping window when compared to TNP Form I (ambient pressure polymorph). Here, the primary reason for the increase in impact sensitivity was attributed to a $10\text{-}40\text{ cm}^{-1}$ pressure-induced vibrational mode hardening effect, rather than due to any differences in the hydrogen-bonding network. This was confirmed by predicting the sensitivity of the ambient pressure polymorph whilst exposed to an external pressure of 5.3 GPa, which resulted in a similar degree of vibrational mode hardening and predicted sensitivity increase as that of Form II. Taken together the work presented in Chapter 3 exemplifies the effect that a change in crystal packing can (but does not always) have on mechanical impact sensitivity, which if understood to a sufficient degree may be utilised to design novel materials with tailored sensitivity properties. Additionally, this work has shown that exposure to pressure can result in a dramatic change in impact sensitivity through vibrational mode hardening, highlighting the need for the working pressure range of EMs to be considered closely prior to their regular use.

Chapter 4 considered a number of metal-containing coordination polymers. The rationale for this work was to attempt to understand an observed trend that the metal salts of EMs often present as highly impact sensitive materials. Understanding the reasons for this, often dramatic, material property change had been lacking prior to this work. Determining the value of Ω_{\max} for the highly coordinated materials proved challenging due to the blurring of the transition between delocalised and localised vibrations, meaning that visual examination of the eigenvectors was unreliable. To rectify this, the CoM analysis script developed in Chapter 2 was modified to neglect the acoustic vibrations (as their large displacements resulted in difficult to interpret plots) which allowed a likely value of Ω_{\max} to be determined (two values in the case of the DBX materials). These values of Ω_{\max} allowed the sensitivity to be predicted successfully. A subsequent challenge was the normalisation within the vibrational up-pumping procedure, as typically the up-pumped density is normalised to the number of molecules in the unit cell (Z) to reflect the energy becoming trapped on the molecular unit. For coordinated materials, no such molecules exist meaning that Z was redefined as Z_{eff} and was set to 1 for each of the systems. As such a new workflow for the prediction of the sensitivity coordinated EMs was developed and is outlined below.

- Complete the geometry optimisation and zone-centre vibrational frequency calculations as usual.
- Undertake the standard CoM analysis but normalise the displacements to the maximum mode distortion omitting the acoustic modes (to prevent the acoustic modes drowning out other points).
- If a number of possible locations for Ω_{\max} exist:
 - Compare to the Ω_{\max} value of the molecular EM component that the coordinated EM is based on (if the crystal structure is known).
 - Track probable target modes using the local mode script outlined in Chapter 2.

The most likely position of Ω_{\max} will agree with the molecular component EM and will result in an increased excitation of probable target modes.

- Set $Z = Z_{\text{eff}} = 1$ for the vibrational up-pumping process, to reflect a fully coordinated network unit cell.

This procedure was used for all coordinated EMs studied in this body of work and outlines the importance of both the CoM script and the local mode tracking script in the prediction of the impact sensitivity of CP EMs.

The first EM considered in Chapter 4 was lead azide (LA) which presented a much larger value of Ω_{max} than is typically shown for molecular EMs. As such, the need for up-pumping of energy was brought into question (i.e., if initial shock heating of this enlarged phonon bath was sufficient to cause initiation) and the shocked phonon bath density was explored. Despite correctly predicting LA to be sensitive, consideration of the shocked phonon bath was disregarded for LA when consideration of the target mode of vibration (the azide angle bend) showed that such motion can only be accessed by the up-pumping of the impact energy. The development of the local mode tracking script was integral to the decision to apply the up-pumping procedure to LA. While the vibrational up-pumping methodology slightly under predicted its sensitivity, it was still reassuringly classified as a primary EM. This suggested that the use of the vibrational up-pumping methodology for coordinated metal containing EMs was appropriate.

Work then moved on to consider of a number of copper-based CP EMs, specifically DBX-1, DBX-2 and DBX-3. These proved challenging to process as the exact nature of the target modes of vibration for these structurally complex materials is unknown, however it is believed to be linked to the cleavage of weak bonds in the EM, such as C/N-NO₂ bonds. When the approach outlined above was used for each of the three DBX EMs, the predicted sensitivities followed the same trend as the experimental sensitivities (DBX-3 > DBX-2 > DBX-1) and each were correctly predicted to be primary EMs. This further suggested that the vibrational up-pumping methodology is capable of successfully predicting the impact sensitivities of coordinated metal salts.

A final EM that was considered was Cu(ADNP) which exhibited both pseudo-molecular and coordinated properties, presenting as two separate coordinated

discs in the unit cell. As such, the standard molecular EM approach was employed to predict the impact sensitivity of Cu(ADNP) assuming $Z = 2$ (as there are two separate coordinated discs). The predicted sensitivity was found to be in excellent agreement with the experimentally determined value. When compared to the molecular EM it is based on (ADNP), it was noted that coordination with Cu increased the sensitivity of the base EM. The reason for this was suggested to have been an increase in low energy phonon bath vibrations due to the presence of copper as well as an increase in the extent of doorway mode character. This provides both an increase in the potential for the material to scatter the energy upwards, but also the ability for it to capture energy – resulting in a more sensitive EM.

Taken together, the up-pumping model was able to give new insight as to why the coordinated metal salt form of an EM often presents with a higher mechanical impact sensitivity. The model highlighted that with introduction of heavy metal ions to the structure, the low energy regions are more vibrationally dense and therefore allow for increased upwards scattering. This likely as a result of the increased atomic mass of the metals considered in this work causing their vibrations to fall at lower frequencies. Increased up-pumping of energy into the molecular modes, which are largely unchanged from the uncoordinated material results in an increase in predicted sensitivity, relative to the parent material. A key exception to this is the case of Cu(ADNP) which has one key copper contribution in the doorway region, allowing for increased energy capture also. This work outlines that the impact sensitivity of coordinated metal EMs can be predicted successfully using the vibrational up-pumping methodology even though it was designed with molecular EMs in mind with the assistance of a number of supplementary scripts which have been developed in this work.

With the vibrational up-pumping method now validated for a broader range of materials, work then turned to consider its application as a design tool for molecular EMs. To this end, the impact sensitivities of a number of molecular EMs from three different chemical families, namely, pyrazoles, tetrazoles and nitrate esters were predicted. A generally good agreement between the experimental and predicted impact sensitivities of each of the EMs was

observed, with a small number of minor exceptions and one notable exception (1,4-DADNP) which was dramatically overpredicted. The over prediction of 1,4-DADNP led to partial $g(\omega)$ spectra of its functional groups being calculated which showed that a significant proportion of the vibrational character within the up-pumping window was attributed to the non-energetically active amino groups. This suggested that the number of vibrational modes that are considered for energy capture should be reduced for this EM. As such the local mode analysis script was used to track the change in the weak bonds (which were determined based on mass decoupled force constants calculated from gas-phase LModeA calculations) for each vibrational mode for each EM. It was noted across the three families of EMs that bonds connecting nitro groups to structures were typically weaker than other bonds in the material and were activated in the up-pumping window frequently. Additionally, some non-nitro containing C-N and N-N bonds were found to be weak. In order to reflect the likelihood of weak bond stretching character being activated by vibrational up-pumping, the up-pumped density for each molecular EM was re-evaluated when projected solely onto modes which result in stretching of a weak bond. This not only rectified the previous overprediction of 1,4-DADNP but also resulted in a tighter correlation overall. This finding outlines the one of the clear benefits provided by the local mode tracking script outlined in Chapter 2. While this approach is a clear oversimplification, it provides a potential route for improvement of the methodology.

It was noted that EMs that have increased KMF values, a measure of molecular flexibility, had generally larger predicted sensitivities. This also correlated with an increase in the number of doorway vibrational modes, which provided a correlation between structure and property. Moreover, calculating the KMF value is quick and straightforward, as it is based solely on the molecular structure. This therefore presents a useful design tool to consider for any experimental investigation into new EMs, where the material property outcome of primary or secondary explosive, is unknown. Correlations were found between predicted sensitivity and the number of weak chemical bonds within the respective EM families. This suggested that the impact sensitivity can be considered from two viewpoints, firstly the ability of a material to

channel energy upwards into higher energy vibrations governed by the number of doorway modes and therefore the KMF and secondly, the number of weak bonds that a material possess.

It was noted for pyrazoles that the strength of weak C-NO₂ bonds are further weakened through placement of additional NO₂ groups in the adjacent positions on the ring, likely as a result of increasing steric hindrance. The same weak C-NO₂ bonds were instead strengthened through addition of NH₂ groups in the adjacent positions as a result of increased H-bonding interactions between the groups. As for the tetrazole EMs, a number of substituted alkyl chains were present on the rings which introduced a number of additional weak C-N bonds. Additionally, the location of the substituted groups around the central tetrazole ring altered the bond strengths of the substituents. While the nitrate esters were found to be comprised almost entirely out of weak bonds, particularly the terminal O-NO₂ bonds which gives credence to their reportedly high experimental sensitivities, it was noted that removing a side chain from the base structure of PETN reduced the sensitivity. Such correlations provide potential starting points for tailored EMs with hand-picked properties through targeted substitution of particular functional groups on previously well-characterised EMs.

In summary, this thesis has proven that the vibrational up-pumping method is a reliable and robust tool that can predict the mechanical impact sensitivities of a broad range of energetic materials. Evidence that it can be applied as a design tool, to obtain important structure/property relationships, has also been put forward. This is of key importance, to help bring new innovation and understanding to a field which has long been constrained to the application of just a handful of materials. There is hope that this work will bring new insight, to better understand the properties of energetic materials, and to usher in the ability to rationalise their design for tailored properties.

6.2 Future outlook

It has been noted throughout this work that the use of Γ -point only vibrational frequencies has led to a systematic under sampling of the phonon bath region. This has direct consequences on the degree of vibrational up-pumping

achieved and therefore the predicted sensitivity values. The predicted outputs result in a decay trace, rather than the slightly more linear trace originally outlined by Michalchuk et al. [1]. This has meant that predictions based on Γ -point sampling, while able to differentiate between primary and secondary EMs, are unable to rank the sensitivities of the secondary EMs relative to one another, as the graph essentially flat-lines across these data points. Moreover, the Γ -point phonon bath region appears fragmented as a result of the under sampling, which adds an increased layer of complexity to the assignment of Ω_{\max} . However, increasing the Brillouin zone sampling would result in dramatically increased computational cost: data points would take months, instead of weeks, to compute. This would have severely limited the number of EMs that could be studied in this work.

One potential approach which could be employed to tackle this problem is through the use of parametrised DFT, such as density functional tight binding (DFTB), which is a semiempirical method that incorporates Hückel theory into DFT [2, 3]. Here parametrisation is introduced to account for the electronic overlap integrals and the repulsive core-core interactions, which are stored in the form of Slater-Koster files and are pre-calculated at DFT level. This approach typically results in a 10x speed-up over standard DFT, as all the steps which involve integral evaluation are now replaced by a numerical approximation [4]. Successful implementation of DFTB vibrational frequency calculations would similarly present an opportunity to access the full Brillouin zone for vibrational frequency sampling at a fraction of the computational cost required by DFT. Thus, introducing DFTB calculations into the vibrational up-pumping procedure presents an obvious next step for further work in this area.

A promising outcome of this work was the development of a workflow for two previously unstudied EM structure types. It should be noted that the workflows outlined have not been tested on further co-crystals/CP EMs, and it is important that this is also done. A number of energetic co-crystals (outlined in Chapter 3) have been synthesised to date, the majority of which are comprised of two EMs (such as the common example of CL-20/HMX) which could be utilised here to further validate the method [5]. There are also a handful of EM/non-EM co-crystals which could also be pursued. In the same vein, a

number of other highly sensitive metal salt EMs have been reported, and these could also be considered to provide additional evidence to support the structure/property relationships highlighted in this thesis.

Finally, the ultimate direction of this work is the development of structure/property relationships, which aims to provide key structural understanding of the origin of impact sensitivity. Exploration over a vast number of documented EMs both through the molecular descriptors outlined in this work (KMF and bond strengths) as well as utilising DFTB to improve efficiency of solid-state studies will allow for detailed conclusions to be drawn. Such structure/property relationships can be used to guide further experimental efforts towards the fields ultimate goal of insensitive EMs.

The knowledge gained through use of the vibrational up-pumping methodology alongside the ever-improving field of crystal structure prediction outlines the potential for the molecular structure, crystal structure and impact sensitivity of novel EMs to be rationalised completely *in silico*. Such work would therefore provide a pipeline for significantly safer and cost-effective novel EMs.

6.3 References

1. A. A. Michalchuk, M. Trestman, S. Rudic, P. Portius, P. T. Fincham, C. R. Pulham and C. Morrison, *Predicting the reactivity of energetic materials: an ab initio multi-phonon approach*, *J. Mat. Chem. A*, 2019, **7**, 19539–19553.
2. B. Hourahine et al., *DFTB+, a software package for efficient approximation density functional theory based atomistic simulations*, *J. Chem. Phys.*, 2020, **152**, 124101.
3. P. O. Dral and J. R ezáč, *Quantum Chemistry in the Age of Machine Learning*, Elsevier, Amsterdam, The Netherlands, 1st edn., 2022.
4. Heather Quayle, PhD candidate, Personal Communication, University of Edinburgh, 2023.
5. O. Bolton, L. R. Simke, P. F. Pangoria and A. J. Matzger, *High Power Explosive with Good Sensitivity: A 2:1 Cocrystal of CL-20:HMx*, *Cryst. Growth Des.*, 2012, **12**, 4311-4314.

Appendix A: Unit Cell Optimisation Data

Table A1: Shows the experimental and optimised unit cell parameters, % change in unit cell volume as a result of geometry optimisation as well as both the space group and the number of molecules in the unit cell (Z) for each EM considered in Chapter 3. Values of Z displayed in brackets are those used for normalisation in vibrational up-pumping due to consideration of the computationally less expensive primitive cell.

| EM | a [Å] | b [Å] | c [Å] | α [°] | β [°] | γ [°] | V [Å ³] | % V Change | Space Group | Z |
|---------------------------------|-------------|-----------|-------------|--------------|-------------|--------------|---------------------|------------|--------------------|--------|
| FOX-7/PPD _(exp) | 9.3491(0) | 6.5227(0) | 10.5140(7) | 71.929(37) | 67.166(72) | 90 | 556.4 | - | C2/c | 8 (4) |
| FOX-7/PPD _(calc) | 9.1597 | 6.5900 | 10.5639 | 71.827 | 66.730 | 90 | 551.0 | - 0.97 | - | - |
| TNP (Form I) _(exp) | 15.1586(13) | 8.2781(8) | 17.2014(16) | 90 | 92.275(2) | 90 | 2156.81 | - | P2 ₁ /c | 12 |
| TNP (Form I) _(calc) | 15.4963 | 8.3610 | 17.3980 | 90 | 92.222 | 90 | 2252.48 | + 4.44 | - | - |
| TNP (Form II) _(exp) | 19.5713(11) | 7.6509(8) | 14.6982(9) | 90 | 127.661(2) | 90 | 1742.30 | - | Cc | 12 (6) |
| TNP (Form II) _(calc) | 19.6649 | 7.7154 | 14.8667 | 90 | 127.845 | 90 | 1781.21 | + 2.23 | - | - |

Table A2: Shows the experimental and optimised unit cell parameters, % change in unit cell volume as a result of geometry optimisation as well as the space group and the number of molecules (Z) in the unit cell of each EM considered in Chapter 4. Values of Z displayed in brackets are those used for normalisation in vibrational up-pumping as a result of the coordinated nature of the materials (Z_{eff}). The asterisk on both the space group and number of molecules for Cu(ADNP) is due to the incomplete structure yielding an incorrect values.

| EM | a [Å] | b [Å] | c [Å] | α [°] | β [°] | γ [°] | V [Å ³] | % V Change | Space Group | Z |
|----------------------------|-------------|--------------|--------------|--------------|-------------|--------------|---------------------|------------|---|--------|
| LA _(exp) | 6.64058(10) | 16.28277(17) | 11.33344(17) | 90 | 90 | 90 | 1225.4 | - | Pnma | 12 (1) |
| LA _(calc) | 6.66381 | 16.19932 | 11.74693 | 90 | 90 | 90 | 1268.1 | +3.4 | - | - |
| DBX-1 _(exp) | 10.513(2) | 10.280(2) | 9.402(2) | 90 | 116.032(3) | 90 | 913.023 | - | P2 ₁ /c | 1 |
| DBX-1 _(calc) | 10.713 | 10.463 | 9.571 | 90 | 116.076 | 90 | 963.630 | +5.3 | - | - |
| DBX-2 _(exp) | 10.8980(10) | 9.2377(9) | 10.3680(10) | 90 | 100.493(10) | 90 | 1026.32 | - | P2 ₁ /c | 4 (1) |
| DBX-2 _(calc) | 10.9786 | 9.4615 | 10.5681 | 90 | 99.707 | 90 | 1082.04 | +5.4 | - | - |
| DBX-3 _(exp) | 11.2866(5) | 11.2866(5) | 9.0555(6) | 90 | 90 | 120 | 999.009 | - | P6 ₃ | 2 (1) |
| DBX-3 _(calc) | 11.5480 | 11.5480 | 9.0302 | 90 | 90 | 120 | 1042.890 | +4.4 | - | - |
| Ntet _(exp) | 5.3320(11) | 9.4551(19) | 8.3027(17) | 90 | 107.07(3) | 90 | 400.138 | - | P2 ₁ | 2 |
| Ntet _(calc) | 5.4311 | 9.5080 | 8.6263 | 90 | 106.06 | 90 | 428.052 | +6.98 | - | - |
| Cu(ADNP) _(exp) | 8.2866(7) | 10.3469(9) | 12.5178(14) | 112.668(5) | 104.748(8) | 90.115(6) | 951.711 | - | P1* | 1 (2)* |
| Cu(ADNP) _(calc) | 8.4920 | 10.2108 | 12.9991 | 113.099 | 105.382 | 92.437 | 985.899 | +3.47 | - | - |
| ADNP _(exp) | 4.7257(5) | 4.7312(6) | 27.063(4) | 90.00 | 90.00 | 90.00 | 605.081 | - | P2 ₁ 2 ₁ 2 ₁ | 4 |
| ADNP _(calc) | 4.7957 | 4.8692 | 26.8362 | 90.00 | 90.00 | 90.00 | 626.655 | + 3.57 | - | - |

Table A1: Shows the experimental and optimised unit cell parameters, % change in unit cell volume as a result of geometry optimisation as well as both the space group and the number of molecules in the unit cell (Z) for each EM considered in Chapter 5. Values of Z displayed in brackets are those used for normalisation in vibrational up-pumping due to consideration of the computationally less expensive primitive cell.

| EM | a [Å] | b [Å] | c [Å] | α [°] | β [°] | γ [°] | V [Å ³] | % V Change | Space Group | Z |
|------------------------------|-------------|-------------|-------------|--------------|-------------|--------------|---------------------|------------|--------------------|-------|
| 3,5-DNP _(exp) | 10.6055(3) | 10.3711(3) | 10.4933(3) | 90 | 90 | 90 | 1154.17 | - | Pca2 ₁ | 8 |
| 3,5-DNP _(calc) | 11.0185 | 10.5158 | 10.3589 | 90 | 90 | 90 | 1200.27 | + 3.99 | - | - |
| 3,4-DNP _(exp) | 9.7013(13) | 12.0797(10) | 9.7587(7) | 90.00 | 93.962(11) | 90.00 | 1140.88 | - | P2 ₁ /c | 8 |
| 3,4-DNP _(calc) | 9.9718 | 12.1604 | 9.8915 | 90.00 | 94.033 | 90.00 | 1196.47 | + 4.87 | - | - |
| 1,3-DNP _(exp) | 5.7084(6) | 9.2664(8) | 11.3570(11) | 90 | 103.315(10) | 90 | 584.59 | - | P2 ₁ /c | 4 |
| 1,3-DNP _(calc) | 5.7283 | 9.7425 | 11.2305 | 90 | 103.958 | 90 | 608.25 | + 4.05 | - | - |
| 3-NP _(exp) | 10.1823(12) | 12.5014(20) | 13.1190(17) | 100.26(1) | 104.41(1) | 111.32(1) | 1438.42 | - | P $\bar{1}$ | 12 |
| 3-NP _(calc) | 10.3277 | 12.4509 | 13.0450 | 100.75 | 105.80 | 112.37 | 1411.65 | - 1.86 | - | - |
| 1-N-3-TNMP _(exp) | 10.542(2) | 8.4713(17) | 10.792(2) | 90 | 106.73(3) | 90 | 922.98 | - | P2 ₁ /c | 4 |
| 1-N-3-TNMP _(calc) | 10.893 | 8.5626 | 10.908 | 90 | 106.56 | 90 | 975.20 | + 5.66 | - | - |
| 5-ADNP _(exp) | 7.2132(3) | 12.4258(5) | 7.1598(3) | 90.00 | 106.814(2) | 90.00 | 614.30 | - | P2 ₁ /c | 4 |
| 5-ADNP _(calc) | 7.2002 | 12.5048 | 7.1888 | 90.00 | 106.668 | 90.00 | 620.06 | + 0.94 | - | - |
| 1,4-DADNP _(exp) | 6.4359(4) | 12.7184(7) | 15.8769(10) | 90.00 | 90.00 | 90.00 | 1299.59 | - | Pbca | 8 |
| 1,4-DADNP _(calc) | 6.5686 | 12.8473 | 15.9878 | 90.00 | 90.00 | 90.00 | 1349.18 | + 3.82 | - | - |
| BP-1 _(exp) | 16.4281(13) | 16.4281(13) | 8.3705(6) | 90 | 90 | 90 | 2259.05 | - | P4 ₂ /n | 8 |
| BP-1 _(calc) | 16.9600 | 16.9600 | 8.2518 | 90 | 90 | 90 | 2373.56 | + 5.07 | - | - |
| BP-2 _(exp) | 8.6064(8) | 11.9636(9) | 10.1200(9) | 90 | 114.148(10) | 90 | 950.81 | - | P2 ₁ /c | 4 |
| BP-2 _(calc) | 8.6531 | 12.1639 | 10.2112 | 90 | 114.127 | 90 | 980.89 | + 3.16 | - | - |
| BP-3 _(exp) | 15.9744(9) | 6.5428(8) | 8.9414(8) | 90 | 118.739(10) | 90 | 819.42 | - | C2/c | 4 (2) |
| BP-3 _(calc) | 16.1239 | 6.4231 | 9.1674 | 90 | 118.474 | 90 | 834.58 | + 1.85 | - | - |

Table A3 (continued)

| | | | | | | | | | | |
|---------------------------|------------|------------|------------|-------------|------------|-------------|---------|---------|-------------------|---|
| LUVPOI _(exp) | 9.175(1) | 6.177(1) | 11.171(2) | 90 | 90.382(11) | 90 | 633.09 | - | P2 ₁ | 2 |
| LUVPOI _(calc) | 9.203 | 6.175 | 11.393 | 90 | 89.171 | 90 | 647.36 | + 2.25 | - | - |
| LUVNIA _(exp) | 11.1953(6) | 9.3248(4) | 9.9411(4) | 90 | 111.217(5) | 90 | 967.45 | - | P2 _{1/c} | 4 |
| LUVNIA _(calc) | 11.3801 | 9.4650 | 10.1046 | 90 | 111.130 | 90 | 1015.22 | + 4.82 | - | - |
| LUVPAU _(exp) | 9.2526(5) | 11.3617(6) | 9.5915(6) | 90 | 106.156(6) | 90 | 968.49 | - | P2 _{1/c} | 4 |
| LUVPAU _(calc) | 9.4647 | 11.1173 | 9.5742 | 90 | 106.391 | 90 | 966.47 | + 0.21 | - | - |
| LUVPIC _(exp) | 6.0193(3) | 6.4786(3) | 8.4598(4) | 90 | 98.952(5) | 90 | 325.89 | - | P2 ₁ | 2 |
| LUVPIC _(calc) | 6.0122 | 6.4823 | 8.5290 | 90 | 98.510 | 90 | 328.74 | + 0.87 | - | - |
| LUVPEY _(exp) | 5.8461(3) | 18.4860(7) | 8.0667(4) | 90 | 110.769(5) | 90 | 815.13 | - | P2 _{1/c} | 4 |
| LUVPEY _(calc) | 5.9000 | 18.4565 | 7.8972 | 90 | 111.564 | 90 | 799.82 | - 1.88 | - | - |
| LUVNAS _(exp) | 8.6244(4) | 6.8715(4) | 12.0481(6) | 90 | 98.263(4) | 90 | 706.59 | - | P2 _{1/c} | 4 |
| LUVNAS _(calc) | 8.6817 | 6.7677 | 11.9150 | 90 | 98.861 | 90 | 691.71 | - 2.11 | - | - |
| PETN _(exp) | 9.3027(3) | 9.3027(3) | 6.6403(2) | 90.00 | 90.00 | 90.00 | 574.653 | - | P4 _{2/c} | 2 |
| PETN _(calc) | 9.4311 | 9.4311 | 6.6968 | 90.00 | 90.00 | 90.00 | 595.659 | + 3.66 | - | - |
| PO-PETN _(exp) | 12.370(3) | 8.1257(14) | 9.9430(18) | 90 | 97.638(6) | 90 | 990.552 | - | P2 _{1/c} | 4 |
| PO-PETN _(calc) | 13.133 | 8.4900 | 10.1960 | 90 | 96.911 | 90 | 1128.54 | + 13.93 | - | - |
| CH-PETN _(exp) | 7.6451(14) | 7.8238(17) | 8.9723(15) | 100.557(19) | 96.753(19) | 114.760(14) | 467.594 | - | P1 | 2 |
| CH-PETN _(calc) | 7.7751 | 7.9840 | 9.0813 | 100.416 | 96.775 | 115.074 | 490.074 | + 4.81 | - | - |
| NG _(exp) | 8.900(2) | 13.608(3) | 6.762(2) | 90 | 90 | 90 | 818.954 | - | Pna2 ₁ | 4 |
| NG _(calc) | 9.076 | 13.965 | 6.920 | 90 | 90 | 90 | 876.443 | + 7.02 | - | - |

Appendix B

Published work:

A. A. L. Michalchuk, J. Hemingway and C. A. Morrison, *Predicting the impact sensitivities of energetic materials through zone-center phonon up-pumping*, *J. Chem. Phys.*, 2021, **154**, 064105.

N. Atceken, J. Hemingway, C. L. Bull, X. Liu, A. A. L. Michalchuk, S. Konar, C. A. Morrison and C. R. Pulham, *High-pressure structural studies and pressure-induced sensitisation of 3,4,5-trinitro-1H-pyrazole*, *Phys. Chem. Chem. Phys.*, 2023, **46**, 31646-31654.

In preparation:

D. I. A. Miller, L. K. Cocker, D. R. Allen, A. S. Cumming, A. Khumsri, J. M. Hemingway, A. A. L. Michalchuk, C. A. Morrison, and C. R. Pulham, *Crystal Engineering of Energetic Materials: Rational Design of a FOX-7 Co-crystal*.

B. Westwater, P. McMaster, L. Brammer, T. Roseveare, J. M. Hemingway, C. A. Morrison, P. Portius and C. R. Pulham, *Synthesis and characterisation of the energetic copper azolates Cu_2TNBI , $Cu_4Cl(DNT)_3$* .

B. Westwater, P. McMaster, L. Brammer, T. Roseveare, J. M. Hemingway, C. A. Morrison, P. Portius and C. R. Pulham, *Why does metal salt formation turn secondary energetics into primaries?*

J. M. Hemingway, A. A. L. Michalchuk, and C. A. Morrison, *Towards development of structure/property relationships of energetic materials*.

Appendix C

Conferences attended:

SCOTCHEM Computational Chemistry Symposium (20th June 2023): University of Glasgow – Presented a poster entitled ‘Towards a lead-free primary energetic to replace lead azide’

Joseph Black Conference (31st May 2023): University of Edinburgh – Gave an oral presentation entitled ‘Towards tailoring energetic materials through evaluation of structure-property relationships: A vibrational approach’

SCOTCHEM Computational Chemistry Symposium (30th August 2022): University of Edinburgh – Presented a poster entitled ‘Towards tailoring energetic materials through evaluation of structure-property relationships: A vibrational approach’

Gordon Research Conference: Energetic Materials (June 26th – July 1st 2022): University of Southern New Hampshire, NH, USA – Presented a poster entitled ‘Towards tailoring energetic materials through evaluation of structure-property relationships: A vibrational approach’

Gordon Research Seminar: Energetic Materials (June 25th – June 26th 2022): University of Southern New Hampshire, NH, USA – Gave an oral presentation entitled ‘Towards tailoring energetic materials through evaluation of structure-property relationships: A vibrational approach’

Joseph Black Conference (24th May 2022): University of Edinburgh – Presented a poster entitled ‘Predicting the impact sensitivity of two primary energetics to replace lead azide’

NTREM New Trends in Research of Energetic Materials (April 6th – April 8th 2022): University of Pardubice, Pardubice, Czech Republic – Presented a poster entitled ‘Predicting the impact sensitivity of two possible lead azide replacements’